Détection et quantification operando de l'endommagement dans les composants automobiles en composite polyamide/renfort continu soumis à la fatigue-pré et/ou post impact par les techniques ultrasonores avancées

Nada Miqoi

HESAM UNIVERSITÉ

Arts et Métiers Sciences et Technologies

ÉCOLE DOCTORALE SCIENCES DES MÉTIERS DE L'INGÉNIEUR
[Laboratoire d'étude des microstructures et de la mécanique des matériaux (LEM3) – Campus de Metz]

THÈSE

présentée par : **Nada MIQOI**

soutenue le : **25 novembre 2021**

pour obtenir le grade de : **Docteur d'HESAM Université**

préparée à : **École Nationale Supérieure d'Arts et Métiers**

Spécialité : **Mécanique et Matériaux**

Detection and quantification of damage in a polyamide-based composite submitted to the fatigue-pre and/or post-impact by advanced ultrasonic techniques

THÈSE dirigée par :
Prof. MERAGHNI Fodil

et co-encadrée par :
Prof. DECLERCQ Nico. F

Jury

M. Badreddine ASSOUAR, Directeur de recherche CNRS, Institut Jean Lamour, Université de Lorraine	Président
M. David S CITRIN, Professeur, IRL, GeorgiaTech Atlanta	Rapporteur
M. Mostapha TARFAOUI, Professeur, IRDL- UMR CNRS 6027, ENSTA Bretagne	Rapporteur
Mme. Lynda CHEHAMI, Maitre de conférences, UVHC, Université de Valenciennes	Examinatrice
M. Stéphane DELALANDE, Docteur, Stellantis-Responsable OpenLab materials and processes	Examinateur
M. Nico F DECLERCQ, Professeur, IRL-LUNE, GeorgiaTech Lorraine	Examinateur
M. Fodil MERAGHNI, Professeur, LEM3, Arts et Métiers Sciences et technologies	Examinateur
M. Pascal POMAREDE, Ingénieur de recherche, IRL-LUNE et LEM3, GeorgiaTech Lorraine et Arts et Métiers Sciences et technologies	Examinateur

THÈSE

A mes parents qui m’ont soutenu par leur amour et leurs encouragements pendant toute la période de mes études.

A mon frère Oussama et ma sœur Rania

A ma famille

A mes amis

Et tous ceux qui ont été là pour moi

Remerciements

L’achèvement de ce travail est dû à la précieuse contribution de nombreuses personnes. Je tiens à remercier mon directeur de thèse Fodil MERAGHNI et mon co-directeur Nico. F. DECLERCQ pour m’avoir encadré durant toute la thèse, pour leur confiance et leur soutien, de m’avoir transmis le goût de la recherche et la curiosité scientifique. Leurs compétences scientifiques ainsi que leurs qualités humaines m’ont permis de mener à terme ce travail. Je tiens à remercier Pascal POMAREDE qui a suivi de près les travaux de recherche, qui m’apportais de nouvelles perspectives grâce à tous nos échanges scientifiques et humains. Je tiens à le remercier spécialement pour sa disponibilité, son support et surtout pour tous ses conseils, son sens de compréhension et de l’écoute. Je tiens également à remercier Stéphane DELALANDE pour son encadrement, son dévouement et sa gentillesse.

Je tiens à remercier Badreddine ASSOUAR, de m’avoir fait l’honneur de présider le jury de soutenance, ainsi qu’à Mostafa TARFAOUI et David CITRIN pour avoir pris le temps de rapporter ce travail. Merci aussi à Lynda CHEHAMI d’avoir été examinatrice de ces travaux. Je remercie tous ceux qui ont contribué à mes travaux de thèse, de près ou de loin, et plus particulièrement, Laurent PELTIER pour sa disponibilité, son aide pour les essais expérimentaux, son sourire et bonne humeur et surtout son soutien moral durant les moments les plus difficiles. Un remerciement spécial à Patrick MOLL, Théophile GROSS, Paul LOHMULLER, Paul DIDIER, Gaël LECOZ, Qiang CHEN et Francis PRAUD pour leur joie de vivre et optimisme. Je remercie toute l’équipe SMART pour leur apport scientifique et moral. Mes remerciements les plus sincères vont aussi à tous les membres du LEM3 pour avoir assuré le bon déroulement de la thèse. J’exprime ma reconnaissance à mes collègues pour la bonne ambiance et la convivialité.

Toutes ma reconnaissance va vers mes parents pour leur soutien régulier aux moments les plus compliqués. Ils ont su m’épauler durant toutes mes années d’étude malgré la distance qui rendais cette période plus compliquée. Un grand merci à ma famille et mes amis pour leur patience, encouragements et ondes positives. Je les remercie pour leur soutien indéfectible et leur encouragement. Une pensée chaleureuse pour Amel, Wafa, Myriam et Névine, qui ont été ma deuxième famille et d’avoir veillé toujours à mon bien-être.

Résumé

La détection et la caractérisation des endommagements dans des composantes automobiles fabriquées en matériaux composites restent un souci majeur que les constructeurs automobiles cherchent à confronter. Le projet de thèse s'inscrit dans cette thématique et a comme but l'analyse qualitative et quantitative des endommagements induits par différentes sollicitations dans un composite à matrice polyamide 66/6 renforcé de fibres de verre tissées sergé 2/2. Pour cela, des essais d'impact à faible vitesse à différents niveaux d'énergie, des essais de fatigue en traction-traction ainsi que des essais d'impact post-fatigue, sont réalisés. Une méthodologie expérimentale qui repose sur l'utilisation des méthodes de contrôle non-destructif est établit et a pour but l'évaluation de l'endommagement induit par différents chargements. Des outils sont utilisés dans cette étude, à savoir : la microscopie optique, la microscopie électronique, la tomographie aux rayons X, les ondes guidées (les ondes de Lamb), l'imagerie C-Scan par propagation des ondes de volumes et d'autres outils ultrasonores. En effet, les mécanismes d'endommagement liés aux multiples sollicitations sont observés et leurs degrés de propagation en fonction du type et du niveau de chargement sont examinés. En outre, une investigation basée sur la propagation des ondes de Lamb est menée. A l'issu de cette étude, des indicateurs d'endommagement, permettant de quantifier l'état d'endommagement induit dans chaque échantillon inspecté, sont proposés. Finalement, des essais de traction quasi-statique sont réalisés pour la prédiction des propriétés résiduelles post-chargement.

Mots clés : Composite, Impact, Fatigue, Endommagement, Ultrasons, Ondes de Lamb.

Résumé en anglais

The detection and characterization of damage in automotive components made of composite materials remains a major concern that automotive manufacturers are seeking to address. The aim of this thesis project is to qualitatively and quantitatively analyze the damage induced by different solicitations in a polyamide 66/6 based composite reinforced with 2/2 woven glass fibers intended for automotive applications. For this purpose, low-velocity impact tests at different energy levels, tensile-tensile fatigue tests as well as impact post-fatigue tests are conducted. An experimental methodology relying on the use of non-destructive testing methods (NDT) is established and aims at the assessment of the damage induced by different types of loads. Several tools are used in this study, namely: optical microscopy, X-ray tomography, guided waves (Lamb waves), C-Scan imaging and other ultrasonic tools. The damage mechanisms associated with the multiple loading are observed and their degrees of propagation as a function of the type and level of loading are examined. The stiffness matrix components are estimated by means of the velocity of propagation of the bulk waves. Furthermore, a Lamb waves-based investigation is conducted. By estimating the velocity of propagation of the waves, velocity profiles as a function of the angle of emission/reception are obtained. As a result of this study, several damage indicators are proposed to quantify the damage state induced in each inspected specimen. A good correlation between all experimental results is found indicating the efficiency of the developed Lamb waves-based method. Finally, quasi-static tensile tests are carried out to estimate the post-loading residual properties.

Keywords: Composites, Impact, Fatigue, dammage, ultrasound, Lamb wav

Table of content

List of tables

List of figures

General introduction

Nowadays, the increase of the petroleum and fuel prices along with the strict European requirements in terms of CO_2 emissions have pushed the automotive industry to make a new generation of vehicles (EU Climate Action, 2019; *Lightweight Materials for Cars and Trucks*, n.d.; US department of energy, 2011). The key aspect of this approach is to build lightweight vehicles by replacing the structural metallic elements by lighter materials with low density and high mechanical properties (Böhm et al., 2020; Sarfraz et al., 2021). To achieve this goal, the interest towards the use of polymer-based composite materials has been continuously evolving during the last decades (Ishikawa et al., 2018; Li et al., 2018; Lukaszewicz, 2013). This interest is motivated by the improvement of certain mechanical properties the resistance to weight ratio, corrosion resistance (Grzesik, 2017) etc. Composites constitute the opportunity to design materials with larges palettes of properties that are not provided by the existing mineral materials (Lopes & Ribeiro, 2012). Additionally, as far as large-scale production is concerned, the flexibility and the ability to be custom made, have encouraged the growth of composite materials in the automotive industry (Cramer & Taggart, 2002; Lopes & Ribeiro, 2012). With the advent of composite materials, that have a higher strength to weight ratio, the less load bearing components in vehicles have been gradually replaced by these new materials (Altenbach et al., 2004).

Composite elements used in the automotive industry are generally divided in two categories: (i) composites that withstand high temperature and humidity, and (ii) composites destined to improve the vehicle's structural performance (Lopes & Ribeiro, 2012). The latter are highly stressed, are operational near their mechanical strength limit and should respect the requirements of security and operational safety. Therefore, the identification of the potential loads that the composite structure can undergo in service and the study of its behavior under these loads remains essential.

Despite their excellent strength to weight ratio, composites are more susceptible to internal damage (Agrawal et al., 2013), especially delamination that can occur in different stages of the structure's life (manufacturing, maintenance operation or in-service). Additionally, composites exhibit damage mechanisms that are different from those occurring in metallic materials in terms of damage initiation and accumulation. Indeed, in the microscopic scale damage mechanisms will gradually develop during service and accumulate throughout the volume of

the material. The combination of the concomitant mechanisms brings about the deterioration of the local properties leading to the finale mesoscopic failure.

Thermoplastic-based composite materials are known to be very sensitive to low-velocity impact (LVI) (Sierakowski & Newaz, 1995) and repetitive loading, such as fatigue loading. These two types of events are considered as serious threats to the integrity of the structures. After an impact event, a microscopic diffused microscopic damage is created through the thickness whereas only a small indentation traces if any are left on the impacted surface. This type of damage is invisible and results in a significant reduction of the structure's load-bearing capacity and therefore influences substantially the performance of composite structures. Indeed, studies have shown that the internal damage related to LVI events reduce the structure's load bearing capacity by more than 50% (Richardson & Wisheart, 1996; Shah et al., 2019). Additionally, under cyclic loading conditions, damage propagation and accumulation occurs in the structure and may result in disastrous in-service rupture.

Consequently, for safety reasons, extra plies are added to make the composite structures more resistant (Shah et al., 2019). However, the addition of the plies results in the increase of the weight of the composite structures, reducing hence its competitiveness compared to metals. Therefore, the improvement of the damage tolerance of composites is of high importance in the transportation industry, notably for automotive applications. The realization of the importance of safety and reliability in the structural parts design and resistance along with a proper identification and assessment of damage occurring during in-service life are essential to respect the standards of damage tolerance. Indeed, the risk of loss of human lives resulting from unexpected structural failure has motivated the scientific community towards innovative projects in the various branches of engineering among them damage detection and evaluation in automotive components.

A great interest is drawn towards non-destructive evaluation (NDE) as a means of early damage detection. In fact, early-stage identification of damage, is intended to prevent structural failure and schedule the repair or the replacement of damaged components. Therefore, meticulous periodic inspections of the components' integrity are entailed. The predominant NDE techniques aimed at the damage identification in composites structures include infrared thermography, acoustic emission, ultrasonic waves propagation, frequency response functions (FRP), shearography, etc. Nevertheless, these techniques have been gradually tested as to their capability to gather both the detectability and the feasibility.

Numerous research studies dealing with the ultrasonic waves' propagation have been performed to demonstrate their outstanding capability to inspect large structures and their high sensitivity to detect internal damage, such as delamination. It is found that ultrasonic investigation provides paramount information for high-quality assessment of damage (Aymerich & Meili, 2000; Castaings et al., 2012). In the case of plate-like structures, guided elastic ultrasonic waves, known also as Lamb waves, have proven their efficiency and reliability regarding early damage detection. Additionally, the capacity to selects modes and frequencies makes the detection and the localization of surface damage like, microcracks and corrosion, and interlaminar damage accurate (Su & Ye, 2008). Their versatile use has encouraged extensive research to develop damage detection tools that are easy to use, effective and low cost.

The present research project is carried out in the framework of the OpenLab "Materials and processes" created and funded by Stellantis. The Open Innovation approach adopted by the former Groupe PSA brings together three scientific partners: Arts et Métiers Sciences et Technologies, GeorgiaTech Lorraine (Georgia Tech-CNRS IRL 2958). The aim of the OpenLabs is to associate scientific corporations with the most advanced academic partners in their field to benefit from their expertise, to have access to the best possible scientific and technological knowledge and to explore novel research spheres. This research consists in a partnership between Stellantis, the laboratory of mechanics, microstructures and materials (LEM3-UMR CNRS 7239) and the laboratory of ultrasound and non-destructive evaluation (GeorgiaTech-Lorraine).

This research work deals with the study and assessment of the damage induced in glass-fiber woven fabric reinforced polyamide composite intended for structural application in the automotive industry by the means of non-destructive evaluation. The main objective is to develop an experimental approach that enables to detect and quantify the damage state of the composite structures subjected to two types of loading that a typical composite structure can undergo during in-service operations, namely low-velocity impact and/or fatigue loading as well as the combination of both loads. The studied thermoplastic based composite labelled hereafter as VizilonTM SB63G1-T1.5-S3 is manufactured by Dupont De Nemours and is constituted of three woven glass fibers plies imbedded in a polyamide 66/6 matrix. Previous research realized in 2013 on the same material indicated that it was possible to detect critical damage in this material. Pomarède (Pomarède, 2018) has studied the damage behavior of Vizilon composite employed by Stellantis (Groupe PSA) undergoing quasi-static tensile tests. Several NDE techniques have been performed to evaluate damage resulting from the

mechanical loadings. Two new damage indicators based on ultrasound waves propagation have been proposed and have shown their effectiveness in estimating and quantifying the damage stage of the composite structure caused by quasi-static tensile loadings. However, the damage indicator based on the Lamb wave signal analysis could not detect the damage initiated by out-of-plane loading, i.e., low-velocity impact. Indeed, damage caused by LVI is different from this resulting from quasi-static tensile test. LVI damage is considered as localized damage while damage occurring due to tensile tests is microscopic damage that is diffused in all the section of the material. Consequently, the main objective of the present work is to propose a practical, easy to use, and efficient NDE tool that detects and estimate the damage state of the composite structure regardless of the type of induced damage.

Two of the most complex and threatening solicitations are performed on the material of the study, namely low-velocity impact, and cyclic loading. These types of loading are most likely to occur during the VizilonTM SB63G1-T1.5-S3 in-service life. The assessment of the damage mechanisms and their kinetics is of high importance. For that matter, appropriate experimental procedures are presented since the polyamide-based composite can exhibit different behaviors depending on the applied load and the environmental conditions. For the present research project, a configuration of the reinforcement oriented 0° under a relative humidity condition of 50% is chosen as a representative material configuration for potential automotive applications. Various methods are meticulously chosen and employed for the study of damage, namely optical microscopy, X-ray microtomography (mCT) and different ultrasonic methods.

To this end, this manuscript is structured as follows:

- Chapter I consists of a non-exhaustive bibliographic review that provides information about the material of the study, its sensitivity to the temperature and the relative humidity and also its mechanical properties. A particular attention is given to the mechanical behavior of woven composites under low-velocity impact, fatigue loading and under a combination of both impact and fatigue loading. The final section is dedicated to specific damage detection methods that represent a primary focus of this research work.
- Chapter II represents a thorough experimental investigation of barely visible impact damage (BVID) resulting from low-velocity impact events. An assessment of the evolution of damage, as a function of the impact energy, and its criticality are the objective of this chapter. A detailed experimental procedure allowing to study and

quantify the created damage is proposed. The suggested experimental procedure enables to: (i) measure the key parameter when investigating low-velocity impact damage which is permanent indentation, (ii) identify the associated damage mechanisms, (iii) estimate the stiffness components through non-destructive evaluation, and finally, (iv) quantify damage employing a novel Lamb waves-based method. As a result, efficient damage indicators are proposed.

- Chapter III is dedicated to the study of damage resulting from tension-tension fatigue loading. For that matter, numerous steps are followed. First, a geometry optimization to promote damage generation in the central area of the samples is accomplished. Next, the Wohler curve describing the fatigue response of the PA66/6 reinforced composite is reconstructed. The damage mechanisms, in the studied composite, are identified by means of X-ray tomography and the created voids is quantified. Then, the developed Lamb waves-based method is employed. The latter has proven its effectiveness in the detection and estimation of diffused damage. The final step is a comparison between the voids content estimation and the results obtained by the ultrasound-based method is conducted.
- The final chapter, i.e., Chapter IV, is devoted to compare the residual performance between post-impact samples, post-fatigue samples, and impact post-fatigue samples. The main goal is to evaluate the influence of fatigue preloading on the impact resistance of samples subjected to low velocity impact, and to analyze the effect of an impact event on the residual ultimate tensile strength (σ_{UTS}) of pre-fatigued samples. The comparison between the different types of loading will help determine which loading configuration is the most penalizing for the Vizilon TM SB63G1-T1.5-S3

References

Agrawal, S., Kalyan Kumar, S., & Sarkar, P. (2013). Impact damage on fibre-reinforced polymer matrix composite – A review. *Journal of Composite Materials*, *48*(3). https://doi.org/https://doi.org/10.1177/0021998312472217

Altenbach, H., Altenbach, J., & Kissing, W. (2004). *Mechanics of composite structural elements* (Springers (Ed.)). https://doi.org/10.1007/978-3-662-08589-9

Aymerich, F., & Meili, S. (2000). Ultrasonic evaluation of matrix damage in impacted composite laminates. *Composite Part B*, *31*, 1–6.

Böhm, R., Hornig, A., Weber, T., Grüber, B., & Gude, M. (2020). Experimental and Numerical Impact Analysis of Automotive Bumper Brackets Made of 2D Triaxially Braided CFRP Composites. *Materials*, *13*(3554). https://doi.org/10.3390/ma13163554

Castaings, M., Singh, D., & Viot, P. (2012). Sizing of impact damages in composite materials using ultrasonic guided waves. *NDT and E International*, *46*, 22–31. https://doi.org/10.1016/j.ndteint.2011.10.002

Cramer, D. R., & Taggart, D. F. (2002). Design and Manufacture of an Affordable Advanced-Composite Automotive Body Structure. *The 19th International Battery, Hybrid and Fuel Cell Electric Vehicle Symposium & Exhibition*, 1–12.

EU Climate Action. (2019). Research and Development in Carbon Fibres & AdvancedHigh-Performance Composites Supply Chain in Europe: A roadmap for Challenges and the Industrial Uptake. https://ec.europa.eu/clima/citizens/eu_en

Grzesik, W. (2017). Advanced Machining Processes of Metallic Materials: Theory, Modelling, and Applications (Elsevier (Ed.); Second edi).

Ishikawa, T., Amaoka, K., Masubuchi, Y., & Yamamoto, T. (2018). Overview of automotive structural composites technology developments in Japan. *Composites Science and Technology*, *155*, 221–246. https://doi.org/10.1016/j.compscitech.2017.09.015

Kharbanda, S., Bhadury, T., Gupta, G., Fuloria, D., Pati, P. R., Mishra, V. K., & Sharma, A. (2021). Polymer composites for thermal applications – A review. *Materials Today: Proceedings*, *xxxx*. https://doi.org/10.1016/j.matpr.2021.03.609

Li, S., Sun, T., Liu, C., Yang, W., & Tang, Q. (2018). A study of laser surface treatment in bonded repair of composite aircraft structures. Royal Society Open Science. https://doi.org/10.1098/rsos.171272

Lightweight Materials for Cars and Trucks. (n.d.). https://www.energy.gov/eere/vehicles/lightweight-materials-cars-and-trucks

Lopes, H., & Ribeiro, J. (2012). Structural health monitoring in composite automotive elements. In J. Carmo & J. Ribeiro (Eds.), New Advances in Vehicular Technology and Automotive Engineering (pp. 286–302). InTech Edition.

Lukaszewicz, D. (2013). Automotive composite structures for crashworthines. In A. Elmarakbi (Ed.), In Advanced Composite Materials for Automotive Applications: Structural Integrity and Crashworthiness.

Pomarède, P. (2018). Détection de l'endommagement dans un composite tissé PA66,6/6 Fibres de verre à l'aide de techniques ultrasonores en vue d'une prédiction de la durabilité de pièces automobiles. ENSAM ParisTech.

Richardson, M., & Wisheart, M. (1996). Review of low-velocity impact properties of composite materials. Composite Part A: Applied Science and Manufacturing, 1123–1131.

Sarfraz, M. S., Hong, H., & Kim, S. S. (2021). Recent developments in the manufacturing technologies of composite components and their cost-effectiveness in the automotive industry: A review study. Composite Structures, 266(February), 113864. https://doi.org/10.1016/j.compstruct.2021.113864

Shah, S. Z. H., Karuppanan, S., Megat-Yusoff, P. S. M., & Sajid, Z. (2019). Impact resistance and damage tolerance of fiber reinforced composites: A review. Composite Structures, 217(February), 100–121. https://doi.org/10.1016/j.compstruct.2019.03.021

Su, Z., & Ye, L. (2008). Lamb wave-based quantitative identification of delamination in composite laminates. Delamination Behaviour of Composites: A Volume in Woodhead Publishing Series in Composites Science and Engineering, 169–216. https://doi.org/10.1533/9781845694821.2.169

US department of energy. (2011). Report on the first quadrennial technology review.

Chapter 1: Context & thesis outline

The main objective work of this thesis resides in the combination of an advanced approach different techniques towards the evaluation and the detection of the anisotropic damage in woven polymer composites. Since this type of material presents high mechanical properties and resistance regarding out-of-plane solicitations, it is extensively used for automotive applications. However, the heterogeneous nature of composites and the effect of their microstructure makes the prediction of their behavior highly complicated notably when accounting for the damage mechanisms.

Indeed, realizing the importance of safety and reliability in the structural components design and resistance, a proper identification and assessment of damage occurring during in-service life are essential to respect the standards of damage tolerance. Knowing the different types of loading that the studied composite part may undergo during its in-service life, a state of the art discussing the behavior of the composite materials under low-velocity impact and fatigue loading is provided.

In this chapter, the studied material is introduced, and its mechanical properties are presented. These properties are either provided by the composite manufacturer or obtained experimentally and numerically by fellow researchers. The influence of humidity (moisture content) on polyamide-based composites is later discussed. The behavior of woven composites under mechanical loadings (fatigue, low-velocity impact and the combination of impact and fatigue) is reviewed and the different associated damage mechanisms are exposed and discussed. Further in this chapter, the attention is drawn towards damage detection methods that represent the main focus of this research work.

I. Material of the study

1. Presentation of the studied material

The material of the study is a woven twill 2.2 composite referred to as VizilonTM SB63G1-T1.5-S3, manufactured by DuPont de Nemours using a thermo-compression moulding process. It is a co-polyamide 6.6 / 6 (semicrystalline thermoplastic polymer matrix) reinforced with a layup of three balanced woven fabric glass fiber layers oriented at 0°/90° (corresponding to weft and warp directions respectively). The composite plates have a thickness of 1.53 mm, with a fiber weight ratio of 63% corresponding to a fiber volume fraction of 43%.

Table 1, provided by DuPont de Nemours, presents the density, the Young's modulus (E) and the ultimate strength (σ_{UTS}) and strain (ε_{UTS}) of the studied composite material. The microstructure and the architecture of the material reinforcement are presented in **Figure 1**.

Pomarède (Pomarède 2018) studied the tensile response of the PA6.6/6 reinforced composite under two configurations 0° and 45°. In terms of elastic constants, the components of the stiffness matrix are determined experimentally using ultrasonic bulk waves (Pomarède 2018) and are compared with those obtained numerically using periodic homogenization (Praud 2018) as represented in Erreur ! Source du renvoi introuvable..

For the overall material response, it is shown that the mechanical behavior is highly influenced by the fibers' orientation. Indeed, under tension loading, the 0° (as well as 90°) configuration test exhibits a linear and brittle while at 45° configuration, the material exhibits a nonlinear ductile response due to the matrix rheology. Typical stress-strain curves showing the response of the woven glass reinforced PA6.6/6 at 0° (or 90°) and that at 45° directions are given in **Figure 2**. The components of the stiffness matrix are determined experimentally using ultrasonic bulk waves

In the present work, impact tests are carried out on samples prepared using a water-cooled circular saw. The plates have rectangular shape of 100 by 150 mm dimensions and 1.53 mm thickness, in agreement with the ASTM D7136/D7136M standards. Afterwards, the initial undamaged state is examined and checked for all samples using ultrasonic C-scan. The samples are maintained close to the same initial conditions in terms of temperature (room temperature) and relative humidity (dry as molded).

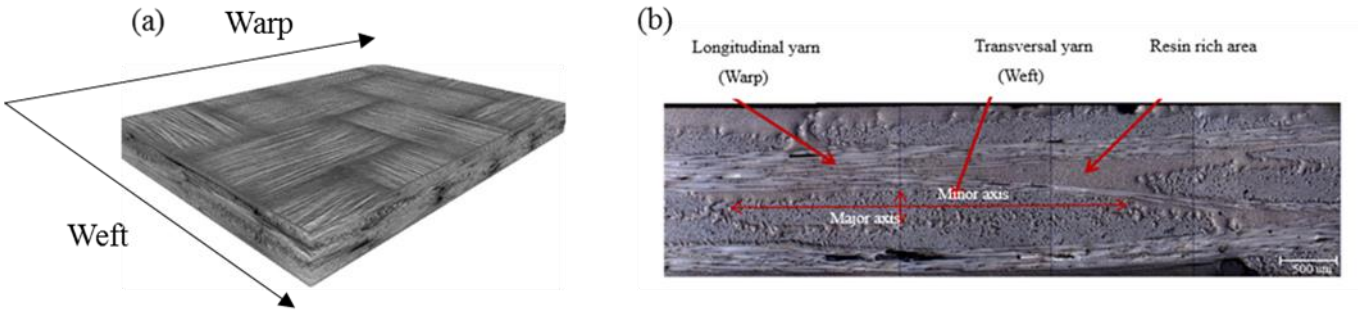

Figure 1: Mesostructure (a) and microstructure microscopic observation (b) of the woven glass fabric-PA66-6 composite showing warp and weft orientation (Pomarède et al. 2018).

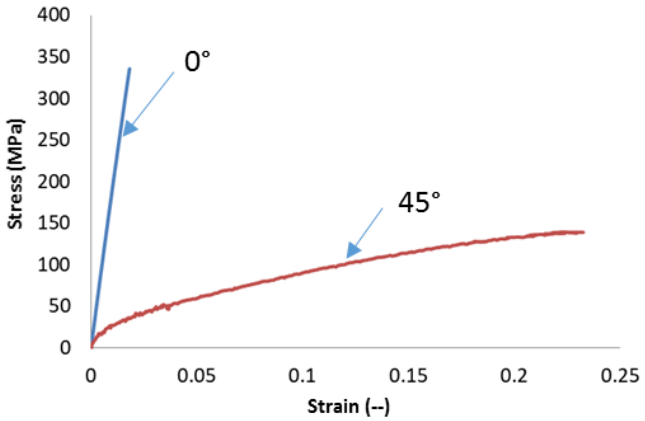

Figure 2: Typical stress-strain responses of the woven glass fabric-PA66-6 composite under tensile loading in 0° and 45° directions (Pomarède 2018).

Table 1: Mechanical characteristics of the studied woven glass fabric-PA66-6 composite.

*Stiffness components (GPa)	C_{11}	C_{12}	C_{13}	C_{22}	C_{23}	C_{33}	C_{44}	C_{55}	C_{66}
Numerical estimation (using periodic homogenization)	20	2.1	1.5	20	1.5	4.5	2.3	1.3	1.3
Experimental	22.21 (0.2)	2.57 (0.15)	1.41 (0.76)	21.81 (0.08)	--	4.1 (0.07)	2.33 (0.09)	1.58 (0.21)	--

Mechanical characteristics	**Density**	**E_0°(GPa) warp direction**	**E_90° (GPa) weft direction**	**σ_{UTS}(MPa) warp direction**	**ε_{UTS} (%) warp direction**
	1.78	17.7	18.1	303	1.9

2. Sensitivity to humidity and water uptake

Polyamides are semi-crystalline polymers known to be sensitive towards temperature variation and relative humidity (Arif et al. 2014; Benaarbia, Chrysochoos, and Robert 2014; Robert and Benaarbia 2015). This kind of polymers can be characterized by two important temperatures: melting point T_m and glass transition temperature T_g. Indeed, the presence of amide groups –HN- in the amorphous part of the polyamide makes it intensively water absorbent. The water fills the free volume at first, and then connect with hydrogen bonds. Reaching a certain level of moisture absorption, the hydrogen bonds, between the amide molecules, tend to be weakened. Consequently, the mobility in the polyamide chains increases leading to what is called the 'plasticizing' effect of water increasing therefore the polymer's flexibility. This phenomenon has been highlighted by several studies and can result in a decrease in glass transition temperature (Obeid 2016).

An increase of the temperature leads to an increase of ductility and a decrease of Young modulus, along with a drop of T_g. The latter is also affected by the variation of the relative humidity due to the water uptake. It drops with the increase of the moister content (Benaarbia et al. 2014). **Figure 3** represents the influence of relative humidity on the glass transition temperature for a polyamide 6.6 reinforced with short glass fibers.

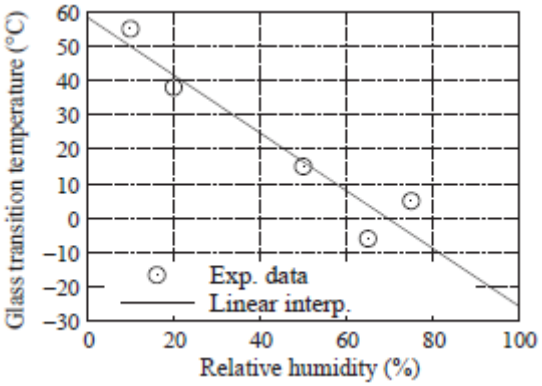

Figure 3: Influence of relative humidity on the glass transition temperature Tg in the case of a polyamide 6.6 reinforced with 35% by mass of short glass fibers (Launay et al. 2013).

Moreover, the moisture content might influence the damage mechanisms created in a polyamide-based composite. Indeed, the damage mechanisms are varying in the material from one relative humidity to another. Arif (Arif, 2014) has shown that different predominant damage mechanisms are observed between samples conditioned at 0% RH, and 50-100% conditioned samples. For 0% RH, fiber/matrix debonding at fiber ends and sides, fiber breakages and brittle matrix crack propagation are identified. Meanwhile, fiber/matrix debonding at fiber ends and sides with a locally strained matrix zone around the debonded fibers along with ductile matrix micro-cracks are observed in the sample with a 50% RH. At a 100% RH, the same damage mechanisms as those observed at 50% RH are retrieved, but with a higher severity, in addition to matrix deformation local shear bands.

II. Impact damage on composite materials

In-service failure of composite parts results from an association of phenomena progressively deteriorating the local characteristics of the material. Impact and fatigue can be among these phenomena. In this section, out-of-plane solicitation on composite materials will be discussed. Damage tolerance concept is introduced a long with the different types of impact events. An exhaustive assessment detailing the behavior of composite materials to low-velocity impact, the different damage mechanisms associated to this out-of-plane solicitation and the influence of the reinforcement architecture on the impact resistance is proposed.

1. Damage tolerance concept

Damage tolerance is a concept that was developed in the 1970s and is defined as the load-carrying ability of a structure once damaged (Oterkus et al. 2016). It refers to the capacity of a permanently damaged or deformed material to maintain the same response to solicitations as a non-damaged material. The safety requirements related to damage tolerance includes the capacity to resist limit loads in the presence of damage, leading hence to the evaluation of the residual strength. It is worth mentioning that the damage tolerance concept is different from damage resistance, i.e., the ability of a structure to resist to a particular load or to external solicitation without showing any signs of permanent deformation (Transportation and Office of Systems Engineering 1993).

Nevertheless, the difference between the design for damage tolerance and the certification according to the design requirements for damage tolerance must be recognized. In the past the emphasis was on high toughness, composites, considered as more fragile materials, are currently certified with relatively low toughness. As described in (Alderliesten 2015), it appears that this difference in approach stems from the distinction between the damage caused by the use of the material and the damage caused during the use of the latter. Furthermore, as an example of the damage caused by the use of the composite materials one can mention environmental degradation due to humidity and temperature, along with fatigue. In the other hand, impact damage is considered as damage caused during the use.

Damage tolerance for metallic structure is primarily governed by fatigue damage and cracks propagation. Since composites appear to be less sensitive to fatigue loading than metals, the main focus in the damage tolerance certifying and assessment is directed primarily towards impact damage (Alderliesten 2015).

The heterogeneous constitution of composite materials, marked by the stacking of layers composed of fibers and a matrix, makes them vulnerable to mechanical loading. Furthermore, damage mechanisms, like delamination, resulting from layers debonding, remarkably reduce their properties. However, one must mention that damage may occur within a layer without leading eventually to the failure of the structure.

Out-of-plane impact is often considered as the most critical solicitation since a damage might be initiated without any possible visibility on the surface. The structure then deteriorates leading to the reduction of the residual properties reaching less than 50% without any noticeable trace

(**Figure 4**). Consequently, considering this type of solicitation is detrimental in the design of composite structures (Bouvet 2011; Hongkarnjanakul, Bouvet, and Rivaillant 2013; Serge Abrat 1998).

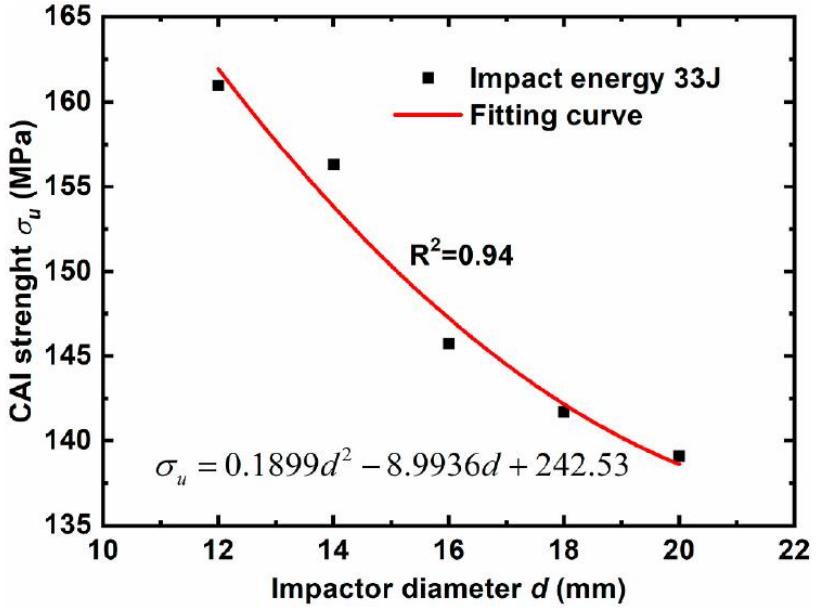

Figure 4: Compression after impact strength as a function of the impact energy for woven carbon/epoxy composite (Yang et al. 2021).

2. Velocity and Impact damage

As mentioned in previous sections, composite materials are highly sensitive and vulnerable to out-of-plane solicitations such as an impact event. The latter is defined as percussion of two or more objects or bodies. This collision can be fluid, elastic, plastic, or a combination of these different modes. Impact can be classified based on the related velocity in four categories: low-velocity, high-velocity, ballistic and hypervelocity (Razali et al. 2014).

Low-velocity impact is defined in the aerospace field as impact occurring at a velocity less than 11 m/s caused by tool dropping during maintenance operations for instance. Conversely, high-velocity impact is happening at a velocity higher than 11 m/s. Ballistic impact occur at much higher velocities, higher that 500 m/s, and is well studied in the military field impact (Razali et al. 2014). Finally, in the spacecraft field impact can be caused by space debris at velocities superior to 2000 m/s. To simplify the understanding of impact events, they can be divided into two main categories: low-velocity impact induced by a large mass and high-velocity impact caused by a small mass (gun shot for example) (Cantwell and Morton 1991).

Post-impact ability to resist remain hard to predict especially for composite materials. Indeed, identifying precisely the damaged area is highly complex making it thus difficult to characterize (Cantwell and Morton 1991). Additionally, the lack of existing standards and developed testing procedures makes it even more complicated to assess impact damage.

Impact damage can also be characterized by the detectability of the damage **(Figure 5)**. It is well known that high-velocity impacts create damage considered as Visible Impact Damage (VID) that can be detected by visual inspection. However, low-velocity impact may lead to internal structural damage that are imperceptible or barely seen. This type of damage is referred to as Barely Visible Impact Damage (BVID). Due to the complex form of this damage, its presence, its propagation along with its non-detectable aspect can be alarming and precarious for in service use (structures subjected to other types of loadings).

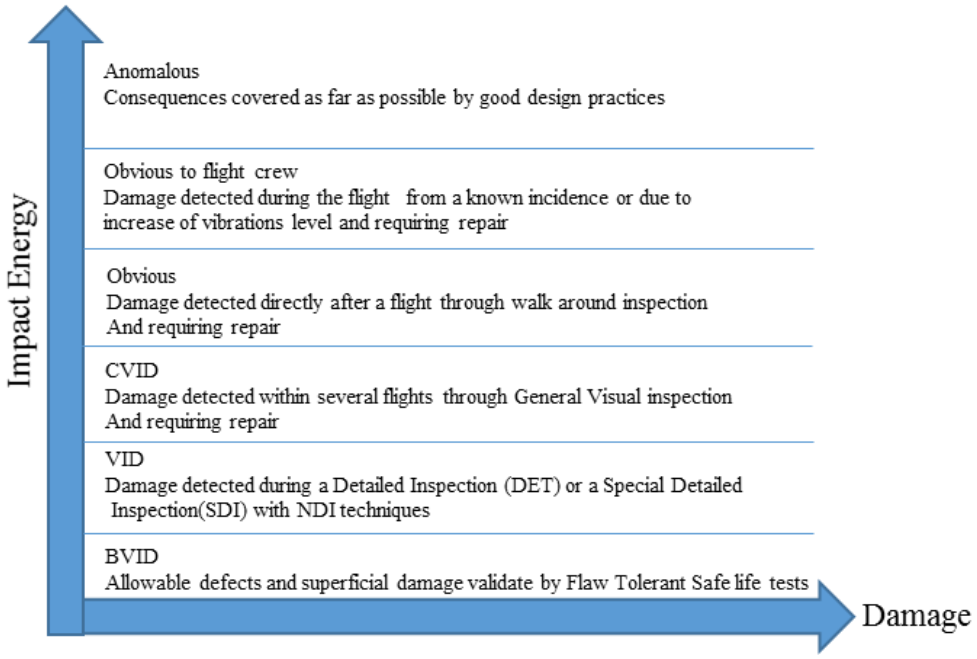

Figure 5: Different levels of impact damage and their severity (inspired from Fatigue and Damage Tolerance Design & Substantiation of Composite Helicopter Parts, 2nd International Summer School on Fatigue and Damage Mechanics of Composite Materials)

3. Damage mechanisms of BVID in composite structures

In automotive structures, BVID may occur at different operation circumstances including stone lofting while driving and tool dropping maintenance operations (Wronkowicz-Katunin, Katunin, and Dragan 2019). The damage mechanisms of impact are highly complex and can be

categorized into four categories: Permanent indentation (PI), matrix cracking, delamination and fiber breakage.

Low-velocity impact damage distribution is extremely complex due to the creation of several types of local stresses. Indeed, the complexity of the mechanisms is explained by the dissipation of the impact energy during the impact event. A part of the energy is absorbed and lead to deformations that stays in the elastic range while another portion results in irreversible damage such as matrix cracking or, in the worst case, fibers failure.

The distribution of the various damage mechanisms occurring throughout a low-velocity impact can be difficult to predict because of numerous parameters influencing the failure process. These parameters include the shape and size of the impactor, the type and mechanical properties of the material, boundary conditions and the thickness of the sample. Nevertheless, some failure mechanisms appearing in most of the low-velocity impact (LVI) cases are distinguished. In the case of thin plates, the damage occurring on external surfaces is usually observed on the non-impacted side of the specimens. During an impact event, and in the case of thin plates, a damage cone is created under the projectile (**Figure 6**) (Hautier 2010). This damage extends towards the non-impacted surface. The contact force under the projectile creates an area of stress concentration. Thus, the damage is initiated on the bottom layer and propagate in a pine tree path caused by the bending stress and waves propagation (Abrat, 1998).

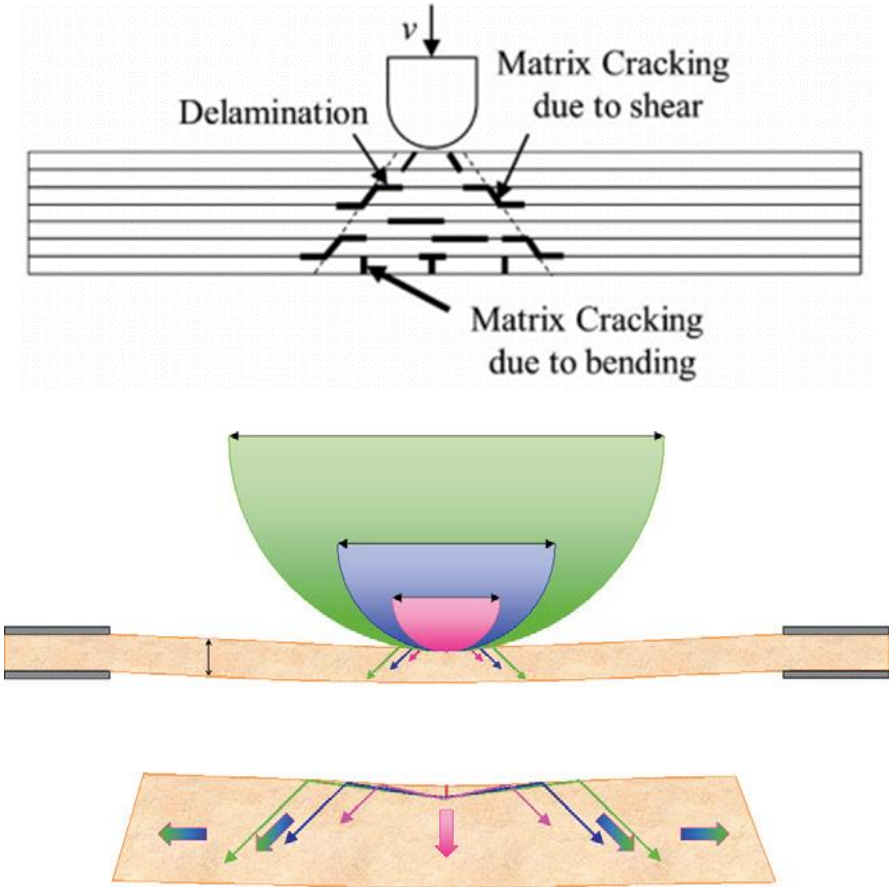

Figure 6: Damage cone is created under the projectile in laminated composites under low-velocity impact (Marguères and Meraghni 2013; Shah et al. 2019).

The first indicator of an impact occurrence is the permanent indentation. The latter is defined as the residual print that the striker leaves on the impacted surface. It is considered as a key parameter for the detectability of damage during a post-impact investigation. A threshold called Barely visible impact damage (BVID) is defined as the limit of detection. Below the BVID, the induced defect is not detectable, and the structure is considered safe. However, despite the non-detectability of damage on the surface, it may exist inside the laminate and have disastrous consequences. Several theories may justify the creation of permanent indentation. Ilyas (Ilyas 2010) linked the presence of permanent indentation to the viscoplastic aspect of the matrix while Faggiani and Falzon (Faggiani and Falzon 2010) suggest that non-linear shear behavior is responsible for its occurrence. Hongkarnjanakul et al. (Hongkarnjanakul et al. 2013) explained the appearance of permanent indentation by the presence of debris from the matrix inside the cracks, preventing their closure (**Figure 7**).

Matrix cracking is the first damage mechanism induced during low-velocity impact. In the case of a laminate, the cracks propagate in the direction parallel to the direction of the fibers and pass through the material in thickness. The cracks propagate in a dispersed manner in the damage cone and are concentrated in a cylinder formed below the impactor (Aymerich, Dore, and Priolo 2009; Chang, Choi, and Jeng 1990).On the upper layers, cracks diffuse at a 45° angle due to transverse shear stresses. However, the normal longitudinal tensile stress at the non-impacted face results in crack propagation in the normal direction at the creases (Davies and Olsson 2004) .

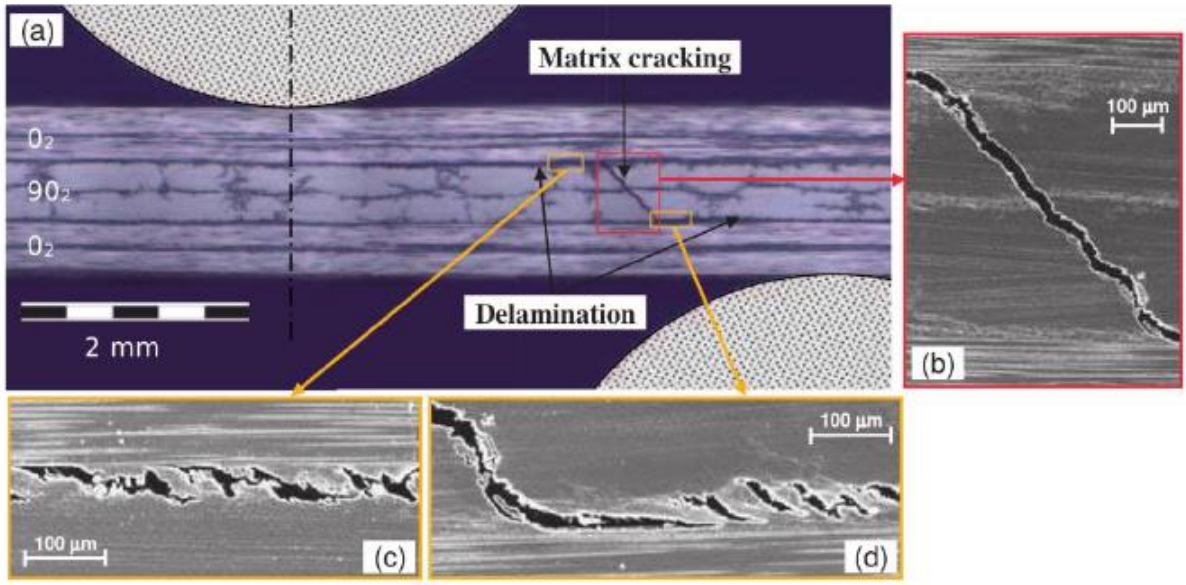

Figure 7: (a) Micrographic observation of a laminate showing : (b) Matrix cracking at 45°, (c) Matrix debris in the cracks, (d) « cusps » caused by the delamination (Hongkarnjanakul et al. 2013).

Delamination is the propagation of cracks in the interface between layers. This interface being rich in matrix promotes the propagation of cracks. When a matrix crack crosses the ply and reaches the interface between two layers having two different fiber orientations, it is initiated by the change of direction and then propagates between layers leading to the creation of delamination. Indeed, when the gap is large, the contrast in rigidity in bending increases and thus delamination between layers is favored. The form of delamination in an impacted composite is generally described as "peanut shape" as shown in **Figure 8**. It is considered the most critical damage mode as it significantly reduces mechanical properties ((Brunner, 2008; Greenhalgh, 2009; Jawaid et al., 2018; Nur Azrie Bt Safri et al., 2018; Sørensen, 2016)).

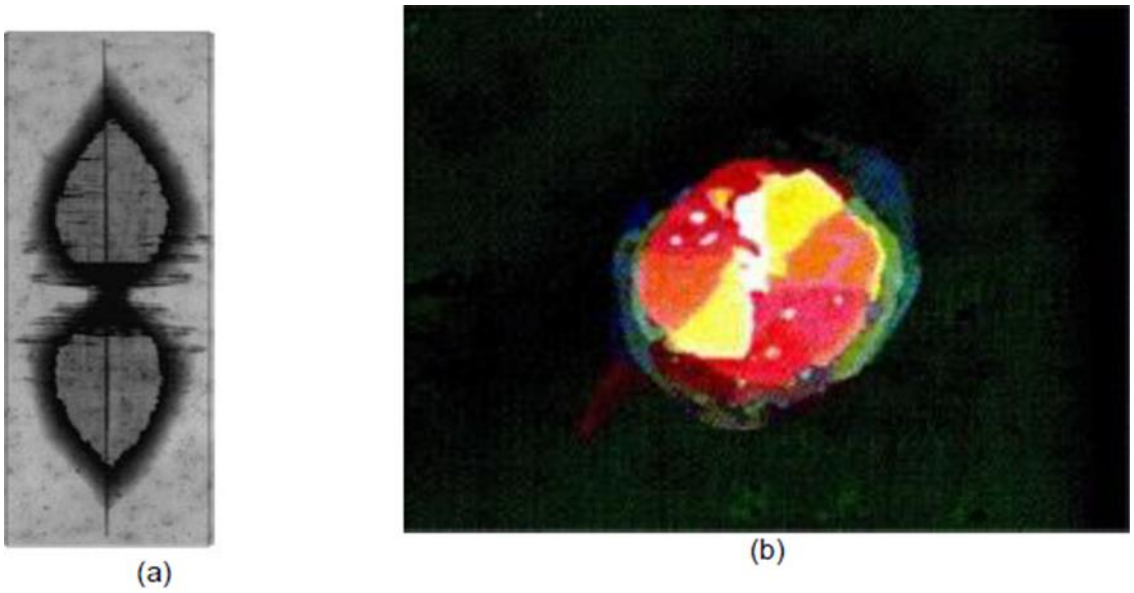

Figure 8: Illustration of the shape of delamination (a) (peanut shape) in a laminate composite reinforced with carbon fibers (Aymerich et al. 2009) et (b) C-scan image of delamination (Renault 1994).

Fibers' fracture is usually first seen plastic, the impacted and the non-impacted surface if the impact energy is significant enough. On the non-impacted surface, the fracture of the fibers is due to the tensile stresses resulting from the bending of the laminate. On the impacted surface, the failure is caused by shear and localized compression stresses. However, fiber fracture becomes the mode of damage that spreads mainly in the case of impact with penetration or perforation (Atas and Sayman 2008; Quaresimin et al. 2013).

4. Influence of the reinforcement architecture on the impact resistance

To understand the effect of fabric architecture on the behavior of composite materials under mechanical loading, numerous studies are carried out. These studies point out to the fact that the woven reinforced composites are very competitive compared to unidirectional composites regarding the impact resistance and the induced damage accumulation. Indeed, Greenhalgh and Hiley (Greenhalgh and Hiley 2003) showed that woven composites are more resistant to delamination than those with unidirectional reinforcements. Kim and Sham (Kim and Sham 2000) focused on the study of two main aspects: delamination and fracture behavior of a woven composite. Advantages of using this type of composite compared to a unidirectional cross-ply are also highlighted based on the microstructure properties. Generally, the induced internal damage in polymer composites has a penalizing effect on the lifetime of the structures (Kara

and Muhammed 2017) and can be one of the major drawbacks for the use of materials for the automotive structural applications.

Atas and Sayman (Atas and Sayman 2008) analyse the response of woven composite plates, made of epoxy resin reinforced with glass fibers, to impact loading for increasing energy levels. Different damage mechanisms are visualized on the samples by varying the impact energy. These damage modes are reflected and highlighted on the characteristic curves of the impact (contact force-displacement, force-time and displacement-time). The authors have established a link between the energy profile and the visually identified damage mechanisms. **Figure 9** shows contact force-displacement curves for different energy levels. Two types of curves were observed: closed and open. As previously mentioned, each area of the contact force-displacement curve describes a mode of damage. In the case of low-impact energy ranging between 4 J and 11 J, only matrix cracking considered as minor are observed. By increasing the impact energy, from 15 J, the phenomenon of fiber breakage on the not impacted surface appears. This phenomenon is reflected on the force-displacement curve by an apparent plateau right after the force peak (**Figure 9**(b)). From an impact energy of 29.6 J, the curve begins to take an open form (**Figure 9**(d)). This phenomenon reflects the beginning of the perforation. When the perforation is complete, the curve tends to take a more open shape.

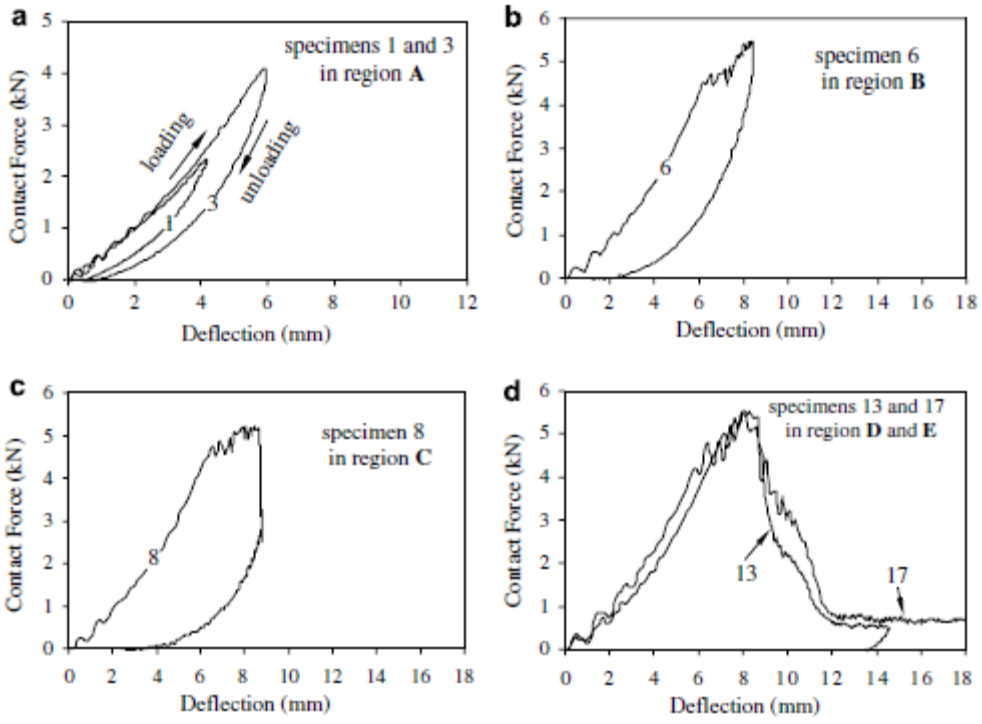

Figure 9: Contact force- displacement curves for different levels of energy describing the levels of induced damage from the first appearance (creation) (a) to perforation (d) (Atas and Sayman 2008).

Baucom et al. (Baucom, Zikry, and Rajendran 2005) also investigated the behavior of epoxy/vinyl-ester composites reinforced with 2D and 3D glass fibers fabrics under impact. A comparison of the size of the damaged area in both materials lead to the following conclusions: 3D reinforcements show a greater dissipative power compared to 2D reinforcement that provide the advantage of shock absorption compared to unidirectional ones. **Figure 10** shows images of two composite samples, one with 3D reinforcement and the other by 2D fabric, damaged by impact at an energy of 18 J up to perforation. These images show a larger damaged area in the case of the 3D-reinforced sample. However, even if 3D reinforcements provide a better resistance with respect to impact compared to 2D reinforcement, the resistance/ cost ratio is considered higher in the case of 2D woven reinforcement.

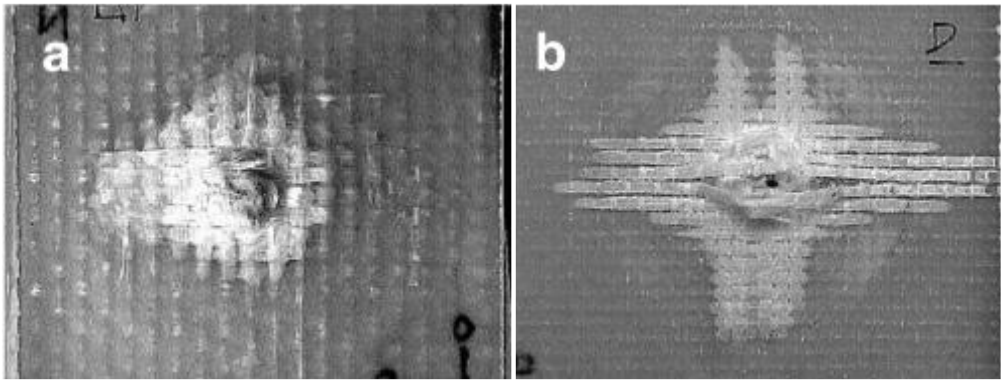

Figure 10: Images of impacted sample until perforation : (a) composite with epoxy/ vinyl-ester matrix reinforced with a 2D fabric, (b) composite reinforced with a 3D fabric (Baucom et al. 2005).

III. Composite materials under fatigue solicitation

The second load type assessed in this study is fatigue and the related features. The probabilistic nature of the response under constant amplitude cyclic loadings and the lack of detectable fatigue limit makes its assessment a high priority. A comprehensive bibliographic review of the different characteristics related to fatigue loading are detailed.

The fatigue phenomenon is defined as a degradation of the mechanical properties of a part under the effect of repeated loads whose amplitude is less than the monotonous fracture value σ_{UTS}. Fatigue of materials is studied for various types of mechanical loading such as uniaxial loading (tension, compression, bending and torsion), multi-axial loading and for variable amplitude loading.

The concepts used in the study of the fatigue behavior of composite materials in the literature are inspired from those already used for metallic materials (Kaminski et al. 2015; Renard 2010), justifying hence the need to determine the life duration of composite structures. However, the phenomenon of fatigue of composite materials is more complex to understand (Colombo, Bhujangrao, and Libonati 2019; Jollivet, Peyrac, and Lefebvre 2013). This is due to the multitude of degradation mechanisms and the variety of their scale, the variability of material characteristics and quality related to the manufacturing process that may change during the study and the multi-axiality due to the geometry of the composite structure and the often-variable real loads.

The service life of a material is defined by the time during which the material, or precisely one of its properties related to its main performance, will retain its functionality under well-defined conditions, without exhibiting major damage. The end of life of a part corresponds to the time when its properties related to a specific use are altered. For a part subjected to fatigue loads, it is necessary to be able to predict its service life or to design it for an infinite service life (Colombo et al. 2019).

By analogy with metallic materials, fatigue life can be splitin two phases: The initiation phase of several cracks and the propagation phase until complete failure (Carraro, Maragoni, and Quaresimin 2015). For composite materials, the difficulty lies in the definition and separation of these two phases. The identification of the degradation kinetics is a necessary step to determine what the dimensional phase is.

1. Fatigue loading parameters

Uniaxial fatigue tests with constant amplitude are carried out in load control or deformation, with a load cycle repeated throughout the test. The loading cycles are normally sinusoidal, with frequency of load in Hz, and vary around an average value σ_m between a minimum value σ_{min} and a maximum value σ_{max} per cycle, as shown in **Figure 11**. The loading type is characterized by the load ratio R relating the values of the minimum and maximum stresses of the cycle.

$$R = \frac{\sigma min}{\sigma max}$$

The value of R determines the type of loading in a fatigue test. If R is negative, it is a traction-compression, if R is between 0 and 1 it is a traction-traction test and if R is higher than 1 it is a

compression-compression test. In the rest of the study a traction-traction fatigue test will be carried out **Figure 11**.

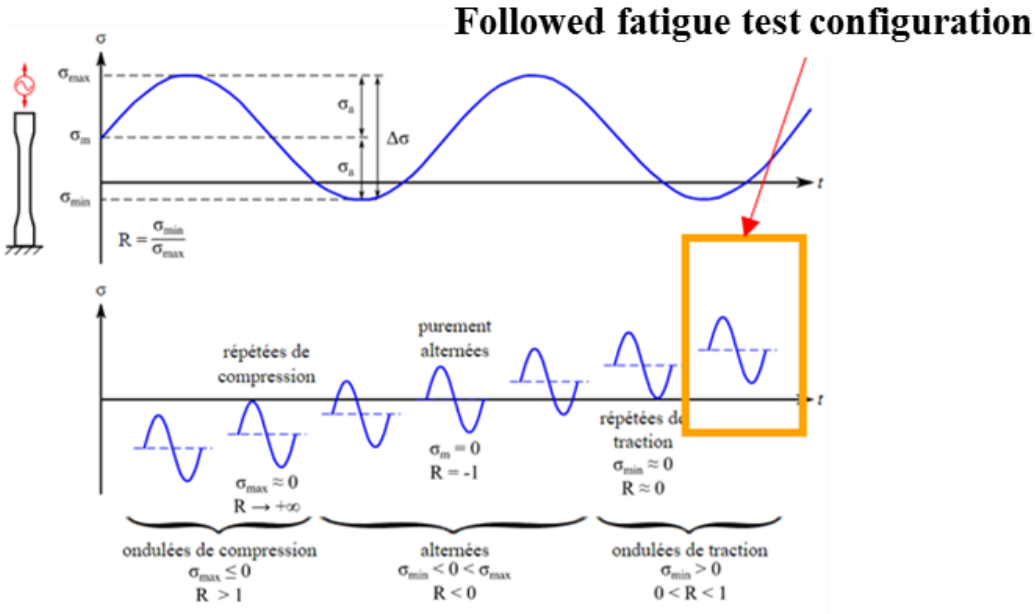

Figure 11: Illustration of the fatigue parameters, the different types of fatigue tests and the followed fatigue configuration in the following study (inspired from the personal work of Christophe Dang Ngoc Chan).

2. S-N curves

The construction of an S-N curve (Stress-Number of cycles curve also known as Wöhler Curves) is established by loading a set of samples until failure at different levels of the ultimate tensile stress in quasi-static varying between 30% and 90%. The life duration of a sample is quantified by the number of cycles to failure. A normal Wohler curve indicates only the 50% median probability of failure of the sample under a determined stress and after a certain number of cycles. It is recommended in the literature to use the equiprobability curves Stress- Number of cycles- Probabilistic (S-N-P). This type of curves associates to each combination of stress and number of cycles a probability of failure.

The allure of the S-N curves in case of composite materials are qualified as quasi-linear (Harris 2003). Numerous models exist to analytically represent the Wöhler curves such as Basquin model. This model describes the central part of the S-N curve as a line in a log-log diagram and is written as follow:

$$\log(N) = \log(C) - m * \log(\sigma)$$

With C and m parameters determined by linear regression in the log-log diagram, N the number of cycles and σ the stress load (1/2 amplitude).

3. Damage and residual properties

In order to quantify the damage in a material after a certain number of loading cycles, several models are proposed in the literature (Cuadra et al. 2013; Giancane et al. 2010; John and Prakash 2018; Mao and Mahadevan 2002). (Toubal, Karama, and Lorrain 2006) measured the temperature on the surface using infrared thermography and introduced the damage as:

$$D = 1 - \frac{E}{E0}$$

With E0 the initial Young's modulus and E the Young modulus at a determined cycle.

Another way to quantify the induced damage is to estimate the residual resistance. To do so, monotonic test until failure take place for samples loaded at a certain number of cycles.

Residual resistance and residual stiffness are two measurable values that can be considered as indicators to the degradation of composite materials. However, the possibility to determine the residual stiffness using non-destructive methods makes it more advantageous than standard destructive testing to determine the residual resistance.

In addition, in the case of loading in the fiber's direction, the stiffness estimation gives more information on the change of its values during the life of the composite compared to the residual resistance. Indeed, the latter show very light decrease function of the number of cycles until showing an important drop when approaching the finale failure (Ryder and Crossman 1983). Thus, one can deduce that stiffness is more sensitive to damage development that the residual resistance.

4. Behavior of woven composites under fatigue loading

The behavior of woven composites under fatigue loading is highly complex and is widely studied in the literature (Albouy, Vieille, and Taleb 2014; Kara and Muhammed 2017; Malpot 2017; Rouault 2013; Song, Wen, and Cui 2017; Vasconcellos 2013). Its understanding relies first on the understanding of the behavior of this type of composite under static tensile loading. During fatigue solicitation, the appearing damage mechanisms are the same occurring during tensile solicitation. The behavior of woven composite under tensile solicitations depend on several parameters such as, fiber architecture and direction of the loading (Osada, Nakai, and

Hamada 2003). Two types of reinforcement are studied: plain weave and satin weave. The authors find that the modulus and tensile strength of satin weave composite are 1.5 times higher than those of plain weave composite. In addition, the cracks density is 20% higher in the case of plain weave when compared to the one observed in satin weave employment. In the case of plane weave, the knee point occurs at lower strains compared to the case of satin weave reinforced composites (**Figure 12)**. It should be reminded that one of the characteristics of woven composite is the presence of an inflection point known as "Knee-point", on the stress-deformation curve when the loading is in the fiber's direction. This non-linearity is linked to the initiation of damage in the composite, most often identified as cracking in the transverse yarns (Osada et al. 2003).

Indeed, the anisotropy of this type of material induces different mechanical behavior depending on the fiber architecture and the fiber-matrix interface (Rasool 2015). In the case of woven composites subjected to tension-tension fatigue loading three main damage mechanisms are revealed (Albouy et al. 2014). The first damage mode appearing is matrix cracking at the tip of the weft yarn precisely at the interlacing region. The cracks density and the size of the cracks will grow until they reach an equilibrium state similar to the one observed in the case of UD laminate (CDS). The second stage of damage is governed by shear failure in warp yarns, matrix cracking and debonding of the fiber/matrix interface at the transverse yarns. Longitudinal Warp cracks appear first reducing consequently the stiffness of the composite. The matrix-cracking occur afterwards. As the loading process continues, the debonding grow until the yarns crack. Indeed, when a crack reaches the edge of the yarn, two propagation scenarios may occur: propagation in matrix-rich areas or propagation at the level of an adjacent longitudinal yarn, thus generating pseudo-delamination. As the number of cycles increases, the cracks grow resulting in stress concentration causing the failure of the longitudinal fibers and therefore a total fracture of the composite. The final failure occurs when the supported force reaches its maximum value. It should be mentioned that the main difference between UD and woven composite lie in the fact that failure is controlled by the breakage of warp fibers in a unit cell whereas damage pass from ply to ply in the case of multidirectional UD composite.

The cinematics of damage evolution in a woven composite subjected to quasi-static tensile loading and cyclic loading is given in **Figure 13** and **Figure 14** respectively.

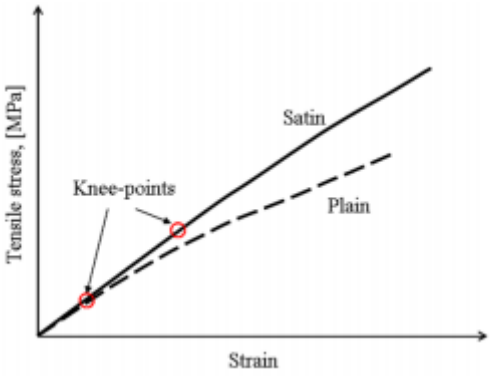

Figure 12: Comparison of the stress-strain curves of two different reinforcement architectures: satin weave and plain weave composites (Osada et al. 2003).

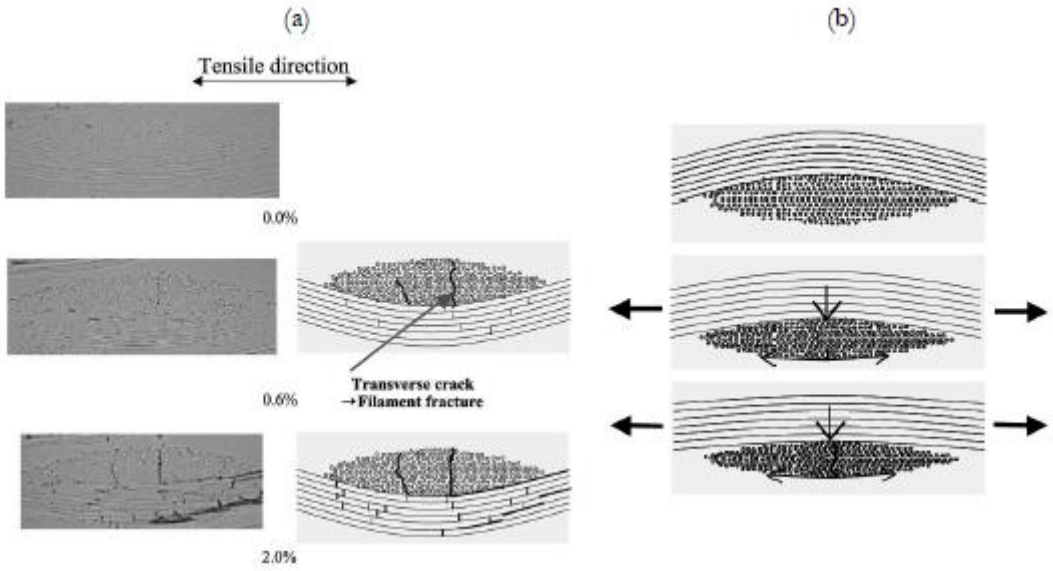

Figure 13: (a) Microscopic observation of a woven vinylester based composite before and after the knee-point and (b) priming of damage in transversal yarns (Osada et al. 2003).

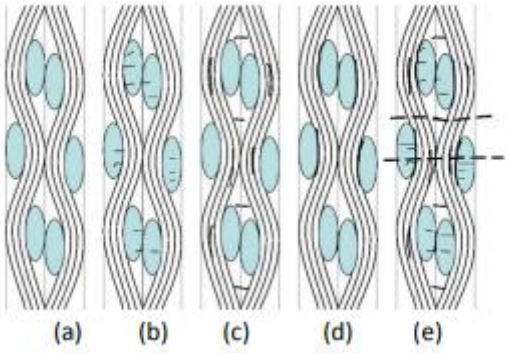

Figure 14: Different damage mechanisms observed in a woven composite : (a) undamaged state, (b) transversal weft yarn cracks, (c) matrix cracking and longitudinal cracks in the warp yarns, (d) pseudo-delamination and (e) the total failure (Naik, Patel, and Case 2001).

The fatigue behavior of woven composites changes depending on the orientation of the fibers. Malpot (Malpot 2017) investigated the influence of fiber orientation on the fatigue behavior of a woven glass fiber reinforced composite. In the case of 0°/90° orientation and below 80% of the ultimate tensile stress, no heating of the specimen is observed (**Figure 15(a)).** For samples with a fiber orientation of 45°/-45°, heating at the yarns cross-section appears in the first cycles **(Figure 15(b)).** The temperature continues to rise with the loading and the number of cycles. This heating, even in the case of low fatigue stress, can be attributed to the sensitivity of the matrix as well as to the reorientation of the fibers (**Figure 16**).

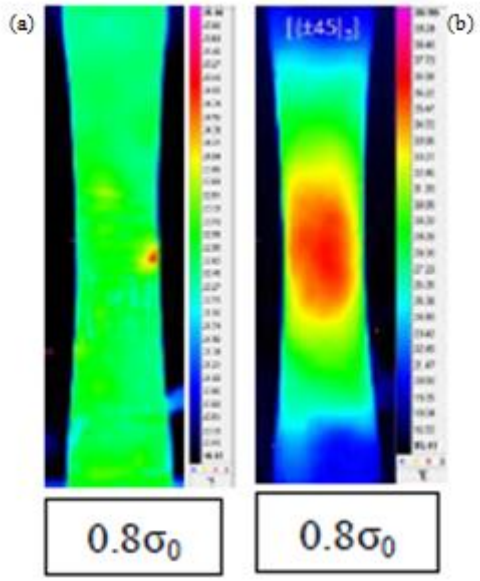

Figure 15: Images obtenues par caméra infrarouge lors des essais de fatigue sur un composite à matrice polyamide renforcée de fibers de verre tissées orientées : (a) [0°/90°], (b) [±45°] (Malpot 2017).

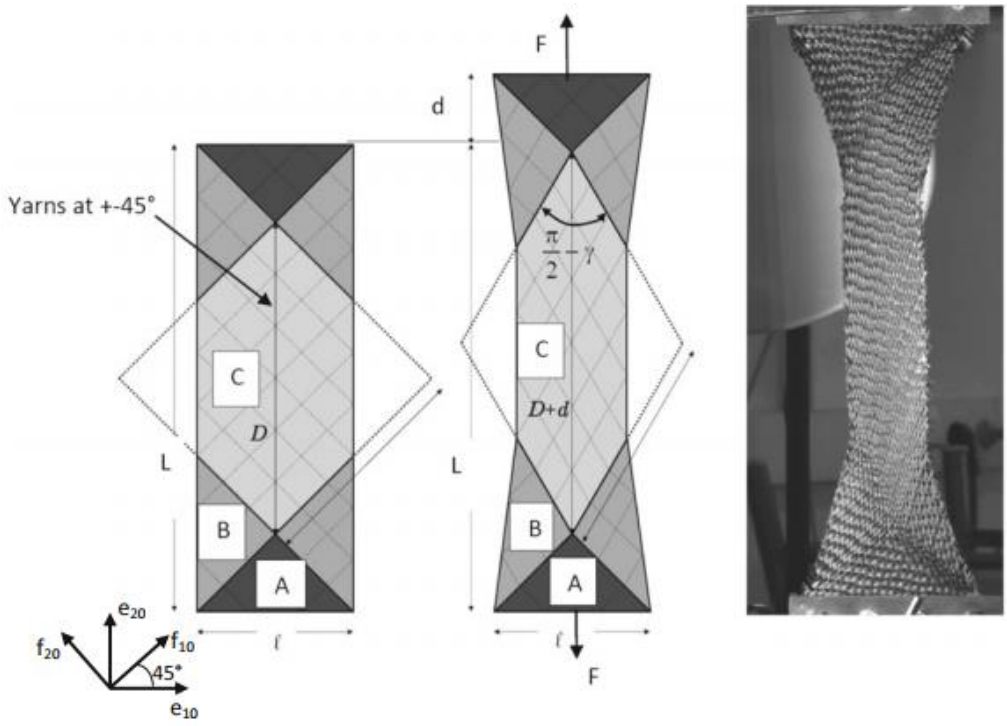

Figure 16: Typical tensile test of a woven fabric showing the fiber reorientation (Boisse et al. 2017).

IV. Fatigue loading and low-velocity impact coupling

Out-of-plane impact and fatigue loading resulting damage is the heart of this study. A proper understanding of the kinetics and of the effect on the residual properties is highly important. The previous sections (Section II and Section III) were dedicated to separately describe the behavior of composites under each solicitation. The coupling of these two kinds of solicitations is not widely studied in the literature. A short review on the influence of low-velocity impact on the residual characteristics is presented in this section.

Some recent studies are carried out to assess the behavior of composite materials subjected to fatigue post-impact. Vallons et al. (Vallons et al. 2010) study the influence of low-velocity impact damage on the static tensile properties and tensile-tensile fatigue properties of a non-crimp fabric composite (NCF composite). The authors have noticed that even at low impact energy levels, impact cause a decrease in the tensile strength in the fibers' direction. A reduction of more than 50% of the static tensile strength is observed in the case of carbon/epoxy woven fabric composite (WFC) after a 3 J impact. Indeed, the authors conclude that, in the fiber direction, and for the WFC, the residual tensile properties are more influenced by low-velocity

impact damage than in the case of NCFC. For the matrix dominated direction, the authors conclude that damage induced by low-velocity impact has a significant influence on the residual tensile properties and thus no difference in the behavior between the two materials is noticed.

A study is established to compare between non-loaded and impacted sample of epoxy based composite reinforced with natural fibers. As expected, the number of cycles to failure of the impacted samples is lower than the one of non-impacted specimen. Based on the data collected using acoustic emission during fatigue tests, it is shown that the damage is concentrated in the impacted area regardless of the level of fatigue loading used (**Figure 17**) (De Vasconcellos et al. 2014).

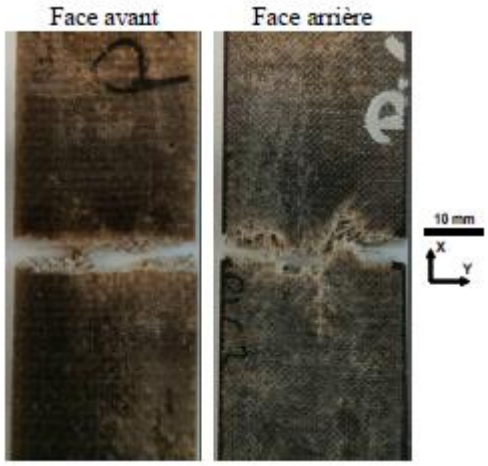

Figure 17: Failure of epoxy based composite reinforced with natural fibers subjected to post-impact at an energy level of 5 J fatigue loading at 80% σ_{max} (De Vasconcellos et al. 2014).

The effect of fatigue on the residual stress of previously impacted samples depends on the growth of the three types of damage mechanisms. Matrix cracking propagate into 45° oriented layers after a relatively small number of cycles. However, arriving at the interface between the layers, these cracks tend to change their propagation path leading consequently to the appearance of local delamination. The growth of the fatigue-induced delamination as well as the one induced by impact generally depends on the stacking sequence and more specifically on the normal stress level in the laminate (Colombo et al. 2019; Pagano, N. J Pipes 1971).

The response of composite materials to post-fatigue impact is not a topic widely studied in the literature. Ding et al. (Ding, Yan, and McIlhagger 1995) assess the effect of the coupling of these two modes of loading, low-velocity impact and fatigue loading, on a plain-weave carbon/epoxy laminate. The authors mentioned that the order of the application of the loads to

the laminate have significant effect on its residual strength. Indeed, fatigue post-impact is found to be more detrimental on the residual properties of the woven composite than the reversed sequence of loading. The authors also compare the effect of the fatigue mode (tensile-tensile and tensile-compression) on the S-N curves (**Figure 18**) and the residual properties. It is shown that tension-tension fatigue mode is more damaging to the material due to the delamination propagation caused by this type of loading.

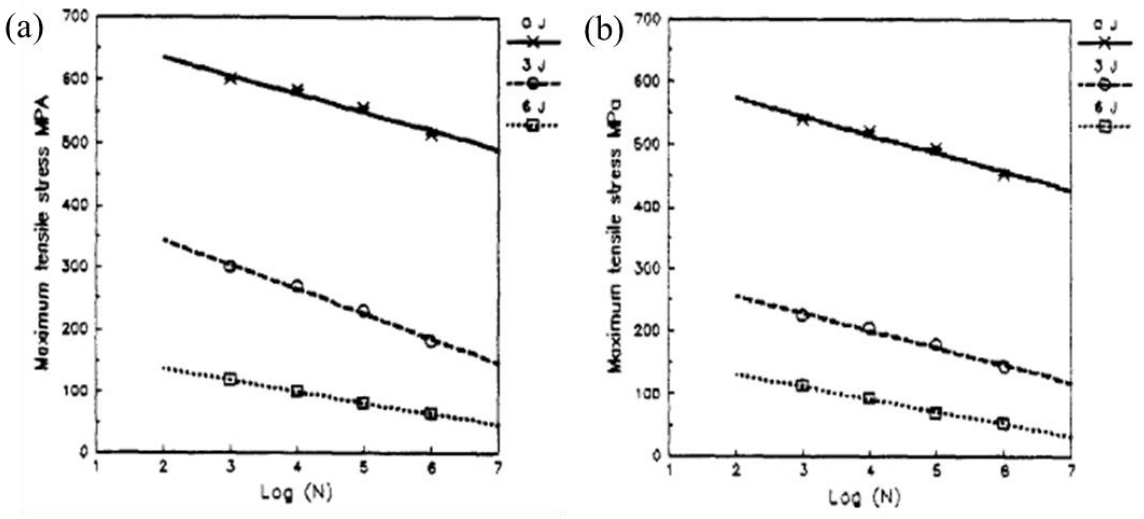

Figure 18: Comparison between S-N curves post-impact at room temperature: (a) tensile-tensile fatigue with R=0 and a frequency of loading of 10 Hz and (b) compression-tensile fatigue with R=-1 and a frequency of loading of 10 Hz (Ding et al. 1995).

V. Damage detection in composite materials

Nowadays, more and more engineered assets are used in daily basis. The presence of damage in these structures, in whatever form exhibited, compromise their integrity and safety if not detected in time. Therefore, structural damage can lead to catastrophic financial losses and in some cases human life losses. The awareness of safety, integrity and sustainability as top priorities for engineered assets require exhaustive and thoroughgoing research and development in the non-destructive evaluation (NDE) field. Indeed, adequate, and efficient NDE techniques can detect and monitor structural damage at early stages and thus prevent eventual failures that may occur, contributing hence to important monetary and human benefits.

Radioscopy, X-Ray imaging, infrared thermography, magnetic resonance imagery, laser interferometry and ultrasonic scanning are the commonly used method (Ewert et al., 2016; X.

Liu et al., 2019; Maierhofer et al., 2014; Pomarède et al., 2018; Ravikara et al., 2006; Usamentiaga et al., 2013). These latter have reached maturity and proved their efficiency in damage detection and evaluation over the past decades.

In this study, different non-destructive technics, complementing each other, are operated to propose a thorough NDE procedure enabling the identification of damage resulting from different type of loading, namely fatigue loading and low-velocity impact, that the studied composite may undergo during in service use.

This section focuses on describing the methods that will later be used in the coming chapters.

1. Infrared thermography (IRT)

Infrared thermography (IRT) is an imaging method that allows non-contact observation of real-time damage during mechanical tests (active) or to detect post-event damage (passive). The observed material is subjected to a thermal load emitted by a heat source. This source passes a thermal flux causing the propagation of the waves inside the sample and subsequently the reflection of the latter by reaching the free edges of the specimen. The reflected waves provide the surface temperature of the material. The presence of damage allows the creation of a heterogeneous medium and the modification of its index. When the waves arrive in this medium, a temperature gradient is generated in the specimen. The two media (healthy and damaged) react differently in terms of thermal conductivity and emissivity, which are subsequently detected by the sensor of infrared camera. As a result, a surface temperature map is obtained and analyzed enabling the detection of defects. The following figure (**Figure 19**) shows the damage observed on two different weaving samples.

Infrared thermography has shown its reliability at providing real-time information during mechanical loading. Meola and Carlomagno (Meola and Carlomagno 2014), and Meola et al. (Meola et al. 2017) use IRT to evaluate glass/epoxy composite structures subjected to impact events. They have shown that it is possible to follow the creation and the propagation of delamination that may occur during an impact event **Figure 19**. Toubal et al. (Toubal et al. 2006) linked the damage created by tension-tension fatigue loading in a carbon fiber reinforced polymer with the heat dissipation employing infrared thermography. The authors classify damage into three damage stages function of damage evolution and stiffness reduction.

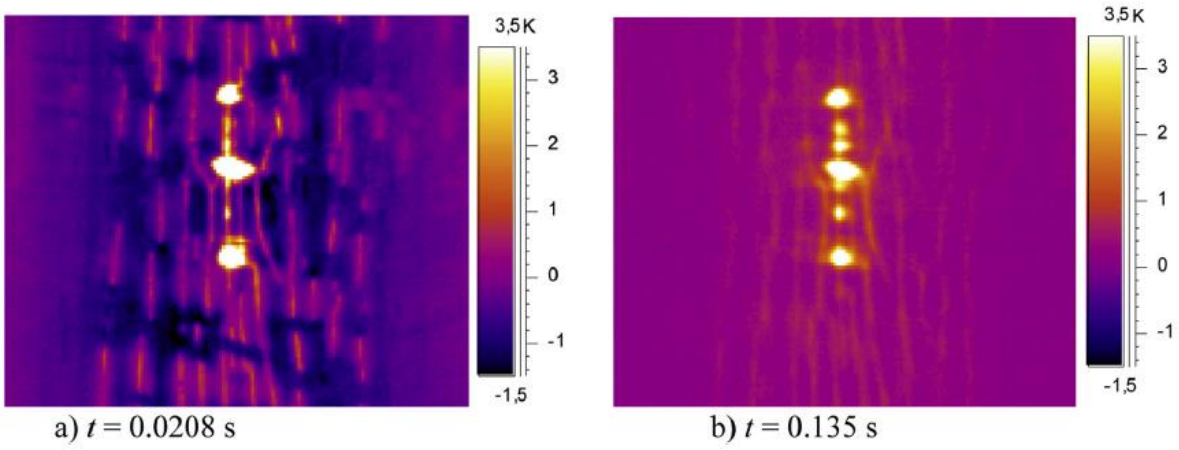

Figure 19: Images taken during an impact event at an energy level of 9.7 J on a GFRP (C. Meola & Carlomagno, 2014).

2. X-ray radiography

X-ray radiography is a technique based on the use of high energy X-ray photons. The beam penetrates the studied solid and is reflected on a special screen. The retrieved image is on a black and white scale function of the X-ray absorption parameter. The different media composing the solid are consequently differentiated and potential defects can be detected.

Since composite materials are considered as heterogeneous media, this technique is widely used in structural investigations to verify porosity levels, fiber concentration and orientation for instance. Additionally, it is also used in numerous fields such as NDT operations to detect damage mechanisms mainly delamination, fiber/matrix debonding and the matrix cracking (Kastner, Plank, and Requena 2012; Palka et al. 2016). Radiography technique has proven its efficiency in the NDT investigations and present a variety of advantages. Indeed, this method do not require the use of a coupling and provides a good defect size and shape detectability due to its high resolution and its power of penetration. However, this method presents some drawbacks since it necessitates the disassembly of the tested structural part to be able to have access to both sides. It is also considered as a high-cost method and a rather highly dangerous method due to the exposure to intensive radiations.

3. Ultrasonic testing

Wave propagation, in solid media has become worldwide used in both Non-Destructive testing (NDT) and Structural Health Monitoring (SHM). Many researchers have focused their interest on the study of the ultrasonic guided waves in solid media. Advances of the past decades have

made the developed inspection techniques more sensitive, faster, and economical compared to traditional used techniques.

In this section, the aim attention is focused on the propagation of two categories of waves namely Bulk waves and guided waves for damage inspection that is an important aspect of the current research project. Bulk waves are waves that travel in infinite media. The coverage volume in the case of Bulk waves propagation consist of a very limited and localised region. Whereas guided waves are waves that reflect and continue to propagate between boundaries providing hence a larger coverage volume. Consequently, to get full information on a studied structure using Bulk waves, transducers sweep all the surface of the structure unlike guided waves that only require a single probe position to inspect the entire structure.

The generation of Bulk waves or guided waves depends mainly on the employed frequency. Indeed, lower frequencies with larger wavelengths (higher than the structural thickness) are used for guided waves production.

Wave propagation has attracted the attention of so many researchers in the domain of mechanics. Ultrasonic testing is used on composite materials to provide information about the occurrence of defects inside or at the interface and hence information about the size and location can be obtained. C-scan is considered as a valuable tool as it is used to monitor the losses of the signals energy when encountering defects such as voids, delamination and debonding (Chang, Zheng, and Ni 2006; Imielinska et al. 2004; Liu et al. 2006; Lloyd 1989). In the case of fiber reinforced composite investigation, the ultrasonic beam propagates along the fibers axis (Barwick and Papathanasiou 2003; Pain and Drinkwater 2013) leading to the detection of fiber misalignment. Delamination in the other hand causes a loss of transmission and a reflection from a certain depth. Research related to the use of US propagation in carbon fiber reinforced polymers show that information about the interlaminar quality can be obtained from the propagation of waves perpendicular to the composite plies. To ameliorate the quality of the results obtained using this technique, several studies are taking place proposing novel-processing procedures in both time domain and frequency domain (Powers et al. 2016; Sejdić, Djurović, and Jiang 2009).

However, even though the US based method have shown their efficiency in terms of damage detection, some techniques such as immersion techniques require the disassemble of the tested structures causing a certain delay in the operation of the structure. Some types of composites are very sensitive to water absorption and necessitate a drying process. To overcome the

previously mentioned drawbacks Nasa Langley propose to use a captive water column coupling approach (Elliott Cramer 2016) providing a coupling similar to water coupling. In addition, advanced studies are considering other types of coupling rather than water use such as air coupling that provides quicker scanning and more simplified in service inspection (Imielinska et al. 2004; Kazys et al. 2006; Zhang et al. 2020). The difficulties related to the coupling have let to the choosing of laser as an ultrasound generator that gives the possibility to investigate more complex structures. Despite all the advantages given by this method, its cost remains very high compared to other method. It reduces hence its application in the industrial field.

3.1. Lamb waves-based investigation

3.1.1. Lamb waves theory

Although extensive literature exists about Lamb waves, it is required to summarize the fundamentals and basic theory of Lamb waves before proceeding to their applications for damage detection and investigation.

Lamb waves, also known as plate waves, are waves that propagate in a plate-like medium. The particularity of this type of waves is that they are continuously guided by the free upper and lower boundaries (surfaces) (**Figure 20**). Lamb waves are generated when the wavelength is comparable to the thickness of the plate. They are known to be very dispersive; meaning that the velocity is frequency-dependent affecting consequently the wavelength. This phenomenon causes the propagation of different waves modes that can be folded into two categories: Symmetric (S_i) and antisymmetric (A_i) modes (**Figure 21**).

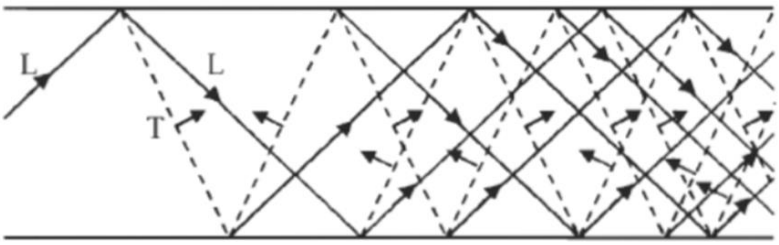

Figure 20: Lamb waves generation from longitudinal (L) and transversal (T) waves (El Abasi 2014).

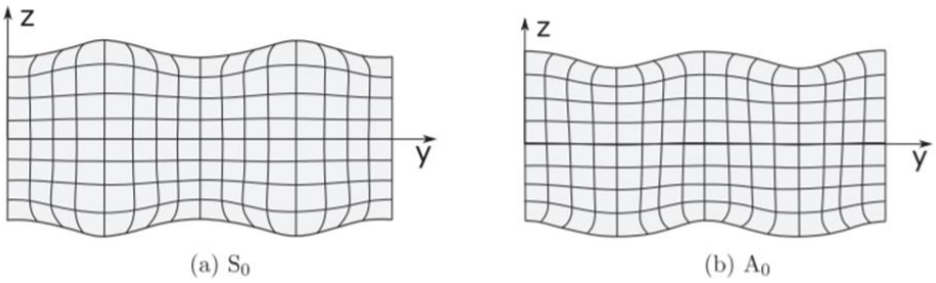

Figure 21: Illustration of symmetric (a) and Antisymmetric (b) Lamb modes (de Miguel, Pagani, and Carrera 2019).

Several symmetric and antisymmetric modes, with several propagation velocities, can co-exist and propagate at the same time. In a homogeneous and isotropic plate, these Lamb waves modes are generally described as follow (Rose, 2014):

$$\frac{\tan(qh)}{\tan(ph)} = \frac{4k^2qp\mu}{(\lambda k^2 + \lambda p^2 + 2\mu p)(k^2 - q^2)}$$

With $p^2 = (w^2/ c_L^2) - k^2$

$q^2 = (w^2/ c_T^2) - k^2$

Where, c_L and c_T, the longitudinal and transverse modes velocities and with h, k, w and λ the half thickness of the plate, the wave number, the pulsation and the Lamé constant respectively.

Lamb waves equation in thin plates can be folded into two parts corresponding to symmetric and antisymmetric modes known as "Rayleigh-Lamb equations" and are presented as follow **Figure 22** (Su and Ye 2009):

$$\text{For symmetric modes: } \frac{\tan(qh)}{\tan(ph)} = -\frac{4k^2qp}{(k^2 - q^2)^2}$$

$$\text{For anti} - \text{symmetric modes: } \frac{\tan(qh)}{\tan(ph)} = -\frac{(k^2 - q^2)^2}{4k^2qp}$$

The graphical representation of Lamb modes velocities function of frequency is known as "dispersion curves" and are presented as follow in **Figure 22** (Su and Ye 2009).

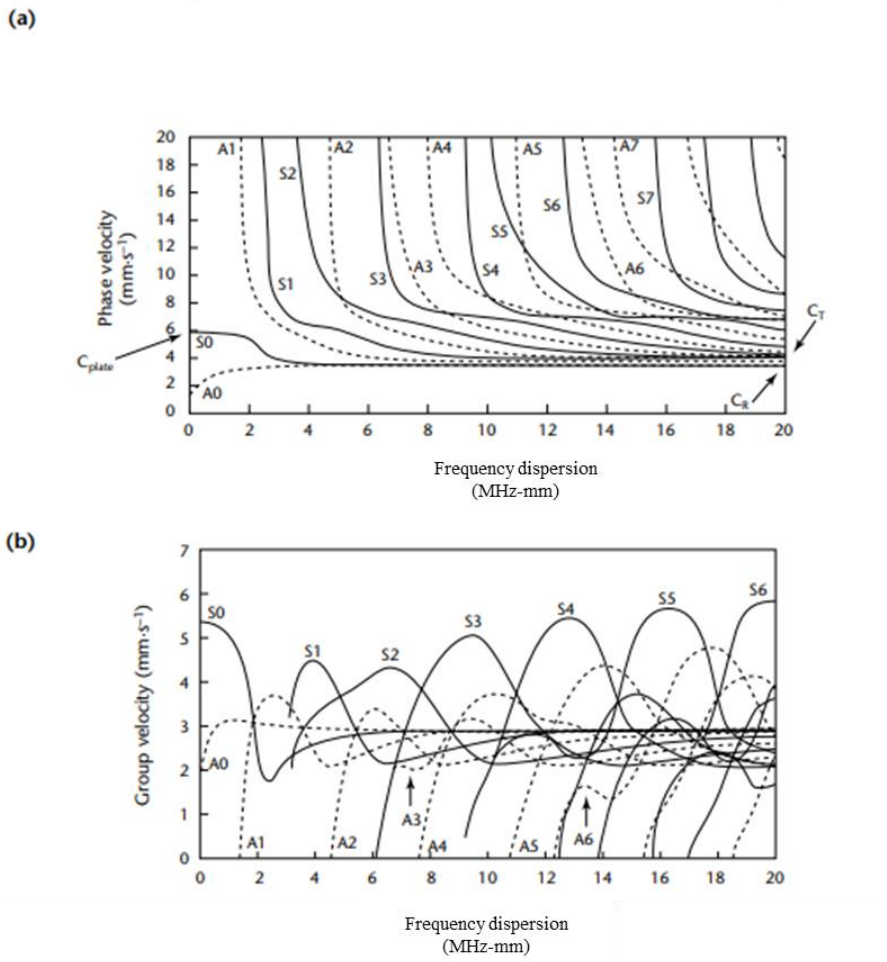

Figure 22: Typical dispersion curves in an aluminum plate with (a) phase velocity dispersion curves; (b) group velocity dispersion curves (Su and Ye 2009).

The particle motion in symmetric and antisymmetric modes show a difference in the displacement direction. Indeed, symmetrical modes have a radial in-plane displacement of the particles whereas antisymmetric modes have an out of plan displacement that can be qualified as complex through-thickness displacement.

In the case of undamaged anisotropic plate, the equations are more complex. In fact, even though the equations look simple mathematically speaking, there resolution remain complicated and require numerical resolution except some limited cases where analytical solution exist.

Thus, the wave equations are given by:

$$C_{11}\frac{\partial^2 u_1}{\partial x_1^2}+C_{44}\frac{\partial^2 u_1}{\partial x_2^2}+C_{55}\frac{\partial^2 u_1}{\partial x_3^2}+2C_{14}\frac{\partial^2 u_1}{\partial x_1\,\partial x_2}+C_{14}\frac{\partial^2 u_2}{\partial x_1^2}+C_{24}\frac{\partial^2 u_2}{\partial x_2^2}+C_{56}\frac{\partial^2 u_2}{\partial x_3^2}+(C_{12}+C_{44})\frac{\partial^2 u_2}{\partial x_1\,\partial x_2}$$
$$+(C_{13}+C_{55})\frac{\partial^2 u_3}{\partial x_1\,\partial x_3}+(C_{34}+C_{56})\frac{\partial^2 u_3}{\partial x_2\,\partial x_3}=\frac{\partial^2 u_1}{\partial t^2}$$

$$C_{14}\frac{\partial^2 u_1}{\partial x_1^2}+C_{24}\frac{\partial^2 u_1}{\partial x_2^2}+C_{56}\frac{\partial^2 u_1}{\partial x_3^2}+(C_{12}+C_{44})\frac{\partial^2 u_2}{\partial x_1\,\partial x_2}+C_{44}\frac{\partial^2 u_2}{\partial x_1^2}+C_{22}\frac{\partial^2 u_2}{\partial x_2^2}+C_{66}\frac{\partial^2 u_2}{\partial x_3^2}+2C_{24}\frac{\partial^2 u_2}{\partial x_1\,\partial x_2}$$
$$+(C_{34}+C_{56})\frac{\partial^2 u_3}{\partial x_1\,\partial x_3}+(C_{23}+C_{66})\frac{\partial^2 u_3}{\partial x_2\,\partial x_3}=\frac{\partial^2 u_2}{\partial t^2}$$

$$(C_{13}+C_{55})\frac{\partial^2 u_1}{\partial x_1\,\partial x_3}+(C_{34}+C_{56})\frac{\partial^2 u_1}{\partial x_2\,\partial x_3}+(C_{34}+C_{56})\frac{\partial^2 u_2}{\partial x_1\,\partial x_3}+(C_{23}+C_{66})\frac{\partial^2 u_2}{\partial x_1\,\partial x_2}+C_{55}\frac{\partial^2 u_3}{\partial x_1^2}$$
$$+C_{66}\frac{\partial^2 u_3}{\partial x_2^2}+C_{33}\frac{\partial^2 u_3}{\partial x_3^2}+2C_{56}\frac{\partial^2 u_3}{\partial x_1\,\partial x_2}=\frac{\partial^2 u_3}{\partial t^2}$$

With C_{ij} the stiffness components and u_i the displacement vector.

Consequently, symmetric and antisymmetric modes are framed as:

$$A = D_{11}G_1\tan(\gamma\alpha_1)-D_{13}G_3\tan(\gamma\alpha_3)+D_{15}G_5\tan(\gamma\alpha_5)=0;\ \text{for the antisymmetric modes}$$

$$S = D_{11}G_1\cot(\gamma\alpha_1)-D_{13}G_3\cot(\gamma\alpha_3)+D_{15}G_5\cot(\gamma\alpha_5)=0;\ \text{for the symmetric modes}$$

Where, α_1, α_3 and α_5 the solution of the wave equations when the displacement field is expressed as:

$$u_j = U_j e^{i\xi(x_1+\alpha x_3-ct)}$$

With

$$G_1 = D_{23}D_{35}-D_{33}D_{25}$$

$$G_2 = D_{21}D_{35}-D_{31}D_{25}$$
$$G_3 = D_{21}D_{33}-D_{31}D_{23}$$

And

$$D_{1q} = C_{13}+C_{34}V_q+C_{33}\alpha_q W_q$$

$$D_{2q} = C_{55}(\alpha_q+W_q)+C_{56}\alpha_q W_q$$

$$D_{3q} = C_{56}(\alpha_q + W_q) + C_{66}\alpha_q W_q$$

And V_q and W_q given by:

$$V_q = \frac{U_{2q}}{U_{1q}} \text{ and } W_q = \frac{U_{3q}}{U_{1q}}$$

3.1.2. Lamb waves for damage investigation in composite materials

Lamb waves based methods are proving themselves as effective alternatives due to their sensitivity, their capacity to select modes and frequencies and the ability to inspect large structures (Levent Degertekin, Honein, and Khuri-Yakub 1995). Their high frequency nature and their low attenuation makes guided waves suitable for small defects detection especially in thin structures. Lamb waves have been used widely in different ways over the years. As expected, damage influences the Lamb waves propagation characteristics. Indeed, it can induce reflection, mode conversion and many more phenomena. The location and the geometrical aspects of the defect produce a unique dispersive response. As an example, a quasi-isotropic composite laminate in a healthy state sample is considered along with defect containing one. A comparison between the propagating signals in both cases is carried out. **Figure 23** shows the signals retrieved in both cases. Additional peaks are observed in the case of damaged sample between the incident S_0 mode and its reflection $S_{0\text{-boundary}}$.

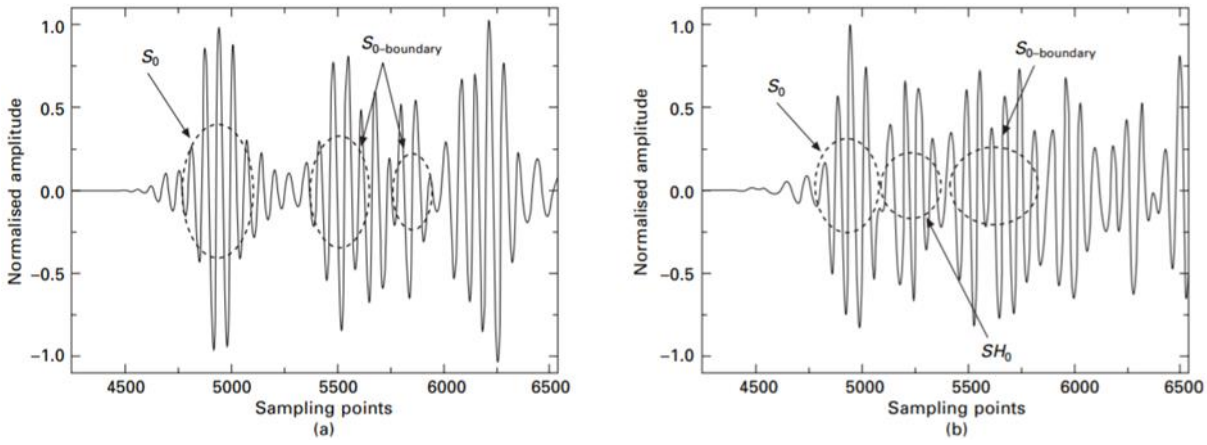

Figure 23: Ultrasonic response of the signal propagating in a healthy structure (a) and in a damaged structure (b) (Su and Ye 2008).

More advanced investigation methods have been later developed. Li et al. (Li, Cho, and Achenbach 2012) have proposed an experimental procedure focusing on the behavior of second harmonic Lamb waves when dealing with thermal fatigue damage in multi-layered composites. The results have revealed the reliability of the non-linear acoustic parameters of Lamb waves as an indicator to study thermal fatigue damage. Yelve et al. (Yelve, Mitra, and Mujumdar 2017) use a method based on fundamental and higher harmonics of Lamb waves to assess delamination in composite structures. Indeed, Lamb waves provide good potential for damage detection. Zheng et al. (Zheng et al. 2019) have employed a combination of an anisotropic wavefront and the time of flight (TOF) algorithm to quantitively determine impact damage and debonding. Experimental test and numerical simulation have revealed many advantages. It occurs that Lamb waves are very sensitive to small debonding; therefor one can locate and determine the size of damage at a very early stage. However, the propagation of Lamb waves in composite plates is extremely complex due to different parameters such as dispersion, multi-mode characteristics and direction dependency of the wave velocity (He et al. 2013; Pant 2014).

3.2. Stiffness estimation

3.2.1. Overview on the elastic properties' determination

To ensure the performance of a composite structure, the identification and the determination of the mechanical properties is necessary. Different methods enabling the determination of the elastic properties for composite materials are widely employed in the literature. One can classify these methods into two main categories: destructive (mechanical) and non-destructive methods. However, the mechanical identification of these properties, following ASTM standards (D 3518/D 3518M for in-plane properties and D3039/D 3039M for tensile properties), are considered as time consuming, necessitate important resources and require a large number of samples (Barazanchy, Roth, and Giurgiutiu 2018). Consequently, more research is directed towards the non-destructive methods that are as efficient as the mechanical techniques in the determination of the materials properties. Bulk wave propagation is the ultimate technique since there is a direct link between the stiffness of the material and the characteristics of the bulk waves (Castagnede, Jenkins, and Sachse 1991; Every and Sachse 1990; Hosten, Castaings, and Kundu 1998; Stijnman 1995). Furthermore, by orienting a specimen in different directions, a single specimen is sufficient to experimentally obtain all the components of the stiffness matrix using adapted algorithms based on the time of flight (TOF) measurements (Castaings, Hosten,

and Kundu 2000; Gieske and Allred 1974; Hosten et al. 1998; Marguères and Meraghni 2013; Marguères, Meraghni, and Benzeggagh 1999; Markham 1970; Smith 1972).s

Markham (Markham 1970) has first introduced the ultrasonic based methods determining the stiffness matrix for laminate composites in 1970. The author has proceeded to measure the velocity of propagation of the ultrasonic wave in multiple directions to obtain the composite elastic constants. Markham's method is later employed by Smith (Smith 1972) enabling him to determine to determine five constants. Gieske and Allred (Gieske and Allred 1974) have used the same method and have succeeded to increase the number of the retrieved elastic constants from five to nine. By closely analyzing the time of flight (TOF) measurements, the authors have found that the velocity obtained using Markham's method correspond s to the group velocity. Thus, phase velocity is the parameter fitted for the determination of the elastic constants. Pearson and Murri (Pearson and Murri 1987) have later showed that the group velocity and the phase velocity are connected leading therefore to the proper values of the elastic properties. Mal et al [11] (Mal, Lih, and Bar-Cohen 1987) have employed Leaky Lamb waves (LLW) to determine all the constants of the unidirectional laminate. The authors analyzed the TOF of the reflected acoustic wave. The principle of the method relies on performing time of flight measurements while the specimen is immersed in water. This approach leads to the identification of the five constants of the material.

Castaings et al. (Castaings et al. 2000) and Hosten et al. (Hosten et al. 1998) use an immersion ultrasonic procedure employing emitter transducer and a large rectangular receiver, oriented both at an angle to the surface of the composite. This technique results in the acquirement of the stiffness constants along with the transverse shear and out-of-plane properties. It is worth mentioning that in the case of thin plates, it is extremely difficult to experimentally obtain these properties. Indeed, the dimensions of the transducers is generally higher than the thickness of the specimen, making the propagation of the wave inside the material less possible/accurate.

Marguères and Meraghni (Marguères and Meraghni 2013) and Marguères et al. (Marguères et al. 1999) applied an immersion ultrasonic approach to retrieve the stiffness matrix components of anisotropic composite materials at both damaged and undamaged state. **Figure 24** shows the different plans of measurements (wave propagation) enabling the extraction of the rigidity constants for an anisotropic material. The authors validated the experimental procedure by the means of numerical confirmation. They have found a decrease in the values of the shear properties for the samples subjected to low-velocity impact. Furthermore, an overall reduction

off the stiffness has been observed when combining fatigue loading with impact damage. This immersion ultrasonic approach is shown to be efficient even on damaged specimen enabling to non-destructively quantify the effect of damage on the mechanical properties. A similar approach was adopted by Pomarède et al. (Pomarède et al. 2018) to estimate the values of the components of the stiffness matrix of a thermoplastic reinforced by glass fibers subjected to tensile loading.

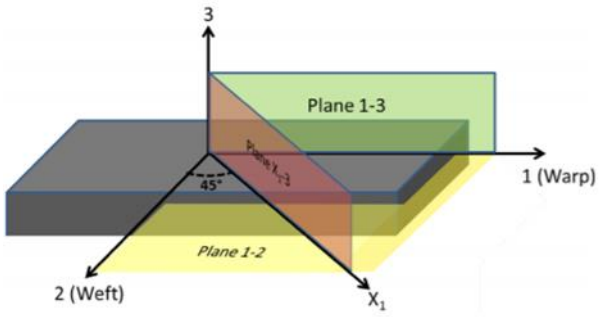

Figure 24: Illustration of the measurement plans enabling the extraction of the rigidity constants for an anisotropic material.

3.2.2. Bulk waves detailed methodology for stiffness constants determination

Marguerès and Meraghni (Marguères and Meraghni 2013) and Marguerès et al. (Marguères et al. 1999) have described a procedure based on Bulk waves propagation to determine the Stiffness constants for multiple composite materials. As previously mentioned, phase velocity is the key parameter to retrieve the stiffness constants. It is important to mention that when dealing with Bulk waves, group velocity and phase velocity are the same, avoiding hence any confusion. The authors followed a specific approach to go from time of flight and obtain the Stiffness matrix. To describe the procedure enabling the non-destructive retrieval of the mechanical properties, a particular interest should be directed towards the understanding of the physics behind the propagation of Bulk waves in a media. By combining three equations:

- The motion equation:

$$\frac{\partial \sigma_{ij}}{\partial x_j} = \rho \frac{\partial^2 u_i}{\partial t^2}$$

- Hooke's law for linear elastic behavior:

$$\sigma_{ij} = c_{ijkl}\varepsilon_{kl}$$

- Relation between strain and displacement field for small perturbations:

$$\varepsilon_{kl} = \frac{1}{2}\left(u_{k,l} + u_{l,k}\right)$$

With σ_{ij} the stress tensor, u_i the displacement, ρ the density of the given material, c_{ijkl} the stiffness tensor and ε_{kl} the deformation tensor.

One can obtain the following relation linking the displacement to the stiffness tensor:

$$\frac{\partial c_{ijkl}}{\partial x_j}\left(u_{k,l} + u_{l,k}\right) + c_{ijkl}\frac{\partial}{\partial x_j}\left(u_{k,l} + u_{l,k}\right) = \rho\frac{\partial^2 u_i}{\partial t^2}$$

In a homogeneous media, stiffness components do not depend on the local position in the material. Consequently, the spatial derivation of the stiffness tensor has a value of zero. The equation 16 is then given as follow:

$$\rho\frac{\partial^2 u_i}{\partial t^2} = c_{ijkl}\frac{\partial^2 u_k}{\partial x_j\,\partial x_k}$$

In the case of Bulk wave, the solution for this equation, in the case of bulk waves is:

$$u_i = U_i \exp\left(i\left(\xi n_j x_j - wt\right)\right)$$

With: ξ the bulk wavenumber, n_j the propagation direction (unit vector), w the angular frequency, U_i the wave polarization.

The Christoffel equation is obtained:

$$\left(C_{ijkl} n_k n_j - \rho v^2 \delta_{ij}\right) U_l = 0$$

With: $v = \frac{w}{\xi}$

The Christoffel matrix, which is symmetric, is defined as:

$$C_{ijkl} n_k n_j = G_{ik}$$

The Christoffel equation can be written as follows:

$$\left(G_{ik} - \rho v^2 \delta_{ij}\right) U_l = 0$$

Solving the Christoffel equation leads to obtaining three solutions corresponding to three wave modes that can appear for every considered direction n. These modes can be defined as: quasi-longitudinal mode (QL), quasi-transversal mode 1 (QT1) and a quasi-transversal mode 2 (QT2). The representation of these three modes constitutes the slowness curves i.e., the inverse of the phase velocity that are inversely proportional to the stiffness constants in the wave mode propagation direction and are characteristic of the sample. **Figure 25** exhibits a representation of the slowness curves for a unidirectional composite.

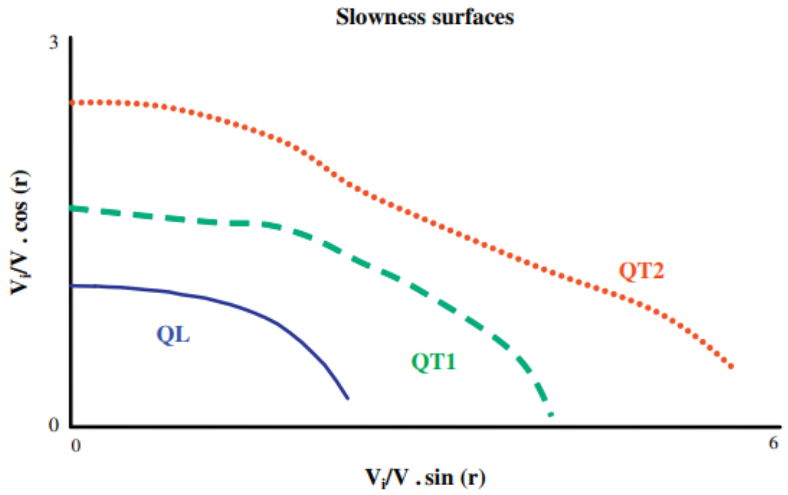

Figure 25: Schematic representation of typical slowness curves showing the three propagating modes function of the incidence angle: Quasi-longitudinal (QL), quasi-transversal 1 (QT1) and quasi-transversal 2 (QT2) (Marguères and Meraghni 2013).

Mode conversion occurs when changing the incidence angle leading hence to the appearance of the aforementioned modes. Indeed, depending on the incidence angle, the mode can coexist and propagate simultaneously. **Figure 26** represents the order of appearance of the three modes function of the incidence angle and also show the two critical angles corresponding to the propagation of a single mode. It is worth mentioning that after reaching the second critical angle, only surface waves i.e., Rayleigh waves propagate in the surface of the material.

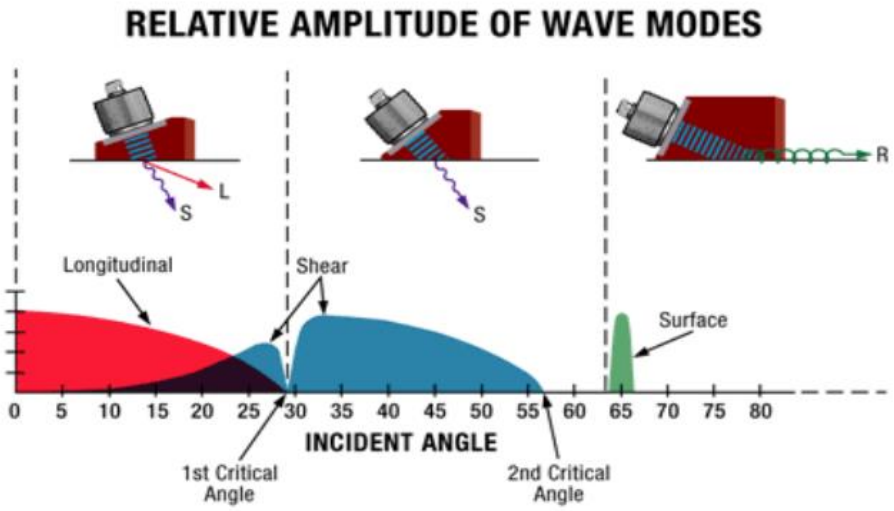

Figure 26: Illustration of the propagating modes function of the incident angle pointing to the two critical angles corresponding to the angles relative to one mode propagation [www.olympus-ims.com].

VI. Conclusions and perspectives

This chapter has been dedicated to present the aspects that will be assessed in the following chapters. The aim is to introduce all the themes that will be studied and to provide a global bibliographic review enabling to understand the need and necessity to resolve the main problematic of this PhD research project. Moreover, since safety and reliability are two important features in the automobile sector, maintaining the same performances during all the in-service life is a very sensitive matter. Being able to determine the tolerance limit i.e., the maximum damage that the material can withstand without having any influence on its performance to fit the automotive industry requirements in terms of safety and lightweight.

The first step of this bibliographic review has been devoted to highlight and understand the complexity of the mechanical behavior under probably occurring solicitations during in-service life. Consequently, a thoroughly experimental analysis of the behavior of the VizilonTM SB63G1-T1.5-S3 composite material under low-velocity impact and fatigue loading is crucial.

The second step has been dedicated to a review on the commonly used damage detection techniques. Indeed, quantifying the induced damage using non-destructive techniques is proven to be efficient in the evaluation of its criticality. Therefore, it is used as a tool that helps decide whether the criterion of damage tolerance is still respected.

A non-exhaustive study will take place in the up-coming chapters based on the element discussed in the present chapter.

VII.Reference

El Abasi, Driss. 2014. “Contribution à La Caractérisation Non-Destructive Des Roches Terrestres et Extraterrestres Par Des Techniques Ultrasonores.” Université Ibn Zohr, Agadir, Maroc.

Albouy, W., B. Vieille, and L. Taleb. 2014. “Influence of Matrix Ductility on the High-Temperature Fatigue Behavior of off-Axis Woven-Ply Thermoplastic and Thermoset Laminates.” International Journal of Fatigue 63:85–96. doi: 10.1016/j.ijfatigue.2014.01.010.

Alderliesten, R. C. 2015. “Designing for Damage Tolerance in Aerospace: A Hybrid Material Technology.” Materials and Design 66(PB). doi: 10.1016/j.matdes.2014.06.068.

Arif, M. 2014. “Damage Mechanisms in Short Glass Fiber Reinforced Polyamide-66 under Monotonic and Fatigue Loading: Effect of Relative Humidity and Injection Molding Induced Microstructure.” Ecole Nationale Supérieure d’Arts et Métiers.

Arif, M. F., F. Meraghni, Y. Chemisky, N. Despringre, and G. Robert. 2014. “In Situ Damage Mechanisms Investigation of PA66 / GF30 Composite : Effect of Relative Humidity.” COMPOSITES PART B 58:487–95. doi: 10.1016/j.compositesb.2013.11.001.

Atas, Cesim, and Onur Sayman. 2008. “An Overall View on Impact Response of Woven Fabric Composite Plates.” Composite Structures 82:336–45. doi: 10.1016/j.compstruct.2007.01.014.

Aymerich, F., F. Dore, and P. Priolo. 2009. “Simulation of Multiple Delaminations in Impacted Cross-Ply Laminates Using a Finite Element Model Based on Cohesive Interface Elements.” Composites Science and Technology 69(11–12):1699–1709. doi: doi.org/10.1016/j.compscitech.2008.10.025.

Barazanchy, D., W. Roth, and V. Giurgiutiu. 2018. “A Non-Destructive Material Characterization Framework for Retrieving a Sti Ff Ness Matrix Using Bulk Waves.” Composite Structures 185:27–37. doi: 10.1016/j.compstruct.2017.10.071.

Barwick, S. C., and Thanasis Papathanasiou. 2003. “Identification of Fiber Misalignment in Continuous Fiber Composites.” Polymer Composites 24(3):475–86. doi: doi.org/10.1002/pc.10046.

Baucom, J. N., M. A. Zikry, and A. M. Rajendran. 2005. “Low-Velocity Impact Damage Progression in Woven E-Glass Composite Systems.” Composite Part A: Applied Science and Manufacturing 36(5):658–64. doi: doi.org/10.1016/j.compostesa.2004.07.008.

Benaarbia, Adil, André Chrysochoos, and Gilles Robert. 2014. “Influence of Relative Humidity and Loading Frequency on the PA6 . 6 Cyclic Thermomechanical Behavior : Part I . Mechanical and Thermal Aspects.” Polymer Testing 40:290–98. doi: 10.1016/j.polymertesting.2014.09.019.

Boisse, P., N. Hamila, E. Guzman-Maldonado, A. Madeo, G. Hivet, and F. Dell’Isola. 2017. “The Bias-Extension Test for the Analysis of in-Plane Shear Properties of Textile Composite Reinforcements and Prepregs: A Review.” International Journal of Materials Forming 10(4):473–92.

Bouvet, Christophe. 2011. “Dommages d’impact Sur Stratifié Composite.” in 17èmes Journées Nationale sur les Composites (JNC17). Poitiers.

Brunner, A. J. 2008. “Experimental Study of Delamination in Cross-Ply Laminates.” in Delamination Behavior of Composites: A volume in Woodhead Publishing Series in Composites Science and Engineering.

Cantwell, W. J., and J. Morton. 1991. “The Impact Resistance of Composite Materials - a Review.” Composites 22(5):347–62. doi: 10.1016/0010-4361(91)90549-V.

Carraro, P. A., L. Maragoni, and M. Quaresimin. 2015. “Influence of Manufacturing Induced Defects on Damage Initiation and Propagation in Carbon/Epoxy NCF Laminates.” Advanced Manufacturing: Polymer and Composites Science 1(1). doi: 10.1179/2055035914Y.0000000004.

Castagnede, B., J. Jenkins, and W. Sachse. 1991. “Optimal Determination of the Elastic Constants of Composites Materials from Ultrasonic Wave Speed.” Journal of Applied Physics 67(6):2753–61. doi: doi.org/10.1063/1.345441.

Castaings, Michel, Bernard Hosten, and Tribikram Kundu. 2000. “Inversion of Ultrasonic, Plane-Wave Transmission Data in Composite Plates to Infer Viscoelastic Material Properties.” NDT and E International 33(6):377–92. doi: doi.org/10.1016/S0963-8695(00)00004-9.

Chang, Fu-Kuo, Hyung Yun Choi, and Syh-Tsang Jeng. 1990. “Study on Impact Damage in Laminated Composites.” Mechanics of Materials 10(1–2):83–95. doi: doi.org/10.1016/0167-6636(90)90019-C.

Chang, Junjie, Changliang Zheng, and Qing-Qing Ni. 2006. “The Ultrasonic Wave Propagation in Composite Material and Its Characteristic Evaluation.” Composite Structures 75(1–4):451–56. doi: doig.org/10.1016/j.compstruct.2006.04.040.

Colombo, Chiara, Trunal Bhujangrao, and Flavia Libonati. 2019. “Effects of Delamination on the Fatigue Life of GFRP: A Thermographic and Numerical Study.” Composite Structures 218. doi: doi.org/10.1016/j.compstruct.2019.03.023.

Cuadra, Jefferson, Prashanth A. Vanniamparambil, Kavan Hazeli, Ivan Bartoli, and Antonios Kontsos. 2013. “Damage Quantification in Polymer Composites Using a Hybrid NDT Approach.” Composites Science and Technology 83:11–21. doi: 10.1016/j.compscitech.2013.04.013.

Davies, G. A. O., and R. Olsson. 2004. “Impact on Composite Structures.” The Aeronautical Journal 108(1089):541–63. doi: doi.org/10.1017/S0001924000000385.

Ding, Y. Q., Y. Yan, and R. McIlhagger. 1995. “Effect of Impact and Fatigue Loads on the Strength of Plain Weave Carbon-Epoxy Composites.” Journal of Materials Processing Tech. 55(2):58–62. doi: 10.1016/0924-0136(94)01785-9.

Elliott Cramer, K. 2016. “Research Developments in Nondestructive Evaluation and Structural Health Monitoring for the Sustainment of Composite Aerospace Structures at NASA.” Pp. 1–7 in Congress of the international Council of the Aeronautical Sciences.

Every, G. A., and Wolfgang Sachse. 1990. “Determination of the Elastic Constants of Aniotropic Solids from Acoustic-Wave Groupe-Velocity Measurements.” American Physical Society 42(13). doi: doi.org/10.1103/PhysRevB.42.8196.

Ewert, Uwe, Stefan Tschaikner, Martin Hohendorf, Carsten Bellon, Misty. I. Haith, Peter Huthwaite, and Michael. J. S. Lowe. 2016. “Corrosion Monitoring with Tangential Radiography and Limited View Computed Tomography.” in AIP Conference proceedings.

Faggiani, A., and B. G. Falzon. 2010. “Predicting Low-Velocity Impact Damage on a Stiffened Composite Panel.” Composite Part A: Applied Science and Manufacturing 41(6):737–49. doi: doi.org/10.1016/.compostesa.2010.02.005.

Giancane, S., F. W. Panella, R. Nobile, and V. Dattoma. 2010. “Fatigue Damage Evolution of Fiber Reinforced Composites with Digital Image Correlation Analysis.” Pp. 1307–15 in Procedia Engineering. Vol. 2. Elsevier.

Gieske, J. H., and R. E. Allred. 1974. “Elastic Constants of B-A1 Composites by Ultrasonic Velocity Measurements.” Experimental Mechanics 14:158–65. doi: doi.org/10.1007/BF02322839.

Greenhalgh, Emile. S. 2009. “Delamination-Dominated Failures in Polymer Composites.” in Failure Analysis and Fractography of Polymer Composites.

Greenhalgh, Emile, and Matthew Hiley. 2003. “The Assessment of Novel Materials and Processes for the Impact Tolerant Design of Stiffened Composite Aerospace Structures.” Composite Part A: Applied Science and Manufacturing 34:151–61.

Harris, Bryan. 2003. Fatigue in Composites: Science and Technology of the Fatigue Response of Fiber-Reinforced Plastics. edited by B. Harris. Woodhead Publishing.

Hautier, M. 2010. “Analyse Des Réparations Des Matériaux Composites : Mise En Oeuvre d’un Procédé Par Infiltration et Étude Du Comportement Mécanique.” Université de Toulouse.

He, Cunfu, Hongye Liu, Zenghua Liu, and Bin Wu. 2013. “The Propagation of Coupled Lamb Waves in Multilayered Arbitrary Anisotropic Composite Laminates.” Journal of Sound and Vibration 332(26):7243–56. doi: 10.1016/j.jsv.2013.08.035.

Hongkarnjanakul, N., C. Bouvet, and S. Rivaillant. 2013. “Validation of Low Velocity Impact Modelling on Different Stracking Sequences CFRP Laminates and Influence of Fiber Failure.” Composite Structures 106:549–59. doi: doi.org/10.1016/j.compstruct.2013.07.008.

Hosten, Bernard, Michel Castaings, and Tribikram Kundu. 1998. “Identification of Viscoelastic Moduli of Composite Materials from the Plate Transmission Coefficients.” in Review of Progress in Quantitative Nondestructive Evaluation.

Ilyas, M. 2010. “Damage Modeling of Carbone Epoxy Laminated Composites Submitted to Impact Loading.” Université de Toulouse.

Imielinska, K., M. Castaings, R. Wojtyra, J. Haras, E. LeClezio, and B. Hosten. 2004. “Air-Coupled Ultrasonic C-Scan Technique in Impact Response Testing of Carbon Fiber and Hybrid:

Glass, Carbon and Kevlar/Epoxy Composites." Journal of Materials Processing Tech. 157–158:513–22. doi: doi.org/10.1016/j.jmatprotec.2004.07.143.

Jawaid, Mohammad, Mohamed Thariq, and Naheed Saba. 2018. Durability and Life Prediction in Biocomposites, Fiber-Reinforced Composites and Hybrid Composites.

John, Mathew, and Raghu V. Prakash. 2018. "Quantification of Fatigue Damage in Carbon Fiber Composite Laminates through Image Processing." Pp. 16995–5 in Materials Today: Proceedings. Vol. 5. Elsevier Ltd.

Jollivet, Thomas, Catherine Peyrac, and Fabien Lefebvre. 2013. "Damage of Composite Materials." Procedia Engineering 66:746–58. doi: 10.1016/j.proeng.2013.12.128.

Kaminski, M., F. Laurin, J. F. Maire, C. Rakotoarisoa, and E. Hémon. 2015. "Fatigue Damage Modeling of Composite Structures: The ONERA Viewpoint Life Prediction Methodologies for Materials and Structures Fatigue Damage Modeling of Composite Structures: The ONERA Viewpoint." Life Prediction Methodologies for Materials and Structures (9).

Kara, Memduh, and K. Muhammed. 2017. "Effects of the Number of Fatigue Cycles on the Impact Behavior of Glass Fiber / Epoxy Composite Tubes." Composite Part B 123:55–63. doi: 10.1016/j.compositesb.2017.04.021.

Kastner, Johann, Bernhard Plank, and Guillermo Requena. 2012. "Non-Destructive Characterisation of Polymers and Al-Alloys by Polychromatic Cone-Beam Phase Contrast Tomography." Materials Characterization 64:79–87. doi: 10.1016/j.matchar.2011.12.004.

Kazys, R., A. Demcenko, E. Zukauskas, and L. Mazeika. 2006. "Air-Coupled Ultrasonic Investigation of Multi-Layered Composite Materials." Ultrasonics 44:819–22. doi: doi.org/10.1016/j.ultras.2006.05.112.

Kim, Jang-kyo, and Man-lung Sham. 2000. "Impact and Delamination Failure of Woven-Fabric Composites." Composites Science and Technology 60(5):745–61. doi: 10.1016/S0266-3538(99)00166-9.

Launay, A., Y. Maitournam, H. M, and I. Raoult. 2013. "Modelling the Influence of Temperature and Relative Humidity on the Time-Dependent Mechanical Behavior of a Short Glass Fiber Reinforced Polyamide." Mechanics of Materials 56:1–10.

Levent Degertekin, F., B. V Honein, and B. T. Khuri-Yakub. 1995. “Efficient Excitation and Detection of Lamb Waves for Process Monitoring and NDE.” in IEEE Utrasonics Symposium. Stanford.

Li, Weibin, Younho Cho, and Jan D. Achenbach. 2012. “Detection of Thermal Fatigue in Composites by Second Harmonic Lamb Waves.” Smart Materials and Structures 21(8).

Liu, Ling, Bo-Ming Zhang, Dian-Fu Wang, and Zhan-Jun Wu. 2006. “Effects of Cure Cycles on Void Content and Mechanical Properties of Composite Laminates.” Composite Structures 73:303–9. doi: doi.org/10.1016/j.compstruct.2005.02.001.

Liu, Xianglei, Peipei Wang, Zhao Lu, Kai Gao, Hui Wang, Chiyu Jiao, and Xuedong Zhang. 2019. “Damage Detection and Analysis of Urban Bridges Using Terrestrial Laser Scanning (TLS), Ground-Based Microwave Interferometry, and Permanent Scatterer Interferometry Synthetic Aperture Radar (PS-InSAR).” Remote Sensing 11(5). doi: 10.3390/rs11050580.

Lloyd, P. A. 1989. “Ultrasonic System for Imaging Delaminations in Composite Materials.” Ultrasonics 27(1):8–18. doi: doi.org/10.1016/0041-624X(89)90003-6.

Maierhofer, Christiane, Philipp Myrach, Mercedes Reischel, Henrik Steinfurth, Mathias Röllig, and Matthias Kunert. 2014. “Characterizing Damage in CFRP Structures Using Flash Thermography in Reflection and Transmission Configurations.” Composites Part B: Engineering 57:35–46. doi: 10.1016/j.compositesb.2013.09.036.

Mal, A., S. Lih, and Y. Bar-Cohen. 1987. “Ultrasonic Determination of the Elastic Properties of Unidirectional Laminates.” Pp. 1093–1101 in Rev Progress Quant Nondestr Eval.

Malpot, Amélie. 2017. “Etude Du Comportement En Fatigue d ’ Un Composite à Matrice Polyamide Renforcée d ’ Un Tissu de Fibers de Verre Pour Application Automobile.” Ecole Nationale Supérieure De Mécanique et d’Aérotechnique.

Mao, H., and S. Mahadevan. 2002. “Fatigue Damage Modelling of Composite Materials.” Composite Structures 58(4):405–10. doi: 10.1016/S0263-8223(02)00126-5.

Marguères, Philippe, and Fodil Meraghni. 2013. “Damage Induced Anisotropy and Stiffness Reduction Evaluation in Composite Materials Using Ultrasonic Wave Transmission.” Composite Part A: Applied Science and Manufacturing 45:134–44. doi: https://doi.org/10.1016/j.compositesa.2012.09.007.

Marguères, Philippe, Fodil Meraghni, and M. L. Benzeggagh. 1999. “Determination of Stiffness Reduction and Damage Accumulation Monitoring in Composite Materials Using Ultrasonic Techniques.” in Sampe Europe International Conference.

Markham, M. 1970. “Measurements of the Elastic Constants of Fiber Composite by Ultrasonics.” Composites 1(3):145–49. doi: doi.org/10.1016/0010-4361(70)90477-5.

Meola, Carosena, S. Boccardi, G. M. Carlomagno, N. D. Boffa, F. Ricci, G. Simeoli, and P. Russo. 2017. “Impact Damaging of Composites through Online Monitoring and Non-Destructive Evaluation with Infrared Thermography.” NDT and E International 85:34–42. doi: 10.1016/j.ndteint.2016.10.004.

Meola, Carosena, and Giovanni M. Carlomagno. 2014. “Infrared Thermography to Evaluate Impact Damage in Glass/Epoxy with Manufacturing Defects.” International Journal of Impact Engineering 67:1–11. doi: 10.1016/j.ijimpeng.2013.12.010.

de Miguel, A. G., A. Pagani, and E. Carrera. 2019. “Higher-Order Structural Theories for Transient Analysis of Multi-Mode Lamb Waves with Applications to Damage Detection.” Journal of Sound and Vibration 457:139–55. doi: 10.1016/j.jsv.2019.05.053.

Naik, R. A., S. R. Patel, and S. .. Case. 2001. “Fatigue Damage Mechanism Characterization and Modeling of a Woven Graphite/Epoxy Composite.” Journal of Thermoplastic Composte Materials 14(5):404–20.

Nur Azrie Bt Safri, Syafiqah, M. T. H. Sultan, and Mohammad Jawaid. 2018. “Damage Analysis of Glass Fiber Reinforced Composites.” in Durability and Life Prediction in Biocomposites, Fiber-Reinforced Composites and Hybrid Composites.

Obeid, Hassan. 2016. “Durabilité de Composites à Matrice Thermoplastique Sous Chargement Hygro-Mécanique : Étude Multi-Physique et Multi-Echelle Des Relations Microstructure-Propriétés-États Mécaniques.” Ecole doctorale Sciences pour ingénieur, Géoscience, Architecture (Nantes).

Osada, T., A. Nakai, and H. Hamada. 2003. “Initial Fracture Behavior of Satin Woven Fabric Composites.” Composite Structures 61(4):333–39.

Oterkus, E., C. Diyaroglu, D. De Meo, and G. Allegri. 2016. “Fracture Modes, Damage Tolerance and Failure Mitigation in Marine Composites.” Pp. 79–102 in Marine Applications of Advanced Fiber-Reinforced Composites. Elsevier Inc.

Pagano, N. J Pipes, Byron. 1971. “The Influence of Stacking Sequence on Laminate Strength.” Journal of Composite Materials 5(1):50–57. doi: doi.org/10.1177/002199837100500105.

Pain, Damien, and Bruce. W. Drinkwater. 2013. “Detection of Fiber Waviness Using Ultrasonic Array Scattering Data.” Journal of Nondestructive Evaluation 32:215–27. doi: doi.org/10.1007/s10921-013-0174-z.

Palka, Norbert, Robert Panowicz, Marek Chalimoniuk, and Rene Beigang. 2016. “Non-Destructive Evaluation of Puncture Region in Polyethylene Composite by Terahertz and X-Ray Radiation.” Composites Part B: Engineering 92:315–25. doi: 10.1016/j.compositesb.2016.02.030.

Pant, Shashank. 2014. “Lamb Wave Propagation and Material Characterization of Metallic and Composite Aerospace Structures for Improved Structural Health Monitoring (SHM).” Carleton University Ottawa, Ontario.

Pearson, L. H., and W. .. Murri. 1987. “Measurement of Ultrasonic Wavespeed in Off-Axis Directions of Composite Materials.” in Review of Progress in Quantitative Nondestructive Evaluation. Springer, Boston, MA.

Pomarède, Pascal. 2018. “Détection de l’endommagement Dans Un Composite Tissé PA66,6/Fibers de Verre à l’aide de Techniques Ultrasonores En Vue d’une Prédiction de La Durabilité de Pièces Automobiles.” ENSAM ParisTech.

Pomarède, Pascal, Fodil Meraghni, Laurent Peltier, Stéphane Delalande, and Nico F. Declercq. 2018. “Damage Evaluation in Woven Glass Reinforced Polyamide 6 . 6 / 6 Composites Using Ultrasound Phase-Shift Analysis and X-Ray Tomography.” Journal of Nondestructive Evaluation 123. doi: 10.1007/s10921-018-0467-3.

Powers, E. J., Y. J. Shin, W. Mack Grady, J. F. Böhme, S. Carstens-Behrens, A. Papandreou-Suppappola, F. Hlawatsch, G. F. Boudreaux-Bartels, A. Beghdadi, R. Iordache, Boualem Boashash, A. Djebbari, S. Ouelha, and D. M. Onchis. 2016. “Time-Frequency Diagnosis, Condition Monitoring, and Fault Detection.” in Time-Frequency Signal Analysis and Processing: A Comprehensive Reference.

Praud, Francis. 2018. “Multi-Scale Modelling of Thermoplastic-Based Woven Composites, Cyclic and Time-Dependent Behavior.” Ecole Nationale Supérieure d’Arts et Métiers.

Quaresimin, Marino, Mauro Ricotta, Livio Martello, and Stefano Mian. 2013. “Energy Absorption in Composite Laminates under Impact Loading.” Composites Part B: Engineering 44(1). doi: 10.1016/j.compositesb.2012.06.020.

Rasool, Shafqat. 2015. “Fatigue of Woven Thermoplastic Composites: The Effect of the Fiber Matrix Interface.”

Ravikara, N.K. Venkataramanaiah, A., M. R. Bhat, and C. R. L. Murthy. 2006. “Detection and Evaluation of Impact Damage in CFRP Laminates Using Ultrasound C-Scan and IR Thermography.” in National seminar on non-destructive Evaluation.

Razali, N., M. T. H. Sultan, F. Mustapha, N. Yidris, and M. R. Ishak. 2014. “Impact Damage on Composite Structures- A Review.” The International Journal Of Engineering And Science 3(7):08–20.

Renard, Jacques. 2010. “Fatigue Des Matériaux Composites Renforcés de Fibers Continues.” Techniques de l’Ingénieur.

Renault, Michel. 1994. “Compression Après Impact d’une Plaque Stratifiée : Étude Experimentale et Modelisation Élements Finis Associée.” Université de Nantes.

Robert, Gilles, and Adil Benaarbia. 2015. “In Fl Uence of Relative Humidity and Loading Frequency on the PA6 . 6 Thermomechanical Cyclic Behavior : Part II . Energy Aspects.” Polymer Testing 41:92–98. doi: 10.1016/j.polymertesting.2014.10.012.

Rose, Joseph L. n.d. Ultrasonic Guided Waves in Solid Media. Pennsylvania State University: Cambridge University Press.

Rouault, Thomas. 2013. “Propagation de Coupure En Fatigue Sur Composites Tissés – Etude Expérimentale et Modélisation.”

Ryder, J. .., and F. .. Crossman. 1983. A Study of Stiffness, Residual Strength and Fatigue Life Relationships for Composite Laminates. California.

Sejdić, Ervin, Igor Djurović, and Jin Jiang. 2009. “Time-Frequency Feature Representation Using Energy Concentration: An Overview of Recent Advances.” Digital Signal Processing: A Review Journal 19(1). doi: 10.1016/j.dsp.2007.12.004.

Serge Abrat. 1998. Impact on Composite Structures. Cambridge: Cambridge university Press.

Shah, S. Z. H., S. Karuppanan, P. S. M. Megat-Yusoff, and Z. Sajid. 2019. “Impact Resistance and Damage Tolerance of Fiber Reinforced Composites: A Review.” Composite Structures 217(February):100–121. doi: 10.1016/j.compstruct.2019.03.021.

Smith, R. 1972. “Ultrasonic Elastic Constants of Carbon Fibers and Their Composites.” Journal of Applied Physics 43(6):2555–61.

Song, Jian, Weidong Wen, and Haitao Cui. 2017. “Fatigue Behaviors of 2 . 5D Woven Composites at Ambient and Un-Ambient Temperatures.” Composites Structures 166:77–86. doi: doi.org/10.1016/j.comstrcut.2017.01.055.

Sørensen, B. F. 2016. “Delamination Fractures in Composite Materials.” in Modeling Damage, Fatigue and Failure of Composite Materials.

Stijnman, P. W. A. 1995. “Determination of the Elastic Constants of Some Composites by Using Ultrasonic Velocity Measurements.” Composites 26(8):597–604. doi: doi.org/10.1016/0010-4361(95)92624-L.

Su, Z., and L. Ye. 2008. “Lamb Wave-Based Quantitative Identification of Delamination in Composite Laminates.” Pp. 169–216 in Delamination Behavior of Composites: A volume in Woodhead Publishing Series in Composites Science and Engineering. Elsevier Ltd.

Su, Zhongqing, and Lin Ye. 2009. Identification of Damage Using Lamb Waves From Fundamentals to Applications.

Toubal, Lotfi, Moussa Karama, and Bernard Lorrain. 2006. “Damage Evolution and Infrared Thermography in Woven Composite Laminates under Fatigue Loading.” International Journal of Fatigue 28(12):1867–72. doi: 10.1016/j.ijfatigue.2006.01.013.

Transportation, U. S. Department and, and Office of Systems Engineering. 1993. No T. Atlantic City.

Usamentiaga, R., P. Venegas, J. Guerediaga, L. Vega, and I. López. 2013. “Automatic Detection of Impact Damage in Carbon Fiber Composites Using Active Thermography.” Infrared Physics and Technology 58:36–46. doi: 10.1016/j.infrared.2013.01.004.

Vallons, Katleen, Alex Behaeghe, Stepan. V Lomov, and Ignaas Verpoest. 2010. “Impact and Post-Impact Properties of a Carbon Fiber Non-Crimp Fabric and a Twill Weave Composite.”

Composite Part A: Applied Science and Manufacturing 41(8):1019–26. doi: doig.org/10.1016/j.compositesa.2010.04.008.

De Vasconcellos, Davi .. .., Fabrizio Sarasini, Fabienne Touchard, Laurence Chocinski-Arnault, Monica Pucci, Carlo Santulli, Jacopo Tirillò, Salvatore Iannace, and Luigi Sorrentino. 2014. "Influence of Low Velocity Impact on Fatigue Behavior of Woven Hemp Fiber Reinforced Epoxy Composites." Composites Part B: Engineering 66:46–57. doi: 10.1016/j.compositesb.2014.04.025.

Vasconcellos, Davi Silva De. 2013. "Comportement En Fatigue Avant et Après Impact de Composites Tissés Chanvre / Époxy." Ecole Nationale Supérieure de Mécanique et d'Aérotechnique Poitiers.

Wronkowicz-Katunin, Angelika, Andrzej Katunin, and Krzysztof Dragan. 2019. "Reconstruction of Barely Visible Impact Damage in Composite Structures Based on Non-Destructive Evaluation Results." Sensors 19. doi: 10.3390/s19214629.

Yang, Bin, Yuan Chen, Juhyeong Lee, Kunkun Fu, and Yan Li. 2021. "In-Plane Compression Response of Woven CFRP Composite after Low-Velocity Impact: Modelling and Experiment." Thin-Walled Structures 158. doi: 10.1016/j.tws.2020.107186.

Yelve, Nitesh P., Mira Mitra, and P. .. Mujumdar. 2017. "Detection of Delamination in Composite Laminates Using Lamb Wave Based Nonlinear Method." Composite Structures 159:257–66.

Zhang, Fenglin, Yongdong Pan, Jinfeng Zhao, and Xiaoqing Zhang. 2020. "Test, Modeling, and Analysis of Air-Coupled Ultrasonic Transducer Based on Piezoelectret Film." AIP Advances 10(6). doi: doi.org/10.1063/5.0004688.

Zheng, Kaihong, Zheng Li, Zhaooyang Ma, Jianlin Chen, Jie Zhou, and Xianyue Su. 2019. "Damage Detection Method Based on Lamb Waves for Stiffened Composite Panels." Composite Structures 225.

Chapter 2: Overall investigation of the PA66/6 based composite subjected to low-velocity impact events

During its lifetime, a structure can encounter progressive degradation like impact damage that can have serious consequences on the structure's integrity and performances.

Impacts are generally fall into four major categories as a function of their detectability: BVID (Barely Visible Impact Damage), VID (Visible Impact Damage), CVID (Clearly Visible Impact Damage) and Obvious Damage (Gordon et al., 2014).

For aerospace applications, the BVID is defined as the small damage that may not be detected by visual inspections using typical lighting conditions from a distance of 1.5 m (Jiang et al., 2021). It has been reported that BVID is the most critical kind of damage, (Giurgiutiu, 2016), due to the fact that no trace can be seen on the surface whereas internal damage forming a tree root, in the case of thin plates, is propagating and leading to a decrease in the residual properties. Indeed, this kind of damage can be threatening and remains unnoticed causing a loss of the structure integrity and therefor lead to a total failure. However, in aircraft, aerospace and automotive industries, the repercussion of not detecting this type of damage in time and preventing its propagation are fatal. The concept of damage tolerance relies on determining the threshold allowing a damaged structure to be operational. That said, if the residual properties are not degrading, the structure is considered as damage tolerant.

This chapter represents an overall overview of impact damage. As mentioned in previous sections, and due to the complexity of this damage, a range of impact energies is chosen to remain in the BVID domain. A study of the evolution of this type of damage and its criticality will be the object of the present chapter. For this matter, an experimental procedure enabling the inspection and the quantification of the residual damage is proposed. Indeed, the suggested procedure allows the measurement of the permanent indentation (PI), the identification of the different damage mechanisms and extend of their propagation, the estimation of the stiffness

matrix components using Non-destructive techniques and finally, the quantification of damage using an original Lamb waves-based method. The obtained results employing the different techniques will be cross-linked and damage indicators will be assessed.

I. Experimental procedure

1. Sample preparation

1.1. Geometry of the samples

The material of the study, as mentioned in chapter I, is a woven twill 2.2 composite referred to as VizilonTM SB63G1-T1.5-S3, manufactured by DuPont de Nemours using a thermo-compression molding process. It is a co-polyamide 6.6 / 6 (thermoplastic matrix) reinforced with a layup of three balanced glass fiber layers oriented at 0°/90°. The composite, with a thickness of 1.53 mm, has a fiber weight ratio of 63% corresponding to a fiber volume fraction of 43%.

The geometry of the sample is chosen in agreement with ASTM D7136/D7136M standards. Low-velocity impact tests are carried out on rectangular shape plates of 100 by 150 mm dimensions and 1.6 mm thickness (**Figure 27**). Afterwards, the initial undamaged states are verified for all samples using ultrasonic C-scan.

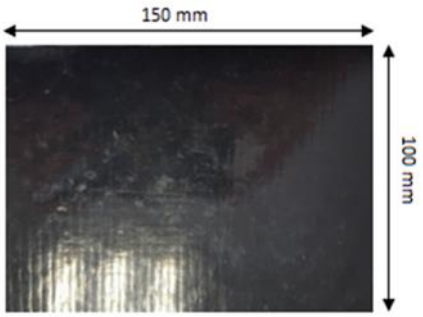

Figure 27: Dimensions of the studied samples (Miqoi et al., 2021).

1.2. Desorption procedure

A typical automotive part needs to withstand a wide range of temperatures varying from -40° to + 80° along with dry and humid environments. These environmental conditions can be highly crucial for polyamide or polyamide based composite material as previously explained in Chapter I. Fiber glass is known to be insensitive when it comes to changes in temperatures and humidity (Malpot, 2017).

However, important variations in the environmental conditions can induce the loss of resistance and deterioration in the fiber/matrix interface leading to the degradation of the mechanical properties of the polyamide-based composites (Arif, 2014; Obeid, 2016; Panaitescu et al., 2019; Zhang et al., 2014).

In the rest of the study, following the standard environmental conditions for automobile applications, a relative humidity of 50% is chosen (Pivdiablyk et al., 2020).

The material was delivered and was stored at undefined conditions. Thus, a proper desorption/ absorption procedure should be followed to control and reach the 50% RH. To accelerate the desiccation (drying) process without modifying the behavior of the material, a temperature higher than the ambient and lower than the T_g (glass-transition temperature) should be used. To accelerate the drying process, the samples are put in a homemade climatic chamber equipped with a special salt. Before proceeding to the desiccation process, five samples are arbitrary selected and weighed and are regularly monitored to calculate the loss of the moisture content until saturation.

The graphic showing the evolution of the water content as a function of the time spent in the climatic chamber is presented in **Figure 28**. Once the water content reaches the stabilization plateau, the specimens are considered as dry. It should be stated that in this study, we assume that no chemical damage occurred whatsoever during the desorption process.

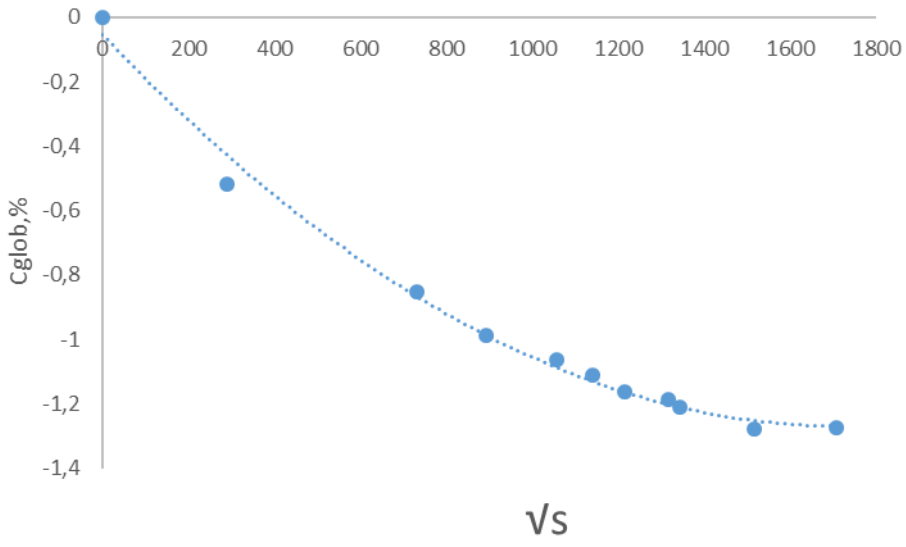

Figure 28: The evolution of the water content in the studied polyamide-based composite as a function of the time spent in the climatic chamber for the desorption procedure.

The percentage of water content (C_{glob} %) is calculated by a gravimetric method following ASTM D5229 standard used by several authors (International ASTM, 2020). By comparing the mass of the witness samples before the desorption and at different time-steps during the process, the C_{glob} % can be deduced using the following equation:

$$Cglob\% = \frac{M-M0}{M0} * 100\%$$

With M the mass of the witness specimens at a defined time-step and M0 the initial mass registered just before putting the samples in the climatic chamber.

1.3. Conditioning procedure

After eliminating the retained water, the samples are placed in a temperature and humidity controlled climatic chamber (MEMERT).

The witness samples are weighed beforehand in order to monitor the weight uptake at different time-steps. To assure a faster moisture absorption, the samples are conditioned at 65% RH and a temperature of 50° until reaching a weight gain of 2.7% corresponding to the target as water uptake of the polyamide at 50% RH. The samples are then maintained at 50% RH at ambient temperature for two weeks to assure a proper and regular profile of through-thickness water diffusion. The moisture absorption is calculated using the same equation mentioned in the previous section by comparing the weight of the dried witness samples with their weight at different time steps.

2. Drop-weight impact tests

2.1. Experimental set-up

Impact tests are performed using a drop test device equipped with a 1.02 kg striker having a 16 mm diameter hemispherical end. One should mention that an assembly of a series of masses is used to reach the desired mass. The experimental device, shown in **Figure 29**, consists of a piezoelectric load sensor and two laser displacement sensors, as well as a data acquisition system. The tested composite plates are clamped at both ends as illustrated in **Figure 29**, and the impactor strikes the plates in their center. The displacement of the sample is subsequently measured under the impacted plate using a laser displacement sensor. The acquisition of the striker's (impactor) displacement, the displacement of the center of plate, and the contact force

are measured for data analysis. By only varying, the height of the impact, different energy levels are obtained.

Twenty-one samples are impacted from heights variating from 1 m to 3 m, three sample per chosen height. Indeed, for repeatability reasons, and to reduce the experimental uncertainties, each three samples are impacted from the same height. Due to the large number of the considered samples, the results of only seven of them, representing different levels and ranges of the BVID, are more focused on and discussed in the following sections. The methodology of calculation of the velocity of impact, the impact energy and the absorbed energy will be detailed in the following section.

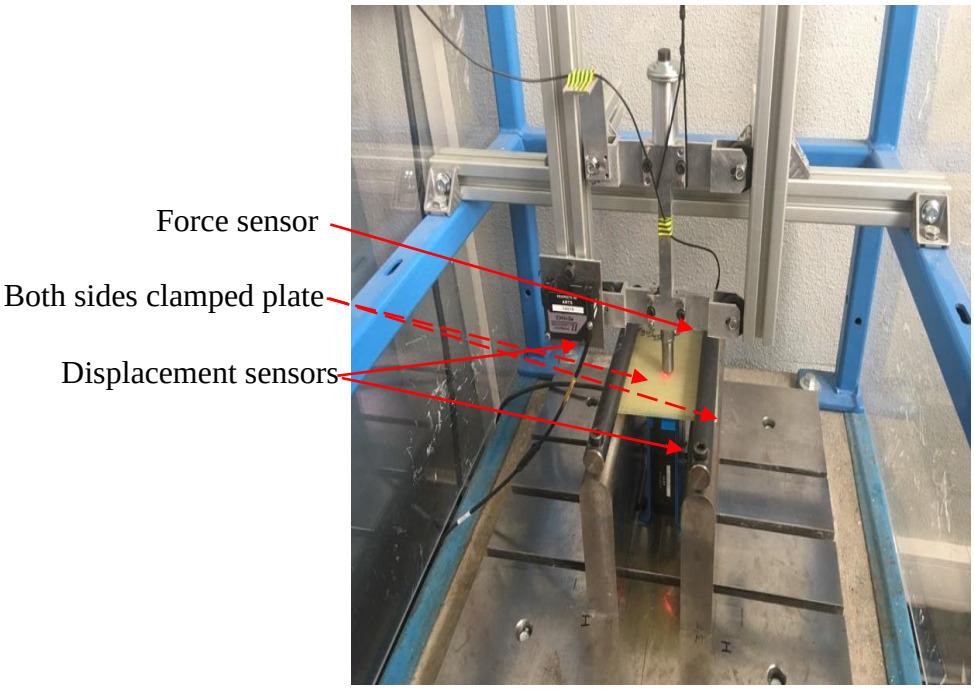

Figure 29: The experimental device used to perform drop weight impact tests showing: a force sensor, a first displacement sensor that monitors the displacement of the striker and a second one placed under the clamped sample to record the deflection (Miqoi et al., 2021).

2.2. Data reduction and impact response analysis

Low-velocity impact tests are performed at different heights variating from 1 m to 3 m. The mechanical results collected after an impact event following the previously detailed experimental set-up are mainly: the impactor displacement function of time, the displacement of the impacted sample function of time i.e., the deflection during the impact event, and finally the evolution of the applied force function of time.

The post-processing of the mechanical data enables to calculate the impact velocity, the real impact energy and the absorbed energy. Indeed, from the striker displacement-time curve, one can estimate the impact velocity. It consists of the slop of the first part of the curve (**Figure 30**). The second part of this same graph represents the displacement of the impactor after hitting the sample. Indeed, it consists in the rebound of the impactor after hitting the sample. The slop of this part of the graph depicts the rebound velocity. It is important to mention that a linear regression was used to estimate the velocities. Using the following formula, the impact velocity and the propulsion velocity are linked to the absorbed energy. The latter matches the amount of energy that passes from the impactor to the sample during an impact event. It is defined as the difference between the impact energy and the rebound velocity called the 'excessive energy' (Dhakal et al., 2012).

$$E_A = \frac{1}{2} m (v_1^2 - v_2^2)$$

v_1 and v_2 are respectively the impact and the rebound velocity. m is the impactor's mass and is of 1.02 kg. An example illustrating the estimated velocities using the displacement-time curve of the impactor for the sample impacted at 12.6 J is shown in **Figure 30**. The calculated parameters i.e., impact velocity, the real impact energy, and the absorbed energy for the seven chosen samples are represented in **Table 2**.

Table 2: Impact velocity and absorbed energy for the seven considered samples impacted at 7.20 J, 10.54 J, 12.6 J, 14.58 J, 19 J, 21.15 J and 24 J respectively.

Impact energy (J)	**7.20**	**10.54**	**12.6**	**14.58**	**19**	**21.15**	**24**
Impact velocity (m/s)	3.778	4.633	5.010	5.383	6.170	6.504	6.928
Absorbed energy (J)	4.09	7.40	9.30	11.43	14.90	16.95	21.77

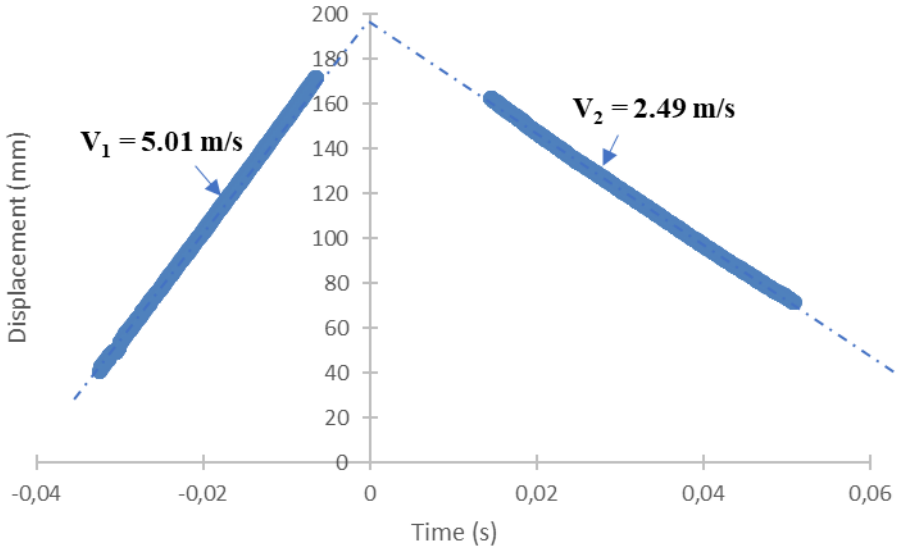

Figure 30: Impactor's displacement- time curve for the sample loaded at 12.6 J detailing the followed method to compute the absorbed energy showing the impact velocity V1 and the rebound velocity V2.

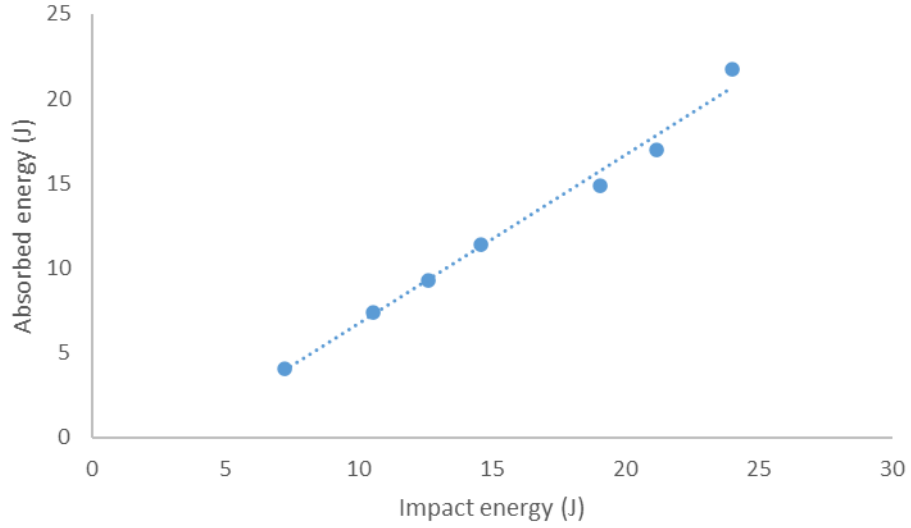

Figure 31: Evolution of the absorbed energy function of the impact energy for the seven considered sample impacted at 7.2 J, 10.54 J, 12.6 J,14.58 J, 19 J, 21.15 J and 24 J respectively.

The calculated absorbed energies for the seven chosen sample impacted at 7.2 J, 10.54 J, 12.6 J, 14.58 J, 19 J, 21.15 J and 24 J, based on the previously detailed procedure are represented in **Figure 31.** As forseen, the absorbed energy increases with the impact energy.

Figure 32 and **Figure 33** illustrate the contact force- time histories and the deflexion-time curves for the seven selected samples impacted at 7.2 J, 10.54 J, 12.6 J, 14.58 J, 19 J, 21.15 J and 24 J, respectively. From the obtained results, one can easily conclude that the maximum deflection and the maximum contact force increase with the impact height. An obvious shift of amplitude

is noticed between the lower and higher energies. On some curves in **Figure 33**, mainly the curves corresponding to the samples impacted at 19 J, 21.15 J and 24 J, one can easily notice that the displacement values do not return to zero. It is explained by the fact that because of the boundary conditions when the impact energy reaches a certain level, the samples do not go back to the initial position and remains deformed. This event causes the compression of the first layer of the composite sample resulting thus in the creation of damage on the impacted surface.

It is important to point out the fact that oscillations are observed in all force-time histories. Two types of discontinuities are noticed at high and low frequencies. The vibrations at high frequency are assigned to the natural frequencies of the impactor and are referred to as 'impact ringing'. Gliszczynski et al. (Gliszczynski et al., 2019) have shown that the severity of this phenomenon is accentuated when the parts constituting the impactor are rigidly assembled. As previously discussed in section 2.1, an assembly of a series of masses is used to reach the desired mass (1.02 kg), explaining thus the occurrence of this vibration effect. The second type of oscillations, at lower frequency, is related to the flexural response of the samples. It is important to mention that both types of vibrations take place during the contact between the impactor and the sample and could be associated to the damage induction (Abrat, 1998). However, the first set of discontinuities (blue box on **Figure 32**) should be dissociated from the rest of the oscillations. Indeed, it is considered as initial discontinuities resulting from the first contact between the striker and the plate.

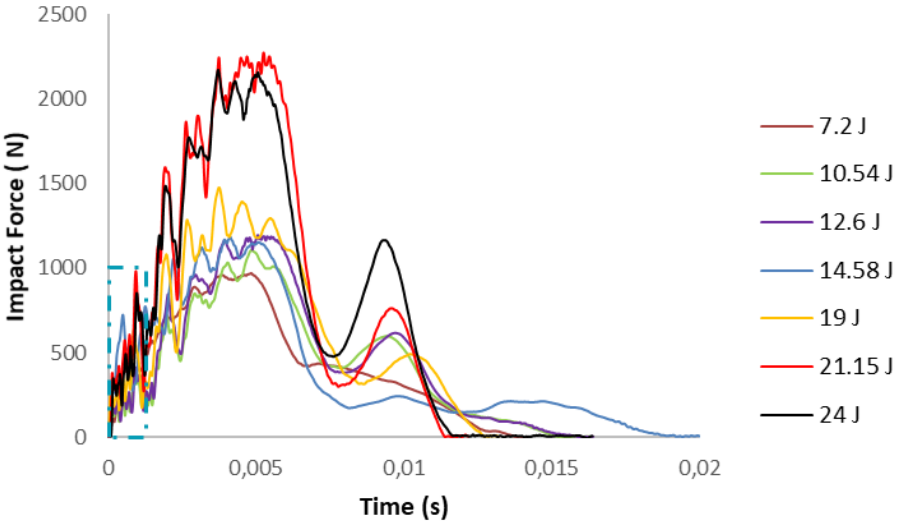

Figure 32: Force-Time curves for the seven chosen sample impacted at 7.2 J 10.54 J, 12.6 J,14.58 J, 19 J, 21.15 J and 24 J respectively showing the increase of the values of the applied force with the impact energy.

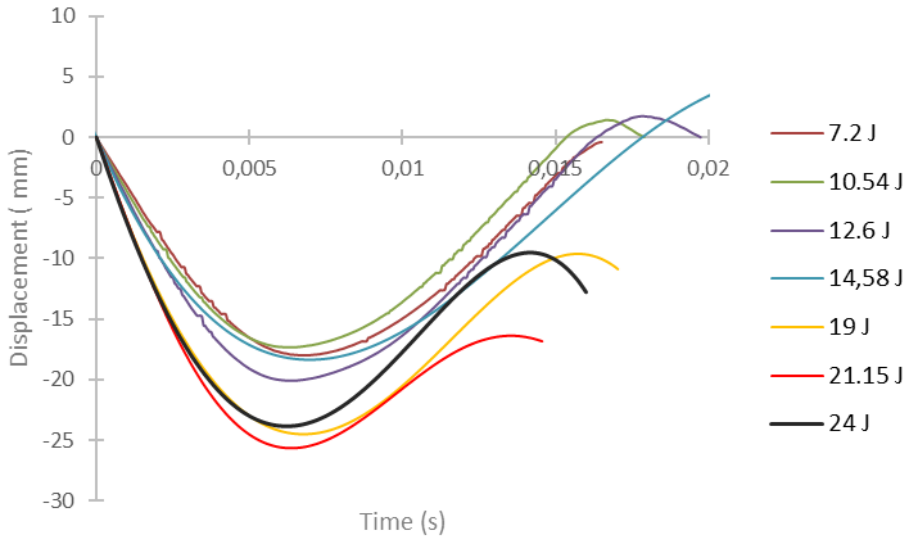

Figure 33: The samples' displacement function of time curves for the seven chosen samples impacted at 7.2 J, 10.54 J, 12.6 J,14.58 J, 19 J, 21.15 J and 24 J respectively showing the increase of the maximum values of the deflection when increasing the impact energy.

3. Post-impact surface investigation

3.1. Visual inspection

As detailed in Chapter I, in the case of thin plates, impact damage is first observed on the non-impacted surface. Indeed, the damage cone is initiated under the striker. That said, damage is first noticed on the last layer of the composite and spread in a pine tree path due to the bending stress and wave propagation. However, depending on the energy level and the boundary conditions, damage can also occur on the impacted surface of the sample. Indeed, the high force applied on the impacted surface induces the compression of the first layer and thus, the creation of damage. The latter occur as fiber buckling and matrix microcracking as visible in **Figure 34.**

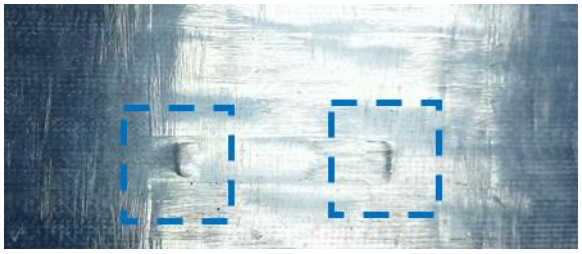

Figure 34: Fiber buckling, and matrix cracking observed on the impacted surface of the sample impacted at 21.15 J.

A visual inspection of the non-impacted side of the samples shows no visible damage on the sample impacted at 7.20 J. A first damage stage is observed on the sample impacted at 10.54 J. This damage consists in a small opening, barely visible to the naked eye. Due to the very small dimension of the damage, an observation using optical microscope is performed. **Figure 35** represents the obtained images of the small opening. Starting from 12.6 J as impact energy, cracks propagating longitudinally and transversely leading to fiber breakage are noticed. **Figure 36** shows the images of this damage on the non-impacted surface of each sample.

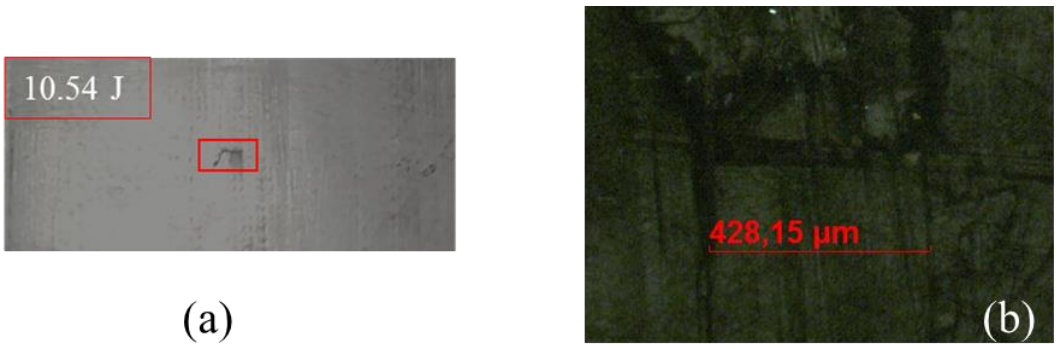

Figure 35: Damage observed on the non-impacted surface (a) and a microscopic measurement of the crack (b) for the sample impacted at an energy level of 10.54 J.

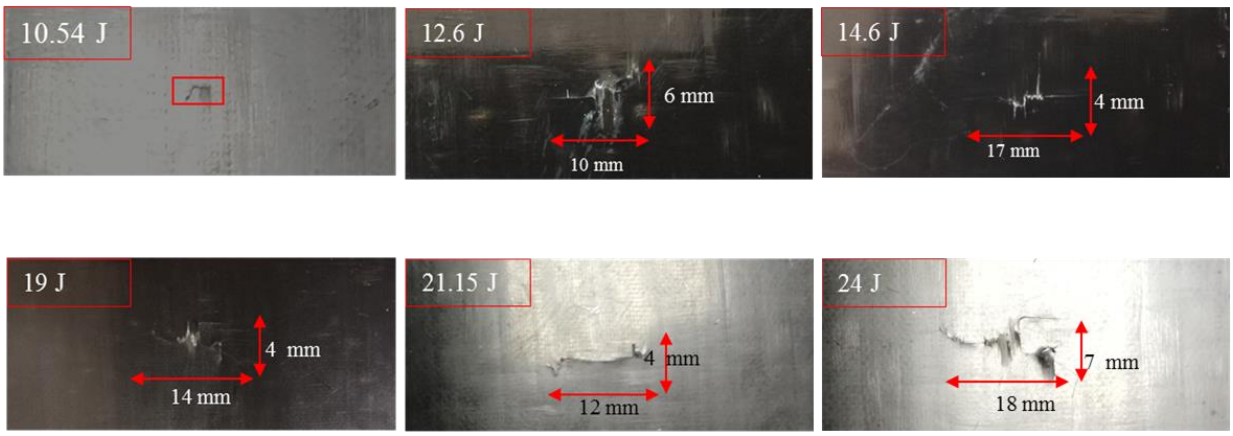

Figure 36: Visual observation of the non-impacted side of each sample showing the damage resulting from the impact tests and its dimensions for samples loaded at energy of 10.54 J, 12.6 J,14.58 J, 19 J, 21.15 J and 24 J observed by the naked eye.

3.2. Permanent indentation measurement

Permanent indentation is known to be a very reliable parameter for a damage state estimation in the case of impact damage (Bouvet, 2011; Miqoi et al., 2021; Mustapha et al., 2016). A proper estimation of this parameter gives information about the damage by an impact event. In this section, this key parameter is determined by an ultrasonic measurement using first C-scan imaging to localize the impact area and later B-scan to measure the depth of the print left on the impacted surface. The found values are then confirmed using a more resolved method, i.e., optical profilometry.

3.2.1. Localization of the damaged area and permanent indentation measurement

Ultrasonic experimental procedure

The ultrasonic C-scan method is carried out to detect and to characterize the damage in terms of localization and evolution in the composite plates. The acquisitions are performed using a customer designed five axes immersion scanner made by Inspection Technology Europe BV. The pulses are generated using the dual pulse-receiver DPR500 made by JSR ultrasonics. The experimental data acquisition is achieved via the Winspect software and post-processed using a Matlab code. The acquisitions are performed in reflection mode using a single focused 10 MHz piezoelectric transducer positioned in the arm of the five-axis scanner. The particularity of this scanning mode is to provide more information on the propagation of the damage in the thickness. The scans are carried out following a serpentine path for an area of 95 mm x 95 mm, with a spatial resolution of 0.1 mm. The samples are positioned in such a way that the impacted surface is facing the transducer. The displacement speed is 10 mm/s along the X and Y Axes. **Figure 37** represents the experimental setup for ultrasonic C-scan scanning.

This setup allows the measurement of the wave's maximum amplitude for each point of the scanned sample. An attenuation of the signal is observed when a defect or a material discontinuity is encountered. Indeed, the emitted ultrasonic wave is attenuated and some of its energy is reflected when coming across defects or inhomogeneities.

After localizing the damaged area on each sample using C-scan in reflection, ultrasonic B-scan observations are performed in the identified damaged region to extract information relative to the permanent indentation (PI).

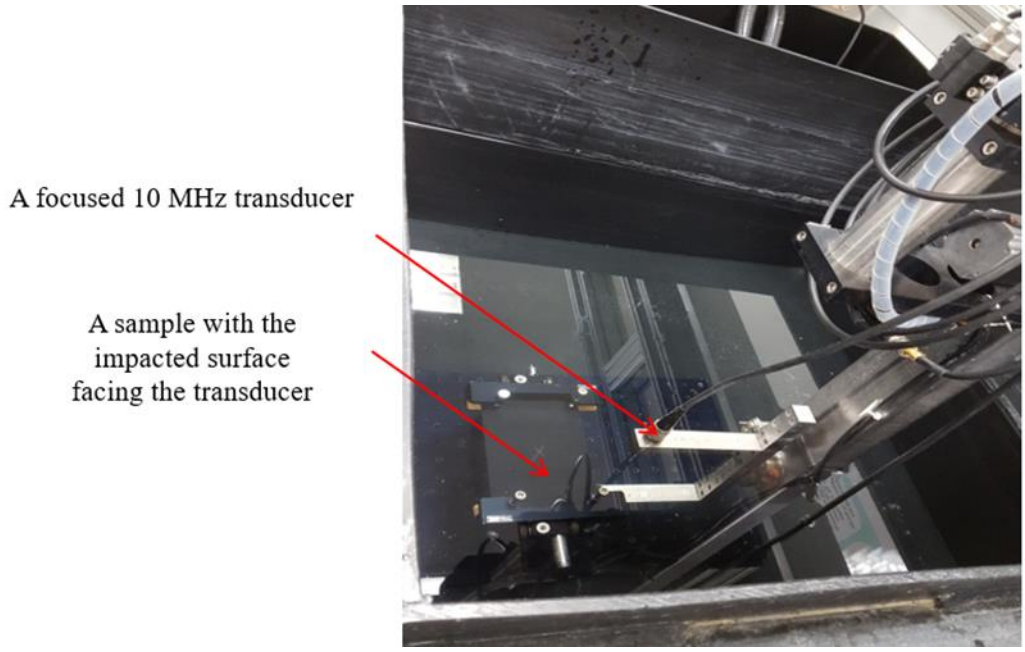

Figure 37: Experimental underwater set-up employed for the ultrasonic scanning of the impacted surface for each of the considered samples showing a transducer assembled to the five-axis robot enabling the translation along the X and Y axis and the system holding a sample with the impacted surface facing the transducer (Miqoi et al., 2021).

Ultrasonic results

The results of the ultrasonic C-scan are generally represented as cartographies of the field variation of a chosen parameter, for instance the amplitude or the Time of Flight (TOF), along the scanned surface. This variation may reflect the transition from one phase to another or in this case the variation of the flatness of the surface caused by an impact event. In this sub-section, the isocolor map, i.e., the results of the C-scan, exhibit the change in the TOF of the various areas of the scanned surface. The dark red corresponds to a higher TOF indicating that the signals of this area arrive later than the signals reflected from the rest of the sample due to a difference in the flatness caused by the impactor. An example of a C-scan for the sample impacted at 21.15 J is depicted in **Figure 38(a).** A dark red area, in the middle of the sample, with a visible local change in signal TOF is clearly visible. This is due to change in the flatness in the sample indicating the location of the PI.

B-scan representations of the PI are carried out in the localized indented area to extract information about the depth of the indent (**Figure 38(b)** for the sample impacted at 21.15J). The latter is calculated by measuring the difference between the time of arrival corresponding to the impacted area and the one corresponding to the non-impacted area. Knowing that the wave propagation velocity is 1478.8 m/s in water (Pomarède, 2018), an estimation of the indent depth

for the seven plates is given in **Table 3**. The distance between these two areas corresponds to the depth of the indent. It should be noted that for the sample impacted at 7.20 J, the supposedly indented area on the impacted surface could not be detected. Consequently, due to the low level of damage, the measurement of the permanent indentation is inaccessible.

A substantial increase of PI dimensions, depth, and diameters is noticed when elevating the impact energy. Nevertheless, ultrasonic measurement of the PI comes with significant uncertainty as mentioned in **Table 3**. Indeed, pulse/echo C-scan cannot be considered as a highly resolved method regarding microscopic damage detection, especially when the damage does not exhibit a through-thickness propagation. However, in terms of easy access and applicability in the industrial fields, ultrasound-based method remains the most reliable methods. To verify the efficiency of this estimation method, measurement using a more resolved method are achieved in the next sub-section.

Table 3: Values of the depth of the permanent indentation obtained using the ultrasonic estimation method for the seven considered samples impacted at 7.20 J, 10.54 J, 12.6 J, 14.58 J, 19 J, 21.15 J and 24 J respectively.

Impact energy (J)	**7.20**	**10.54**	**12.6**	**14.58**	**19**	**21.15**	**24**
Depth (µm) ± 7 µm	-	59.5	44.36	62.84	122	177	199.3
Diameter (mm)	-	6.3	3.9	5.1	3.6	7.2	5.7

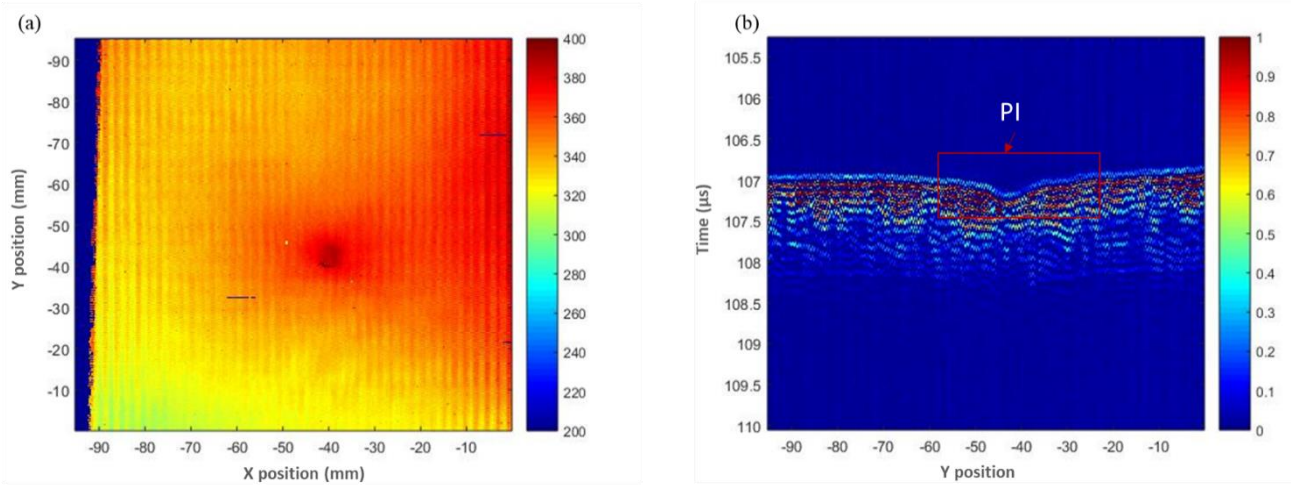

Figure 38: (a) TOF C-scan of the sample impacted at 21.15 J showing the late arrival of the signal corresponding to the localized indented part and (b) the B-scan of the impacted area enabling the measurement of the difference of the TOF between the bottom of the hollow and the surface of the sample.

Optical profilometry procedure

An optical profilometry method is used to confirm the accuracy of the previous measurement based on US techniques. A LEICA DCM3D (**Figure 39**) is employed with a magnification of five times, imaging an area of 27 x 20.23 mm. The surface of each sample is scanned according to predefined steps during which each point of the surface crosses the focal plane. The magnification leads to a lateral resolution along X and Y of 0.94 mm, and a vertical resolution lower than 150 nm.

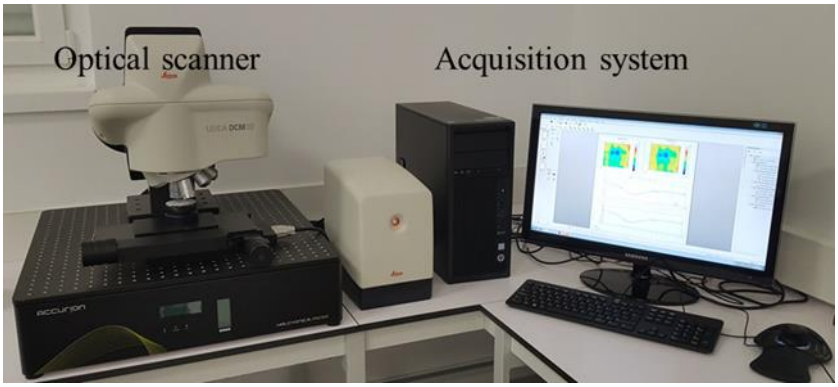

Figure 39: The employed Leica DCM3D device used to validate the measurements of the permanent indentation performed by means of ultrasonic method showing the optical scanner and the acquisition system (Miqoi et al., 2021).

Optical profilometry results

After the scanning, raw data are obtained, and several post-processing procedures are performed using Leica Maps software as depicted in **Figure 40.** The software enables to obtained different dimensions of the permanent indentation such as the diameter, the depth, and the volume. An example of a raw data is given in **Figure 40(a)** for the sample impacted at 21.15 J. First, a filter **(Figure 40(b))** is used to elevate the surface around the impacted area and to separate the roughness from the waviness. The primary purpose is to identify the location of the indentation area and then the PI is accurately measured. In fact, the profile is extracted in the line corresponding to the deepest area. This latter provides information about the depth of the permanent indentation **(Figure 40(c)).** Finally, by selecting the area of interest point by point, the software calculates the volume of the permanent indentation **(Figure 40(d)).** Information relative to the depth, the diameter and the volume of the scanned area is presented in **Table 4** for the seven chosen samples.

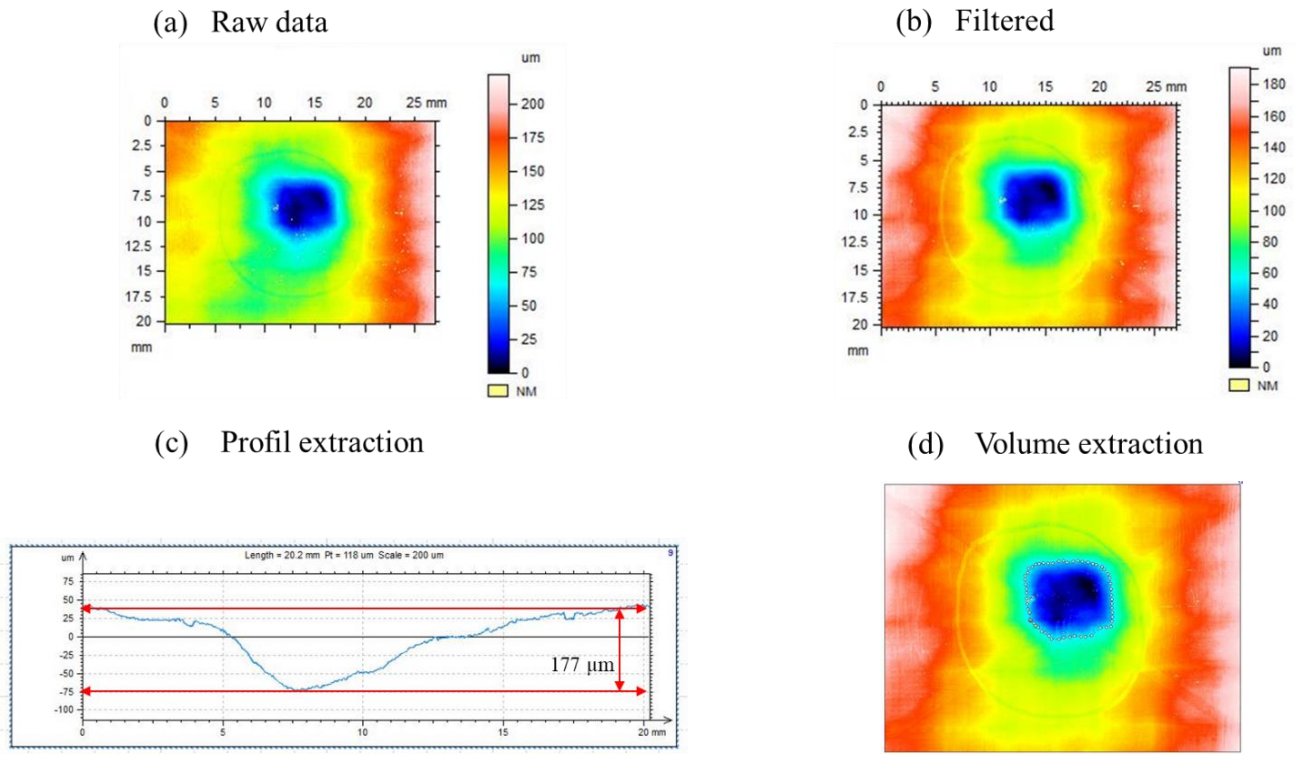

Figure 40: Detailed post-processing procedure using Leica Maps performed on the plate impacted at 21.15 J: (a) raw data, (b) filtered data, (c) profile extraction and (d) volume extractions.

Table 4: Values of the depth, the diameter and the volume of the permanent indentation obtained using the optical profilometry for the seven considered samples impacted at 7.20 J, 10.54 J, 12.6 J, 14.58 J, 19 J, 21.15 J and 24 J, respectively.

Impact energy (J)	**7.20**	**10.54**	**12.6**	**14.58**	**19**	**21.15**	**24**
Depth (um) ± 0.15 µm	25.4	54.7	49.7	67	76.5	173.74	202.27
Diameter (mm) ± 0.15 µm	8.11	6.12	6.04	6.34	5.45	6.12	5.16
Volume (mm^3)	0.01085	0.155	0.164	0.262	0.169	0.859	0.344

A comparison between the results provided by the two methods i.e., ultrasound-based method and optical profilometry, for the seven considered sample and also for all the studied sample is established and represented in **Figure 41** and **Figure 42** respectively. One can conclude that the same tendency is retrieved in both figures confirming hence the representative aspect of the seven chosen samples. The values of the PI depth increase until reaching an energy of 10.54 J, the later stabilize and start to increase again when the energy exceeds 19 J. The comparison shows a good correlation between the two methods as well as a satisfying accuracy for the

ultrasound-based method. However, in the case of low indentations resulting from very low impact energies, the PI cannot be measured using the ultrasound-based method due to its relatively low resolution compared to the optical profilometry. Indeed, the damage state at low energies of impact makes it very complicated to localize the damaged area and thus the measurement of the depth of the indented area is inaccessible.

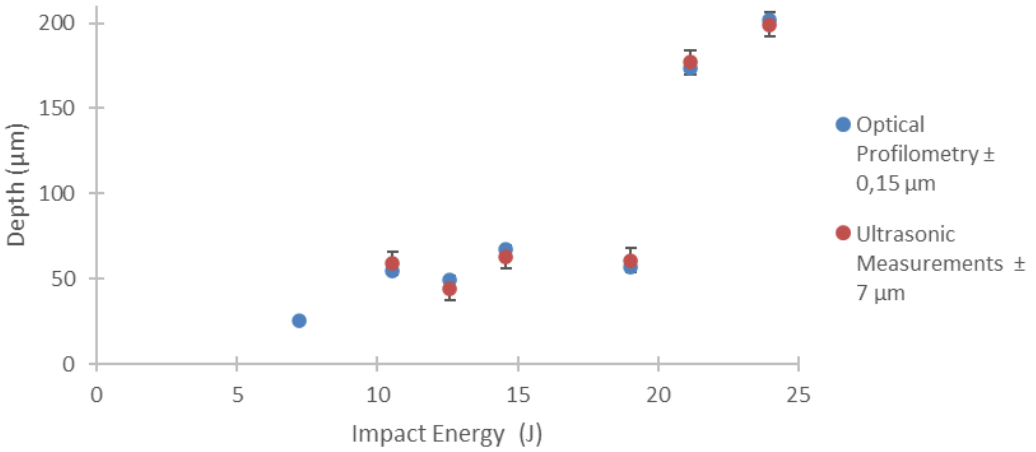

Figure 41: Comparison between the values of the depth of the permanent indentation (PI) obtained using both the ultrasonic based method and the optical profilometry for the seven considered samples impacted at 7.20 J, 10.54 J, 12.6 J, 14.58 J, 19 J, 21.15 J and 24 J showing a good correlation between the two methods and validating thus the ultrasonic based method as an efficient method for a proper estimation of the PI.

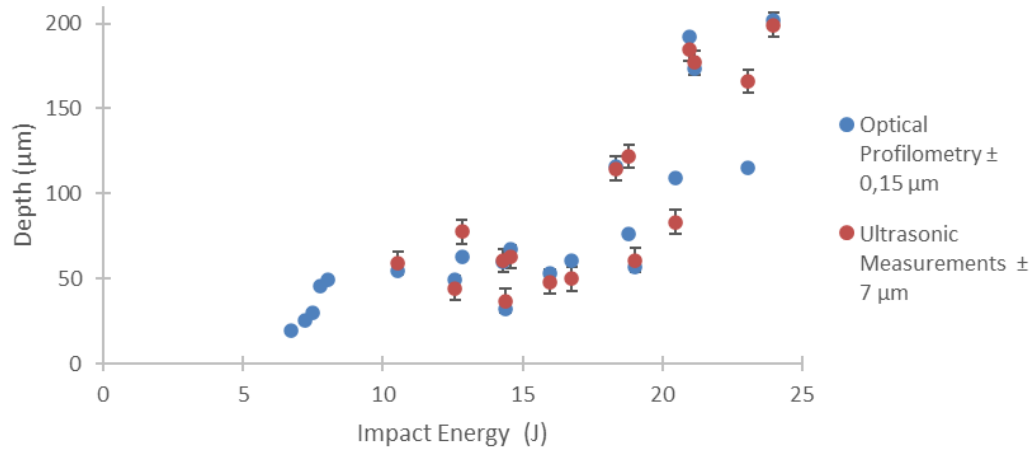

Figure 42: Values of the depth of the permanent indentation measured using an ultrasonic-based method and confirmed by means of the results obtained employing the optical profilometry which is a highly accurate method for each one of the twenty-one studied samples impacted at energies ranging from 6.7 J to 24 J. The comparison points out and proves the effectiveness of the US based method.

II. Through-thickness damage investigation using X-Ray Tomography

1. Principle of the method and Experimental acquisitions

To inspect deeply the effect of the impact loading on the studied composite, an X-Ray micro-computed tomography investigation is carried out. The X-Ray images acquisition is achieved using an EasyTom (Nano) system developed by RX solutions. This imaging method determines the impact zones, distinguishes the different damage mechanisms, and draws the propagation path of the induced damage with a high spatial resolution. Following the principle of the X-Ray tomography detailed in **Figure 43**, the X-Ray beam penetrates the sample, which is positioned on a rotating table and is then projected on a flat panel detector. Its ability to provide internal information about the investigated area makes the technique more suitable and helpful compared to other in-situ investigation methods. A voxel size is set to 12 µm corresponding to the resolution of the observation. It represents a good compromise in terms of accuracy up to the level of the fiber diameter ranging from 10 to 15 µm. Radiographic images recorded at different rotation angles are then processed for the 3D volume reconstruction of the targeted area of the sample.

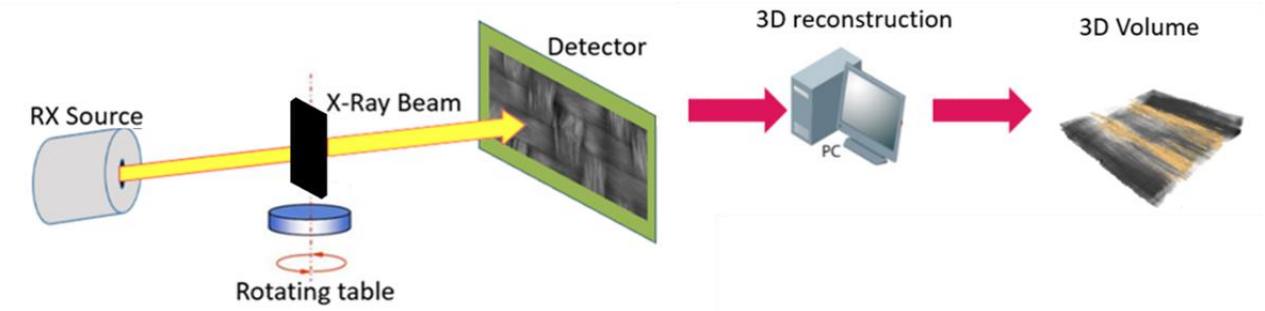

Figure 43: Principle of X-Ray tomography technique showing: The source sending an X-ray beam penetrating the investigated object positioned on a rotating table and projected on a flat detector enabling using suited software the reconstruction of a 3D Volume (Miqoi et al., 2021).

2. Post-processing and Results

Through-thickness damage is investigated through the reconstructed 3D volume of the impacted area. The latter is generated from the multiple saved images during the acquisition using X-act software. The 3D volume is represented on a grey scale according to the X-ray

absorption index of each phase constituting the composite. The AVIZO software is employed afterward to significantly reduce the amount of noise in the reconstructed images employing the median filter and the related thresholding levels that the software provides to highlight the damaged zones. The inspection of the reconstructed layers, lead to the observation of several damage mechanisms. The latter generate the creation of void that is represented in black when coming across the X-Ray beam. It should be mentioned that for the sample impacted at an energy of 7.20 J, the tomography results indicate no damage in the impacted area confirming hence that this level of energy is not sufficient to create a permanent internal damage in the studied material. All the tomography results for the considered samples impacted at 10.54 J, 12.6 J, 14.58 J, 19 J, 21.15 J and 24 J are represented in **Figure 45, Figure 46, Figure 47, Figure 48** and **Figure 49** respectively.

The main damage mechanism observed on the majority of the considered samples is matrix cracking. Indeed, it consist of the first detected damage mechanism. Consequently, through-thickness damage grows and propagates towards the impacted surface as the impact energy raises. That said, matrix cracking spread from ply to ply through the rich polymer matrix areas when increasing of the impact energy.

Furthermore, in the case of low-velocity impact in thin plates, damage is first noticed on the non-impacted surface due to the bending effect resulting from the impact event (Hautier, 2010) as illustrated in the figures below (**Figure 44(b), Figure 45(c), Figure 46(c), Figure 47(b), Figure 48(b)** and **Figure 49(b)).**

The sample impacted at 10.54 J showed a small crack in the visual inspection stage. A more profound investigation is established to verify its through-thickness propagation. The tomography results point out to the fact that the crack is contained in the same layer and damped by the architecture effect as illustrated in **Figure 44(a)**.

For the rest of the considered samples, one can conclude that the severity of the damage increases with the increase of the impact energy. Indeed, X-Ray tomography reveal larger cracks resulting in the creation of a more evolved crack network that propagates through the different layers. When the impact energy raises to 12.6 J, 14.58 J and 19 J matrix breaking spread from the first to the second layers as seen in **Figure 45(a), Figure 46(b)** and **Figure 47(a)** respectively. As the energy increases to 21.15 J **(Figure 48(a))** and 24 J **(Figure 49(a)),** it propagates into the third layer constituting the laminate and is slowed down by the weaving of the fibers.

In fact, when matrix cracking propagates from one ply to another, this phenomenon is generally accompanied by delamination and fiber breakage. Furthermore, the cracks propagate into and along the yarns in a transversal and longitudinal path. Presuming that the energy in high enough, the cracks develop and turn to delamination that wrap around the yarns. This damage mechanism is known as pseudo-delamination and is shown in **Figure 47(a), Figure 48(a)** and **Figure 49(a)**. When inspecting the fiber breakage zone in the perpendicular plane, a slight lift of the broken area is noticed. This uplift result in the appearance of delamination between transversal and longitudinal yarn of the same layer.

As a partial conclusion of the overall X-Ray tomography inspection, one can establish that the damage mechanisms developed in the studied woven glass reinforced composite undergoing low-velocity impact loading are similar to those observed under monotonous loading (Pomarède et al., 2018). The damage kinetics for the initiation, the accumulation and the propagation are as follow: the first distinguished damage mechanism is the matrix cracking. The latter is introduced into the non-impacted surface assignable to the nature of the material (thin material) and spread in surface, in both longitudinal and transversal directions, due to the deflection effect related to the boundary conditions. When the impact energy increases, these cracks start to propagate into the yarns causing the deterioration of fiber/Matrix interface. The cracks then diffuse between the yarns in the areas rich in polymer leading to the breakage of the reinforcements.

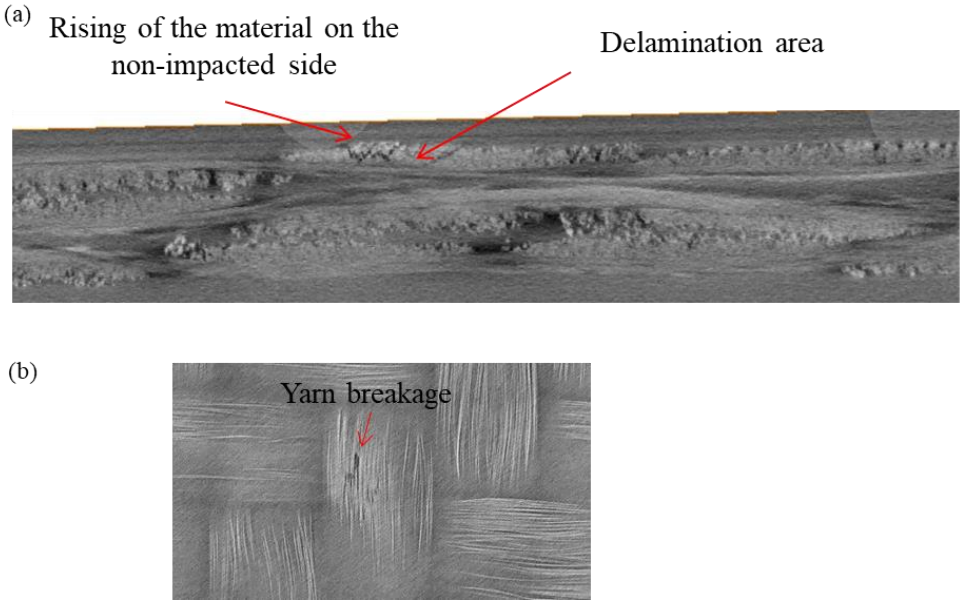

Figure 44: The damage mechanisms observed in the sample impacted at an energy level of 10.54 J, contained in the first layer, showing: (a) the rising of the material on the non-impacted side and the pseudo-delamination between the longitudinal and the transversal yarn, and (b) the non-impacted showing the fibers breakage.

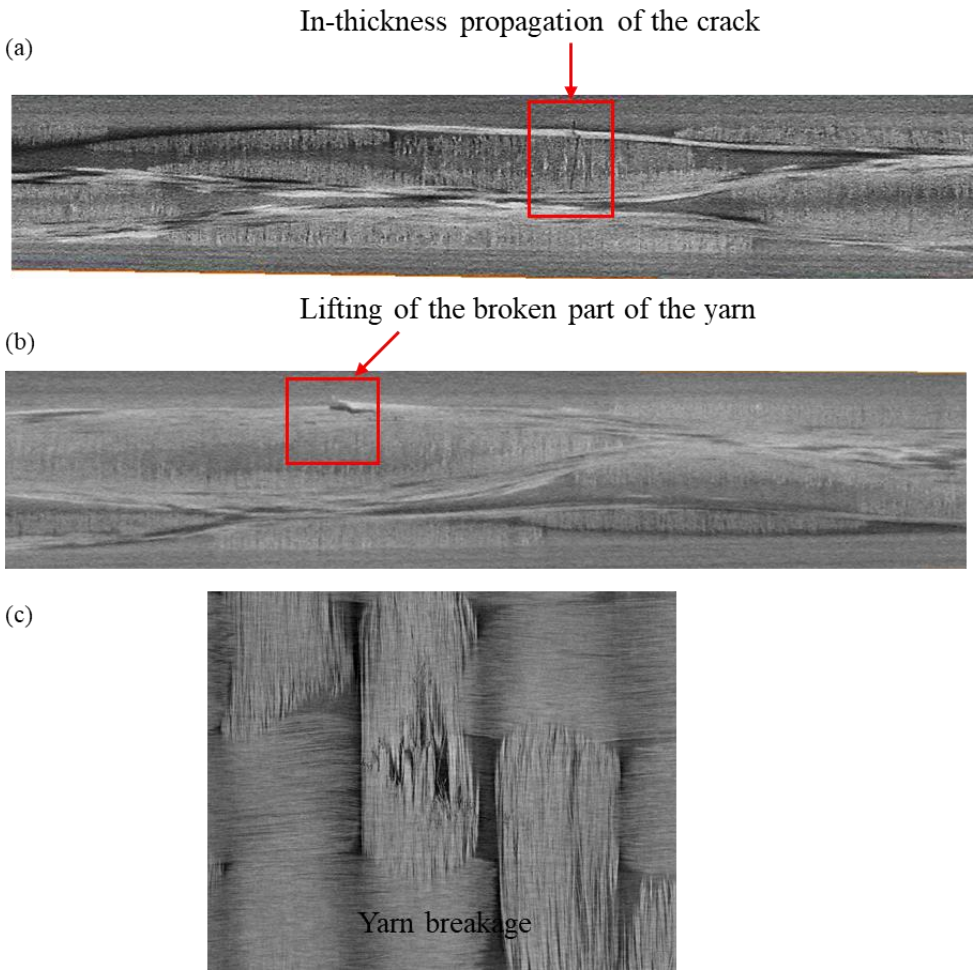

Figure 45: The damage mechanisms observed in the sample impacted at an energy level of 12.6 J showing: (a) the propagation of the cracks into the second layer, (b) the rising of the material on the non-impacted side and the pseudo-delamination between the longitudinal and the transversal yarn, and (c) the non-impacted showing the fibers breakage.

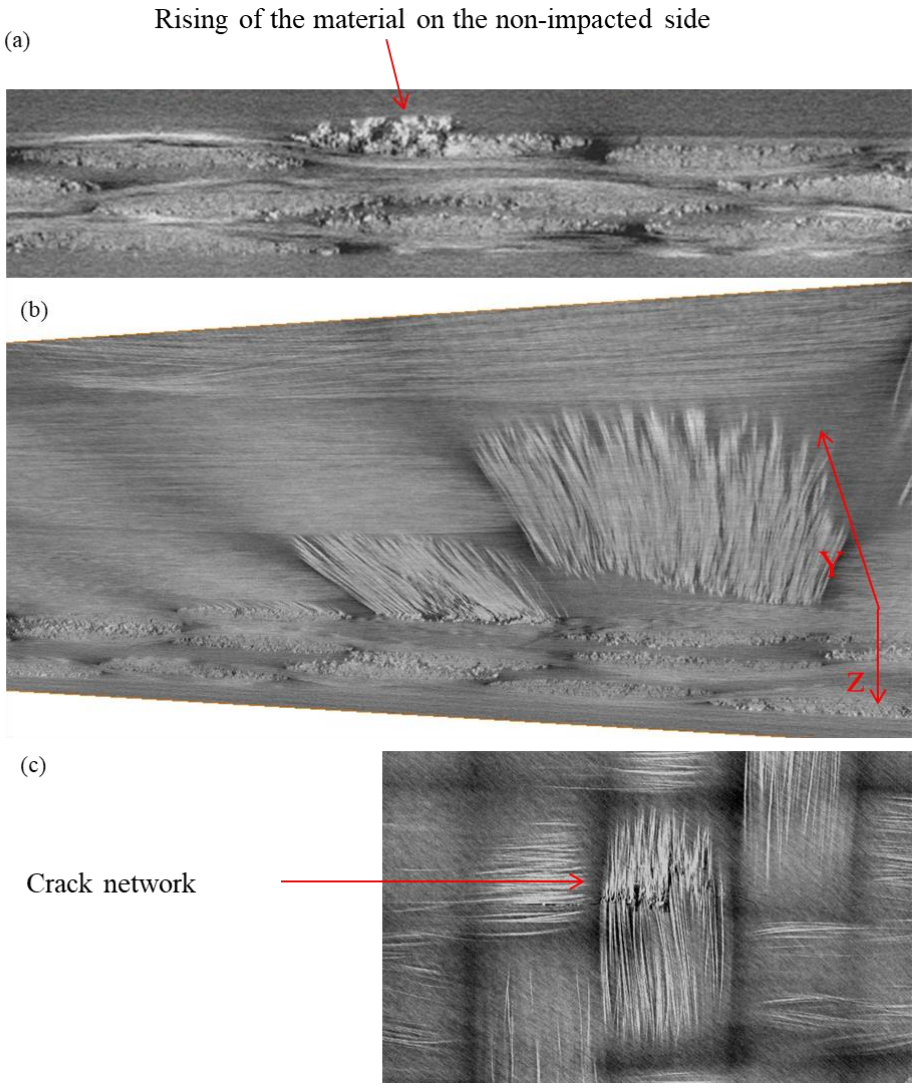

Figure 46: The damage mechanisms observed in the sample impacted at an energy level of 14.58 J showing: (a) the rising of the broken part of the yarn on the non-impacted side the propagation of the cracks into the second layer, (b) 3D propagation of the cracks in thickness in the longitudinal and transversal yarns, and (c) the non-impacted showing the fibers breakage.

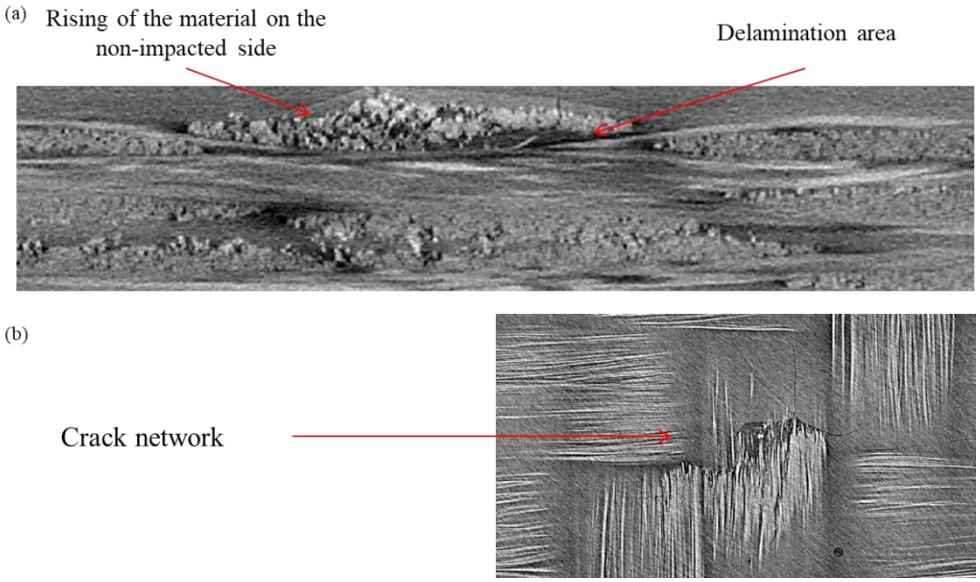

Figure 47: The damage mechanisms observed in the sample impacted at an energy level of 19 J showing: (a) the rising of the material on the non-impacted side, propagation of the cracks in the yarns and the pseudo-delamination between the longitudinal and the transversal yarn, and (b) the non-impacted showing the fibers breakage and the crack pattern.

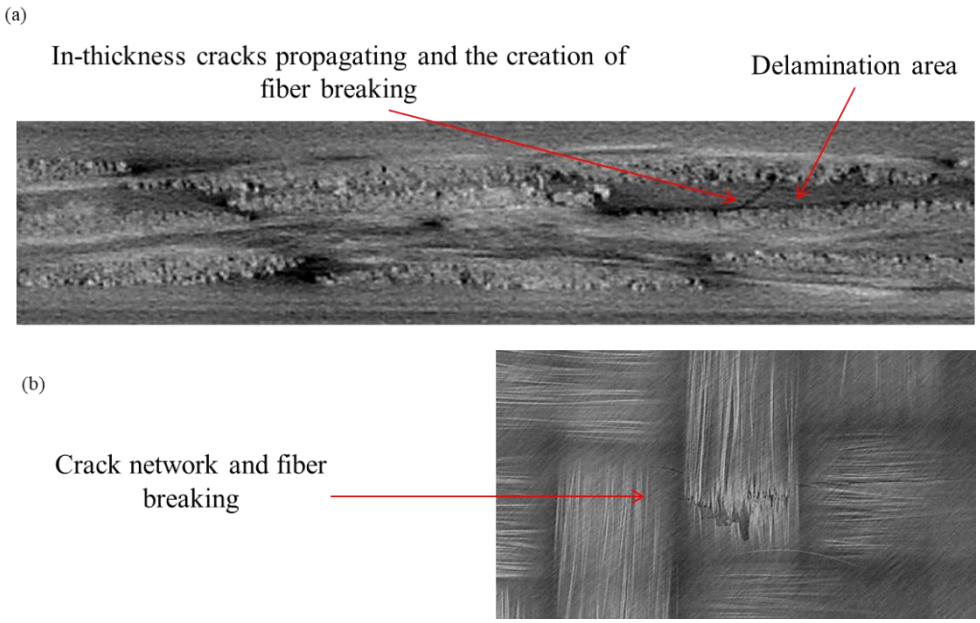

Figure 48: The damage mechanisms observed in the sample impacted at an energy level of 21.15 J showing: (a) the through-thickness crack diffusion, the creation of fiber breakage resulting in the propagation of the cracks in the yarns along with the occurrence of the pseudo-delamination between the longitudinal and the transversal yarn, and (b) the non-impacted showing the fibers breakage and the crack pattern.

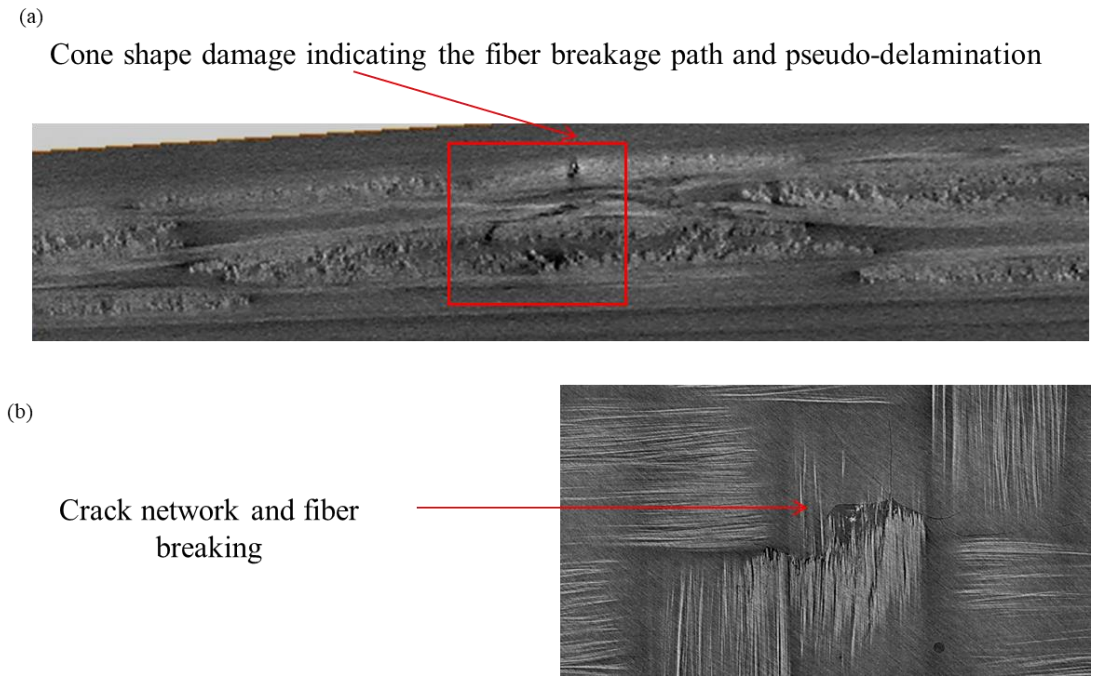

Figure 49: The damage mechanisms observed in the sample impacted at an energy level of 24 J showing: (a) The Cone shape damage indicating the fiber breakage path inducing the creation of pseudo-delamination when propagation from a yarn to another through the three layers, and (b) the non-impacted showing the fibers breakage and the crack pattern.

III. Non-destructive evaluation of the damage

After analyzing the impact response and the mechanical aspects of the impact damage, both macroscopically and microscopically, on surface and in thickness, the quantification of the residual damage is the subject of this section. One of the main objectives of this research work is to propose a method of damage detection by nondestructive testing. Non-destructive testing (NDT), more specifically Bulk waves and Lamb waves propagation method, are the main focus. The choice of ultrasound is based on its sensitivity, efficiency, and ease of use in industrial testing. On one hand, bulk waves are those that propagate in volume. Their nature enables the detection of damage propagating through-thickness. In the other hand, Lamb waves allows the investigation of large areas by means of a scan on a line. Consequently, the Lamb waves exploitation is acknowledged as considerably time saving. More details about these two types of waves are given in Chapter I.

A first sub-section is dedicated to the estimation of the stiffness matrix components of each of the seven chosen samples. The second sub-section details an original approach consisting in the determination of the propagation velocity profile of Lamb waves.

1. Stiffness reduction determination

This section is devoted to the determination of the measurements of the stiffness matrix components for each sample considered. The experimental procedure followed will be detailed in the first subsection. The steps followed to find the right values of the different components are explained afterwards. Finally, a damage indicator will be proposed.

1.2. Experimental procedure

This section is dedicated to the step-by-step description of the experimental procedure followed to determine the components of the stiffness matrix. The employed experimental stiffness components measurements method is described and used in the works of (Pomarède et al., 2018). The theoretical principle of this technique has been detailed in Chapter I. The main idea of this method is to determine the velocity of the propagating wave at different incidence/emission angles on the different principal planes. The velocity of wave propagation along with the stiffness and density of a solid homogeneous medium are linked by the equation known as Christoffel's equation (Chapter I).

Due to the orthotropic nature of the material, the first step is, ideally, to perform the acquisition of the signal propagating in the three principal planes (**Figure 50**) enabling to obtain the nine stiffness components. However, in this case, and because of the low thickness of the samples (1.53 mm), only two main planes are considered. Indeed, 1-3 plane and 2-3 plane are those allowing the propagation of Bulk waves in transmission. Thus, the computation of only seven out of the nine components is possible.

Indeed, the 1-3 plane enables the determination of C_{11}, C_{33}, C_{13} and C_{55} while the 2-3 plane C_{22}, C_{33}, C_{23} and C_{44}. It should be mentioned that measurements are performed on a reference sample and damage samples impacted at 10.54 J, 12.6 J, 14.58 J, 19 J, 21.15 J and 24 J.

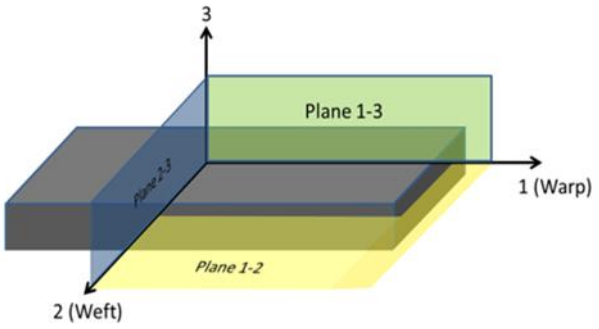

Figure 50: An illustration of the three principle planes of ultrasonic waves propagation considered in the case of orthotropic material (Pomarède, 2018).

The acquisitions are performed at GeorgiaTech Lorraine ultrasound laboratory (LUNE) employing Winspect software and the five-axis customer-designed immersion scanner manufactured by Inspection Technology Europe BV. Since the measurements are realized in transmission, two immersion transducers of the brand Panasonic are used. The latter are chosen with a central frequency of 2.25 MHz satisfying hence the hypothesis of the homogenous media. The distance between the emitter and the receiver is of 19.1 cm. A measurement in the water without the sample is first done. The latter enables the estimation of the time taken by the wave to cross the composite. The wave takes about 121.2850 µs to propagate in the water. Knowing the distance between the transducers, one can easily deduce that the velocity of wave in water is about 1574 m/s. It should be mentioned that the velocity of propagation of the wave is very sensitive to temperature variation. The experimental set-up used in this study is detailed in **Figure 51** and shows the system used to maintain the sample. For a better understanding of the acquisition process, a schematic representation is presented in **Figure 52**. The entire measuring system (transducers and samples) is immersed in a water tank used as a coupling fluid allowing to provide better ultrasound coupling compared to air. Measurements are carried for an angle of incidence varying from -30° to 30° with an angular step equal to 0.25°. Data acquisitions are achieved through Winspect software and post-processed using a script in Matlab software.

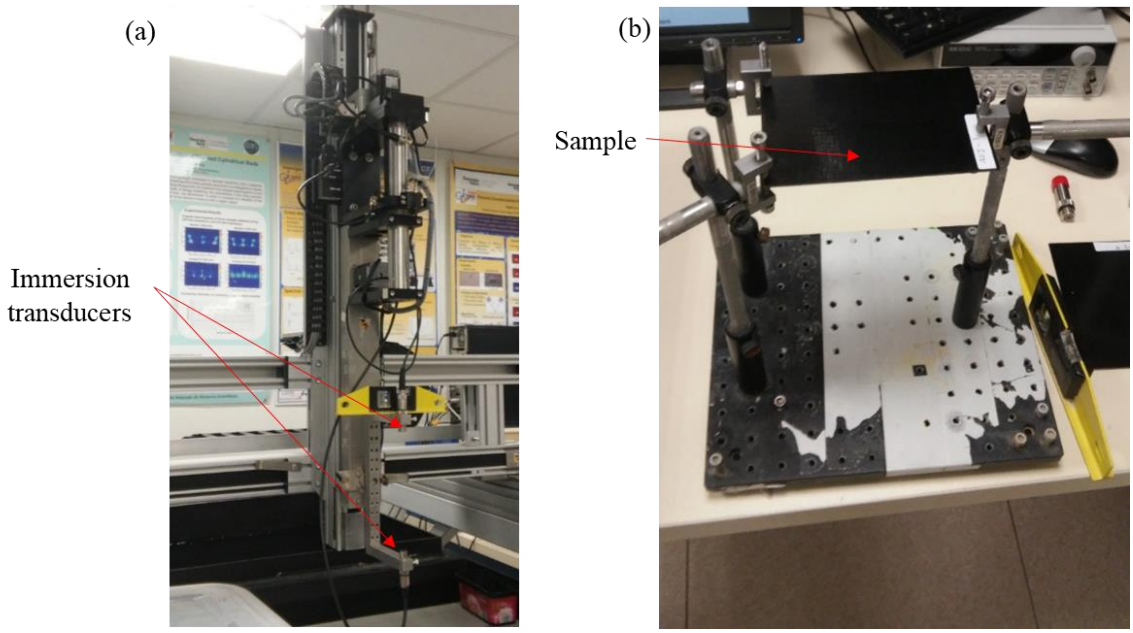

Figure 51: Experimental set-up used for the acquisitions of the signals showing: (a) the five-axis immersion scanner with the implemented transducers distanced by 19.1 cm and (b) an example of a sample with a special holding enabling the scanning at different angles and directions.

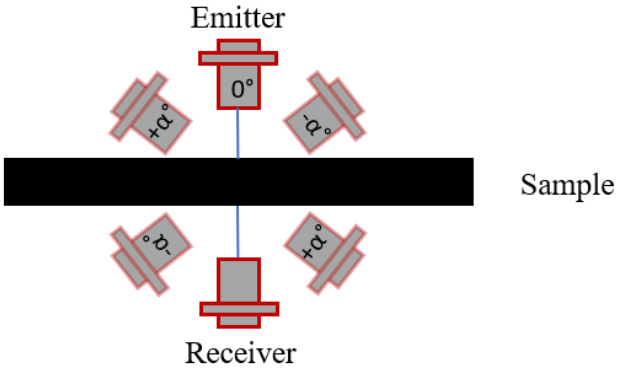

Figure 52: Schematic representation of the acquisition process with angle variation (a=30°).

1.3. Post-processing and velocity calculation

The method followed to measure the velocity in the two considered planes is the one proposed by Markham (Markham, 1970). Signals are recorded while variating the emission/ reception angle simultaneously. After the acquisitions, the TOF is registered for each signal. The latter corresponds to the first positive peak. The difference of time between a measurement with and without the sample indicates the time of propagation of the wave in the sample. This value is noted δ_t and is defined as:

$$\delta_t = t_W - t_S$$

With $$t_W = \frac{e*cos\,(\theta_r - \theta_i)}{V_W * cos\,(\theta_r)}$$

And $$t_S = \frac{\mathrm{e}}{V_S * \cos\,(\theta_r)}$$

e corresponds to the thickness of the sample, θ_r the refraction angle, θ_i the incidence angle, and V_W and V_S the velocity of propagation of the wave in the water and in the sample, respectively.

With the help of Snell's Law, the angle of refraction and the velocity of propagation of the wave in the sample are given by:

$$\theta_r = \mathrm{atan}\,(\frac{\sin\,(\theta_i)}{\cos(\theta_i) - \frac{V_W \delta_t}{e}})$$

$$V_S = \frac{\sin(\theta_r) * V_W}{\sin\,(\theta_i)}$$

It should be noted that normally the phase velocity is used for the estimation of the stiffness matrix components. However, this experimental method enables the calculation of the group velocity which is different from the phase velocity. As proven in (Rokhlin & Wang, 1989, 1992), due to the changes that can occur in the velocity and the propagation paths, the use of δ_t to retrieve the phase velocity is considered as physically correct.

A large number of experimental data i.e., values of TOF corresponding to emission angles, is required for a proper computation of the stiffness tensor. It should be noted that when varying the emission angle merger occurs. Indeed, different modes can propagate in the samples namely quasi-longitudinal and quasi-transversal modes. Consequently, the measurement of the correct value corresponding to the right mode are more difficult inducing hence incorrect values of the mode propagation velocity. For that matter, it is important to follow the wanted peak at different angles. As a result, one can see the appearance and the disappearance of the propagating modes. For a better understanding, one can refer to **Figure 53** that illustrate a signal recorded at 0° and one recorded at 27.25°. The localized quasi-transversal mode can be easily identified at the

signal with 27.25° as incident angle. Experimental assessment of the signals leads to the following conclusions: (1) Only the quasi-longitudinal mode QL and the first quasi-transversal mode QT1 can be easily identified and (2) For a given angle of incidence θ Є [-25°, +25°] the longitudinal mode is predominant. Around θ = 0°, the first peak corresponding to the longitudinal mode is easily identifiable (**Figure 53**). By increasing the angle of incidence from θ = 0°, a decrease of the amplitude of the first peak is observed and corresponds to the progressive transfer of the energy from the longitudinal mode to the transversal mode (**Figure 53).** In a same way, by decreasing the angle of incidence from θ = ± 30°, a decrease of amplitude of the first peak (now from the transversal mode) leads to a progressive transfer from the transversal mode to the longitudinal mode. In other words, from a critical angle of incidence, modes become evanescent. Indeed, starting from ± 24°, only the quasi-transversal modes are propagating.

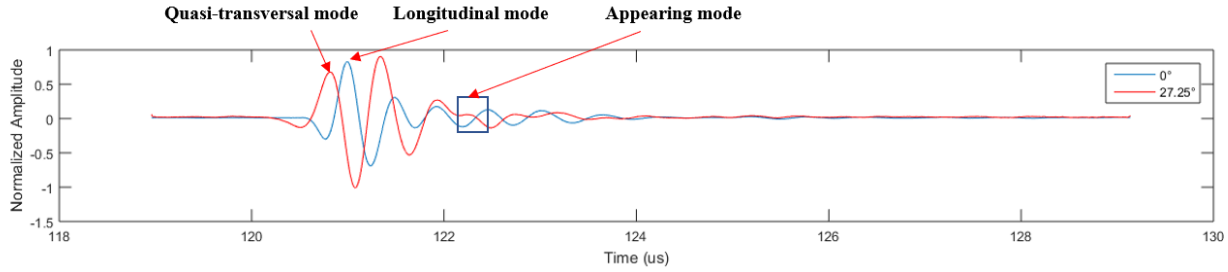

Figure 53: Received signal at 0° and 27.25° showing the longitudinal mode on the signal corresponding to 0° and the quasi-transversal mode as the only type of mode propagating at 27.25°.

After the proper measurements of the TOF values of the quasi-longitudinal and the quasi-transversal modes in the two considered planes, the values of velocity of each mode are computed using equation (7). For the non-damaged sample, the retrieved values of the velocities are illustrated in **Figure 54**. One can see that the values of the phase velocity remain stable around 2230 m/s in the range of angle between ±10° approximately, and then increase with the increase of the incidence angle. The same results are found in the works of Pomarède (Pomarède, 2018).

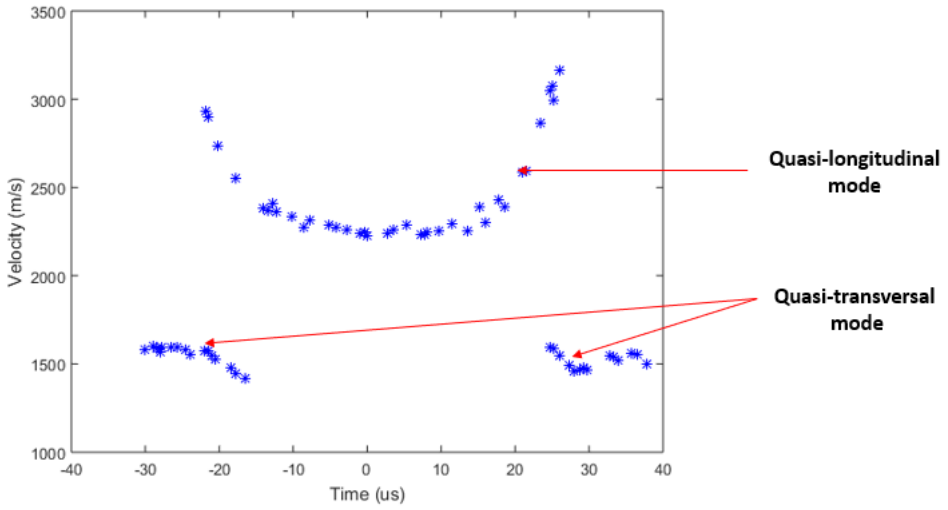

Figure 54: Experimental velocities of waves propagating in a non-impacted sample showing the velocities of quasi longitudinal mode and the quasi-transversal mode.

The stiffness components are determined by resolving the inverse problem of the Christoffel equation.

$$\left(C_{ijkl}n_k n_j - \rho v^2 \delta_{ij}\right)U_l = 0$$

To do so, an optimization approach is used. A Levenberg-Marquardt algorithm is employed to minimize the difference between the analytical and the experimental velocities. The optimization problem is introduced as:

$$F\left(C_{ij}\right) = \sum_n [V_{exp} - V_{num}(C_{ij})]^2$$

with n: the number of the values of experimental velocities, V_{exp} the experimental values obtained using the measured TOF and $V_{num}$the analytical velocities.

The velocities are computed by resolving the Christoffel equation for a provided set of stiffness matrix values. It should be noted that the algorithm needs to be initialized. A correct first estimation of the initialization values is crucial for a smooth running of the calculations. Moreover, Levenberg-Marquardt algorithm is very sensitive to these initial values. The latter can induce errors in the calculations if the initiation values are not properly estimated. The

accuracy of the determined stiffness components depends also on the number of the measured values of velocities and the number of the considered plans. Consequently, it is more accurate to consider a confidence interval for each identified value of the stiffness matrix components (Baste & El Guerjouma, 1989; Marguères et al., 1999; Marguères & Meraghni, 2013). As proposed by Audoin et al. (Audoin et al., 1991), the covariance matrix is used to estimate the confidence interval. It enables the obtention of information relative to the statistical variation between the analytical solutions of the C_{ij}.

The estimated confidence intervals are calculated from the diagonal values of the covariance matrix and are given as:

$$ci(i) = \sqrt{\phi_{ii}}$$

$$\phi = \frac{\boldsymbol{r}^t * \boldsymbol{r}}{n - m} * [\![([J]]\!]^t * [J])^{-1}$$

With: $[J] = \frac{\partial F(C_{ij})}{\partial C_{ij}}$ the Jacobian matrix, **r** the vector containing of residual values, n the number of the considered experimental velocities and m the number of the stiffness constants to identify.

1.4. Stiffness constants estimation: Results

Since only two planes are considered during the acquisitions due to the low thickness, only seven out of the nine stiffness matrix components can be directly obtained. However, since C_{44} appear in the Christoffel equation relative to both investigated planes, the latter can also be estimated. As for the remaining constant, namely C_{12}, it is fixed to the initialization values retrieved from periodic homogenization. The values of the eight stiffness matrix components along with the confidence interval relative to each value are found in **Table 5** for the seven investigated samples. The evolution of each component can be visualized in **Figure 55**.

A progressive decrease is noticed for the values of the C_{11} component from 7.20 J to 14.58 J **(Figure 55(a)).** The values are stabilized afterwards. For C_{22} component **(Figure 55(a)),** a reduction is noticed at higher energies, specifically at 19 J. The values of this component do not seem to have an important variation before the last energy. An important fall of the values of C_{33} component **Figure 55(b)** is visible starting from 12.6 J. Less marked drop is seen for the rest of the components C_{66}, C_{55}, C_{13} and C_{23} (**Figure 55(d)** and **Figure 55(c)** respectively). That said, C_{23}

varies as follows: the values decrease starting from 10.54 J until they reach a threshold where they are maintained even at higher energies (**Figure 55(c)**). As for C_{13}, the values gradually decrease as the impact energy grows (**Figure 55(c)**). However, C_{66} and C_{55} values do not appear to change (**Figure 55(d)**). Finally, the value of C_{44} component decrease starting from 7.20 J until 14.58 J and then the values stabilize as the impact energy increases.

One can conclude that several components decrease with the increase of the impact energy. The variation of certain components rather than others depends mainly on the type of loading. However, some estimated values have relatively high uncertainty.

Table 5: Values of the eight retrieved stiffness matrix components with their relative confidence interval.

Impact energy (J)	0	7.20	10.54	12.6	14.58	19	24
C_{11} (GPa)	18.80 ± 0.97	18 ± 1.7838	17.25 ± 1.60	16.75 ± 1,66	15.19 ± 1.66	15.01 ± 3	15 ± 6.01
C_{22} (GPa)	19.26 ± 0.64	18.05 ± 0.80	18.08 ± 0.78	16.50 ±0,84	18.2 ± 0.84	18.16 ± 2.3	16.61 ± 2.13
C_{33} (GPa)	8.8 ± 0.13	8.73 ± 0.16	8.8 ± 0.14	8.8 ± 0,16381	7 ± 0.16	6.71 ± 0.44	5.76 ± 0.5
C_{13} (GPa)	3.35 ± 0.78	3.11 ± 0.52	3.1 ± 0.44	3,18 ± 0,48	2.76 ± 0.48	2.5 ± 1.11	2.32 ± 1.64
C_{23} (GPa)	3.04 ± 0.13	3 ±0.42	2.5 ± 0.18	2.5 ± 0,16	2.6 ± 0.41	2.5 ± 1.03	2.55 ± 1.1
C44 (GPa)	3 ± 0.31	2.96 ± 0.28	2.51 ± 0.25	2,11 ± 0,28	2.08 ± 0.35	2.14 ± 0.63	2.4 ± 0.78
C_{55} (GPa)	1.85 ± 0.35	1.85 ± 0.09	1.88 ± 0.07	1.98 ± 0,09	2.1 ± 0.09	1.9 ± 0.19	1.99 ± 0.23
C_{66} (GPa)	1.92 ± 0.09	1.92 ± 0.09	1.94 ± 0.06	2.05 ± 0,08	2.1 ± 0.08	1.79 ± 0.19	1.74 ± 0.21

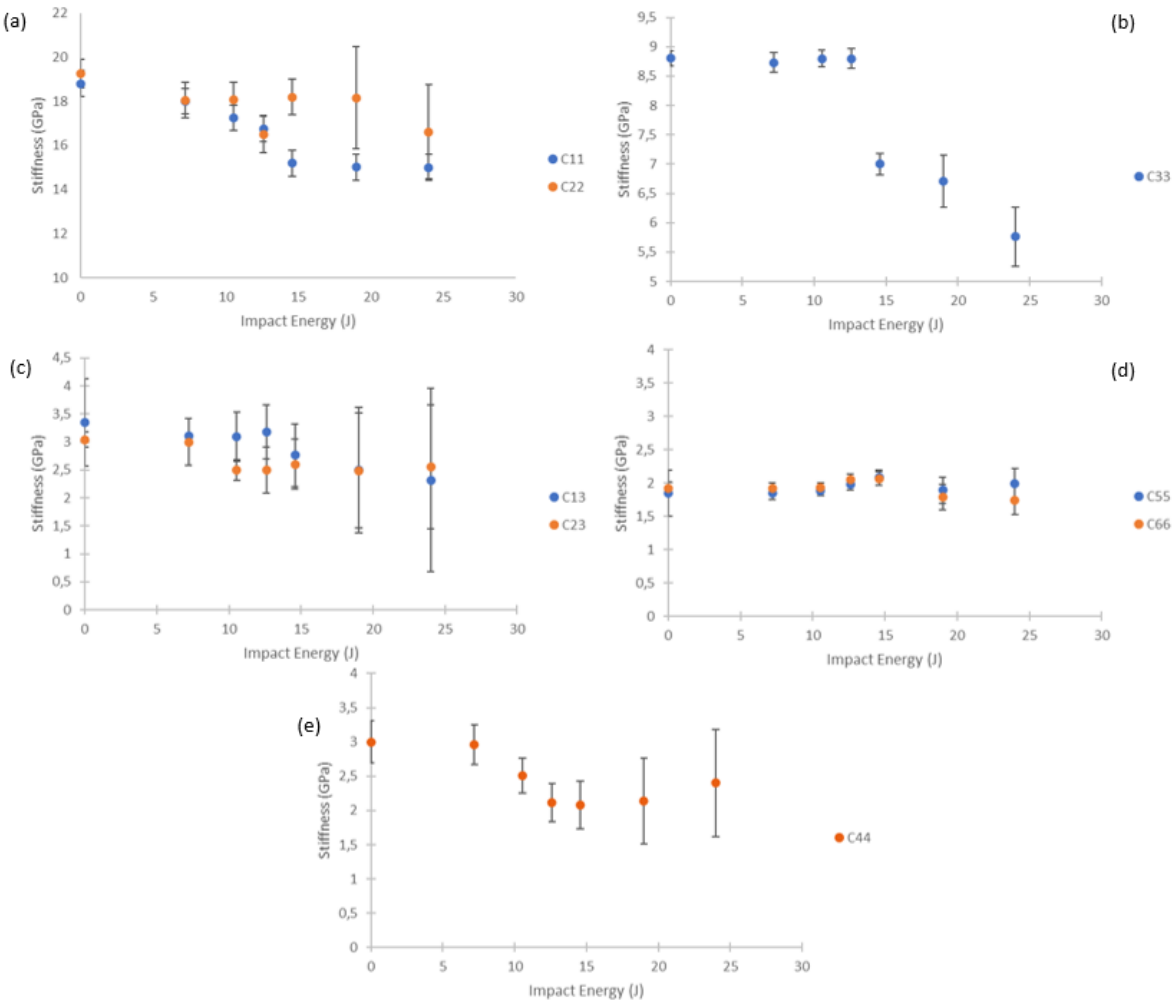

Figure 55: Evolution of the seven stiffness components function of the impact energy, namely: (a) C11 and C22, (b) C33, (c) C55 and C66 and (d) C23.

2. Lamb waves-based method

The guided waves are used to determine the damage in the composite. Indeed, as mentioned in the literature review, Lamb waves are shown to be very effective when it comes to the evaluation and the study of the damage state of a complex structure. The main idea is to change the direction of propagation of the guided wave in the sample, and to compute the velocity of propagation for each direction. Since the velocity of propagation is directly linked to the stiffness of the media, the variation of the angles of emission/ reception i.e., the direction of propagation enables to retrieve information concerning the anisotropy resulting from damage initiation.

The results will be presented as velocity profiles function of the angle position describing the interaction between the wave and the propagation media.

Different steps are followed to determine an operational experimental set-up. The preliminary tests point out to different parameters that should be considered. One can divide these parameters into two categories: ultrasonic parameters and geometrical parameters. The most important ultrasonic parameter is the frequency. Indeed, choosing the right frequency for the signal is crucial for a good assessment of the signals. As geometrical parameters, one can cite the distance between the transducers, the position of the latter on Z axis, and the positioning of the sample. The preliminary works, considered to respond to each of the mentioned aspects, are discussed in the following sub-sections.

Indeed, a procedure is followed for the determination of the emission frequency. Solutions are proposed to minimize the error due to geometrical variations mainly of the position of the transducers and the position of the sample.

2.1. Sample and transducers positioning

Since guided waves are very sensitive to any variation especially geometrical variation, keeping a fixed distance between the transmitter and the receiver throughout the acquisitions is highly important for a good understanding of the phenomena occurring during the propagation of the wave. For that matter, two devices are custom designed by 3D printing. A transducer holder is designed to guarantee a distance of 6 cm between the centers of the transducers as shown in **Figure 56**. The transducers' holder in then positioned on a five-axis immersion scanner made by Inspection Technology Europe BV to automatize the displacement of transducers position on Z axis and therefor maintain the same pressure on the samples at each position.

As previously mentioned, the experimental measurements consist in variating the angle of emission and reception simultaneously (**Figure 57**). A step of five degrees is chosen for this experiment. A custom-made 3D printed system is designed. The latter consists of two parts: a sample holder and a device that allows the rotation of the sample at the pre-defined steps (**Figure 58**).

Figure 56: 3D printed custom carrier ensuring a constant distance of 6 cm between the centers of the transducers.

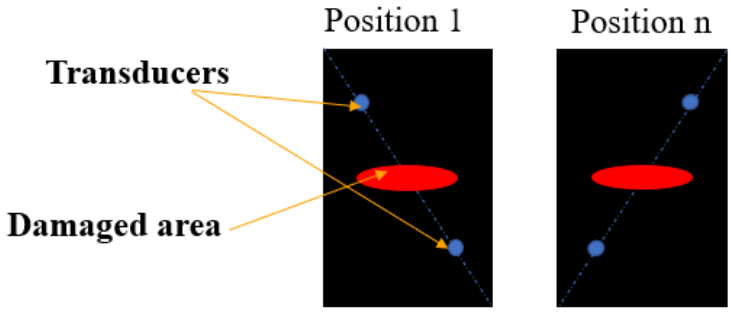

Figure 57: Schematic representation of the experimental measurements' principal showing the emission and reception transducer, and the angle variation from position 1 to position n.

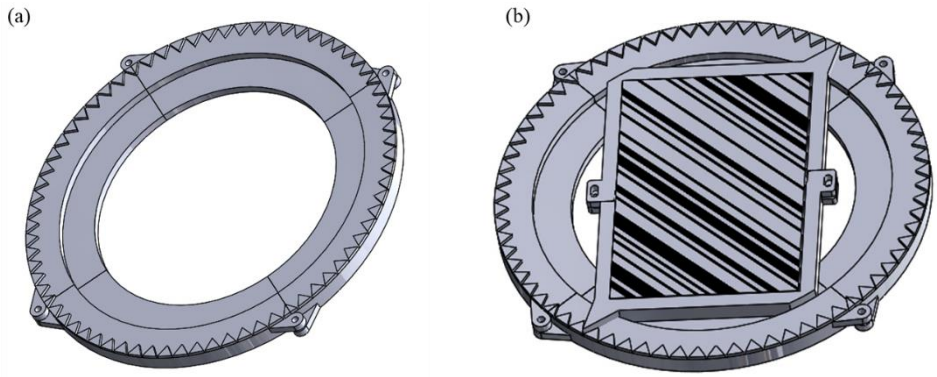

Figure 58: The 3D custom designed experimental device used to ensure the rotation of the sample at a pre-defined step of five degrees showing: (a) the rotation support and (b) the entire set-up with the rotating sample holder.

2.2. Determination of the emitting frequency

The first step in the determination of the adequate emission frequency is the knowledge of the modes propagating at each frequency. The latter is given in the dispersion curves. For that matter, the "Disperse" software, developed at the Imperial College NDT lab , is used. By giving the stiffness tensor, the size of the Representative Elementary Volume (REV) and the thickness of the studied material, one can numerically generates the dispersion curve. To avoid any confusion when post-processing the signals, the range of the chosen frequency corresponds to where only S_0 and A_0 modes propagate in the material. The dispersion curve describing the group velocity function of the frequency is given in **Figure 59**. Based on the dispersion curve, a range of frequency varying between 50 KHz and 175 KHz is selected.

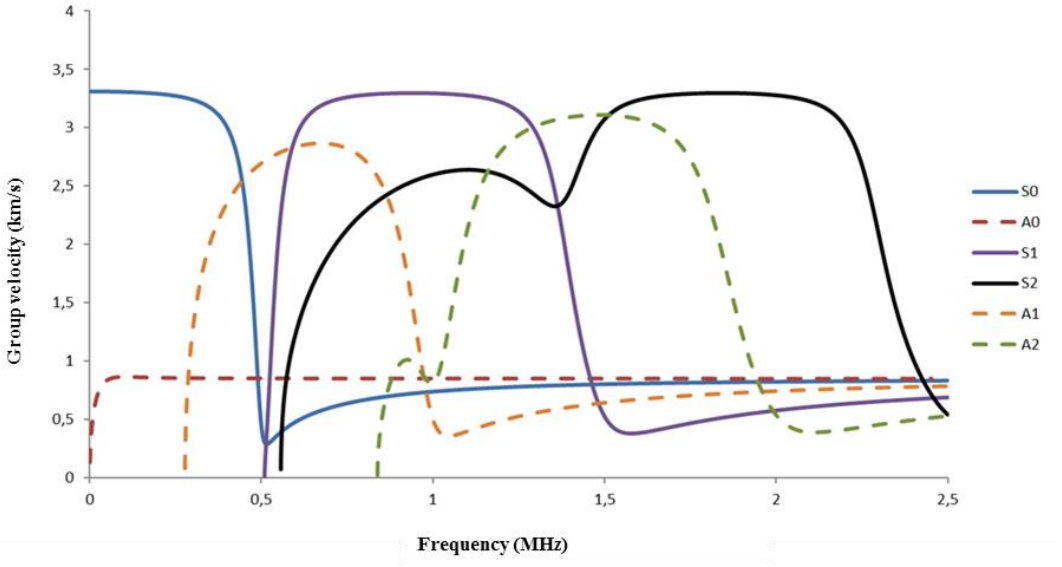

Figure 59: Dispersion curve corresponding to the studied material showing the group velocity function of the frequency (Pomarède et al., 2018).

The acquisitions are made on a non-impacted sample (reference sample) at the position 0°. Signal are emitted at frequency varying between 50 KHz and 175 KHz with a step of 25 KHz. The frequency corresponding to the clearest signal will be selected for the rest of the study. The clearer the signal in the position 0° in the non-damaged sample, the better the effect of the introduction of damage can be seen on the signal. **Figure 60** and **Figure 61** illustrate the saved signal for each tested frequency. **Figure 60** depicts the signals propagating at low frequencies namely 50 KHz, 100 KHz and 125 KHz. One can easily observe that the three signals show a disturbance that is reflected by the appearance of multiple merging cycles. On **Figure 61**, in addition to the 125 KHz signal, signals emitted at 150 KHz and 175 KHz are exhibited. From a close observation, one can conclude that the signal with defined cycles correspond to the signal emitted at 150 KHz. That said, for the rest of the study, a frequency of 150 KHz is chosen because the "overlap of the modes" occurs later in the signal than at other frequencies.

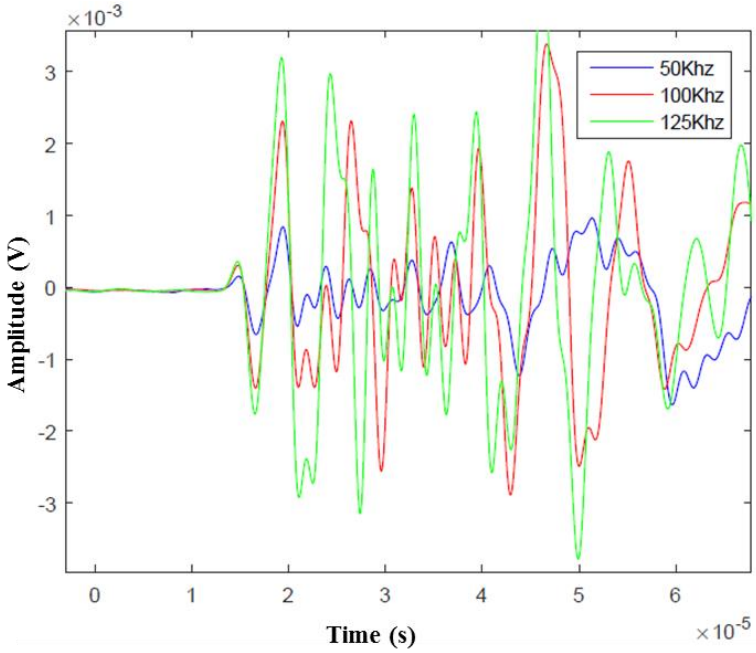

Figure 60: Signals propagating in the non-impacted sample at different frequencies namely 50 KHz, 100 KHz and 125 KHz.

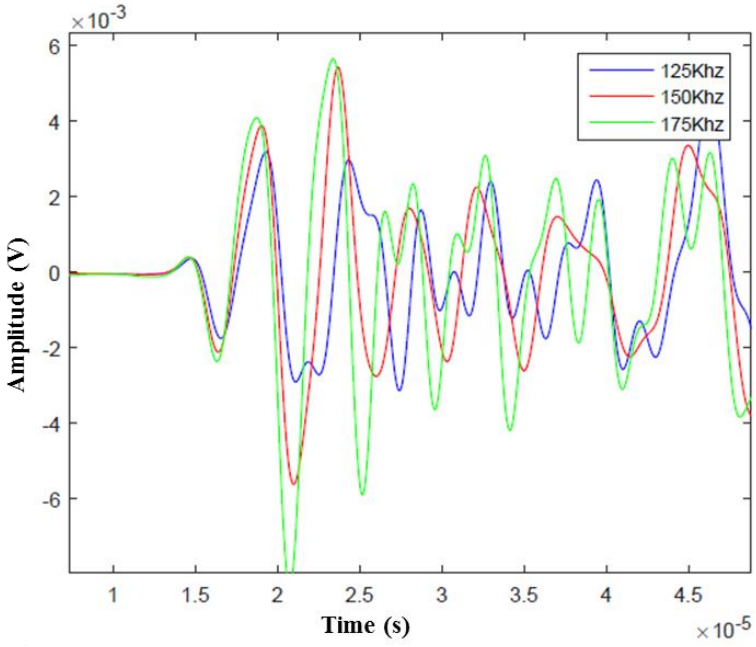

Figure 61: Signals propagating in the non-impacted sample at different frequencies namely 125 KHz, 150 KHz and 175 KHz.

2.3. Experimental set-up

A single sinusoidal pulse is generated at a frequency of 150 KHz with an amplitude from peak to peak of 10 V using a Hewlett Packard 33120 A generator. The latter is connected to one of the transducers (the emitter). The signal propagates in the sample and is then captured by the receiver. The transducers employed in this experimental set-up are 1 MHz transducers of the brand Olympus. Knowing the attenuation effect that the composite has on the signal, a Krohen-Hite model 7500 amplifier is utilized. The output of the amplifier is linked to a Lecroy waverunner 64Xi oscilloscope that enable the visualization and the recording of the signals. It should be mentioned that all acquisitions are realized at LUNE Laboratory located at GeorgiaTech Lorraine.

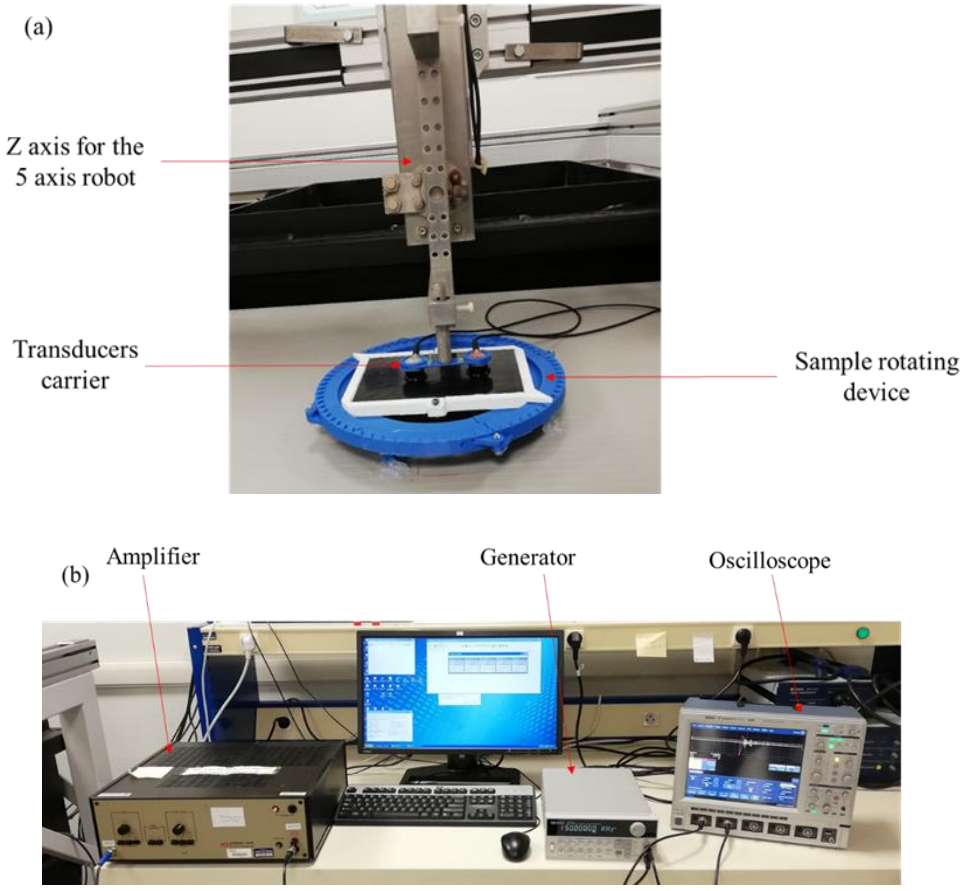

Figure 62: The employed experimental setup showing: (a) the transducers maintained by the 3D printed holder that is fixed on the five axes robot allowing the translation on the Z axis along with the 3D printed custom-designed device allowing the rotation of the sample with a pre-defined step of 5°, and (b)the setup used to generate and save the signal revealing the generator, the amplifier and the oscilloscope.

2.4. Post-processing and results

After recording the 13 signals at each angle for all the considered samples (reference and seven impacted samples), the next step is to identify of the time of arrival of the first propagating mode. To do so, a convolution between a reference signal and the signals recorded for each sample at each defined position is performed. One should remind that the convolution of two functions is given as the integral of the product of the latter after one is shifted:

$$f * g = \int f(t)g(t-\tau)d\tau$$

The reference signal corresponds to the first wave packet (from the second to the sixth peak) of the signal recorded on the reference sample at angle 0° as show in **Figure 63**. The resulting convolution signals are then superimposed on each corresponding signal. In other words, each signal is compared and correlated to the first wave packet of the signal propagating at 0° in the non-impacted sample. This method allows the determination of the exact position where there is a correlation between the reference signal and the rest of the signals. This position corresponds to the time of arrival of the first peak i.e., the S_0 mode, that will consequently lead to the calculation of the velocity. The whole procedure of TOF selection is explained by an example of measurement on a signal recorded on the reference plate at angle 0° illustrated in **Figure 64**. Furthermore, knowing the distance between the emitter and the receiver, one can easily calculate the velocity of propagation for all sample at each position. To clearly observe and quantify the gap between the reference and the impacted specimens, trend curves are used.

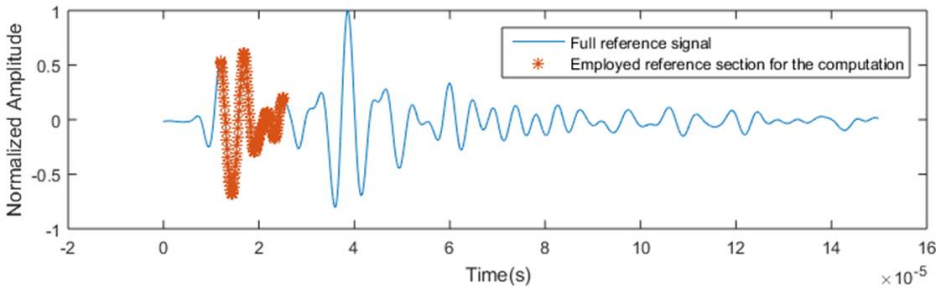

Figure 63: Signal recorded at angle 0° on a reference sample and the part of the signal used in the computations.

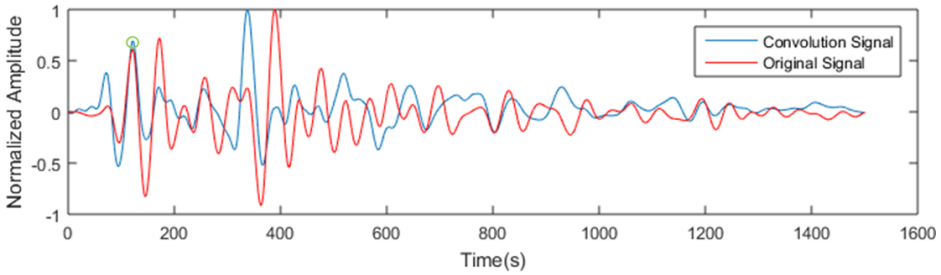

Figure 64: Example of a convolution signal superimposed with an original signal recorded at angle 0° on the reference sample, and the peak of the convolution signal on which the value of the TOF is extracted circled in green.

To have a clear trend of the evolution of the velocity function of the angle of emission/reception, one must select the proper type of approximation curve. For that matter, a special procedure is followed. The previously mentioned software 'Disperse' is used to determine the values of velocity at each emission angle for the first propagating mode. By entering the stiffness matrix of the non-impacted sample obtained by periodic homogenization as discussed in Chapter I, the thickness, the REV, and the emission angle as inputs, one can retrieve the numerical values of the velocity of propagation at each angle for a frequency of 150 KHz (**Figure 65**). It is deduced from the comparison of the experimental values with the numerical values that the propagating mode corresponds to S_0 mode. Finally, a fourth-order polynomial trend curve is found to be the best fit for the numerical values. Consequently, and for the rest of the study, fourth-degree polynomial trend curves are used. The results are then illustrated as velocity profiles function of the angle (emission/reception) as exhibited in **Figure 66** for all the considered samples.

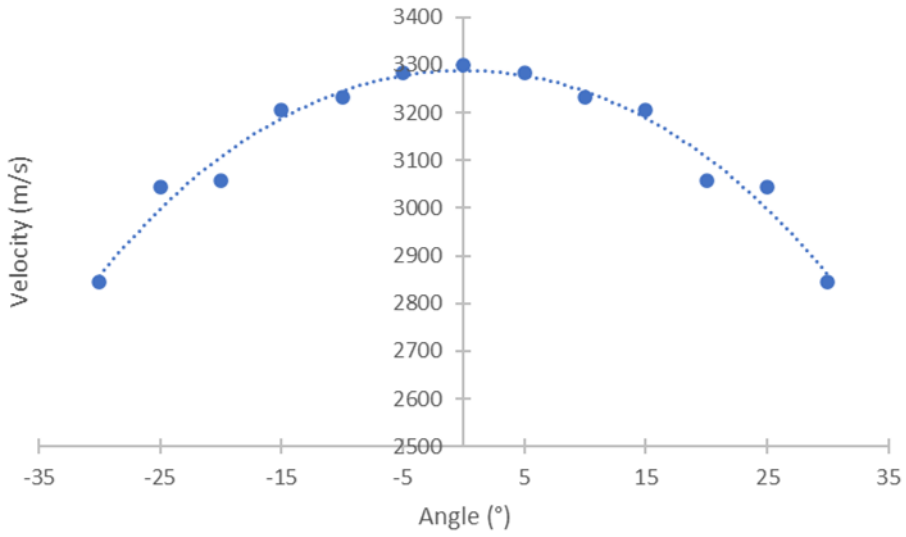

Figure 65: Velocity profile obtained using the software 'Disperse' employing the stiffness matrix obtained by periodic homogenization for a non-damaged sample.

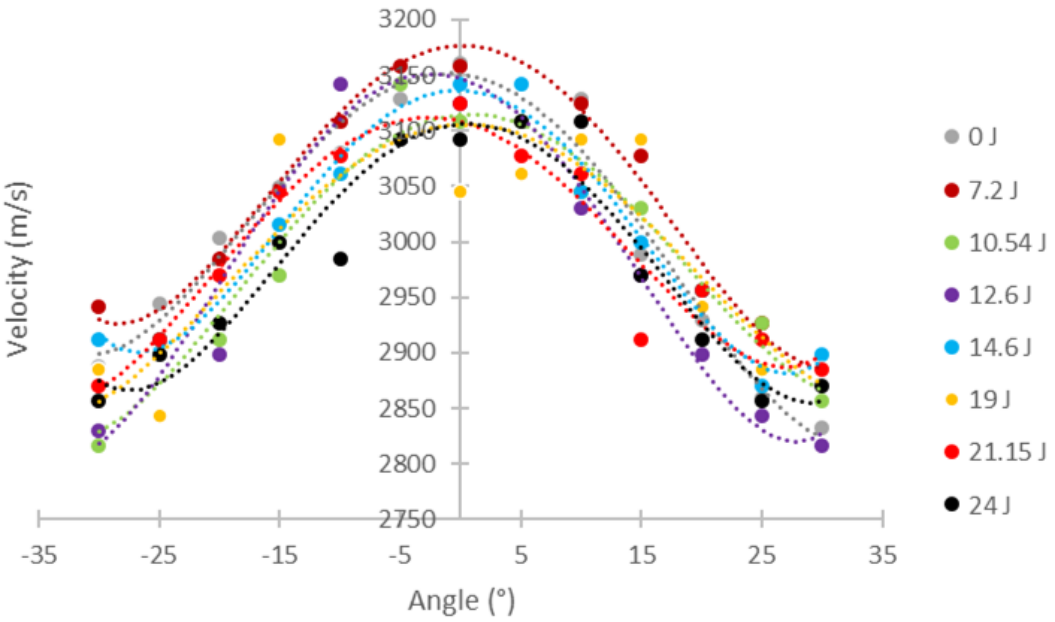

Figure 66: Velocity profiles of each of the considered sample namely, the reference sample and the seven impacted samples loaded at: 7.2 J, 10.54 J, 12.6 J, 14.58 J, 19 J, 21.15 J and 24 J with a fourth-degree polynomial approximation.

Figure 66 shows that a difference between the velocity profiles corresponding to the reference sample and those related to the impacted sample occurs. Indeed, all the velocity profiles are below the velocity profile of the reference sample. This gap is explained by stiffness reduction at early stages of damage creation and its development as the impact energy increases. To clearly quantify the effect of damage on the decrease of the propagation velocity, the calculation of the area under the curve is proposed. Therefore, a damage indicator is suggested.

$$D = 1 - \frac{\mathrm{A_{damaged}}}{\mathrm{A_{ref}}}$$

With $A_{damaged}$ the surface under the velocity profile of a damaged sample and A_{ref} the surface under the velocity profile of the reference sample.

After the calculation of the values of the damage indicator (D) for each sample, one can illustrate the results as shown in **Figure 67**. One can clearly see the increase of the DI with the increase of the impact energy.

Compared to the results previously obtained when measuring the damage indicator based on the permanent indentation measurement, the present damage indicator has proved its efficiency in describing the evolution of damage function of the impact damage.

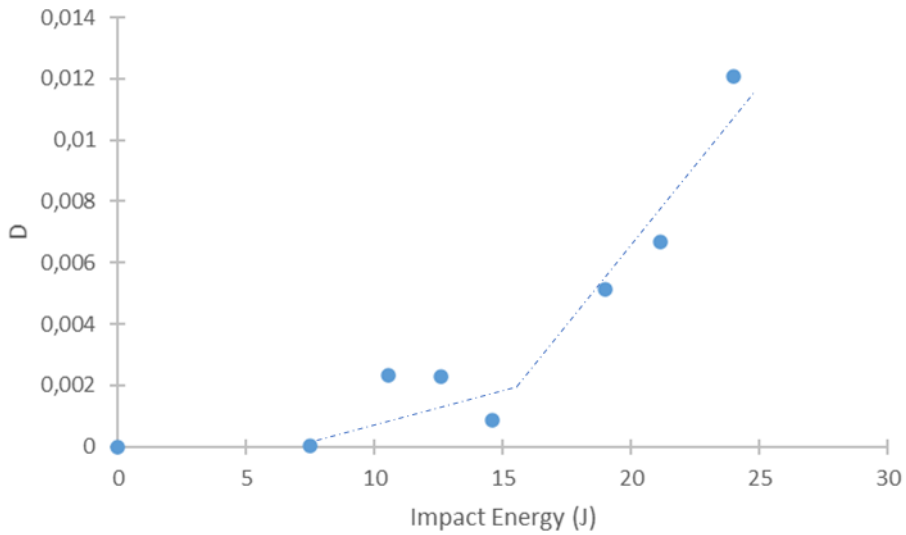

Figure 67: A comparison between the evolution of the damage indicator and the evolution of the values of the permanent indentation function of the impact energy showing the same trend between the two curves.

IV. General overview

This chapter is dedicated to a detailed study of damage resulting from low-velocity impact damage. The focus is drawn towards seven samples impacted at energies of 7.20 J, 10.54 J, 12.6 J, 14.58 J, 19 J, 21.15 J and 24 J. The assessment methodology discussed in the previous sections lead to the following outcomes:

- The mechanical response during impact tests is analyzed and showed a change of response when damage is initiated. Indeed, a gap in the deflection-time curves is noticed between the samples impacted at 7.20 J and the rest of the considered samples. This gap can be related to damage initiation.
- A visual inspection by naked eye have shown that the first damage state appeared as matrix micro-cracking on the non-impacted surface of the sample impacted at 10.54 J. Cracks propagation increases with the increase of impact energy. Indeed, it was found that the cracks diffuse on the surface following the fibers orientation and their length grow as the impact energy raises. Furthermore, a particular aspect is noticed on the sample impacted at higher energies i.e., 21.15 J and 24 J. It is the buckling of the fibers on the impacted side close to the edges of the samples. This phenomenon results from the bending of the sample during the impact event and the non-return to its initial position.

- Permanent indentation (PI) measurements are performed using the ultrasonic scanning method. The obtained values are validated using a more resolved method which is optical profilometry. It has been found that: (1) the values of the depth of the PI increase with the increase of impact energy, and (2) the ultrasound-based method is very efficient in estimating the values of the permanent indentation.
- Through-thickness inspection is carried out using X-ray micro-computed Tomography. The investigation on the 3D reconstructed volume has shown that at low impact energy (7.20 J), no damage is created. As the energy of impact grows, matrix micro-cracking begins to appear (starting from 10.54 J as impact energy). The later propagate into the yarns causing fibre breakage, and between the yarns deteriorating hence the fiber/matrix interface. The debonding between the longitudinal and the transversal yarns create the most penalizing damage that can occur in multilayer composites, i.e., delamination. As the impact energy increases, these damage mechanisms spread into the different layers of the composite.
- To quantify the effect of the impact damage on the integrity of the composite samples, two NDE technics are employed. First, a stiffness reduction estimation method, that uses the velocity of the propagation of Bulk waves in different planes, is employed. The latter has shown that C_{11} and C_{33} are the most affected components when it comes to impact damage. This can be explained by damage propagation patterns observed earlier using mCT influenced by the architecture of the material. A damage indicator is proposed based on the evolution of the values of the components of the three principal planes C_{11} and C_{33}, and can be expressed as follow:

$$\mathrm{DCij} = 1 - \frac{\mathrm{Cji_{damaged}}}{\mathrm{Cij_{ef}}}$$

With $Cij_{damaged}$ the stiffness component of a damaged sample, and Cij_{ref} the stiffness component of a non-damaged sample i.e., reference sample.

The evolution of these damage indicators is illustrated in **Figure 68**. One can see that DC_{11} increases progressively until 14.58 J and then the values stabilize (**Figure 68(a)**). On **Figure 68(b)**, C_{33} behaves differently than C_{11}. In fact, at low energies, i.e., 7.20 J and 10.54 J, the values of C_{33} do not seem to vary. As the energy of impact grows above 10.54 J, DC_{33} grows progressively until reaching its maximum value. The difference in evolution between C_{11} and C_{33} can be explained by the growth of the cracks in the warp and weft direction for C_{11} and through-thickness for C_{33} as the impact energy rises.

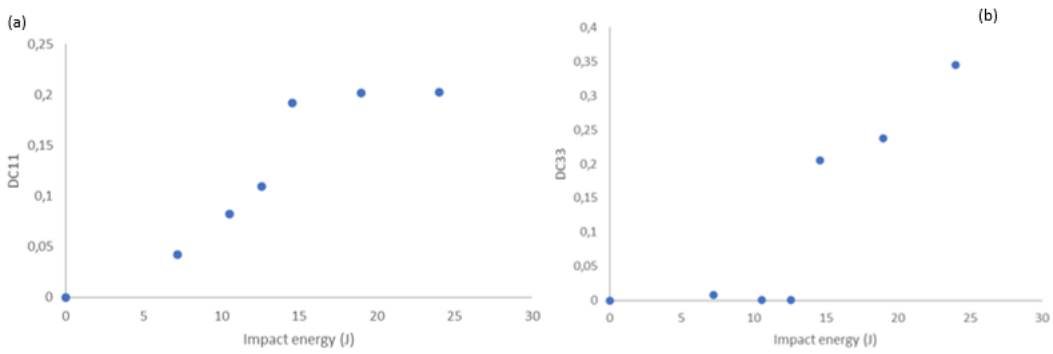

Figure 68: Damage indicators evolution for: (a) C11 component and (b) C33 component.

- By analyzing the surface damage, namely the appearing damage on both impacted and non-impacted surfaces, the through-thickness damage, and the residual properties, one can deduce a link between the absorbed energy, the PI depth, the damage mechanisms and stiffness reduction. Indeed, by quantifying the permanent indentation, one can predict the damage state and foresee the extent of damage propagation through the thickness.
- As a final step of the thorough study of the influence of the low-velocity impact on the response and behavior of the composite, a method based on Lamb wave propagation is proposed. It consists of observing of the changes of the values of the velocity as the anisotropy resulting from the created damage increases. By varying the angles of emission and reception simultaneously, one can establish a velocity profile that is representative of the stiffness evolution as the impact energy rises. The trend of the results obtained using the developed Lamb waves method are compared to the one relative to the evolution of the PI's depth as a function of the impact energy (**Figure 69**). Excellent correlation is found between the two methods, indicating that both damage indicators can be employed differently to predict the overall damage state of the polyamide-based composite samples.

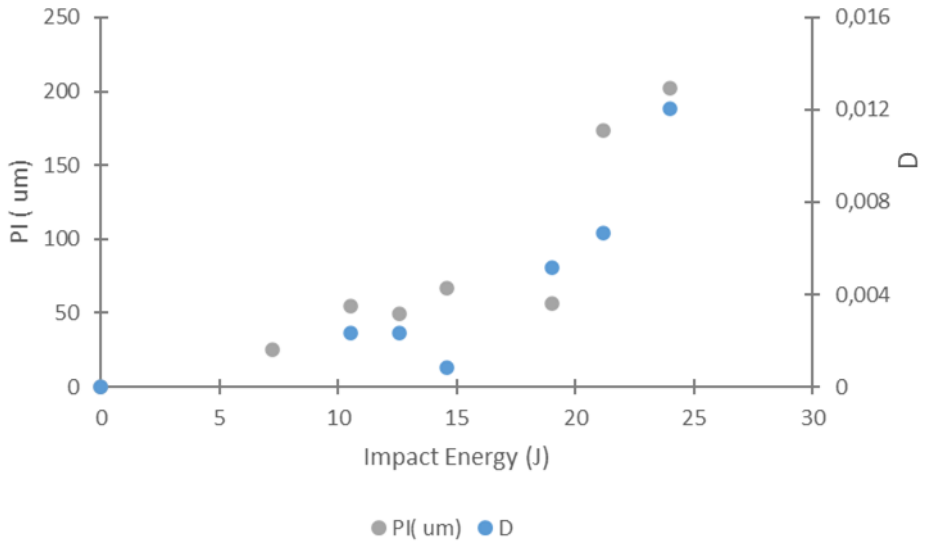

Figure 69: Comparison between the results obtained using both ultrasound-based method and profilometry for the seven samples impacted respectively at energies of: 7.20 J, 10.54 J, 12.6 J, 14.58 J, 19 J, 21.15 J and 24 J.

V. Conclusion

The current chapter presents a qualitative and quantitative characterization of the damage resulting from low-velocity impact on a polyamide-based woven composite employing different NDE techniques. The objective of this study is to provide a comprehensive and reliable characterization of the induced damage using a developed experimental methodology. All the obtained results are linked to different damage indicators that can be used individually. Indeed, it is shown that the PI is a very efficient indicator of the damage state post-impact event. Furthermore, the damage indicator based on Lamb-waves velocity profiles has proven its reliability and one can conclude that the latter can be used alone to reflect the damage condition. The link between the PI and the Lamb-waves based damage indicator establishes the accuracy of the proposed ultrasound-based methodology when applied alone for the investigation of damage in composite materials. Finally, the experimental stiffness matrix components measurement allowed to estimate the effect of the damage on the mechanical properties of the studied composite.

As previously mentioned, the study material is designed to withstand fatigue loading and low-velocity impact. For that matter, the understanding of the damage kinetics resulting from cyclic

loading will be the object of the next chapter. The damage will be assessed using the developed Lamb waves method.

VI. References

Arif, M. (2014). Damage mechanisms in short glass fiber reinforced polyamide-66 under monotonic and fatigue loading: Effect of relative humidity and injection molding induced microstructure. Ecole Nationale Supérieure d'Arts et Métiers.

Audoin, B., Baste, S., & Castagnede, B. (1991). Estimation de l'intervalle de confiance des constantes d'élasticité identifiées à partir des vitesses de propagation ultrasonores.

Baste, S., & El Guerjouma, R. (1989). Mesure de l'endommagement anisotrope d'un composite céramique-céramique par méthode ultrasonore. *Rev. Phys. Appl*, 721–731. https://doi.org/https://doi.org/10.1051/rphysap:01989002407072100

Bouvet, C. (2011). Dommages d'impact sur stratifié composite Dommages d'impact sur stratifié composite Impact damages on composite laminate. https://hal.archives-ouvertes.fr/hal-00597428

Dhakal, H. ., Zhang, Z. Y., Bennett, N., & Reis, P. N. B. (2012). Low-velocity impact response of non-woven hemp fibre reinforced unsaturated polyester composites: Influence of impactor geometry and impact velocity. *Composite Structures*, *94*(9), 2756–2763.

Giurgiutiu, V. (2016). Impact and Acoustic Emission Monitoring for Aerospace Composites SHM. In *Structural Health Monitoring of Aerospace Composites* (pp. 317–394). Elsevier. https://doi.org/10.1016/b978-0-12-409605-9.00009-x

Gliszczynski, A., Kubiak, T., Rozylo, P., Jakubczak, P., & Bieniaś, J. (2019). The response of laminated composite plates and profiles under low-velocity impact load. *Composite Structures*, *207*(August 2018), 1–12. https://doi.org/10.1016/j.compstruct.2018.09.005

Gordon, S., Boukhili, R., & Merah, N. (2014). Impact behavior and finite element prediction of the compression after impact strength of foam/vinylester-glass composite sandwiches. *Journal of Sandwich Structures and Materials*, *16*(5), 551–574. https://doi.org/10.1177/1099636214541575

Hautier, M. (2010). Analyse des réparations des matériaux composites : mise en oeuvre d'un procédé par infiltration et étude du comportement mécanique. Université de Toulouse.

International ASTM. (2020). ASTM D5229 / D5229M-20, Standard Test Method for Moisture Absorption Properties and Equilibrium Conditioning of Polymer Matrix Composite Materials, ASTM International, West Conshohocken, PA, 2020, www.astm.org.

Jiang, F., Guan, Z., Li, Z., & Wang, X. (2021). A method of predicting visual detectability of low-velocity impact damage in composite structures based on logistic regression model. *Chinese Journal of Aeronautics*, *34*(1), 296–308. https://doi.org/10.1016/j.cja.2020.10.006

Malpot, A. (2017). Etude du comportement en fatigue d ' un composite à matrice polyamide renforcée d ' un tissu de fibres de verre pour application automobile. Ecole Nationale Supérieure De Mécanique et d'Aérotechnique.

Marguères, P., & Meraghni, F. (2013). Damage induced anisotropy and stiffness reduction evaluation in composite materials using ultrasonic wave transmission. *Composite Part A: Applied Science and Manufacturing*, *45*, 134–144. https://doi.org/https://doi.org/10.1016/j.compositesa.2012.09.007

Marguères, P., Meraghni, F., & Benzeggagh, M. L. (1999). Determination of stiffness reduction and damage accumulation monitoring in composite materials using ultrasonic techniques. *Sampe Europe International Conference*.

Markham, M. (1970). Measurements of the elastic constants of fibre composite by ultrasonics. *Composites*, *1*(3), 145–149. https://doi.org/doi.org/10.1016/0010-4361(70)90477-5

Miqoi, N., Pomarede, P., Meraghni, F., Declercq, N. F., Guillaumat, L., Le Coz, G., & Delalande, S. (2021). Detection and evaluation of barely visible impact damage in woven glass fabric reinforced polyamide 6.6/6 composite using ultrasonic imaging, X-ray tomography and optical profilometry. *International Journal of Damage Mechanics*, *30*(3), 323–348. https://doi.org/10.1177/1056789520957703

Mustapha, S., Ye, L., Dong, X., & Makki, M. (2016). Evaluation of barely visible indentation damage (BVID) in CF / EP sandwich composites using guided wave signals. *Mechanical Systems and Signal Processing*, *76–77*, 497–517. https://doi.org/10.1016/j.ymssp.2016.01.023

Obeid, H. (2016). Durabilité de composites à matrice thermoplastique sous chargement hygro-mécanique : étude multi-physique et multi-echelle des relations microstructure-propriétés-états mécaniques. Ecole doctorale Sciences pour ingénieur, Géoscience, Architecture (Nantes).

Panaitescu, I., Koch, T., & Archodoulaki, V. M. (2019). Effects of temperature, humidity and automotive fluids exposure on glass fiber/polyurethane composites. *Polymer Composites*, *40*(6), 2357–2367. https://doi.org/10.1002/pc.25094

Pivdiablyk, I., Rozycki, P., Jacquemin, F., Gornet, L., & Auger, S. (2020). Experimental analysis of mechanical performance of glass fibre reinforced polyamide 6 under varying environmental conditions. *Composite Structures*, *245*(February), 112338. https://doi.org/10.1016/j.compstruct.2020.112338

Pomarède, P. (2018). Détection de l'endommagement dans un composite tissé PA66,6/Fibres de verre à l'aide de techniques ultrasonores en vue d'une prédiction de la durabilité de pièces automobiles. ENSAM ParisTech.

Pomarède, P., Meraghni, F., Peltier, L., Delalande, S., & Declercq, N. F. (2018). Damage Evaluation in Woven Glass Reinforced Polyamide 6 . 6 / 6 Composites Using Ultrasound Phase-Shift Analysis and X-ray Tomography. *Journal of Nondestructive Evaluation*, *123*. https://doi.org/10.1007/s10921-018-0467-3

Rokhlin, S. I., & Wang, W. (1989). Ultrasonic evaluation of in plane and out of plane elastic properties of composite materials. *Review of Progress in Quantitative Nondestructive Evaluation*, *8*(B), 1489–1496.

Rokhlin, S. I., & Wang, W. (1992). Double through transmission bulk wave method for ultrasonic phase velocity measurement and determination of elastic constants of composite materials. *Journal of Acoustic Society of America*, *91*(6), 3303–3312.

Serge Abrat. (1998). *Impact on composite structures*. Cambridge: Cambridge university Press.

Zhang, D., Milanovic, N. R., Zhang, Y., Su, F., & Miao, M. (2014). Effects of humidity conditions at fabrication on the interfacial shear strength of flax/unsaturated polyester composites. *Composites Part B: Engineering*, *60*, 186–192. https://doi.org/10.1016/j.compositesb.2013.12.031

Chapter 3: Assessment and analyze of the PA66/6 based composite undergoing to tension-tension fatigue loading

This chapter deals with the investigation of the damage in a polyamide-based composite that could appear within a component during normal operational service. Damage in reinforced polyamides occurs due to operational loads, temperature, and is affected by relative humidity conditions as reported by (Arif et al., 2014; Giurgiutiu, 2016; Pomarède, 2018; Robert & Benaarbia, 2015). Unlike impact damage, which is considered as a result of accidental events causing a sudden decrease of the mechanical properties of the composite, damage due to the operational loading induces a progressive degradation of the latter. The study of damage created by tension-tension fatigue loading will be the focus of this chapter. An optimization of the sample's geometry is achieved to promote the generation of damage in its central area. The Wohler curve characterizing the fatigue response of the material is constructed and discussed for different loading conditions. The identification of the resulting damage mechanisms is carried-out by means of X-ray tomography. The efficiency of the Lamb waves-based method developed in the previous chapter is then tested and assessed on samples subjected to tension-tension fatigue loading. Indeed, the proposed investigation method has proven its ability to detect and to quantify localized and diffused damage caused by accidental impact events. The main objective is to assess the capability of this method to detect diffuse damage resulting from repeated load. For that matter, a comparison is established between the results obtained using the Lamb waves-based method and those achieved by voids content measurements during the X-ray tomography analysis.

I. Optimization of the sample geometry

1. The different geometries of the samples

Different geometries are generally reported in the literature for fatigue tests on composite materials namely: rectangular, constant section dog bone, variable section dog bone (De Baere et al., 2011; De Baere et al., 2011; Eliasson et al., 2019; Malpot, 2017). In the rest of the study, the constant section dog bone geometry will be referred to as dumbbell and the variable section dog bone as dog bone.

To choose one of these geometries, certain requirements should be respected. Indeed, in this work, the aim of the fatigue tests is to create damage in the center of the sample that will be investigated in further sections using non-destructive testing methods. Consequently, preliminary monotonic tensile tests are carried to localize the failure area, decide which of the commonly used geometries is suitable for the intended fatigue tests, and finally identify the ultimate tensile strength (σ_{UTS}) for each geometry.

The length of the samples is the same as the length of impact samples (150 mm). Indeed, in the next chapter, a comparison between the residual properties of impacted samples and the samples loaded in fatigue will be established and discussed. The width of all samples is chosen as function of the size of the material representative volume elements (RVE). Moreover, it is important to consider at least two RVEs to have an accurate representation of the behavior of the material during the tests. For this material, and as measured in the works of Pomarède (Pomarède, 2018), the adopted RVE is a square of 16 mm with a thickness of 1.53 mm.

The dimensions of the rectangular samples are set to 150 mm x 45 mm (**Figure 70**). The chosen width enables to have almost three RVEs that avoids unnecessary deformation localization.

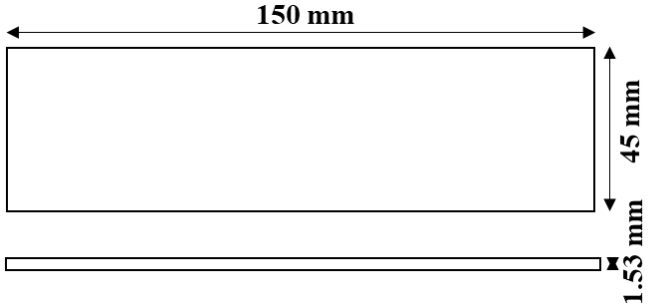

Figure 70: Dimensions of the employed rectangular samples for the fatigue and tensile tests.

Dumbbell samples are being used in several fatigue of multilayers composites studies (Ferreira, Costa, & Reis, 1999; Ferreira et al., 1999; Franco et al., 2008). In the works of Ferreira et al. (Ferreira, Costa, & Reis, 1999), it is pointed out that the failure of the specimen happens at the end of the width change zone. This assumption will be corroborated by a tensile test. Dimensions of the samples employed in this study are given in **Figure 71**.

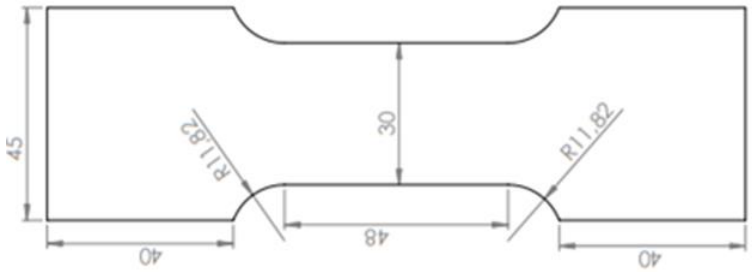

Figure 71: Dimensions of the dumbbell sample that will be destined for tensile and fatigue tests.

The dog bone geometry has been studied by De Baere et al. (De Baere, Van Paepegem, Hochard, et al., 2011) . The highlight of this geometry is that the rupture occurs in the useful zone of the sample. Indeed, the slight curvature in the useful area allows the stress concentration coefficient in the center to be higher than that of the area positioned in the jaws.

In this study a geometry inspired from that proposed by De Baere et al. (De Baere, Van Paepegem, Hochard, et al., 2011) is considered. The geometry proposed by De Baere is presented in **Figure 72**. The radius of curvature (R) is given by the following equation:

$$R = \frac{(\frac{S-1}{S})^2 b^2 + l^2}{4b(\frac{S-1}{S})}$$

With:

- S: stress concentration factor at the heel/sample boundary.
- b: width of the head of the specimen.
- l: length of the gauge zone of the sample.

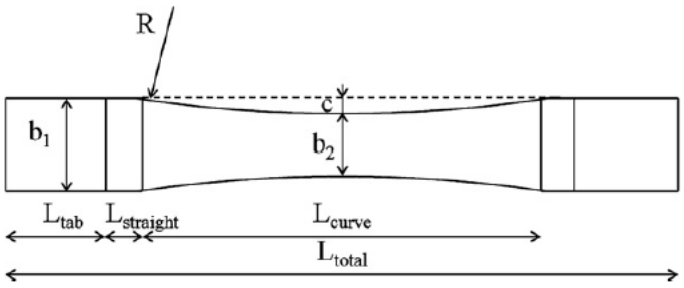

Figure 72: Dog bone geometry proposed in the works of De Baere et al.

In the present work, the previous dog bone geometry has been modified by withdrawing the tapered tabs as that proposed by the authors (De Baere, Van Paepegem, Hochard, et al., 2011). Details about the dimensions of this geometry is given in **Figure 73.** The stress concentration coefficient is set to 1.28 and resulted in a radius curvature value of 126,90 mm. The latter is not tapered and ensures a minimum width of 35 mm of the gauge zone which allows to have a minimum of two RVEs in the center of the specimen.

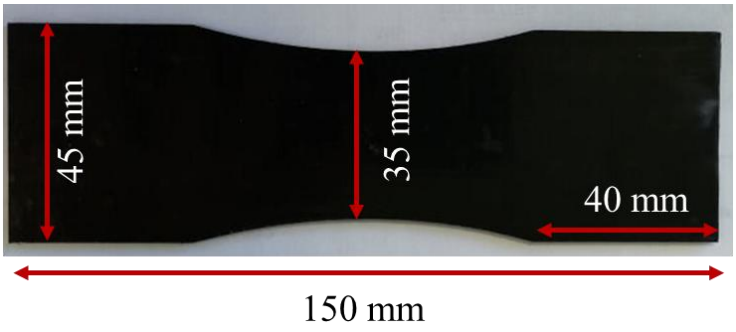

Figure 73: Dimension of the modified dog bone samples tested in the study.

It should be mentioned that for all geometries, and for comparison reasons that will be detailed in the next chapter, a maximum length is set to 150 mm and the maximum width (width in the jaws) is set to 45 mm.

Preliminary tests (tensile and tension-tension fatigue tests) are carried-out beforehand to choose the geometry that meets the requirements.

2. Tensile tests

Samples of each geometry are prepared cut using hyperbaric water jet cutting. They are then loaded in monotonic tensile tests until failure to identify the area of the final rupture. No prior RH conditioning is considered at the stage of preliminary testing. Therefore, the sample are loaded until failure in the as received conditions in terms of RH. The displacement controlled tensile tests are performed in the direction of the longitudinal fibers on specimens oriented 0°/90°. A Zwick Z50 kN machine is employed with a cross-head speed of 1mm/min. It should be mentioned that for all tensile tests of this section, the same machine and parameters are employed for the three geometries.

The experimental findings show that:

- For dumbbell samples, failure occurs in the zones of the section change i.e., the jaws area as a consequence of the Poisson's ratio effect due to stress concentration (**Figure 74(a)).**
- For rectangular samples, the final breakage appears in the center (**Figure 74(b)).**
- For the dog bone samples, failure take place in the zone with the narrow section (center of the samples) (**Figure 74(c)).**

Consequently, and according to the obtained qualitative results, only the dog bone and the rectangular geometries will be tested in tension-tension fatigue for geometry validation.

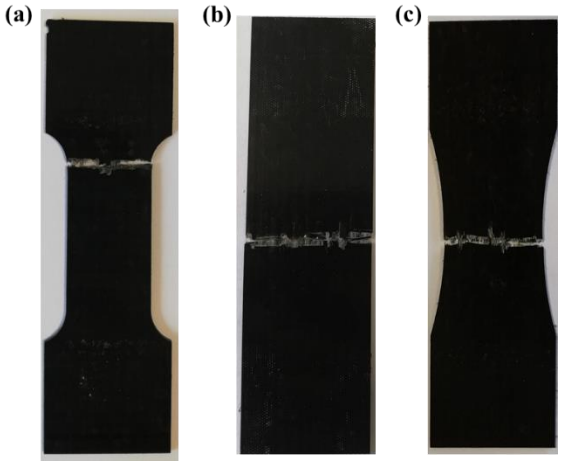

Figure 74: Sample post tensile tests until failure showing the area of the final rupture for: (a) dumbbell geometry, (b) rectangular geometry, and (c) dog bone geometry.

3. Fatigue tests

Fatigue tests are performed using a hydraulic uniaxial machine of the brand MTS Landmark i.e, MTS Hydraulic wedge Grip. This machine is equipped with a load cell of 100 kN as a maximum load capacity and can reach a maximum loading frequency of 100 kHz. The samples are clamped using flat hydraulic serrated (pyramid) jaws of 45 mm width. The acquired and recorded mechanical data related to the fatigue tests are the displacement of the lower jaw, the force, as a function of the time of the test as well as the number of cycles. An infrared camera is used to measure the temperature field variation over the sample's area of interest. The main idea is to identify the rupture zone using the temperature increase that occur with the creation of damage. The experimental set-up is detailed in **Figure 75.**

Two samples of the rectangular and dog bone geometries are loaded until failure at two maximum stress levels namely 80% and 60% σ_{UTS} at a frequency of loading of 1 Hz. The σ_{UTS} values were previously determined using the quasi-static monotonic tensile tests for each geometry. The main reason of these tests is to check that the final failure appears in the center of the sample as found during the monotonic tensile tests leading hence to the validation of the chosen geometries.

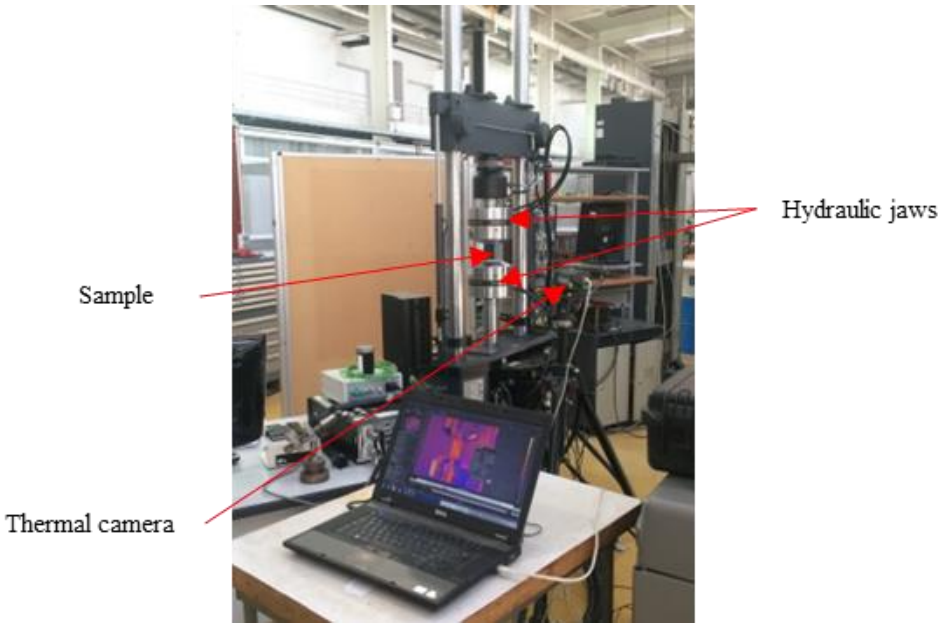

Figure 75: Experimental fatigue tests set-up showing the used MTS hydraulic test machine, the thermal infra-red camera, and the sample positioned between the two hydraulic jaws.

The experimental results of the fatigue test until failure show that the rectangular samples exhibit a final fracture in zone close to the jaws unlike monotonic tensile tests where failure occurs in the center of the specimen.

In the case of dog bone samples, failure happens in the central area as found in the quasi-static tests. **Figure 76** exhibits samples of both geometries loaded in fatigue until failure showing the area of rupture.

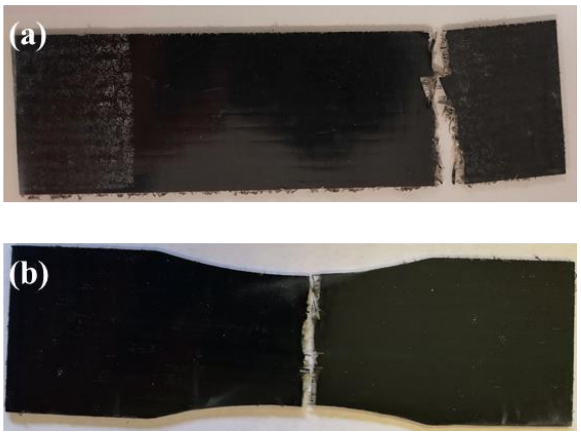

Figure 76: Observation of the final failure zone post-fatigue tests for: (a) the rectangular geometry showing the final rupture close to the jaw area and (b) dog bone samples breaking in the center of the sample.

Considering all the qualitative experimental findings, the dog bone geometry will be considered for the rest of the study.

II. Mechanical tests on the chosen geometry

1. Monotonic tensile tests

1.1. Experimental set-up

In this section, the quasi-static monotonic tests are aimed at identifying the mechanical characteristics of the studied material using the chosen geometry. Indeed, to perform the fatigue tests, certain material's properties, such as $\sigma_{UTS,}$ have to be characterized priorly. To this end, tensile tests are carried out according to the ISO 5893 standards by means of the same tensile

machine noted hereafter ‘Zwick Z50 kN’ employed in section II.2. The tensile tests are displacement controlled with a crosshead speed of 1mm/min. The sample displacement is measured using several devices. Indeed, the displacement is assessed employing various techniques:

- Laser displacement transducer
- Digital Image Correlation technique (DIC)
- Mechanical data given by the tensile machine (crosshead displacement)

The experimental set-up showing the numerous sensors is depicted in **Figure 77**. A black and white speckle is put on one of the sample’s surfaces facing the CCD camera of the brand ‘Limess’ employed for DIC technique. The opposite surface of the sample is facing the laser sensor. It should be mentioned that for the rest of the study, samples are previously kept in a humidity chamber until the latter reach the target in terms of moisture corresponding to 50% of relative humidity. The storage conditions and procedure are the same as those detailed in Chapter II for the impacted samples. The latter went through a drying process followed by a conditioning procedure in two steps: first a stage of accelerated water absorption at 65% RH and a temperature of 50° until reaching 2.7% mass gain, and then, a stabilization step at 50% RH to reach a uniform distribution of the water through the thickness of the sample. Since the polyamide matrix is known to be sensitive to humidity (Arif et al., 2014; Benaarbia et al., 2014; Malpot et al., 2015; Robert & Benaarbia, 2015), and given the conventional use, it is recommended to perform mechanical tests on samples with 50% relative humidity conditions. All the samples are oriented at 0°, i.e., the load is the direction of the longitudinal fibers.

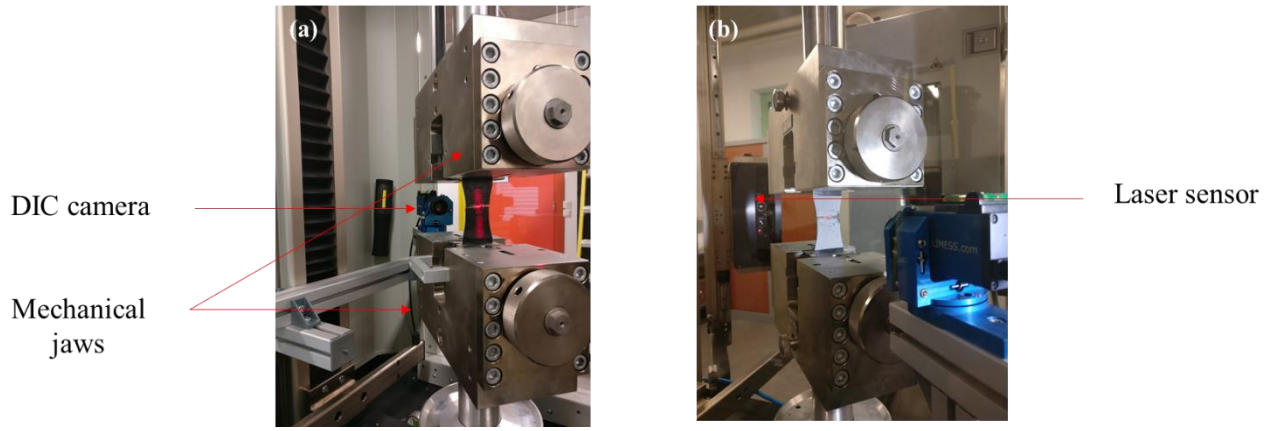

Figure 77: The used experimental set-up to realize the tensile tests showing the DIC camera, the laser sensor and the sample clipped in two mechanical jaws.

1.2. Experimental results

The data acquisition allows to obtain the force applied on the specimen, the corresponding displacement, of the crosshead, the laser sensor measured as well as the displacement field measured by DIC. The analysis of the DIC data with the 'Vic2D' software allows to obtain the evolution of the strain fields during the test and also the global average strain in the loading direction.

Since independent sensors are used during the acquisition, having each its own sampling frequency, and starting point, it is necessary to assign them a common time base. An Excel macro has been used to reconstruct all data on a common time base. The displacement measured using the crosshead machine and the laser sensor are divided by the gauge length to obtain the corresponding strain evolution. The stress-strain curves obtained by the three sensors are presented in **Figure 78.**

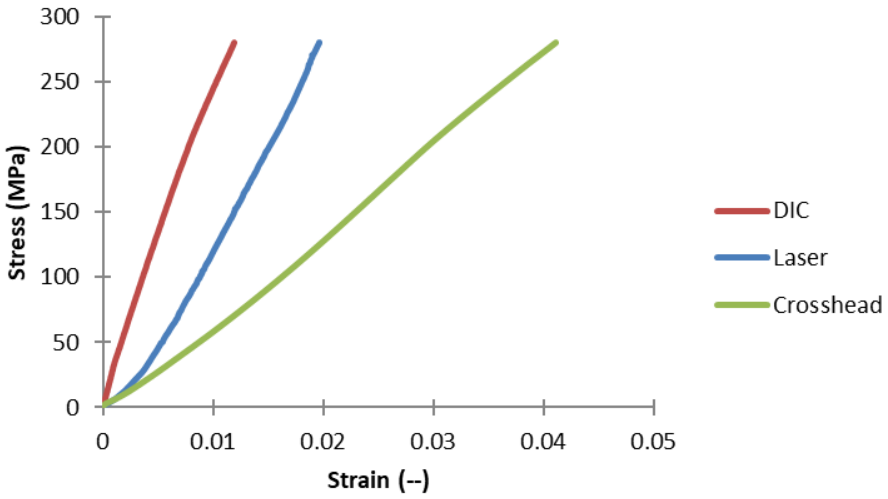

Figure 78: Stress/Strain curves for one of the tested samples with the three considered displacement sensors: DIC, laser and crosshead.

One can clearly distinguish a discrepancy between the strain estimated from the DIC, laser sensor and that measured from the machine displacements. The maximum strain for the data relative to the crosshead is around 4% whereas for the DIC and laser it is less than 2%. The effect of the machine compliance due to the clearance of the fixtures, often badly compensated, reduces the accuracy of the displacement measurement. Indeed, the crosshead data also includes the response of the grips fixture and the related clearance. Consequently, it is preferable to use

the DIC and the laser sensor as reliable sources of data since they are contactless and account for the response of the material.

As expected, the global tensile test response of the material is quasi-linear behavior when the material is loaded along the fiber's axis. The failure area is located in the center of the sample in accordance with the results obtained in previous sections. The average ultimate tensile strength (σ_{UTS}) is of 333 MPa. It is worth mentioning that this value will be kept and considered as a reference of σ_{UTS} in the rest of the chapter.

2. Fatigue tests until failure

2.1. Wöhler curve

Fatigue tests until failure are performed to build the Wöhler curve of the PA66/6 reinforced composite pre-conditioned to 50% RH. As previously mentioned, the objective of the fatigue test is to introduce a different kind of damage that spread in a larger section unlike impact damage that is considered as localized damage. For that matter, knowing the properties of the studied material is necessary.

Composite materials have good cyclic tensile performance compared to metallic materials (Jollivet et al., 2013). The key parameter indicating the fatigue performance of a material is the ratio of the endurance limit to the ultimate tensile strength (σ_D/σ_{UTS}). In the case of composite materials subjected to tensile cyclic loading, this ratio should range between 0.3 and 0.9 (Vasconcellos, 2013). For that matter, four levels of loading levels are chosen: 60%, 45%, 35% and 25% σ_{UTS}. Three specimens are loaded at each level at a frequency of 3 Hz and a loading ratio between R= 0.2. It is important to mention that for a sake of repeatability, a minimum of three samples are tested for each loading configuration enabling an estimation of the Wohler curve. The same experimental set-up previously used in the preliminary geometry validation tests is employed in the rest of this study. To reduce experimental error, a custom-made shim (**Figure 79**) is utilized to ensure that the sample is always positioned in the same way throughout the experimental campaign. This shim (spacer) is made of the same material in order to have the same thickness as the samples being tested.

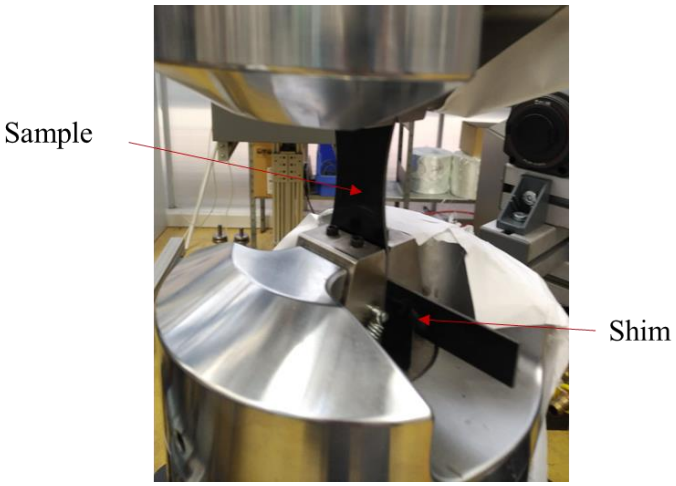

Figure 79: Image of the sample in place and the shim ensuring the same positioning for all samples throughout the fatigue test campaign.

All samples have exhibited a straight and clean rupture. The direction of the area of the final failure is found to be unaffected by the level of loading. Samples loaded at $\sigma = 0.25\ \sigma_{UTS}$ have a lifespan higher than 10^6 cycles. Furthermore, a study on a similar composite (Malpot, 2017) have shown that under 30% σ_{UTS}, corresponding to the knee-point, no damage can be detected through microscopic observations. Hence, for rest of the study, cyclic loadings at only three levels of stress will be carried out, i.e., 35%, 45% and 60% σ_{UTS}.

The results presented in **Figure 80** show a scattering in the value of the number of cycles to failure. Indeed, as we reduce the level of the maximum loadings stress (35% σ_{UTS}), important scattering in terms of lifetime (number of cycles to failure) is observed. It is known that a significant dispersion can occur in a S-N curve of a material, notably for long lifetimes.

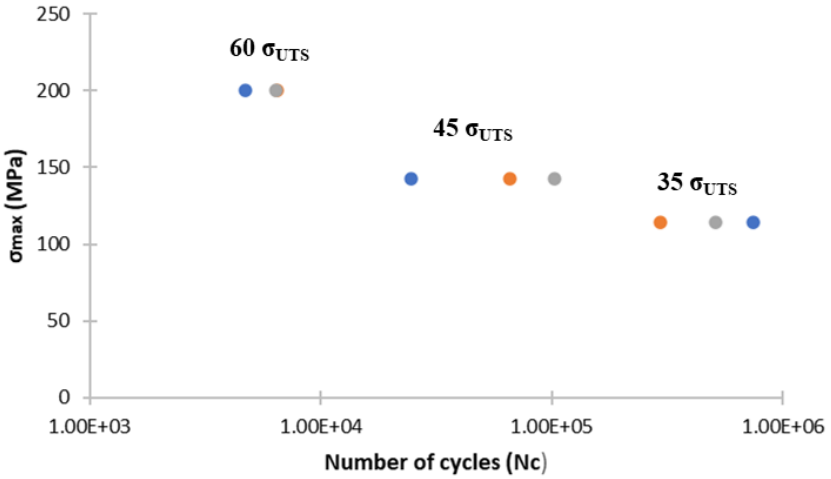

Figure 80: Wöhler curve of the polyamide 66/6 reinforced with woven glass fibers loaded at R=0.2 and f= 3Hz and pre-conditioned at 50% RH.

As indicated in section 3.2 of Chapter I, Basquin model, expressed by the following equation, is applied to describe the central part of the S-N curve in a log-log diagram.

$$\log(N) = \log(C) - m * \log(\sigma)$$

C and m parameters are determined by linear regression in the log-log diagram, N the number of cycles and σ the stress load (1/2 amplitude).

The obtained results are represented in a logarithmic axis in **Figure 81**.

The linear representation of log(N)-log(σ) enables to obtain a mean value of the number of cycles to failure corresponding to each tested loading level.

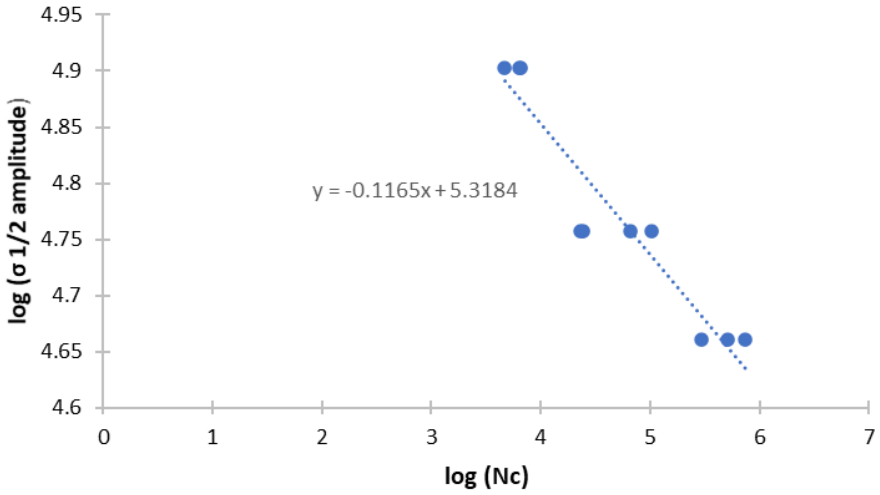

Figure 81: Basquin illustration of Wöhler curve in a logarithmic scale enabling to have a linear representation of the loading stress function of the number of cycles to failure of the tested polyamide 66/6 reinforced glass fibers at humidity conditions of 50% RH.

2.2. Mechanical data analysis

During the fatigue tests, the load force and displacement of the moving jaw are recorded. The load force as a function of time data is processed to determine the apparent Young's modulus throughout the mechanical tests. The applied stress is directly deduced by dividing the measured force per the sample's cross-section. The obtained stress-time curve exhibits two parts, the first part corresponds to a quasi-static pre-loading, and the second part consists of the cyclic loading (**Figure 82**). The latter is triggered by reaching the value of the mean-force calculated using the fatigue loading ratio ($R=F_{min}/F_{max} = \sigma_{min}/\sigma_{max}$, $\sigma_{mean}= (\sigma_{max}+ \sigma_{min})/2$ and $F_{moy}= (F_{max}+ F_{min})/2$). The objective is to estimate the stiffness reduction between the beginning of the load and its

end, just before the complete failure of the specimen. **Figure 83** shows an example of the evolution of the Young's modulus with respect to number of fatigue cycles for two samples loaded at 70% σ_{UTS}. It should be mentioned that in this section, it is considered that no damage is introduced in the quasi-static part of the test. Indeed, the latter is considered as an initiation phase enabling to reach the mean load value (F_{moy}).

One can notice that the material does not exhibit any stiffness reduction until a sudden decrease corresponding to the final failure. The values of the Young's modulus are stable throughout the cycling and decreases of 3 to 4 GPa just before to the final failure. It corresponds to a sudden stiffness reduction ranging between 13 to 19%. Indeed, for the studied composite material, no progressive decrease of the stiffness during the fatigue tests is observed.

However, the final rupture of the composite did not occur at the same number of cycles for the two of the tested specimens. The difference in the lifetime of the two samples loaded at the same conditions is due to the variability of the microstructure resulting from the manufacturing process. In addition, the fact that the samples are not identical (samples cut from different areas of the composite plates) can also explain this discrepancy (Karaouni, 2001; Liang, 2012).

As a conclusion, and for this woven fabric reinforced thermoplastic composite, the stiffness reduction is not an appropriate damage indicator since it occurs just before the total failure of the specimen.

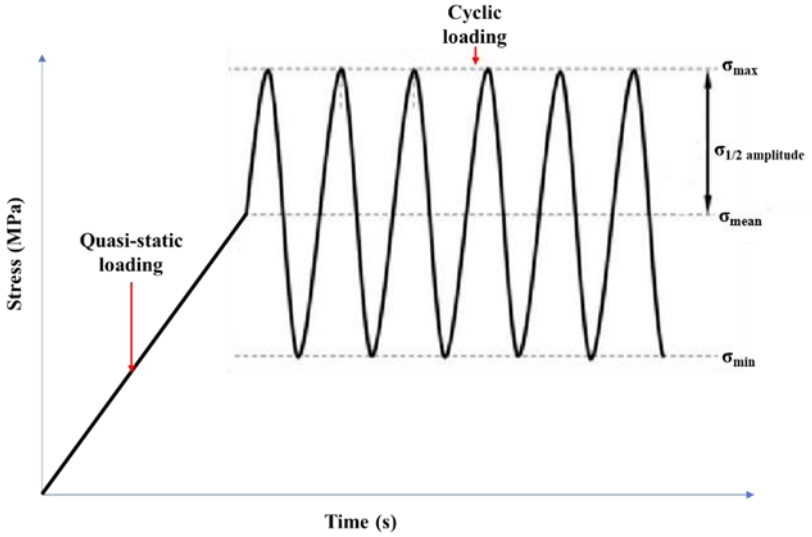

Figure 82: Illustration of the fatigue test showing the two parts of the test: a quasi-static part until reaching the mean value triggering the cycling process.

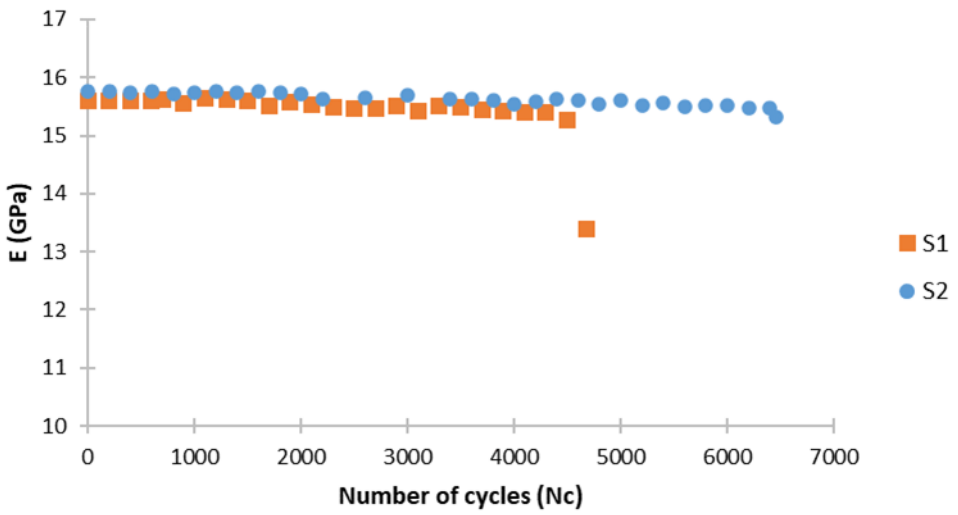

Figure 83: Evolution of the modulus during fatigue tests with σ = 60% σ_{UTS} until failure showing the stabilization of the values until the cycle before the final failure.

3. Interrupted fatigue tests

Interrupted fatigue tests are performed to initiate and propagate the damage mechanisms in the studied composite. Knowing that the damage generated by the cyclic loading remains complex in terms of accumulation, its assessment using a resolved detection technique is of high importance. Indeed, it exhibits a diffuse distribution in all the section of the sample. The objective of this section is to validate the Lamb wave method that has proven its efficiency in detecting localized impact damage in Chapter II. The tested composite samples are loaded at three different stages of their lifespans, and at three levels (proportion) of the static ultimate tensile strength, respectively. So, nine combinations of the loading parameters are achieved and are summarized **Table 6**. A total of twenty-seven samples are tested, i.e., three specimens per combination of loading parameters.

Table 6: Nine combinations of parameters used for interrupted fatigue tests on samples pre-conditioned to 50% RH.

Loading level	**35% σ_{UTS}**			**45% σ_{UTS}**			**60% σ_{UTS}**		
Number of cycles (%)	50%	60%	70%	50%	60%	70%	50%	60%	70%
Number of cycles	222061	266473	310885	33015	39618	46221	1851	2222	2592

The Young's modulus relative to the first (E_0) and the last cycles (E) of the loadings are evaluated. To quantify the damage resulting from the fatigue tests, the results are represented as the ratio (D) of E to E_0, function of the number of cycles.

Figure 84(a), Figure 84(b) and **Figure 84(c)** depict the evolution of damage function of the number of cycles of loading for the three sets of samples loaded at σ_{max} = 60%, 45%, 35% σ_{UTS} respectively.

The experimental findings do not exhibit a clear trend. In fact, the present results come to confirm the scattering observed in the previous section during the fatigue tests until failure.

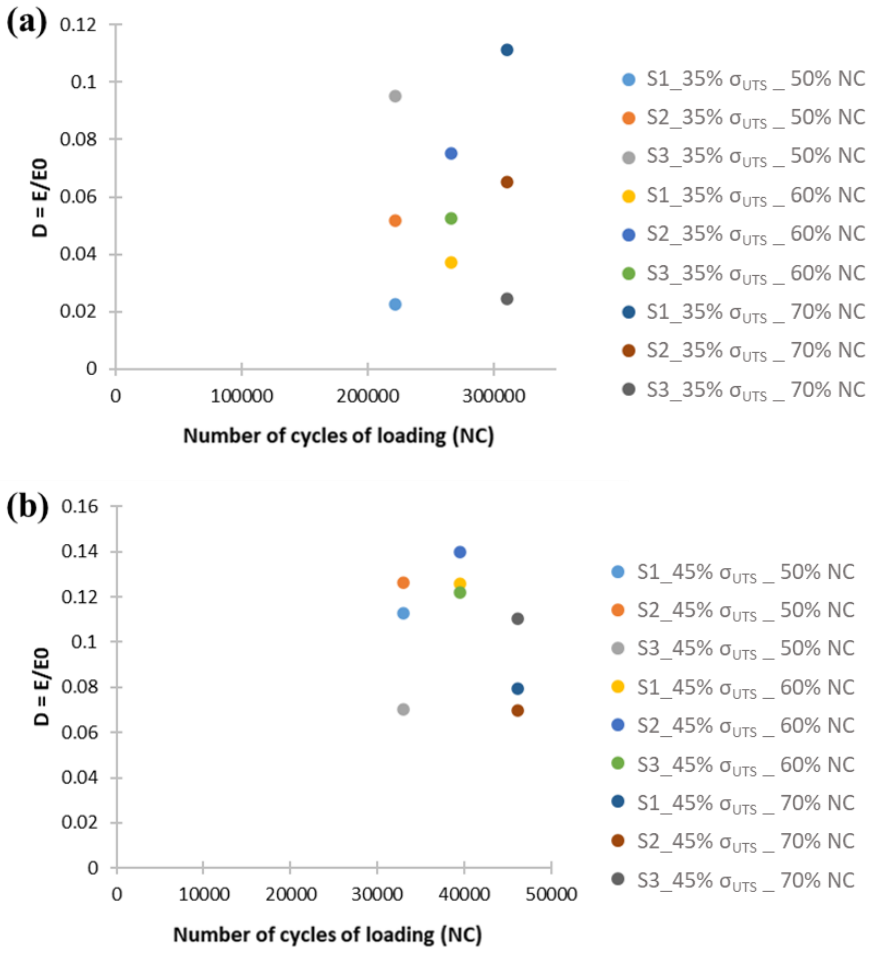

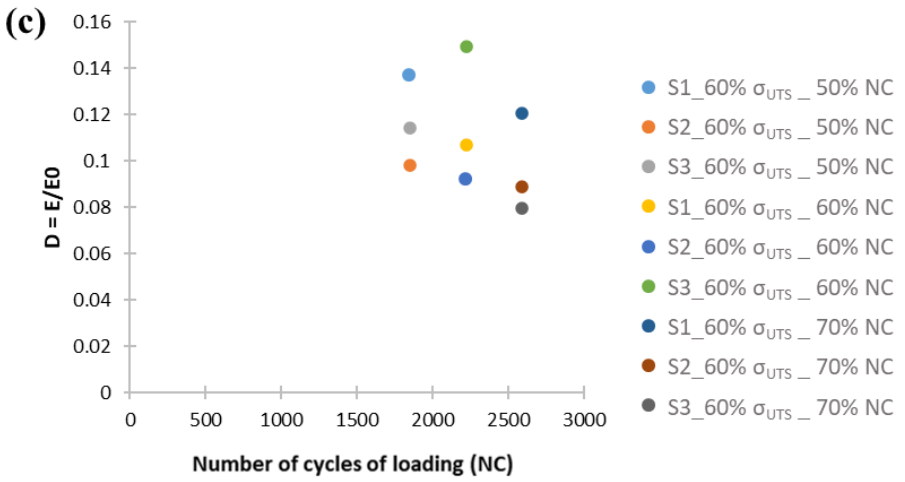

Figure 84: Variation of damage (D) calculated from the mechanical data function of the loading conditions: (a) 35% σ_{UTS}, (b) 45% σ_{UTS} and (c) 60% σ_{UTS}. Scattering of the results is observed in the three figures. It can be explained by the variability of the fatigue tests and the variability of the material's microstructure caused by the thermo-compression process.

3.1. Fatigue damage investigation using Lamb waves

Lamb waves investigation is conducted to assess the damage state of the samples post-fatigue. The experimental protocol for the detection is that presented in Chapter II. The only difference lies in the range of investigated angles. Indeed, since the section is smaller than the one of the impact samples, the evaluated area is comparatively more reduced, and accordingly, the number of the measurement points is reduced. Nevertheless, an angle range varying between ± 15° is considered with an increment of 5°. Consequently, seven angles have been exploited to build the velocity profile of the fatigue samples, which are divided into three sets as a function of the loading level. A non-damaged sample with the same geometry is considered as a reference sample. During the lamb-waves investigation, each set of samples is tested individually with the reference sample. Hence, each set of sample has its own reference data recorded in the same testing conditions. Having the same testing conditions (the pressure applied from transducers on the material's surface and the positioning of the sample) between the damaged samples and the reference sample reduces the occurrence of experimental errors.

The same post-processing script employed in Chapter II, is applied and the obtained results in terms of velocity profiles for each tested sample are reported in **Figure 85.**

One can easily notice a difference between the reference sample and the loaded samples.

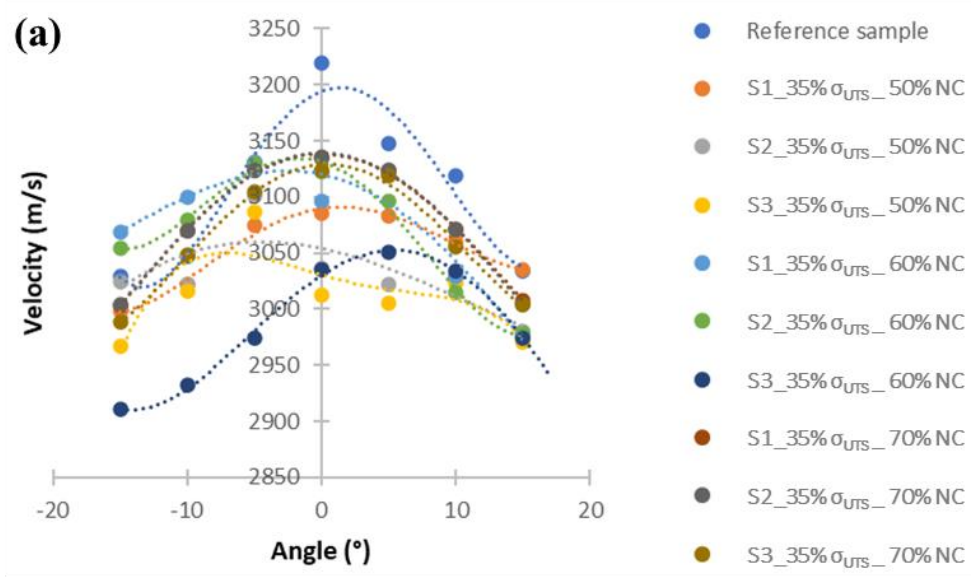
(a)
Velocity (m/s)
3250
3200
3150
3100
3050
3000
2950
2900
2850
-20
-10
0
10
20
Angle (°)
Reference sample
S1_35% σUTS_ 50% NC
S2_35% σUTS_ 50% NC
S3_35% σUTS_ 50% NC
S1_35% σUTS_ 60% NC
S2_35% σUTS_ 60% NC
S3_35% σUTS_ 60% NC
S1_35% σUTS_ 70% NC
S2_35% σUTS_ 70% NC
S3_35% σUTS_ 70% NC

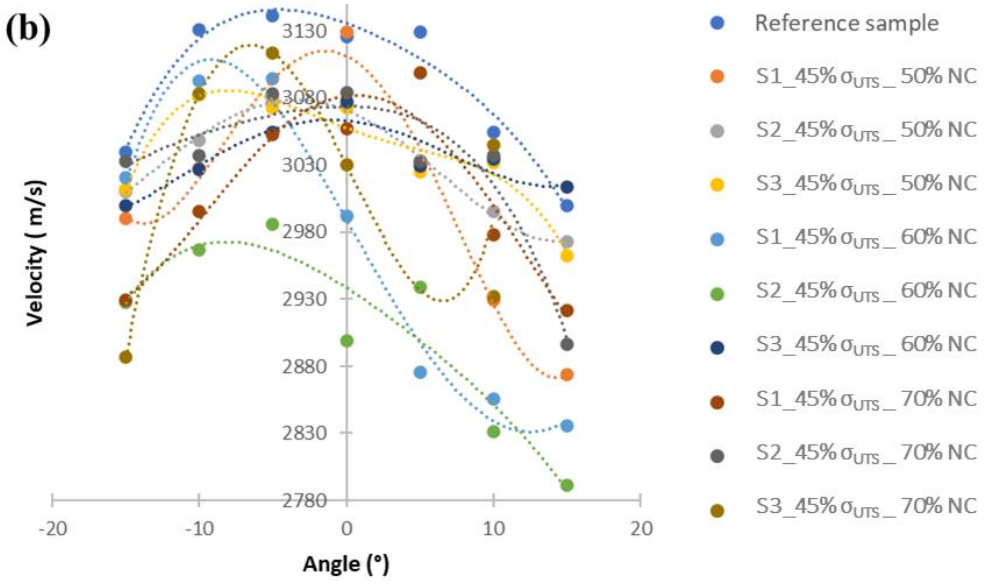
(b)
Velocity (m/s)
3130
3080
3030
2980
2930
2880
2830
2780
-20
-10
0
10
20
Angle (°)
Reference sample
S1_45% σUTS_ 50% NC
S2_45% σUTS_ 50% NC
S3_45% σUTS_ 50% NC
S1_45% σUTS_ 60% NC
S2_45% σUTS_ 60% NC
S3_45% σUTS_ 60% NC
S1_45% σUTS_ 70% NC
S2_45% σUTS_ 70% NC
S3_45% σUTS_ 70% NC

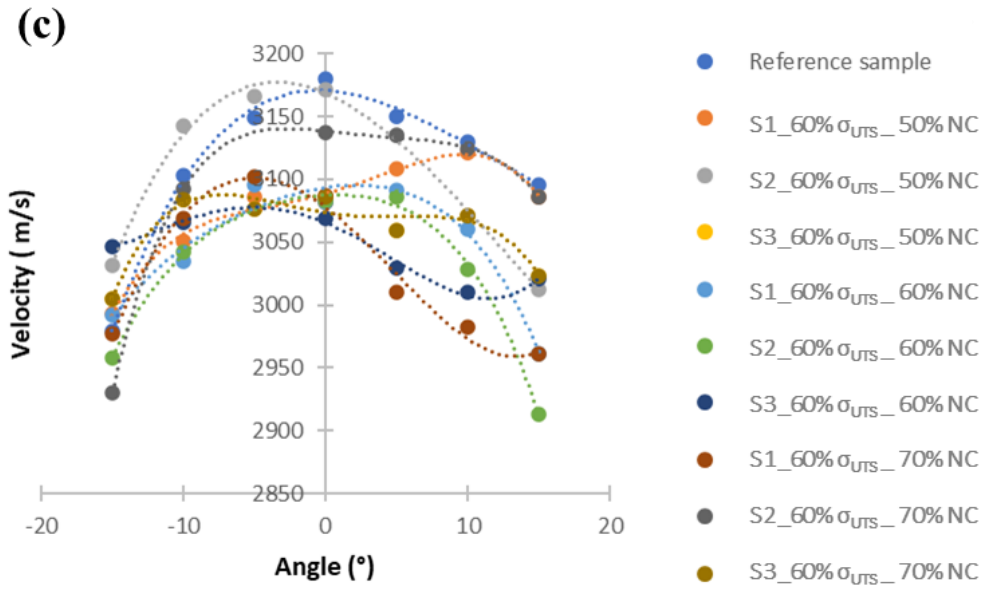

Figure 85: Velocity profiles retrieved using the proposed Lamb waves propagation method on samples subjected to fatigue loading at different levels of loadings: (a) the nine samples loaded at 35% σ_{UTS} and 50%, 60% ,and 70% of number of the cycles to rupture, (b) the nine samples loaded at (45% σ_{UTS} and 50%, 60% ,and 70% of number of the cycles to rupture, and (c) a) the nine samples loaded at 60% σ_{UTS} and 50%, 60% ,and 70% of number of the cycles to rupture (refer to Table 6 for the real numbers of cycles for each set of load).

The following step consists in computing an estimation of the damage indicator for the twenty-seven considered samples. The same computation procedure as that detailed in Chapter II is adopted. To quantify the difference between profiles corresponding to the non-damaged sample and those of loaded samples, the surface area under the velocity profiles is calculated. The damage is estimated using the following equation:

$$D = 1 - \frac{A_{damaged}}{A_{ref}}$$

With $A_{damaged}$ the surface under the velocity profile of a damaged sample and A_{ref} the surface under the velocity profile of the reference sample.

It should be noted that the comparison is performed between the values of the damage indicator corresponding to each set individually. Knowing that Lamb waves are sensitive to test conditions, temperature for instance, no comparison between the three sets will take place since the acquisitions are not realized at the same time.

Values of the damage indicators corresponding to each set of samples are presented in **Figure 86.**

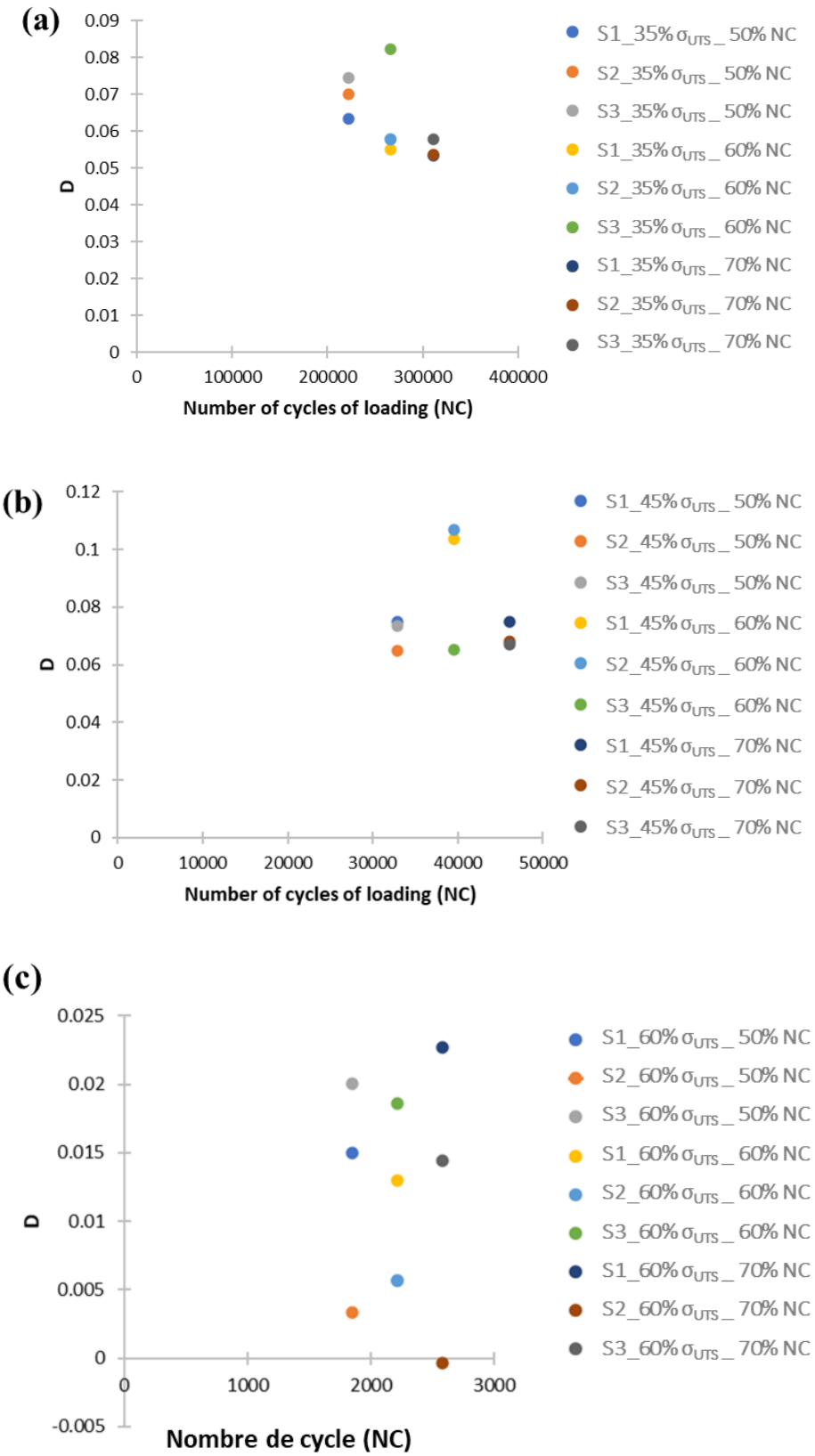

Figure 86: Values of the proposed damage indicator calculated from the surface under the velocity profiles for the three sets of samples: a) the nine samples loaded at 35% σ_{UTS} and 50%, 60% and 70% of number of the cycles to rupture, (b) the nine samples loaded at (45% σ_{UTS} and 50%, 60% ,and 70% of number of the cycles to rupture, and (c) a) the nine samples loaded at 60% σ_{UTS} and 50%, 60% ,and 70% of number of the cycles to rupture (refer to Table 6 for the real numbers of cycles for each set of load).

A clear difference between the damaged samples and the reference sample is noticed confirming hence the efficiency of the damage indicator based on the Lamb-waves investigation to discriminate between damaged and non-damaged specimens. Indeed, the first step in the development of a NDT technique is the ability to differentiate damaged from undamaged samples.

However, one can easily see that the results do not exhibit a clear trend. A gradual increase in the value of the damage indicator is expected with the increase of the number of loading cycles. However, a scattering of the values of the damage indicator is observed. Different values are obtained for the specimens loaded under the same conditions. Several parameters could be the cause of the scattering of the obtained experimental results. In fact, besides the commonly admitted scattering induced by fatigue loading particularly for composite materials, it is worth mentioning that the specimens were not cut from the same area of the composite plates. Indeed, the thermo-compression process can induce some variabilities in terms of microstructure. Even if the number of REVs considered is the same each time, the specimens are not completely strictly identical at the microscopic scale. Indeed, the strength of a specimen with a complete yarn at the edges of the smallest section will not behave like the one with an inter-yarn area or a part of the yarn at the edges. Moreover, architecture defects are observed on some samples during X-rays' tomography investigation. Some of these defects can be induced during the manufacturing process, and others, such as the yarns buckling, can be a result of the repetitive load in the direction of the yarns (**Figure 87**). These defects influence the velocity of propagation of the waves explaining hence the scattered results. Furthermore, the damage induced by cyclic loading is randomly spread in the entire section making the propagation of the wave less predictable and its estimation would be less accurate.

To assess this approach, the observation, and the analysis of the induced damage mechanisms along with the measurement of the void content are performed using X-ray Tomography.

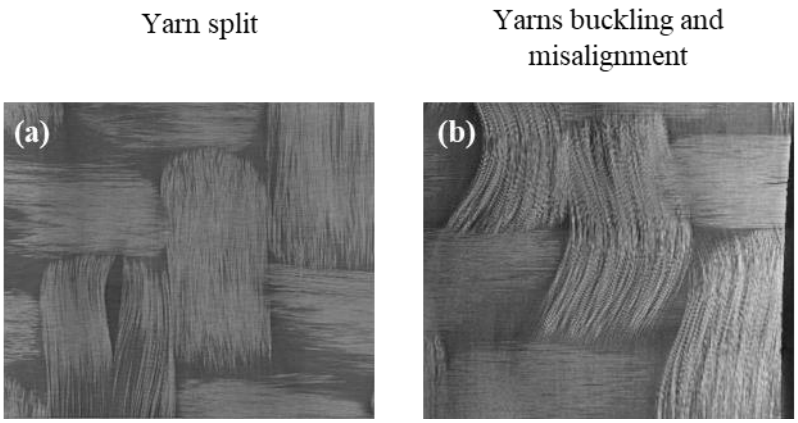

Figure 87: Reconstructed images using X-ray tomography of the composite showing manufacturing defects: (a) the yarn split and (b) the yarns buckling and misalignment.

3.2. X-Ray tomography investigation

The objective of the present section dedicated to the mCT investigation is to reconstruct the volume that corresponds to the area with the smallest section, i.e., the area most likely to contain damage, with the highest possible resolution (around 9 µm). Nine chosen samples are investigated representing the nine combinations of loading. The mCT volume reconstruction and the images post-processing are similar to those described in Chapter II.

Three major damage mechanisms are observed in all samples: transverse weft yarn cracks, longitudinal cracks in the warp yarns and pseudo-delamination as illustrated in **Figure 88, Figure 89** and **Figure 90** respectively. The occurrence of these mechanisms and their propagation vary according to the loading conditions. It is important to mention that in most cases the damage is found in the zone close to the edges of the samples where a stress concentration is expected. However, in some cases, visible damage occurs, mainly matrix cracking (**Figure 88** and **Figure 89**). Indeed, one of the specimens loaded at 35% σ_{UTS} and 70% of the number of cycles to failure (N_c) shows a network of matrix cracks propagating in all three layers (**Figure 89**). Matrix cracking appears at one of the edges of the specimen as reported in **Figure 88**.

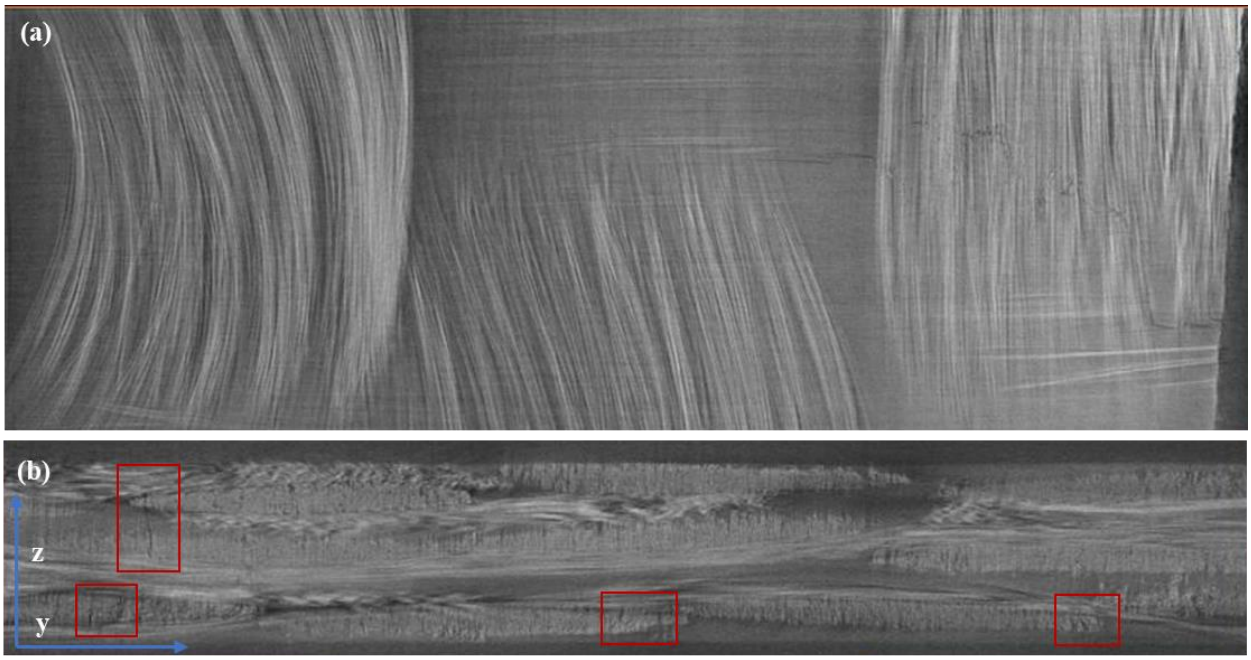

Figure 88: X-ray microtomography investigation of the sample loaded at 35% σ_{UTS} and 50% of the number of cycles to failure showing: (a) macrocracks propagating in the longitudinal and transversal yarns and (b) micro cracks in both longitudinal and transversal yarn propagating from one layer to another.

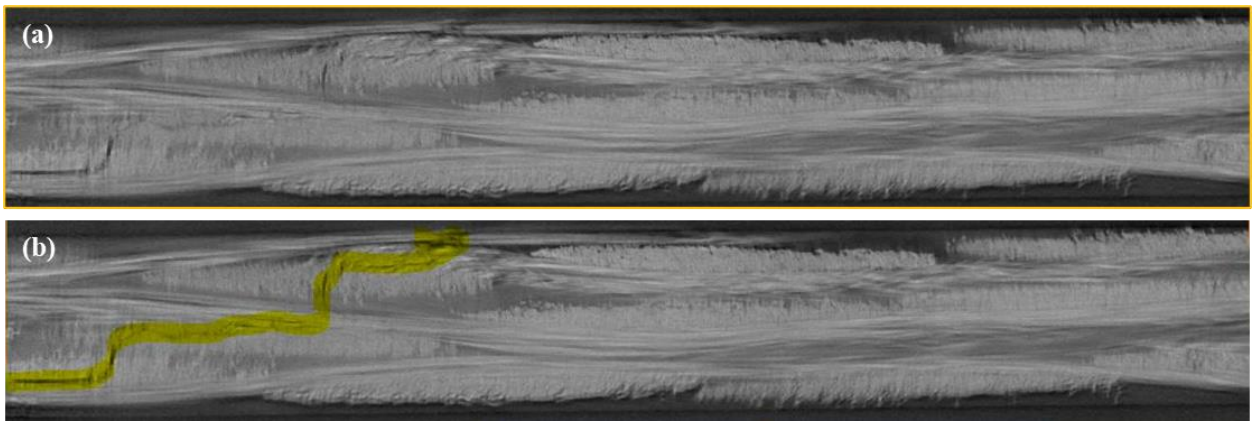

Figure 89: Crack network propagating through the entire thickness in both longitudinal and transversal yarn for the sample loaded at 35% σ_{UTS} and 70% of the number of cycles to failure (Nc): (a) raw image and (b) image with a marker over the crack network for a better visualization.

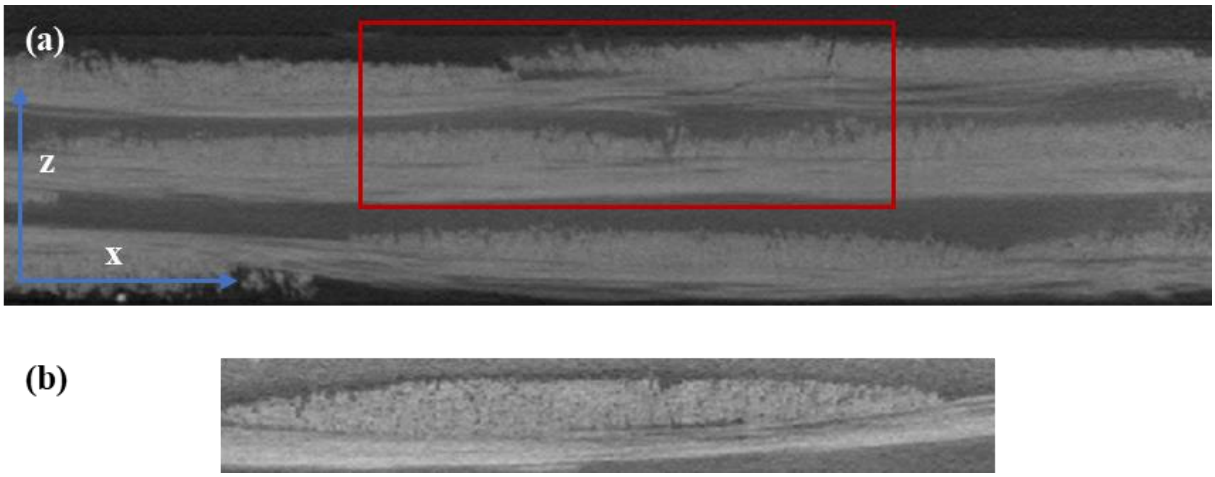

Figure 90: (a) Propagation of the crack network in thickness through both longitudinal and transversal yarns and (b) the propagation of the crack through the yarn creating pseudo-delamination with the perpendicular yarn in a sample loaded at 35% σ_{UTS} and 70% of the number of cycles to failure (Nc).

Since the damage results in the initiation of voids within the sample, an estimation of the voids content is required. Pomarède et al. (Pomarède et al., 2018) have employed voids content measurement as an efficient damage indicator for the same composite material subjected to quasi-static loading. To this end, the mCT images have been processed using a grey level thresholding was performed to discriminate the fibers and the matrix from the cracks. Indeed, the image thresholding replaces one by one the pixels of an image by a fixed threshold range. If a pixel has a value included in the pre-defined interval, it will be black, thus isolating the void. The results obtained are depicted in **Figure 91(a)** for the sample loaded at 35% σ_{UTS}, **Figure 91(b)** for the samples loaded at 45% σ_{UTS} and **Figure 91(c)** for the samples loaded at 60% σ_{UTS}**.** Nevertheless, some acquisition problems accured during the tomography scanning of the sample loaded at 60% σ_{UTS} and 70% NC sample as reported in **Table 6**. Therefore, the observation from this test configuration is not presented nor discussed in **Figure 91(c).** When comparing the trend of the void measurement with that of the results obtained using the Lamb waves technique **Figure 91,** it is found that the studied points exhibit the same trend. The obtained results are in complete correlation with those obtained using the Lamb waves-based method. Consequently, one can conclude that the scattering of the fatigue results in different section of this chapter is mainly due to the behavior of the samples and the microstructure variability besides the type of the applied load. Indeed, given the heterogeneity of the composite's microstructure and also the fact that the samples are cut from several areas of the plates, each sample can behave differently to the same loading conditions. However, the efficiency of the proposed method at detecting the damage state of each sample is proven.

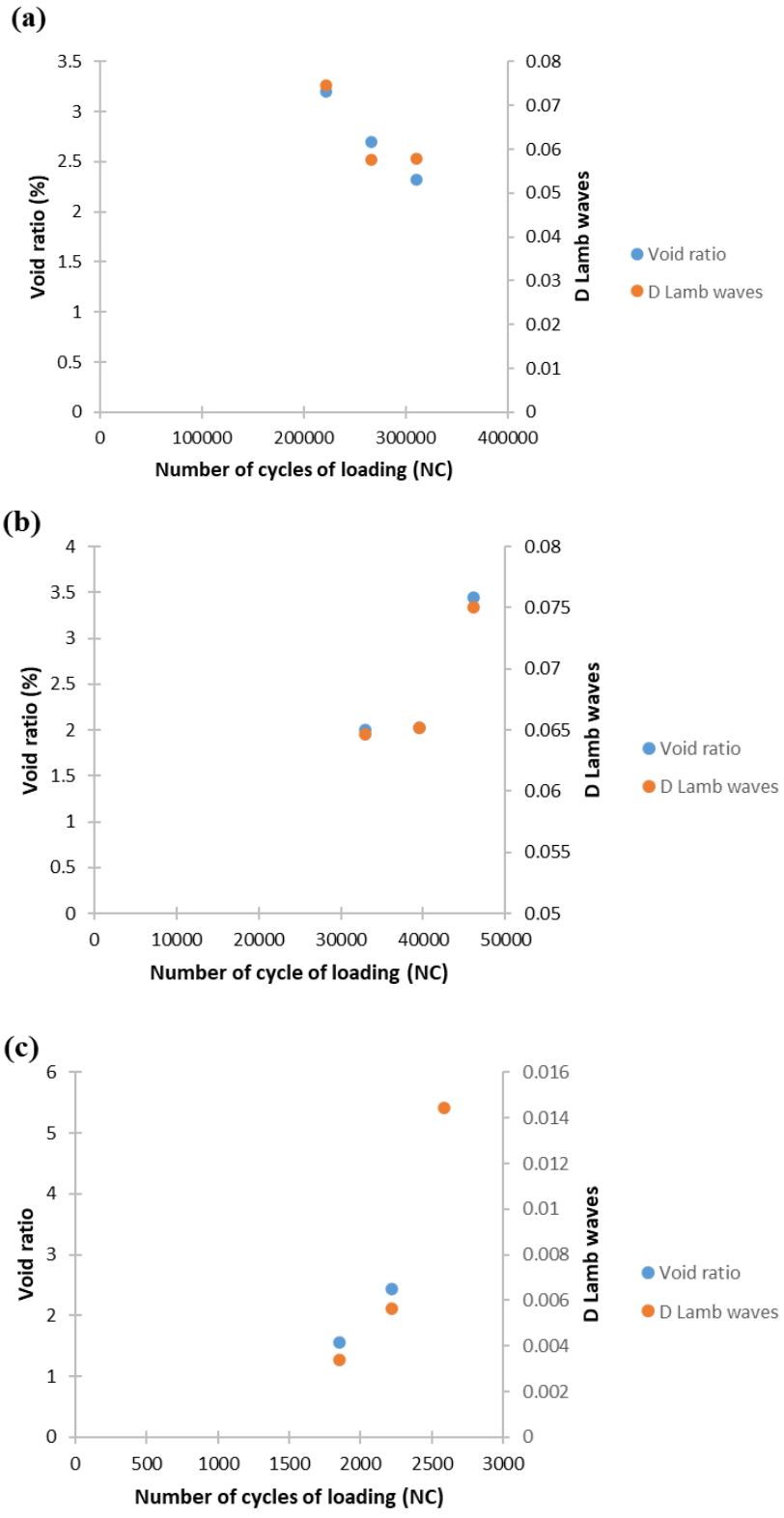

Figure 91: Comparison between the void content and the value of the damage indicator relative to each of the studied samples :(a) the set loaded at 35% σ_{UTS}, (b) the set loaded at 45% σ_{UTS} and (c) the set loaded at 60% σ_{UTS} (Refer to Table 6 for information about the loading).

3.3. Bulk waves investigation

Bulk waves investigation is initially achieved to quantify the damage caused during the cyclic loading in terms of stiffness reduction. During this investigation, the decrease of the mechanical properties of the samples can be noticed at different stages of the process. As detailed in Chapter II, to obtain the components of the stiffness matrix, Christoffel equation, that links the velocity of propagation of the wave at different angles of emission/ reception, is employed. One can extract the change in the velocities of propagation profiles and consequently estimate the stiffness components and their related reduction. The same experimental procedure as the one described in Chapter II is followed. However, due to the difference of geometry between the impacted plates and the fatigue samples, a reduced range of angles is considered during the acquisitions on the smallest section of the samples. The waves are emitted and received over a range of ± 23° in the plane 1-3 (direction 1), and ± 10° when rotating around X axis (plane 2-3 direction 2). The 2.25 MHz transducer are pointed at the center of the samples.

After estimating the time of arrival of each mode (longitudinal mode, and transversal mode), the velocity of both modes is calculated as explained in Chapter II. Nine samples corresponding to the nine considered loading conditions have been tested. One should mention that a non-damaged reference sample is scanned during this procedure to serve as a reference sample in the same testing conditions.

The velocity of the longitudinal mode is presented function of the incidence angle. As explained in the previous chapter, the wave velocity remains stable at a certain range of angles (± 10°) and then it increases with the increase of the angle of emission/reception. Indeed, it must be pointed-out that this behavior is due to the material nature and the direction of the wave propagation within it. Hence, no variation of the velocity is observed between ± 10°. Consequently, the values measured by scanning the 2-3 plane will not be the object of the rest of the study. The variation of the velocity values in the ranges from (-10°) to (-23°) and from (10°) to (23°) reveals a change in C_{11}, $C_{33,}$ C_{13} and C_{55} components. Indeed, the 1-3 plane allows the determination of the four components that interact and affect the variation of the velocity. However, an extraction of the C_{11} components is experimentally impossible with this set-up and for this kind of sample, since it can be estimated only at incidence angle 90° corresponding to the fibers' axis. **Figure 92** illustrates the evolution of the phase velocity of the longitudinal mode function of the incidence angle for each of the considered samples. The difference between the non-damaged and the loaded samples at 35% σ_{UTS}, 45% σ_{UTS}, 60% σ_{UTS} is easily seen in **Figure**

92(a), Figure 92(b) and **Figure 92(c)** respectively. It is noticed that a slight variation of the wave propagation velocity (around 40 m/s) induces a decrease of C_{11} of about 2 to 3 GPa for the investigated material. By comparing the velocity profiles between damaged and non-damaged state, one can predict whether the loading had an influence on the C_{11} component.

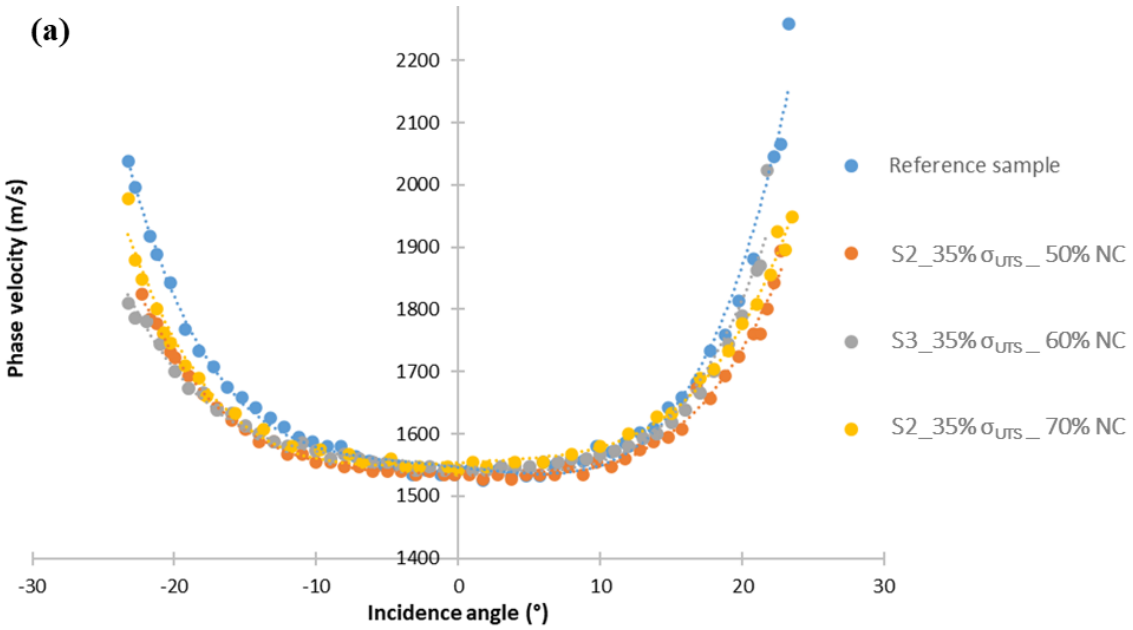

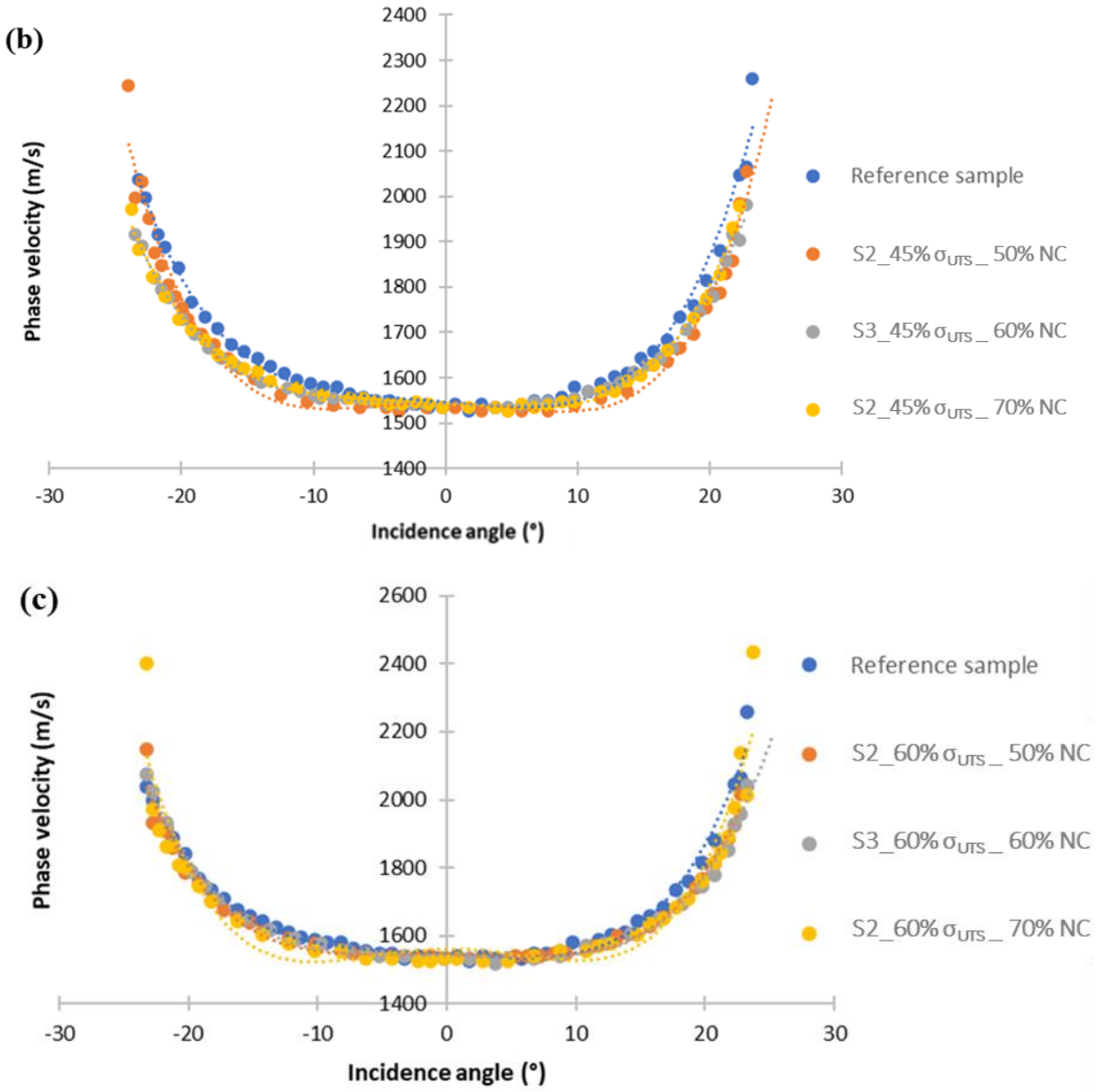

Figure 92: Comparison between the velocity of the longitudinal mode propagating in the plane 1-3 function of the incidence angle for the nine considered samples :(a) the set loaded at 35% σ_{UTS}, (b) the set loaded at 45% σ_{UTS} and (c) the set loaded at 60% σ_{UTS} (Refer to Table 6 for information about the loading).

Since the element that indicates stiffness reduction are missing in the plane 2-3, a proper estimation of the components of the stiffness matrix remains difficult.

As a conclusion, the employment of this method on samples with a small width (35 mm) do not provide the estimation of the nine stiffness matrix components. However, it allows to detect the changes in the velocity profiles of the longitudinal mode with the increase of the applied load and the related conditions. It could hence be used as a qualitative damage indicator.

III. Conclusion

The evaluation and the quantification of the damage resulting from tension-tension fatigue tests has been addressed in this chapter. For that matter, and as a first step, the geometry of the tested sample is preliminary optimized. The choice is adopted considering the localization of the damage area. The dog-bone geometry is used since the failure zone in quasi-static and in cyclic loading is located in the center of the specimen. The analysis of the mechanical measurements shown scattered experimental results indicating a difference in the response of the samples due to their microstructure variability as well as the nature of the cyclic loading. The microstructure variability of the thermo-compressed woven fabric and of the chosen geometry can explain partially the noticed discrepancy. In addition, and unlike impact damage, the fatigue damage caused by cyclic loading is not localized and remains diffuse in the entire section. The developed Lamb-waves based technique is tested on the resulting diffuse fatigue damage. The obtained results showed a similar discrepancy of the results corresponding to samples undergoing the same type of loading. To establish the efficiency of the proposed method, the obtained results are compared with those of voids content measurement performed using X-ray tomography quantitative analysis.

A good correlation is found between the results experimental findings resulting from both methods. This confirms hence the effectiveness of the Lamb-based method for the detection of non-localized damage in the PA66/6 reinforced composite. Finally, the method enabling the stiffness reduction estimation using bulk wave method is conducted. One has concluded that with this method and with the related set-up and samples geometry, it is not possible to estimate the nine stiffness matrix components. In the other hand, it allows to notice the changes in the velocity profiles of the longitudinal mode function of the applied loading conditions making it hence as a reliable damage qualitative indicator.

In the next chapter, a comparison of the residual properties post-impact and post-fatigue will be conducted. The study of the influence of the pre-induced damage on the ultimate tensile strength will be achieved by monitoring the area on the structure showing an increase of the local temperature during monotonic tensile tests.

IV. References

Arif, M. F., Meraghni, F., Chemisky, Y., Despringre, N., & Robert, G. (2014). In situ damage mechanisms investigation of PA66 / GF30 composite : Effect of relative humidity. *Composites part b*, *58*, 487–495. https://doi.org/10.1016/j.compositesb.2013.11.001

Benaarbia, A., Chrysochoos, A., & Robert, G. (2014). Influence of relative humidity and loading frequency on the PA6 . 6 cyclic thermomechanical behavior : Part I . mechanical and thermal aspects. *Polymer Testing*, *40*, 290–298. https://doi.org/10.1016/j.polymertesting.2014.09.019

De Baere, I., Van Paepegem, W., Hochard, C., & Degrieck, J. (2011). On the tension-tension fatigue behaviour of a carbon reinforced thermoplastic part II: Evaluation of a dumbbell-shaped specimen. *Polymer Testing*, *30*(6), 663–672. https://doi.org/10.1016/j.polymertesting.2011.05.005

De Baere, I., Van Paepegem, W., Quaresimin, M., & Degrieck, J. (2011). On the tension-tension fatigue behaviour of a carbon reinforced thermoplastic part I: Limitations of the ASTM D3039/D3479 standard. *Polymer Testing*, *30*(6), 625–632. https://doi.org/10.1016/j.polymertesting.2011.05.004

Eliasson, S., Wanner, S., Barsoum, Z., & Wennhage, P. (2019). Development of fatigue testing procedure for unidirectional carbon fiber composites. *Procedia Structural Integrity*, *19*, 81–89. https://doi.org/10.1016/j.prostr.2019.12.010

Ferreira, J., Costa, J., & Reis, P. (1999). Static and fatigue behaviour of glass-fibre-reinforced polypropylene composites. *Theoretical and Applied Fracture Mechanics*, *31*(1), 67–74. https://doi.org/10.1016/S0167-8442(98)00068-8

Ferreira, J., Costa, J., Reis, P., & Richardson, M. (1999). Analysis of fatigue and damage in glass-fibre-reinforced polypropylene composite materials. *Composites Science and Technology*, *59*(10), 1461–1467. https://doi.org/10.1016/S0266-3538(98)00185-7

Franco, L. A. L., Graça, M. L. A., & Silva, F. S. (2008). Fractography analysis and fatigue of thermoplastic composite laminates at different environmental conditions. *Materials Science and Engineering A*, *488*(1–2), 505–513. https://doi.org/10.1016/j.msea.2007.11.053

Giurgiutiu, V. (2016). Impact and Acoustic Emission Monitoring for Aerospace Composites SHM. In *Structural Health Monitoring of Aerospace Composites* (pp. 317–394). Elsevier. https://doi.org/10.1016/b978-0-12-409605-9.00009-x

Jollivet, T., Peyrac, C., & Lefebvre, F. (2013). Damage of composite materials. *Procedia Engineering*, *66*, 746–758. https://doi.org/10.1016/j.proeng.2013.12.128

Karaouni, H. (2001). Nouveaux outils pour la conception fiable des structures. Ecole Polytechnique.

Liang, S. (2012). Etude de comportement en fatigue des composites renforcés par fibres végétales: prise en compte de la variabilité des propriétés. Université de Bourgogne.

Malpot, A. (2017). Etude du comportement en fatigue d ' un composite à matrice polyamide renforcée d ' un tissu de fibres de verre pour application automobile. PhD thesis, Ecole Nationale Supérieure De Mécanique et d'Aérotechnique.

Malpot, A., Touchard, F., & Bergamo, S. (2015). Effect of relative humidity on mechanical properties of a woven thermoplastic composite for automotive application. *Polymer Testing*, *48*, 160–168. https://doi.org/10.1016/j.polymertesting.2015.10.010

Pomarède, P. (2018). Détection de l'endommagement dans un composite tissé PA66,6/Fibres de verre à l'aide de techniques ultrasonores en vue d'une prédiction de la durabilité de pièces automobiles. PhD thesis, ENSAM ParisTech.

Pomarède, P., Meraghni, F., Peltier, L., Delalande, S., & Declercq, N. F. (2018). Damage Evaluation in Woven Glass Reinforced Polyamide 6 . 6 / 6 Composites Using Ultrasound Phase-Shift Analysis and X-ray Tomography. *Journal of Nondestructive Evaluation*, *123*. https://doi.org/10.1007/s10921-018-0467-3

Robert, G., & Benaarbia, A. (2015). In fl uence of relative humidity and loading frequency on the PA6 . 6 thermomechanical cyclic behavior : Part II . Energy aspects. *Polymer Testing*, *41*, 92–98. https://doi.org/10.1016/j.polymertesting.2014.10.012

Vasconcellos, D. S. De. (2013). *Comportement en fatigue avant et après impact de composites tissés chanvre / époxy*. PhD thesis, Ecole Nationale Supérieure de Mécanique et d'Aérotechnique Poitiers.

Chapter 4: Residual properties post-loading of the polyamide based composite subjected to low-velocity impact and/or fatigue loading

Composite structures may undergo several transient loadings, such as low-velocity impact and fatigue loading, that often cause the progressive degradation of the structural integrity (Agarwal, Broutman, Chandrashekhara, 2006). This deterioration is manifested in the decrease of the residual properties of the composite in terms of static and fatigue load-bearing capacity (Curtis, 2000). Therefore, the estimation of the tensile strength reduction of the composites post-loads is mandatory to guarantee damage tolerance and safety margins in the design of composite components (Shahzad, 2018). In addition, the understanding of the influence of different types of loads combination on the damage evolution and, thus, on the residual tensile strength, is highly required. In realistic working conditions, the composite structure is subjected to a distinct case of loading where both low-velocity impact and fatigue loading occur and interfere.

The present chapter is devoted to the proposition of an experimental methodology enabling to assess and analyze the effect of the nature of the load on the quasi-static response of the composite material residual properties after an event (impact, fatigue loading and impact post-fatigue). For that matter, quasi-static tensile tests are performed on samples subjected to low-velocity impact tests and fatigue loading respectively. A comparison between the response of blank test specimens and that of damaged samples is achieved. The novelty of this chapter is the assessment of the influence of the combined loads, i.e., LVI and cyclic loading, on the residual properties of the composite material. Post-fatigue impact tests are carried out in conditions equivalent to those of low-velocity impact tests and fatigue loadings, respectively. The analysis of (i) the effect of LVI damage on the residual tensile strength of pre-fatigued samples, and (ii) the effect of the fatigue pre-load on the impact response of the composite samples, is established.

I. Experimental set-up quasi-static tensile tests

Quasi-static tensile tests are performed using the MTS universal uniaxial hydraulic machine previously employed to perform the fatigue tests. The same experimental set-up as the one employed to achieve the fatigue tests is used (**Chapter III, section 3**). The choice of the machine is made to maintain the same test conditions and reduce the experimental errors. The specimens are loaded in displacement-controlled mode at a velocity of 0.016 mm/s. Tensile tests are carried out in the same experimental environment and using the same parameters (velocity).

The tensile tests until rupture are carried out to analyze the influence of impact damage, fatigue damage and impact post-fatigue damage on the tensile strength and the stiffness. To monitor the evolution of damage during the tests, an infrared camera to record temperature variations is used. Moreover, the increase of the temperature in some areas indicates the areas of initiation and/or the propagation of damage.

II. Post-impact quasi-static tensile tests analysis

Low-velocity impact tests were performed beforehand. A detailed thorough assessment of the impacted samples was carried out in Chapter II. Indeed, surface and through thickness investigations were achieved to understand and assess the damage evolution and propagation function of the impact energy. This investigation allows to identify the numerous damage mechanisms that occur as the impact energy varies, using the X-ray tomography (mCT). The permanent indentation (PI) and the stiffness reduction were estimated to quantify the resulting damage. Moreover, a Lamb waves propagation-based method was proposed towards the suggestion of a new damage indicator enabling a proper estimation of the damage state of the studied samples.

As a final step of the overall post-impact analysis, quasi-static tensile tests are carried out on post-impact samples. The residual ultimate tensile strength (σ_{UTS} (%)) is estimated and the extent of the caused damage on the residual lives is observed. The experimental findings are correlated with those obtained using the mCT. The objective is to link the macroscopic response (tensile strength decrease) to the microscopic damage mechanisms.

First, the impact plates assessed in Chapter II are machined by a water cutting, with the impact point in the center of each sample, to match the dimensions and the geometry of the samples destined for fatigue tests. They are then conditioned to reach a humidity rate of 50% RH.

A thermal camera is employed to see if the damage caused by low-velocity impact test is the starting point of the total failure during the tensile test. As previously mentioned in Chapter II, the main focus will be on the seven selected sample impacted at energies levels of 7.2 J, 10.54 J, 12.6 J, 14.6 J, 19 J,21.15 J and 24 J respectively. A non-damaged sample is also tested to provide a basis of comparison achieved in the same loading conditions.

1. In-situ and post-mortem observations

As mentioned above, a thermal camera is used to monitor the evolution of the heat flux generated by the cracks until the final failure. The main idea is to assess if the presence of a previous damage (impact damage) in the center of the samples affects the crack pattens leading to the final rupture. The monitoring of the samples during quasi-static tensile tests reveals that, regardless of the extent of the damage resulting from the achieved impact tests, the final failure begins at the edges of the samples corresponding to the area with the lowest section. The failure of the material during the quasi-static tensile tests is not triggered by the residual impact damage. Indeed, when the cracks in the edges are initiated **(Figure 93(a)),** they propagate and accumulate as the tensile test continues until coalescing with the central damage caused by low-velocity impact tests. The cracks then spread until joining the two edges of the samples announcing hence, the final failure of the composite material. An example of thermal camera images corresponding to the tensile test performed on the sample impacted at 12.6 J is depicted in **Figure 93**. **Figure 93(a))** corresponds to the moment of the initiation of the matrix cracking and **Figure 93(b)** shows the final rupture following a straight line.

A visual post-mortem surface observation is performed on the seven chosen samples along with a non-damaged one. It is noticed, as found in Chapter III, that the final rupture follows a straight line along the center of the non-impacted sample on its two surfaces. However, the crack propagation path varies from one surface of the laminate to another as the impact energy increases. It is observed that the final rupture of the impacted samples is asymmetrical between the impacted, i.e., the surface with the permanent indentation, and the non-impacted surface. The fracture of the material on the impacted surface is perpendicular to the tensile axis when the latter do not exhibit an apparent previously induced damage. Whereas the final rupture on the non-impacted surface tends to follow the crack networks as the latter get wider and wider

with the increase of the impact energy. When the impact damage occurs on both surfaces of the laminate, the original linear rupture pattern is disturbed and follows the network of the cracks. **Figure 94** depicts the observation on the two surfaces of three samples: (a) a sample impacted at 7.2 J and showing no surface damage on both surfaces, (b) a sample impacted at 12.6 J exhibiting matrix cracking and fibers breaking on the non-impacted surface, and (c) a sample impacted at 19 J with noticeable damage on both surfaces. The effect of the different damage stages on the residual properties of the composite samples is assessed and discussed in the following sections.

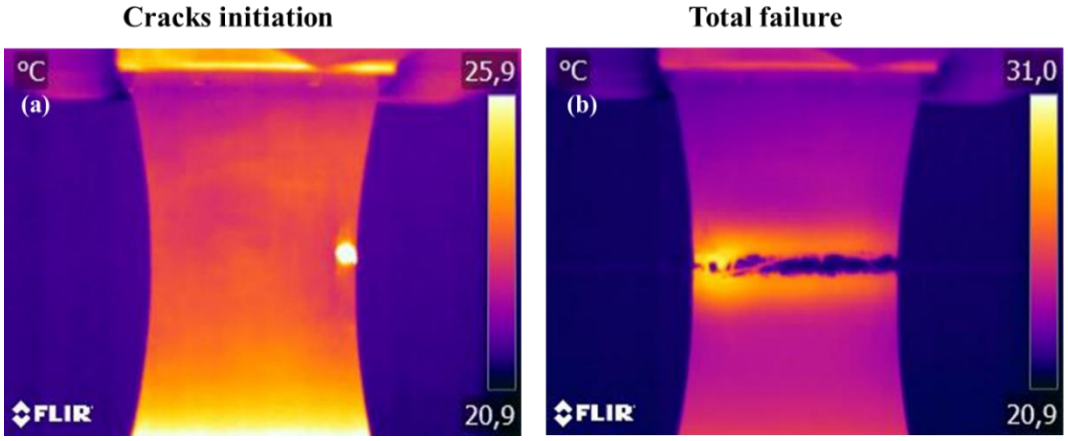

Figure 93: Images obtained during the monitoring of the sample impacted at 12.6 J, during a quasi-static tensile test showing: (a) the location of the cracks initiation, and (b) the final failure.

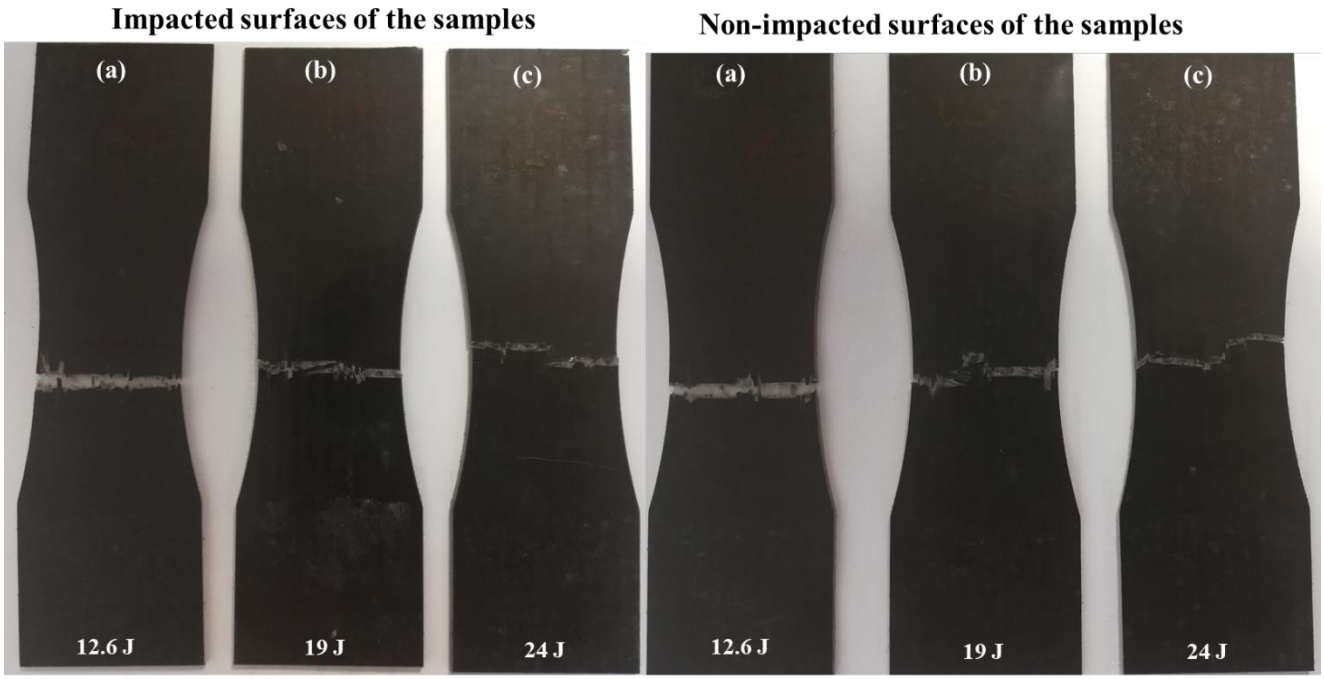

Figure 94: Images of the impacted and non-impacted surfaces of three samples impacted at energy levels of (a) 7.2 J, (b)12.6 J and (c) 19 J respectively. The figure point-out the changes in the paths of the final fracture the impact energy increase and hence as the damage occurs on both surfaces.

2. Experimental results and analysis

Figure 95 represents the tensile response of the eight considered samples, i.e., the non-damaged sample and the seven impacted samples. The stress-strain curves show a quasi-brittle behavior of the studied composite material. A comparison between the tensile response of the non-impacted sample and that of the impacted samples is achieved (**Figure 95**). Two information are consequently extracted from the curves, namely the Young's modulus and the ultimate tensile strength. The evolution of each parameter, function of the impact energy is depicted in **Figure 96** and **Figure 97**, respectively. In **Figure 96**, the values of the Young's modulus seem to be relatively stable. Moreover, no important decrease of the modulus, with impact energy increase, is noticed. The experimental findings indicate, as discussed in Chapter III, that the variation of the Young's modulus is not the most appropriate representative indicator of the deterioration of the polyamide based-composite samples.

Figure 97 represents the evolution of σ_{UTS} as a function of the impact energy. By carefully observing the σ_{UTS} function of the impact energy curve, one can see that the material response exhibits two stages of damage development as the impact energy increases. The first stage,

corresponding to impact energies ranging from 7 J to 12.6 J, indicates the range of damage initiation and propagation from the first to the second ply of the laminate, as observed through X-ray tomography analysis in Chapter II. It is characterized by matrix cracking and fiber's breakage. A slight but quantifiable effect on the residual ultimate tensile strength of the composite is noticed at this stage. The damage mechanisms result of a decrease in the residual σ_{UTS} of less than 5% (**Figure 98**).

The second part of the evolution curve, from 12.6 J to 24 J, points-out the range of energies where the damage propagates in the second ply and through-thickness to the third layer of the woven composite. This stage is associated to the growth and the accumulation of the matrix cracks leading to delamination and fibers breakage as a final stage of the macroscopic failure of the specimen. The residual tensile strength reduces about 13% to 30%, shown in **Figure 98**, indicating hence that the polyamide-based composite is remarkably damaged.

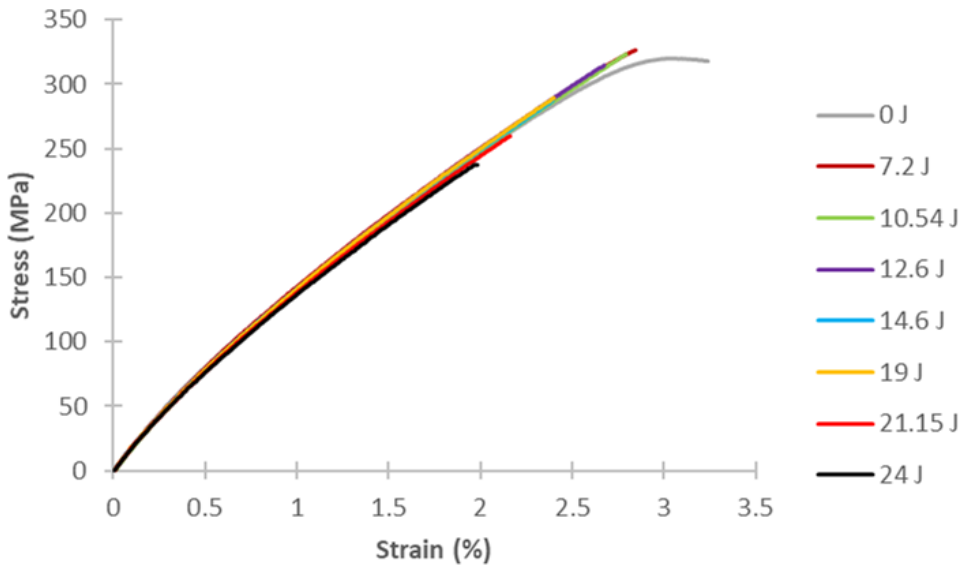

Figure 95: Tensile stress-strain curves of a non-damaged sample along with the seven samples impacted at 7.2 J, 10.54 J, 12.6 J, 14.6 J, 19 J, 21.15 J and 24 J respectively.

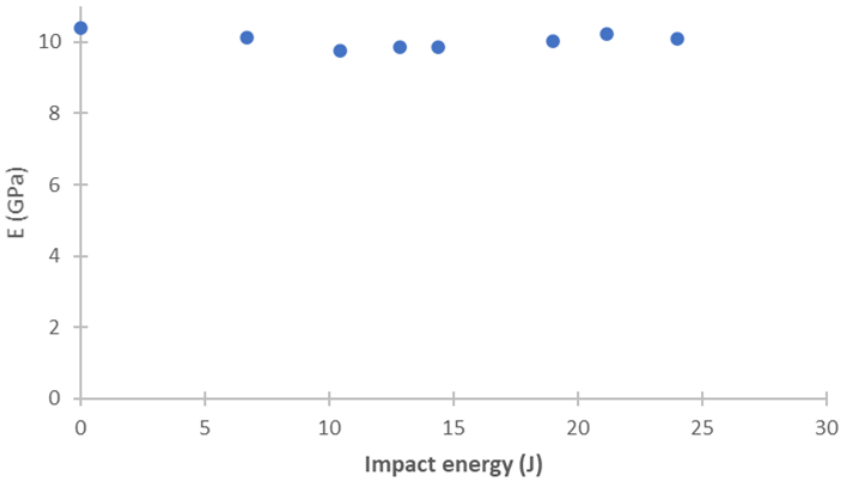

Figure 96: The evolution of the Young's modulus of the reference sample and the seven samples subjected to low-velocity impact at energy levels of 7.2 J, 10.54 J, 12.6 J, 14.6 J, 19 J,21.15 J and 24 J, respectively.

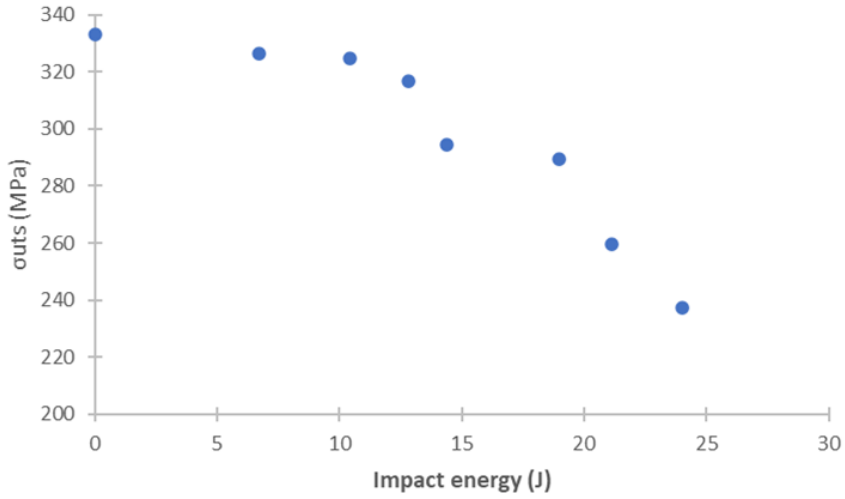

Figure 97: The evolution of the ultimate tensile strength (σ_{UTS}) of the reference sample and the seven samples subjected to low-velocity impact at energy levels of 7.2 J, 10.54 J, 12.6 J, 14.6 J, 19 J, 21.15 J and 24 J, respectively.

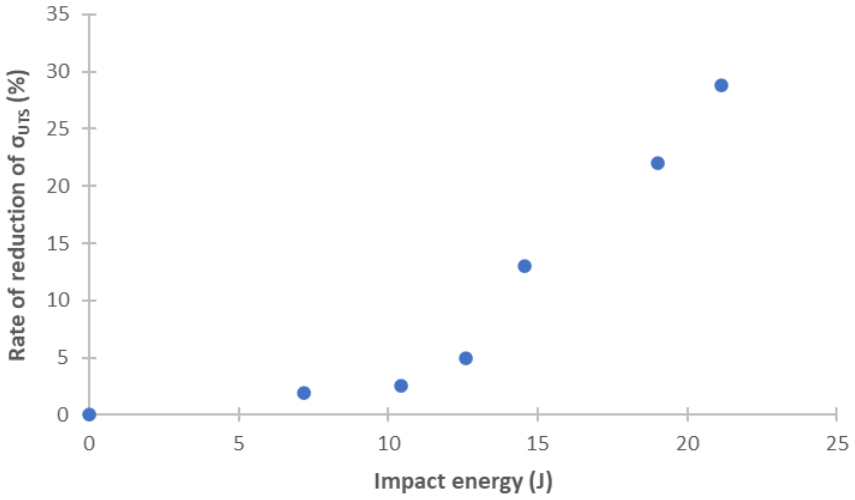

Figure 98: The reduction of the ultimate tensile strength (% σ_{UTS}) of the reference sample and the seven samples subjected to low-velocity impact at energy levels of 7.2 J, 10.54 J, 12.6 J, 14.6 J, 19 J, 21.15 J and 24 J, respectively.

III. Post-fatigue tensile tests

The use of mechanical properties estimation to evaluate fatigue damage has gained considerable attention due to its quantitative nature. Induced stress redistributions and concentration caused by fatigue loading are directly linked to the strength and stiffness reduction (Reifsnider et al., 1983). The change in the strength of composite structures under cyclic loading is an important factor affecting their design (Shahzad, 2018).

Fatigue tests at different loading conditions were performed in Chapter III. A study using multiple NDE methods was performed. The experimental results enabled the validation of the proposed Lamb waves propagation method in detecting non-localized damage caused by fatigue loading.

The present section is dedicated to the assessment of the post-fatigue residual properties of the polyamide-based composite. For that matter, quasi-static tensile tests are achieved on nine corresponding to the nine combinations of parameters previously introduced in Chapter III (**Table 7**). A meticulous conditioning procedure is followed to maintain the samples at 50% relative humidity conditions prior to the tensile tests, is followed. The residual mechanical performances are represented by the estimation of the post-fatigue ultimate tensile strength (σ_{UTS}). The influence of the fatigue loading on the mechanical properties of the studied samples is later discussed in the following sections.

Table 7: Nine combinations of parameters used for interrupted fatigue tests on samples pre-conditioned to 50% RH.

Loading level	35% σ_{UTS}			45% σ_{UTS}			60% σ_{UTS}		
Number of cycles (%)	50%	60%	70%	50%	60%	70%	50%	60%	70%
Number of cycles	222061	266473	310885	33015	39618	46221	1851	2222	2592

1. Post-mortem observations

Post-mortem observations on the fatigue pre-loaded samples subjected to quasi-static tensile tests are presented in,

Figure 100 and **Figure 101**. The objective is to assess the occurrence of damage (fatigue's diffused micro-damage), initiated in the areas of the samples with the minimum width, affects the final rupture's pattern. Since fatigue loading induces micro-cracking in the gauge area (central zone of the sample), notably close to the edges of the sample, the rupture of the material is always initiated from the edges of the samples. Typically, the failure follows a linear pattern. However, in some cases, and assuming that micro-damage resulting from fatigue loading is not localized in the areas with the minimum widths, the final rupture patterns can be disturbed and redirected to go through the weakest areas of the sample, i.e., stress concentration areas and fatigue damage.

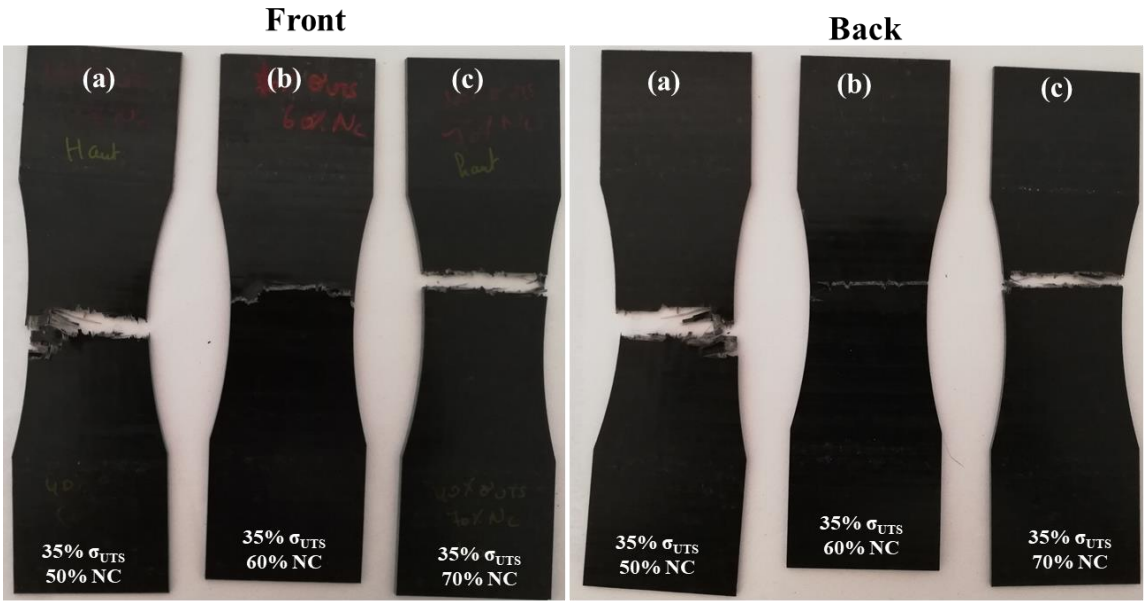

Figure 99: Post-mortem observations of the sample pre-loaded in cyclic loading at a maximum stress of 35% σ_{UTS} at different stages of fatigue life, front and back, subjected to destructive tensile tests: (a) 50%NC, (b) 60% NC and (c) 70% NC.

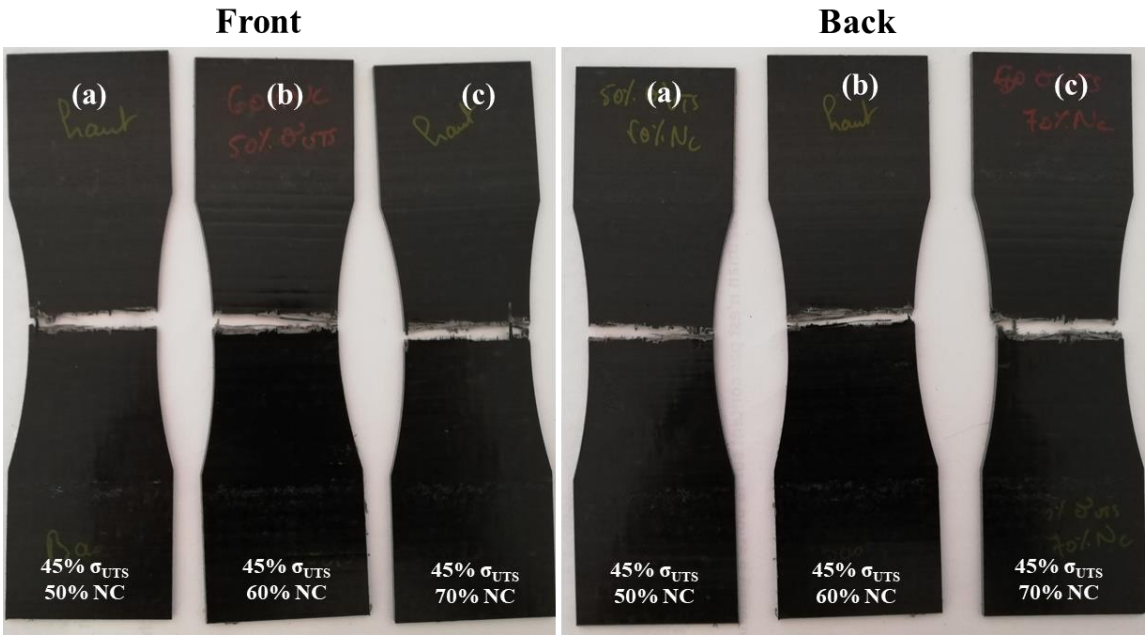

Figure 100: Post-mortem observations of the sample pre-loaded in cyclic loading at a maximum stress of 45% σ_{UTS} at different stages of fatigue life, front and back, subjected to destructive tensile tests: (a) 50%NC, (b) 60% NC and (c) 70% NC.

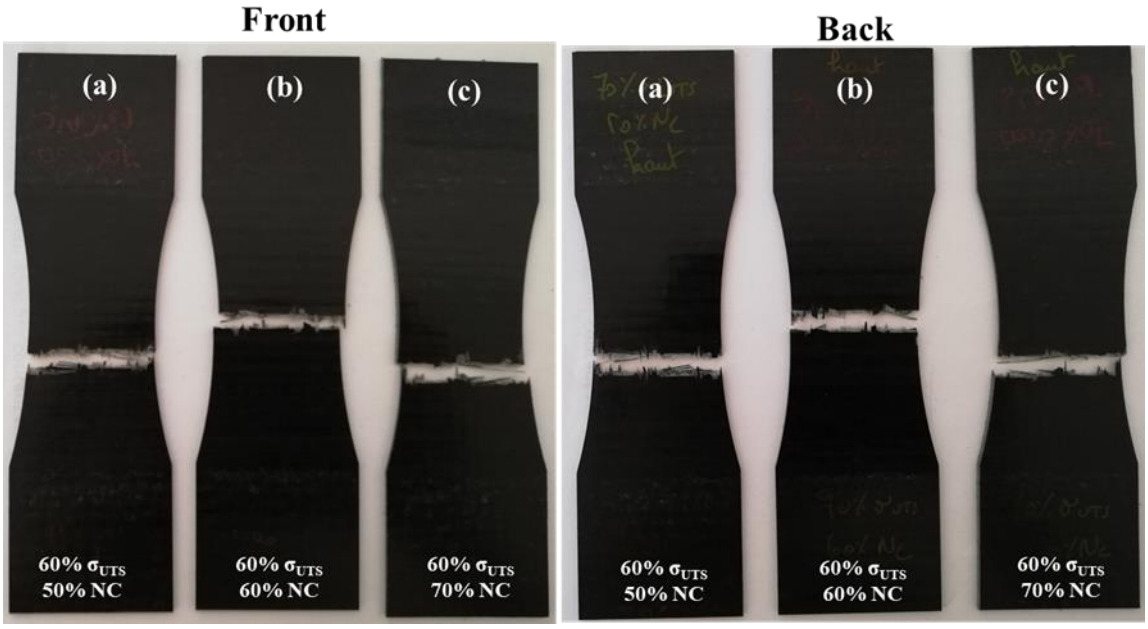

Figure 101: Post-mortem observations of the sample pre-loaded in cyclic loading at a maximum stress of 60% σ_{UTS} at different stages of fatigue life, front and back, subjected to destructive tensile tests: (a) 50%NC, (b) 60% NC and (c) 70% NC.

2. Analysis of the experimental results

A comparison is established between the tensile response of a non-loaded sample and the one exhibited by the samples loaded at the nine combinations of parameters detailed in **Table 7**.

Figure 102, Figure 103 and **Figure 104** illustrate the stress-strain curves of the reference and the pre-fatigued samples. In the three figures, one can notice that the maximum stress decreases due to the cyclic loading. However, the reduction in this visually observed value suggests that the effect of loading at low stress levels and high numbers of cycles is more significant for the residual strength of the composite material. To quantify the loss in the post-fatigue residual properties of the studied samples, the maximum stress value of each of the stress-strain curves is extracted and compared with that of a non-loaded sample. Furthermore, these curves confirm the insensitivity of the Young's modulus as a damage indicator of the progressive degradation induced by a fatigue loading at different proportions of number of cycles to failure and stress levels in the studied thermoplastic composite.

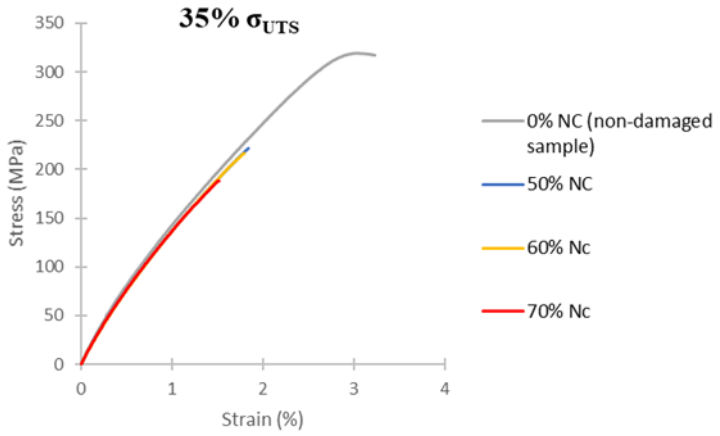

Figure 102: Stress-strain curves of a reference sample and three samples subjected to fatigue loading at a maximum stress level of 35% σ_{UTS} for 50%, 60% and 70% of the number of cycles to failure respectively showing the residual strength reduction.

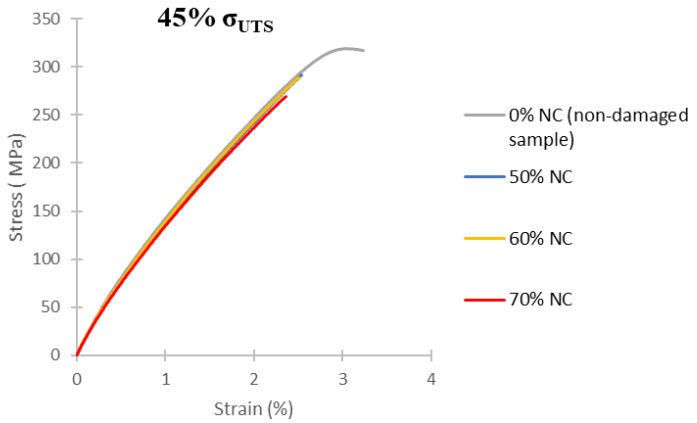

Figure 103: Stress-strain curves of a reference sample and three samples subjected to fatigue loading at a maximum stress level of 45% σ_{UTS} for 50%, 60% and 70% of the number of cycles to failure respectively showing the residual strength reduction.

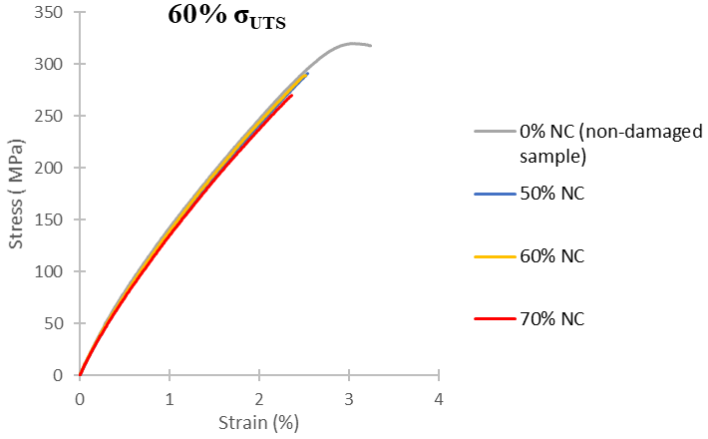

Figure 104: Stress-strain curves of a reference sample and three samples subjected to fatigue loading at a maximum stress level of 60% σ_{UTS} for 50%, 60% and 70% of the number of cycles to failure respectively showing the residual strength reduction.

Figure 105, Figure 106 and **Figure 107** represent the evolution of the ultimate tensile strength (σ_{UTS}) of the samples subjected to interrupted fatigue loadings at three stress levels namely, 35%, 45% and 60% σ_{UTS}. At first glance, one can see that the residual ultimate tensile strength values are lower for the sets of samples, loaded at a maximum stress corresponding to 35% and 45% σ_{UTS}. Indeed, it is found that, for the set of samples loaded at a maximum stress level of 35% σ_{UTS}, the sample loaded at 50% NC (number of cycles until failure) exhibits a loss of residual strength of about 33%. The residual strength reduction continues as the number of cycles increases to 35% for the sample loaded at 60% NC, and to about 43% for the sample loaded at 70% NC. The samples loaded at a maximum stress level of 45% σ_{UTS} also show a decrease of the residual strength caused by repetitive tension-tension loading. The residual strength reduction is ranging between 37% and 42% as the number of cycles increases. The third set of samples loaded at a maximum stress level of 60% σ_{UTS} demonstrate a lower loss of the residual strength as the

number of cycles varies. Indeed, it is about 12% to 13% for the sample loaded at 50% and 60% NC, respectively, and 19% for the sample loaded at 70% NC. These experimental findings point-out to the fact that the final rupture for the samples subjected to fatigue loading at high maximum stress levels occurs suddenly after 70% NC, since the loss in the residual strength between 50% and 70% NC is less than 20%. Moreover, the residual performances of the two sets of samples loaded at 35% and 45% $\sigma_{UTS,}$ respectively are close and comparable. It is important to mention that no equivalence between the different combinations of parameters is established in this chapter. The latter requires a meticulous testing campaign considering a large number of samples. The objective of this section is to observe the influence of the fatigue loading on the mechanical properties in a qualitative approach.

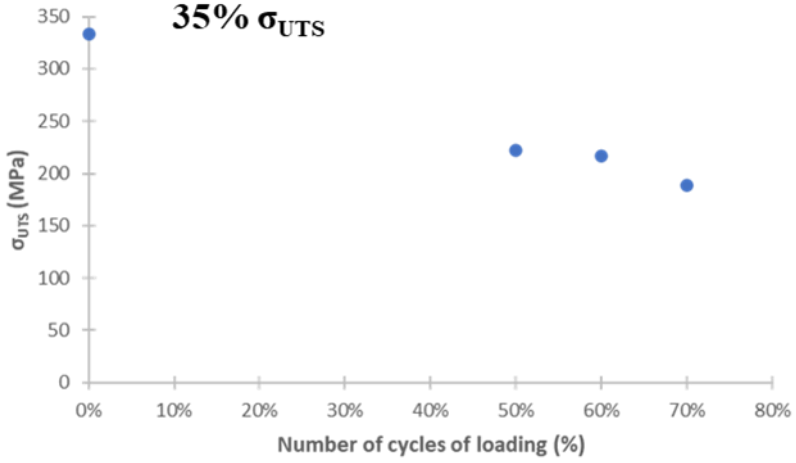

Figure 105: The evolution of the ultimate tensile strength (σ_{UTS}) of the reference sample and the three samples subjected to fatigue loading at a maximum stress level of 35% σ_{UTS} for 50%, 60% and 70% of the number of cycles to failure respectively, respectively.

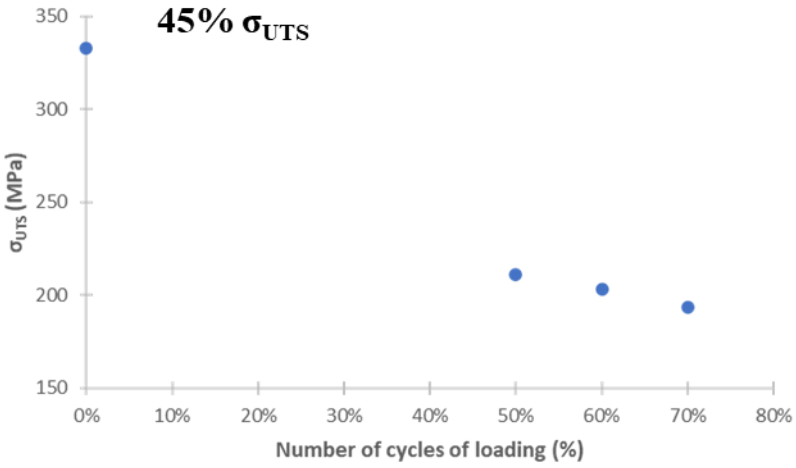

Figure 106: The evolution of the ultimate tensile strength (σ_{UTS}) of the reference sample and the three samples subjected to fatigue loading at a maximum stress level of 45% σ_{UTS} for 50%, 60% and 70% of the number of cycles to failure respectively, respectively.

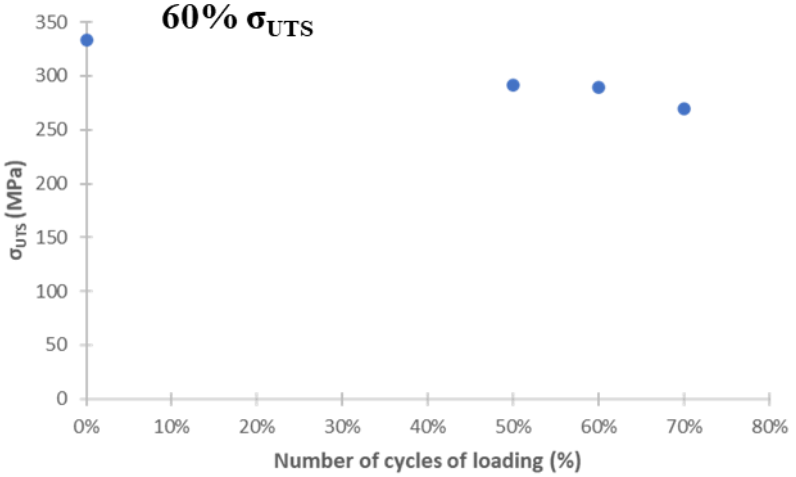

Figure 107: The evolution of the ultimate tensile strength (σ_{UTS}) of the reference sample and the three samples subjected to fatigue loading at a maximum stress level of 60% σ_{UTS} for 50%, 60% and 70% of the number of cycles to failure respectively, respectively.

IV. Impact post-fatigue tests

Impact post-fatigue tests are the object of this section. These tests are carried out to inspect the influence of the coupling of fatigue loading and low-velocity impact on the residual properties of the polyamide-based composite material. In the literature, post-fatigue impact remains relatively scarcely investigated topic in the field of composite materials. The lack of references and deep research works makes the interpretation of the obtained results very challenging due to the complexity of the loading modes. In this study, an experimental procedure to achieve the

coupling of low-velocity impact and fatigue loading is proposed. The macroscopic response of the composite in terms of residual strength will be the main focus. Qualitative assessment of the experimental findings is achieved. The major scope is to qualitatively observe the effect of (i) the fatigue loading on the residual strength and stiffness of the impacted samples, and (ii) low-velocity impact tests on the residual properties of samples subjected to repetitive cyclic loadings. Two sets of samples previously loaded in fatigue following the nine parameter combinations are detailed in **Table 7.** Low-velocity impact tests are carried out on the same samples at two different levels of impact energy.

1. Impact and fatigue testing conditions

Fatigue tests were previously performed on two sets of dog bone samples using the nine combinations of parameters detailed in Chapter III. After the assessments of the resulting damage using the different NDE techniques, the samples were then put back in the humidity-controlled oven to be reconditioned until saturation at a relative humidity level of 50% (RH 50%). Low-velocity impact tests were carried out afterwards using the same procedure and set-up described in Chapter II. The impact energies were chosen to match the impact tests achieved beforehand on rectangular plates. The choice is based on finding similarities in terms of impact heights and energies between the two tested geometries (plates of 150 x 100 mm^2 and dog bone geometry). Since the major difference between the two geometries is the width, the impact heights for the rectangular samples are divided by a factor of 2.85 to match the width of the dog bone samples. Consequently, the height-controlled impact tests are realized at 0.5 m and 1 m.

After impact tests the conditioning procedure at 50% RH is followed to ensure the same humidity conditions for all the samples that will undergo the quasi-static tensile loading until failure. Tensile tests using the same parameters are carried out afterwards.

2. Impact post-fatigue experimental results

Several data, namely the displacement of the impactor, the displacement of the specimen and the applied force, as a function of the time of the test respectively, are collected following height-controlled impact event. In this section, the attention will be focused only on the impactor displacement versus time curves enabling to extract the impact velocities (before and after the impactor hits the sample) and therefore deduce the real impact energies along with the absorbed energies.

One should point out that the slop of the first part of the graph corresponds to the real impact energy while the slop of the second part of this same graph represents the rebound (propulsion) velocity of the impactor after hitting the sample. It is important to remind that a linear regression was used to estimate the velocities. Using the following formula, the impact velocity and the propulsion velocity are linked to the absorbed energy. The latter matches the amount of energy that passes from the impactor to the sample during an impact event. It is defined as the difference between the impact energy and the rebound velocity called the 'excessive energy' (Dhakal et al., 2012).

$$E_A = \frac{1}{2} m (v_1^2 - v_2^2)$$

With v_1 and v_2 the impact and the rebound velocity, m is the impactor's mass and is of 1.02 Kg. An example explaining the estimated velocities using the displacement-time curve of the impactor for the pre-loaded fatigue sample impacted at 4.34 J is exhibited in **Figure 108**. The calculated parameters i.e., impact velocity, the real impact energy, and the absorbed energy for the two sets of pre-fatigued samples impacted are represented in **Table 8**. Technical issues occurred during the low-velocity impact test of the sample pre-loaded in fatigue at 35% σ_{UTS} for 70% of the fatigue life, hence no data relative to the impact test are discussed in the rest of the study.

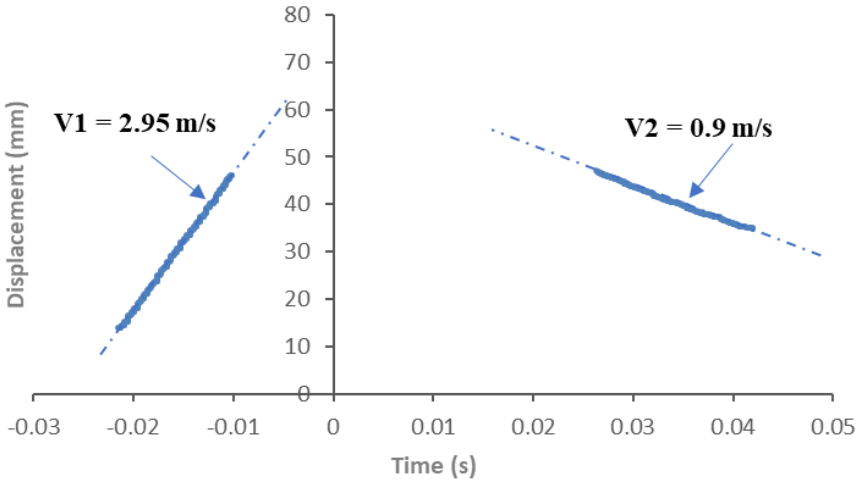

Figure 108: Impactor's displacement- time curve of the pre-loaded fatigue sample, loaded at 35% σ_{UTS} and 50% NC, impacted at 4.34 J detailing the followed method to compute the absorbed energy showing the impact velocity V1 and the rebound velocity V2.

Table 8: Parameters of impact post-fatigue tests for the eighteen considered samples impacted from 0.5 m and 1 m respectively, showing the maximum stress level, the number of cycles of loading, the impact energy and the absorbed energy.

Loading level	35% σ_{UTS}			45% σ_{UTS}			60% σ_{UTS}		
Number of cycles (%)	50%	60%	70%	50%	60%	70%	50%	60%	70%
Number of cycles	222061	266473	310885	33015	39618	46221	1851	2222	2592
Impact energy (J) (impact height 0.5 m)	4.34	4.09	-	4.25	4.32	4.38	4.26	4.44	4.34
Absorbed energy (J) (impact height 1 m)	3.93	3.50	-	3.77	3.52	3.60	3.73	3.78	3.75
Impact energy (J) (impact height 1 m)	9.1	8.61	8.79	8.9	7.52	9.2	8.63	8.26	8.35
Absorbed energy (J) (impact height 1 m)	8.37	8.1	8.45	8.1	7	8.7	8	7.65	7.69

Tensile tests are conducted after conditioning the sample at a relative humidity level of 50%. The main focus is to identify trends of the macroscopic response of the composite materials to prepare a more advanced post-fatigue impact test campaign. To do so, a large number of specimens enabling a proper characterization of the behavior of the composite material subjected to this type of complex loading should be considered. Therefore, a qualitative interpretation of the experimental findings will take place.

2.1. In-situ and post-mortem observations

As previously mentioned, macroscopic observations during the tests and post-mortem are achieved. The primary focus for in-situ investigation is on the edges and the center of the samples containing impact damage. Indeed, during post-fatigue tensile tests, one has noticed that the final failure starts from the edges of the samples. The objective is to see if impact damage influences the final rupture pattern.

Figure 109, Figure 110 and **Figure 111** represent images of the samples post-tensile tests showing the final failure patterns for all samples subjected to impact post-fatigue at different levels of impact energies, stress levels and numbers of cycles of loading. The infrared monitoring (**Figure 112** and **Figure 113**) and the post-mortem observations of the samples during tensile tests (**Figure 109, Figure 110** and **Figure 111)** reveal that despite the damage caused by fatigue loading and low-velocity impact, the final failure always starts from the edges of the samples, i.e., the zone with the lowest section. Indeed, the failure initiation happens in the edges (**Figure 112(a)** and **Figure 112(b)**). Generally, the cracks continue to propagate until they join the localized impact damage

(**Figure 112(c), Figure 112(d)** and **Figure 112(e)).** The same phenomenon was seen during the post-impact tensile tests. Nevertheless, in some cases like the sample pre-loaded in fatigue at a maximum stress level of 45% σ_{UTS} for 60% NC **Figure 111(c),** and impacted from 0.5 m, the final rupture occurs in areas that do not contain impact damage (**Figure 113(b)**); This phenomenon can be explained by a more important micro-cracking and localized stress concentration in the hot spots (**Figure 113(a)**) resulting from the cyclic loadings. One can assume that in some cases, if preload damage occurs at the edges of the specimen, and if the impact damage is not very diffused through the thickness and in the surface, the final fracture path is more likely to not pass through the impact damage.

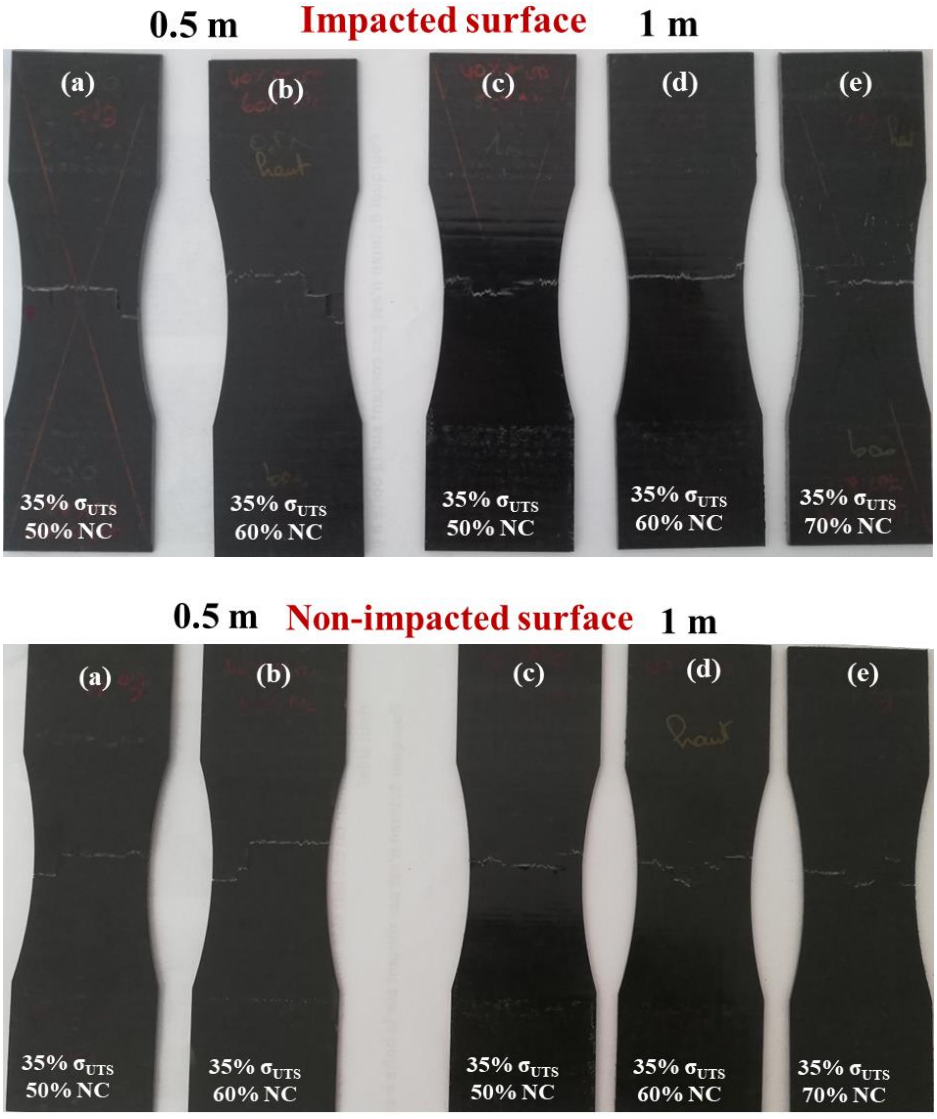

Figure 109: Observations of the final failure pattern occurring post-impact, from two different heights namely 0.5 m and 1 m, on the non-impacted and impacted surfaces of the samples pre-loaded in fatigue at 35% σ_{UTS}: (a) and (c) 50% NC, (b) and (d) 60% NC, and (e)70% NC.

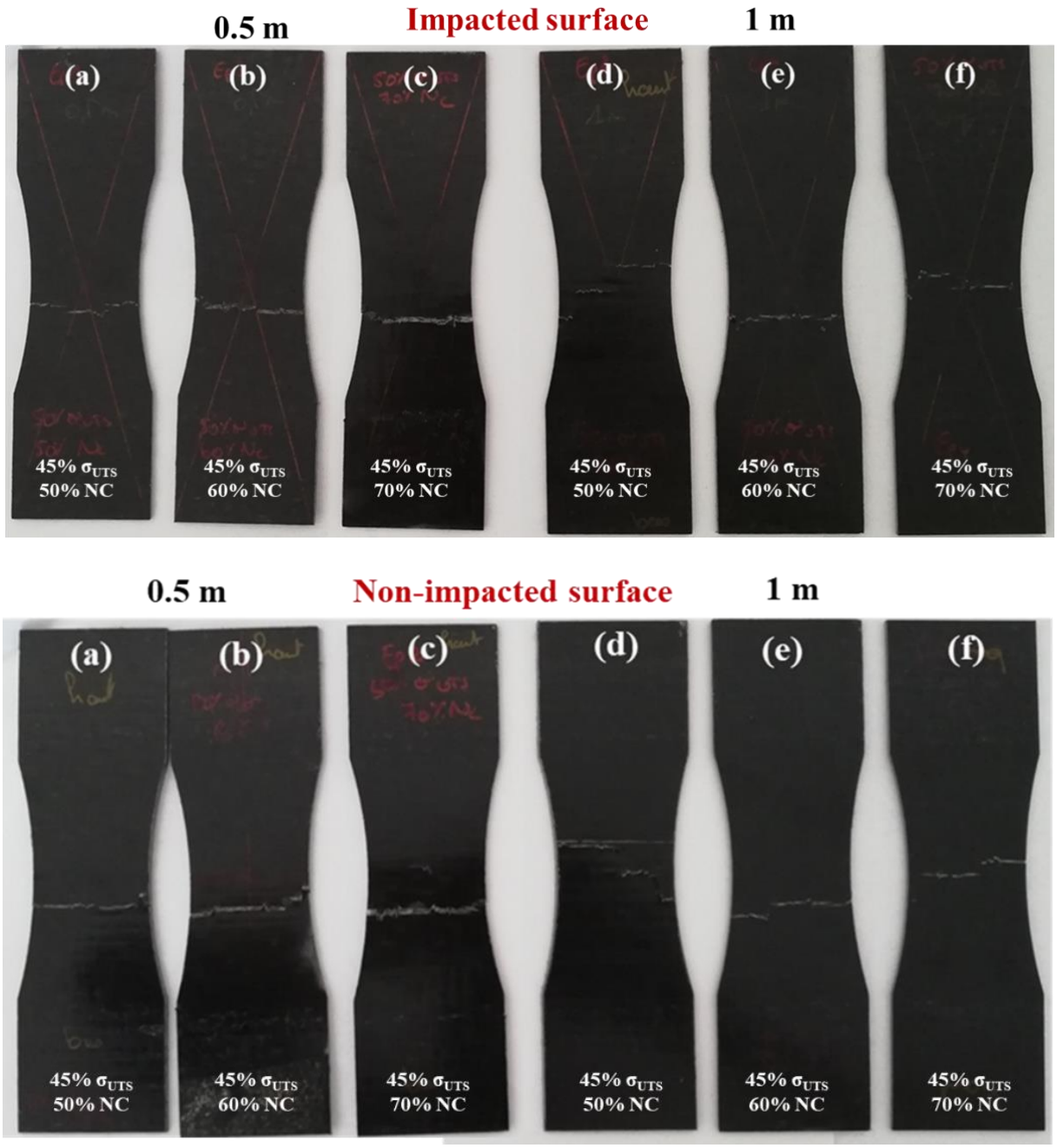

Figure 110: Observations of the final failure pattern occurring post-impact, from two different heights namely 0.5 m and 1 m, on the non-impacted and impacted surfaces of the samples pre-loaded in fatigue at 45% σ_{UTS}: (a) and (c) 50% NC, (b) and (d) 60% NC, and (c) and (f) 70% NC.

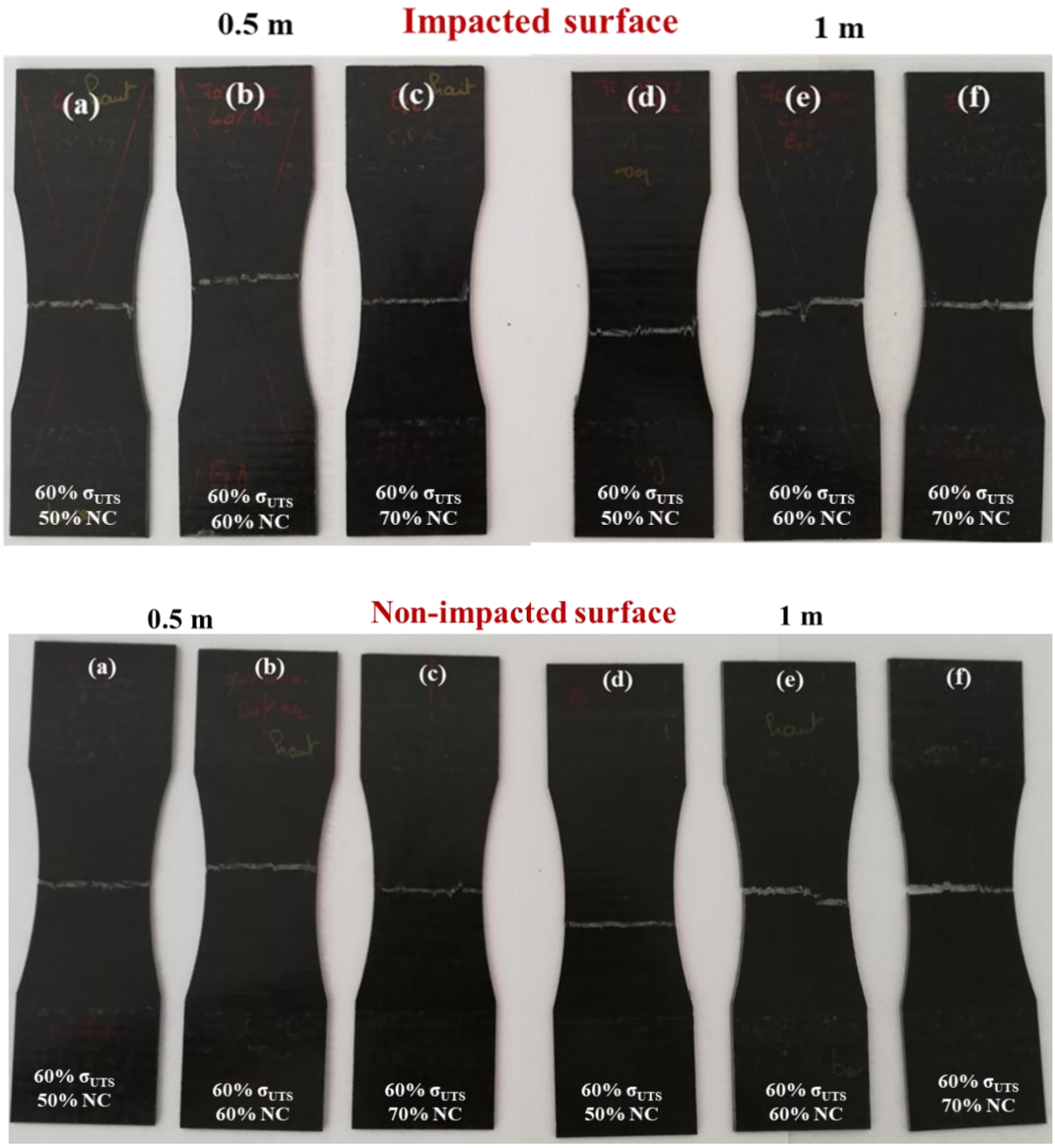

Figure 111: Observations of the final failure pattern occurring post-impact, from two different heights namely 0.5 m and 1 m, on the non-impacted and impacted surfaces of the samples pre-loaded in fatigue at 60% σ_{UTS}: (a) and (c) 50% NC, (b) and (d) 60% NC, and (c) and (f) 70% NC.

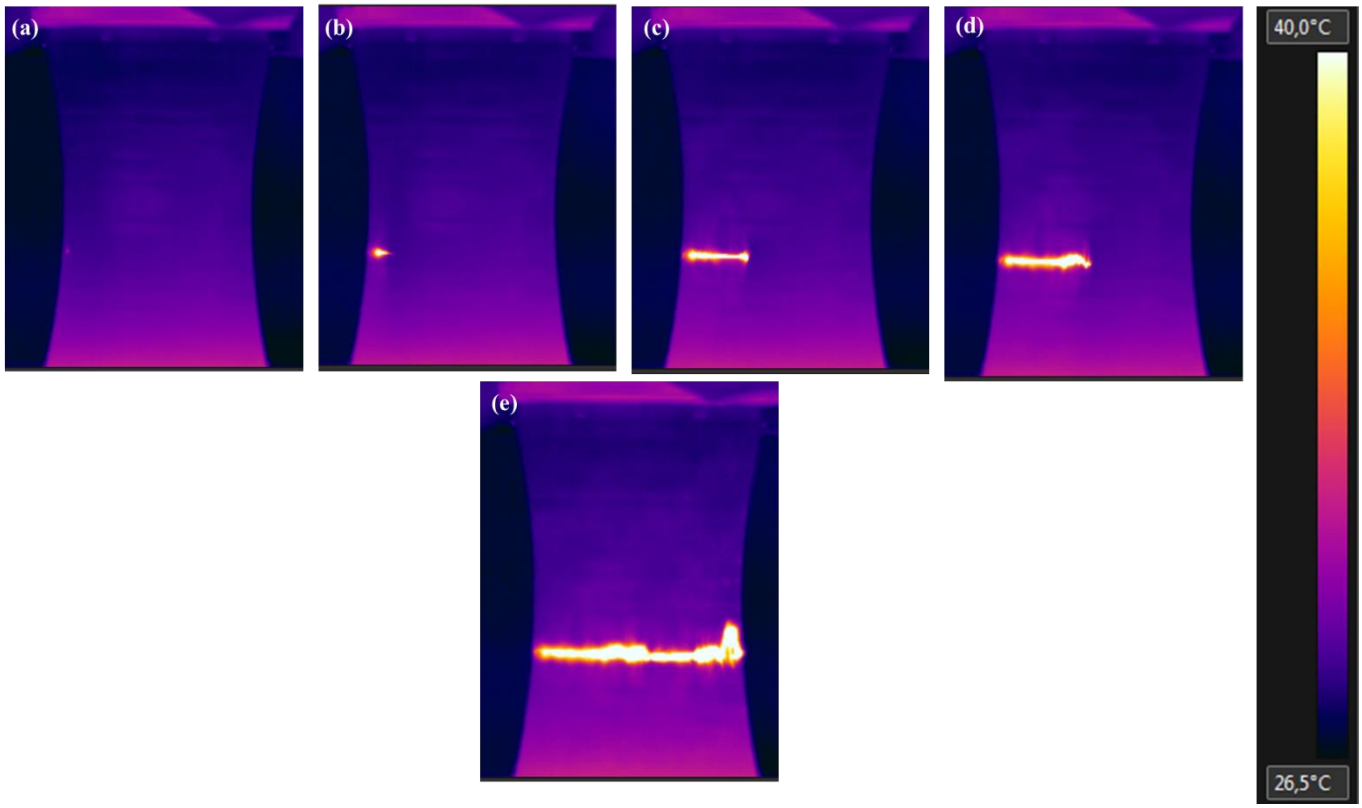

Figure 112: Images recorded during the tensile of the sample pre-loaded in fatigue at a maximum stress level of 45% σ_{UTS} during 50% NC, and impacted from a height of 0.5 m showing: (a) hot spot temperature indicating the damage occurrence, (b) a local increase of the temperature, (c) the biggening of the propagation of the crack, (d) the coalescence of the crack with the impact damage and (e) the final rupture of the sample.

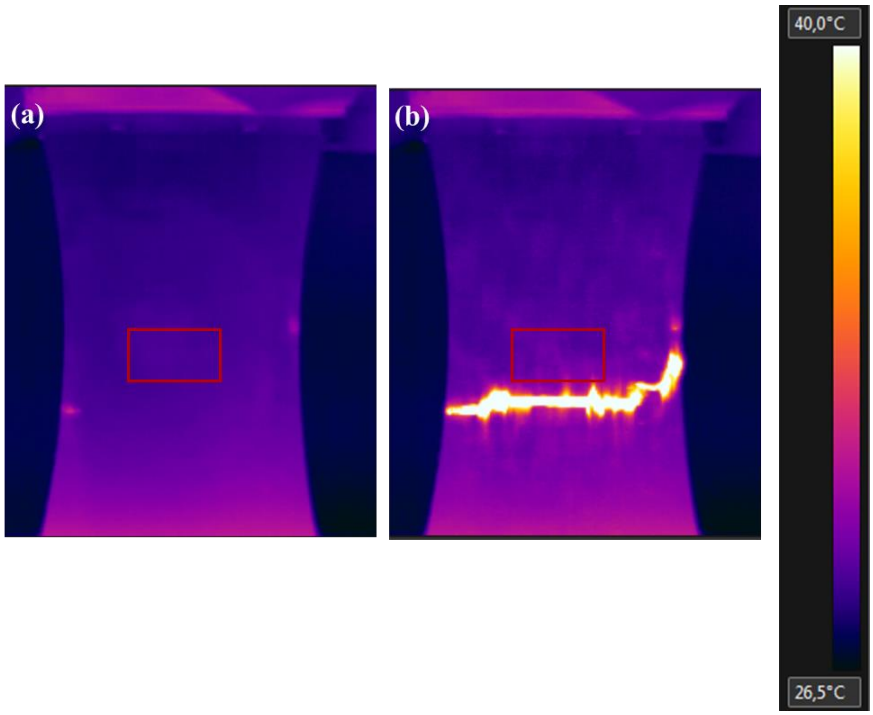

Figure 113: Images recorded during the tensile of the sample pre-loaded in fatigue at a maximum stress level of 45% during 60% NC and impacted from a height of 0.5 m showing the impact damage in the center of the sample: (a) hot spots on the edges of the sample indicating the damage occurrence and (b) the final rupture's pattern that joins the two hot spots.

2.2. Tensile tests results

Figure 114, Figure 115, Figure 116, Figure 117, Figure 118 and **Figure 119** illustrate the stress-strain graphs of samples subjected to impact post-fatigue. For simplification reasons, average values are considered for the impact energies, namely 4.3 J for the tests performed with the impactor positioned at 0.5 m from the sample, and 8.6 J for the tests performed with the impactor positioned at 1 m from the sample. One can clearly notice on all the figures that there is a gap between the non-loaded and loaded samples. A decrease in the values of the maximum stress is observed on all figures. However, on **Figure 116** and **Figure 119**,it is seen that the maximum stress is higher for samples subjected to pre-fatigue loading at a stress level of 60% σ_{UTS}. It can be assumed that when the maximum stress level is relatively high, the final rupture is sudden and brutal. Indeed, as discussed in previous sections, damage creation inside a composite sample under high stress fatigue loadings occurs faster, leading to a rapid deterioration of the sample's integrity and may induce hence a more disastrous failure.

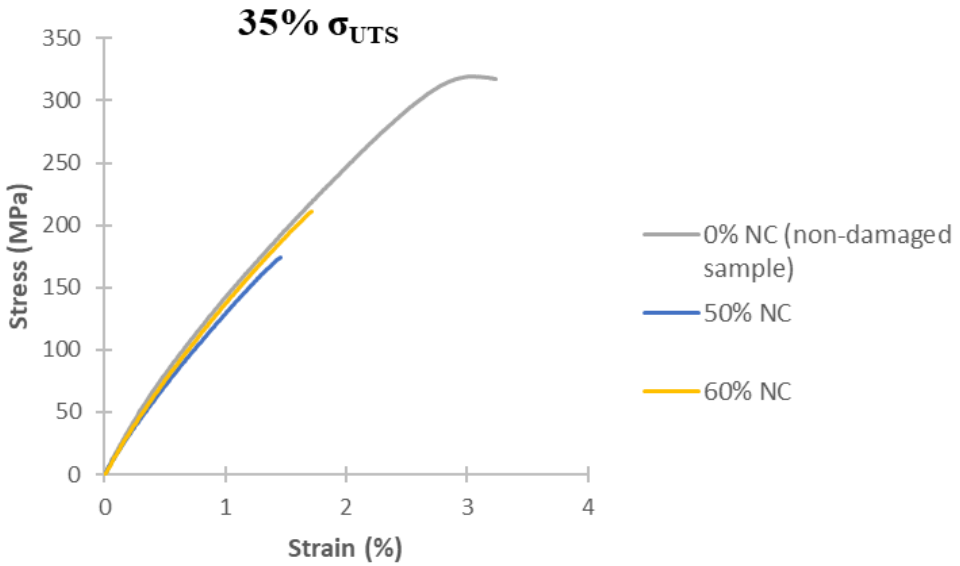

Figure 114: Stress-strain curves of a reference sample and two samples subjected to fatigue loading at a stress level of 35% σ_{UTS} for 50% and 60% of the number of cycles to failure and impacted at an energy level of 4.3 J showing the residual strength reduction.

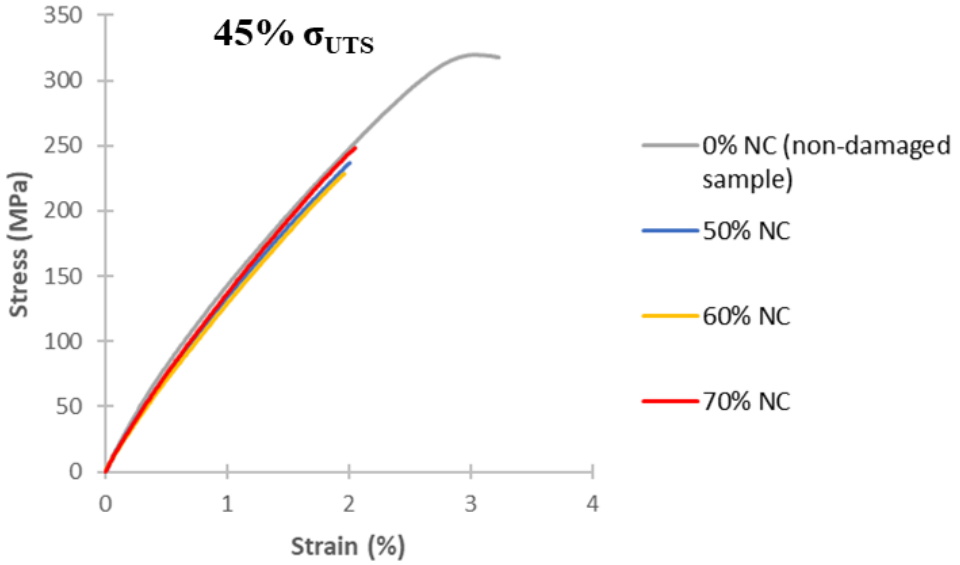

Figure 115: Stress-strain curves of a reference sample and two samples subjected to fatigue loading at a stress level of 45% σ_{UTS} for 50%, 60% and 70% of the number of cycles to failure and impacted at an energy level of 4.3 J showing the residual strength reduction.

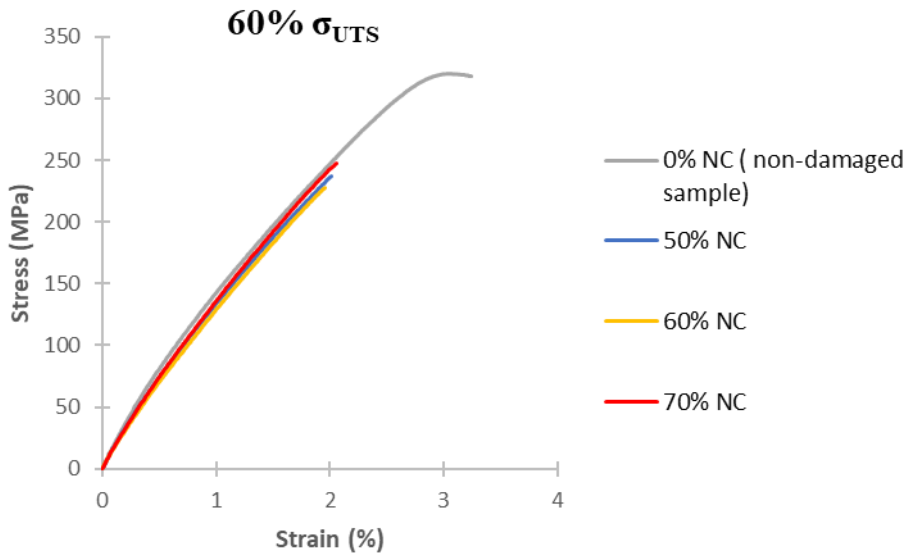

Figure 116: Stress-strain curves of a reference sample and two samples subjected to fatigue loading at a stress level of 60% σ_{UTS} for 50%, 60% and 70% of the number of cycles to failure and impacted at an energy level of 4.3 J showing the residual strength reduction.

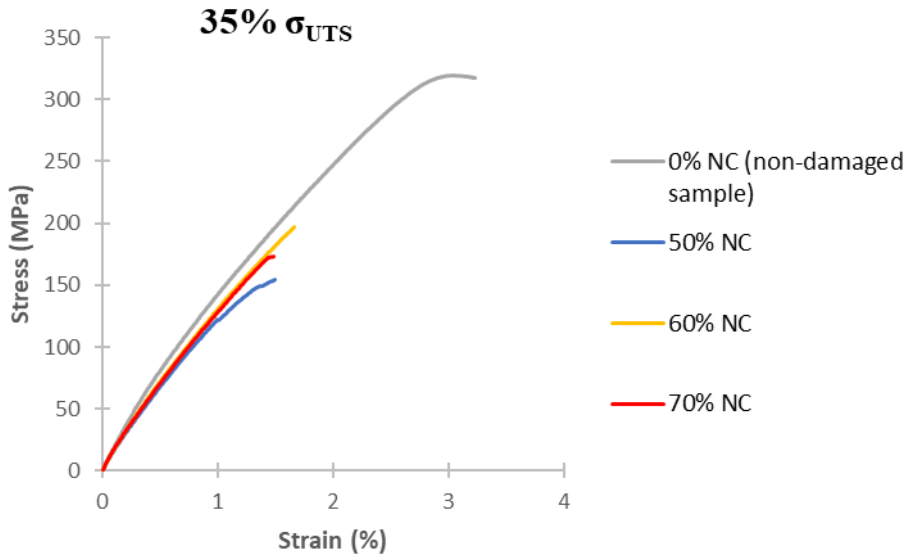

Figure 117: Stress-strain curves of a reference sample and three samples subjected to fatigue loading at a stress level of 35% σ_{UTS} for 50%, 60% and 70% of the number of cycles to failure and impacted at an energy level of 8.6 J showing the residual strength reduction.

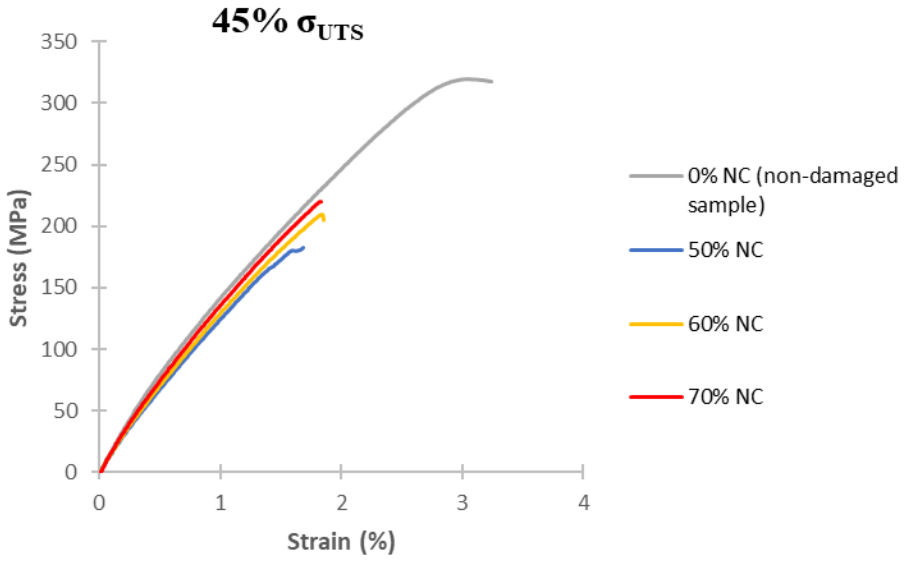

Figure 118: Stress-strain curves of a reference sample and two samples subjected to fatigue loading at a stress level of 45% σ_{UTS} for 50%, 60% and 70% of the number of cycles to failure and impacted at an energy level of 8.6 J showing the residual strength reduction.

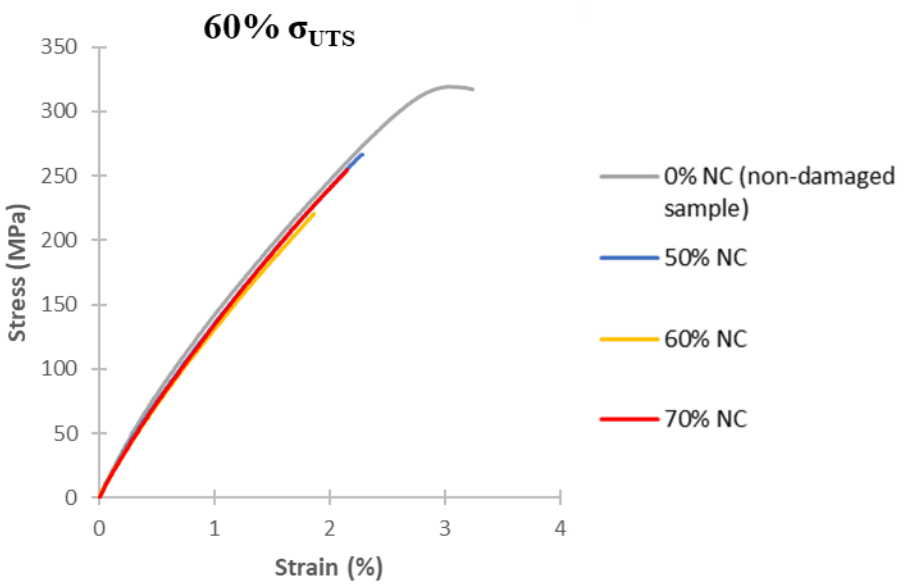

Figure 119: Stress-strain curves of a reference sample and two samples subjected to fatigue loading at a stress level of 60% σ_{UTS} for 50%, 60% and 70% of the number of cycles to failure and impacted at an energy level of 8.6 J showing the residual strength reduction.

As mentioned in section 4.1, the employed impact energies for the dog bone geometry (to realize impact post-fatigue tests) are chosen by dividing the impact energies used during the chapter II by a factor of r = 2.85 (r = Minimum width of the dog-bone geometry/ Width of the impact plate). Consequently, one can establish a comparison between post-impact tensile results and those retrieved during the tensile tests on samples subjected to impact-fatigue coupling.

Figure 120, Figure 121 and **Figure 122** represent the values of the residual strength of a sample that underwent low-velocity impact event and those subjected to impact post-fatigue. The samples presented in each figure are impacted at an equivalent energy, namely (a) 4.3 J/35 mm (energy/width), and 8.6 J/35 mm. On all the figures, the values of the residual strength of the sample that went through low-velocity impact tests at an equivalent energy (geometry equivalence) are presented in blue. In most of the cases, the residual strength values of the impact post-fatigue samples are below the values corresponding to the sample subjected to low-velocity impact event only. However, in some cases, namely the set of samples pre-loaded in fatigue at a maximum stress level of 45% σ_{UTS} then impacted at an average energy level of 8.6 J, discrepancies are found. Indeed, the values of the residual strength of this set of impact post-fatigue samples are higher than this of a sample undergoing exclusively an impact event.

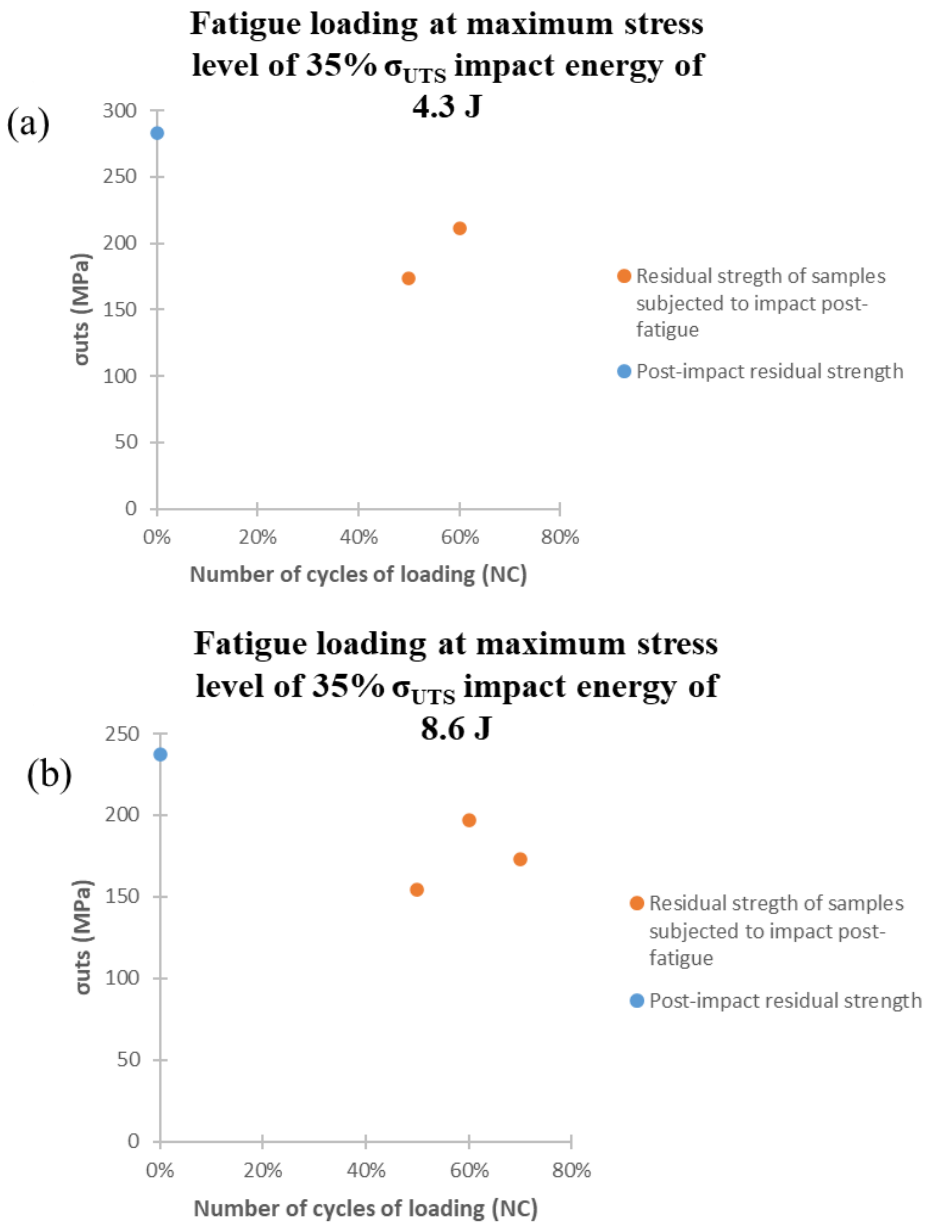

Figure 120: Values of the residual strength of the samples subjected to impact post-fatigue (35% σ_{UTS}) at energy levels of (a) 4.3 J and (b) 8.6 J.

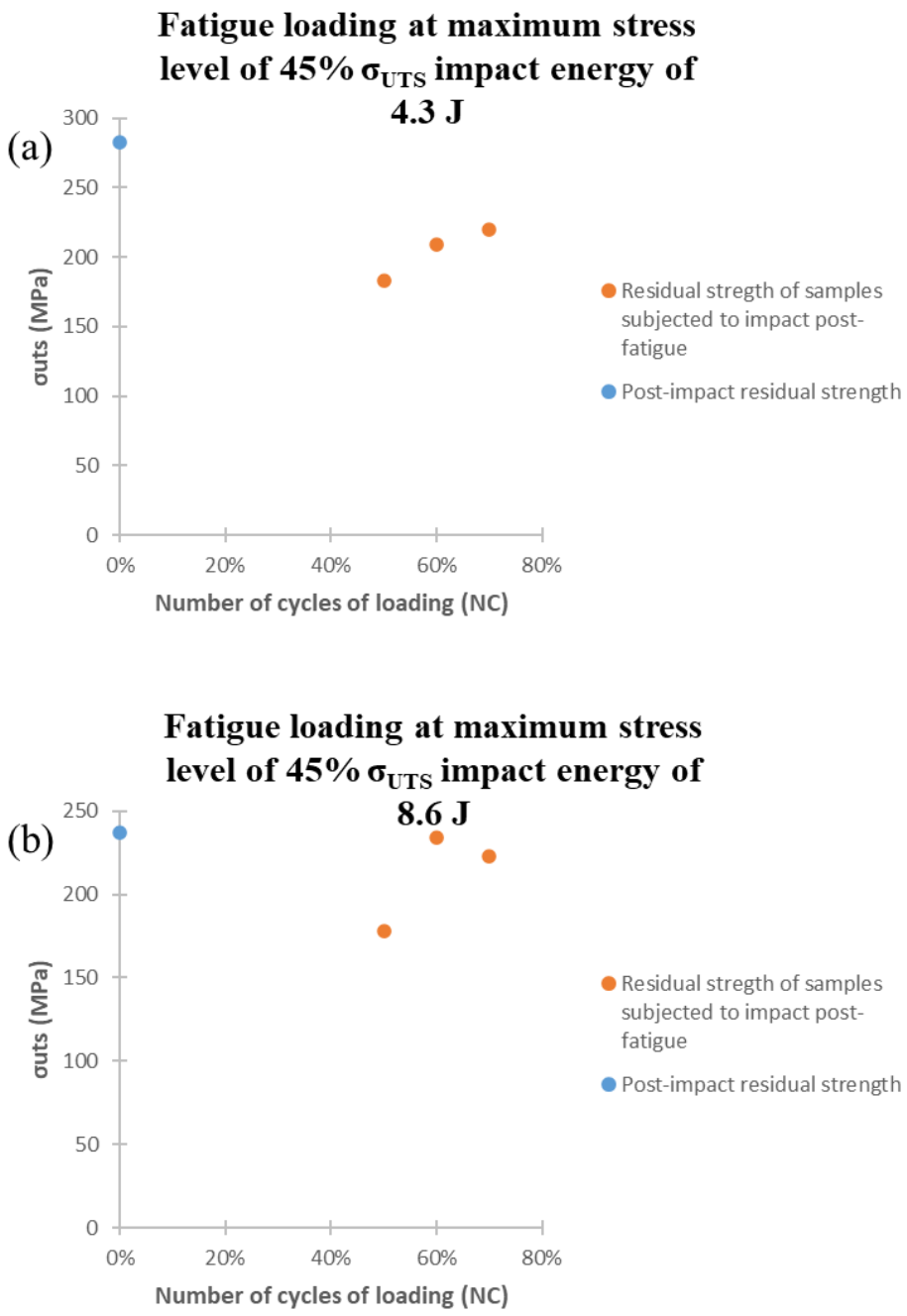

Figure 121: Values of the residual strength of the samples subjected to impact post-fatigue (45% σ_{UTS}) at energy levels of (a) 4.3 J and (b) 8.6 J.

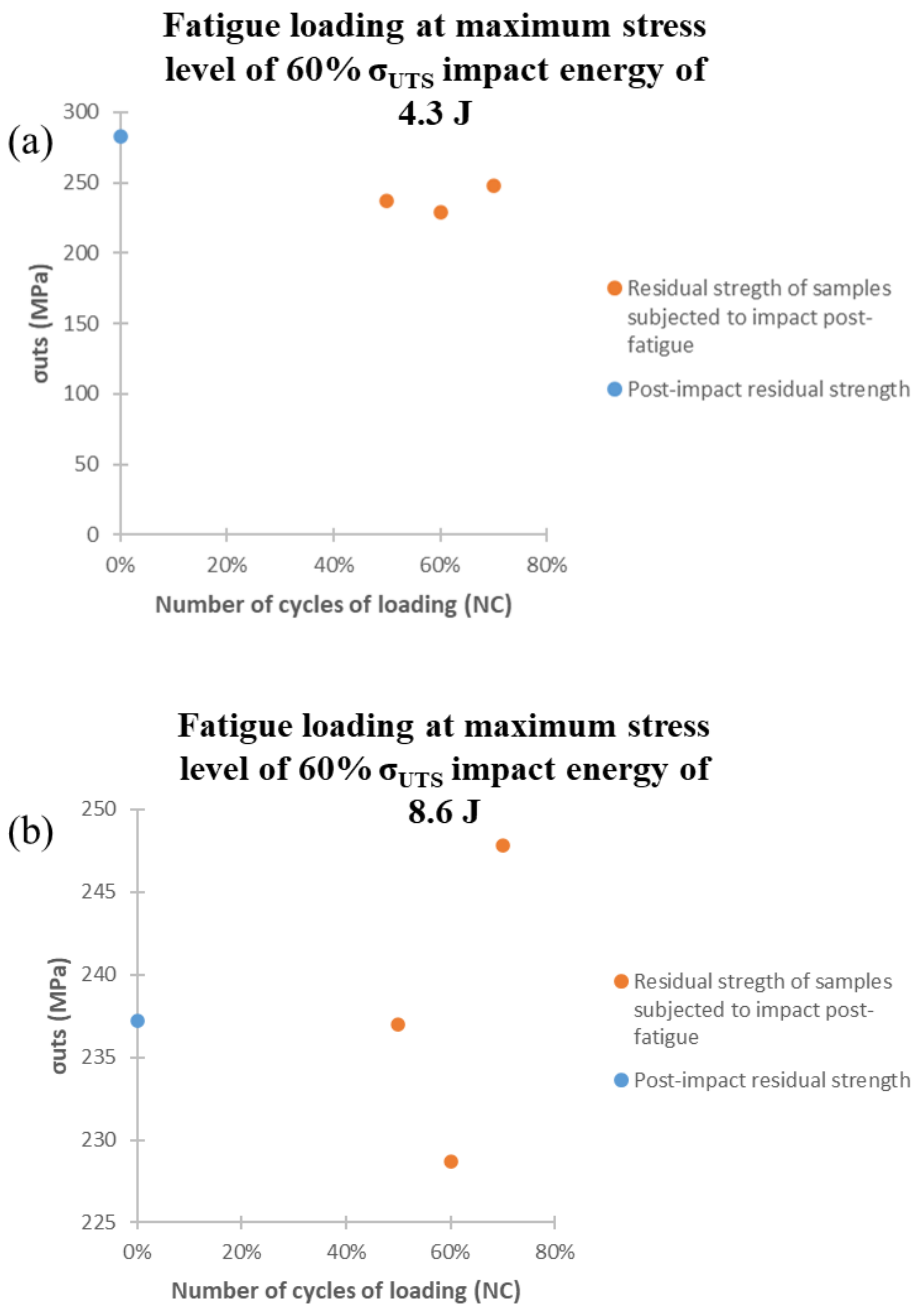

Figure 122: Values of the residual strength of the samples subjected to impact post-fatigue (60% σ_{UTS}) at energy levels of (a) 4.3 J and (b) 8.6 J.

Figure 123, **Figure 124** and **Figure 125** represent the ultimate tensile strength of a non-damaged sample (yellow) and those of: samples subjected to fatigue loading (maximum stress level of 35%, 45% and 60% σ_{UTS} ,respectively) (blue), samples subjected to impact post-fatigue (maximum stress level of 35%, 45% and 60% σ_{UTS} ,respectively) impacted at energy level of 4.3 J (orange) and samples subjected to impact post-fatigue impacted at energy level of 8.6 J

(grey). In all figures, one can clearly see the difference between damaged and non-damaged samples. Nevertheless, the experimental findings do not exhibit a clear trend in terms of evolution. A gradual decrease in the value of the residual strength was expected with the increasing number of loading cycles and low-velocity impact energy.

As explained in the previous chapter, such discrepancies are expected when assessing fatigue damage in composite materials. These experimental findings can be explained by multiple parameters such as:

(i) the fact that the samples are not completely identical, since the thermo-compression process may induce some variability in the microstructure and the cutting of the samples was done in different areas of the composite plates

(ii) the geometry of the sample: the strength of a specimen with a whole yarn at the edges of the smallest section will not behave like the one with an inter-yarn area or a part of the yarn at the edges

(iii) the variability and the dissipative nature of the fatigue damage

(iv) Micro-damage present in the composite prior to the different loadings caused by the cutting process and/or the manufacturing process

Consequently, this section is considered as a preliminary-testing phase allowing to provide preliminary results and to capture the different trends. The present work should be completed by a thorough experimental campaign enabling to provide a quantitative assessment of damage induced by the impact post-fatigue. Furthermore, it is important to have enough samples to quantify the influence of combining fatigue loading and low-velocity impact events, on the service life of the polyamide-based composite material.

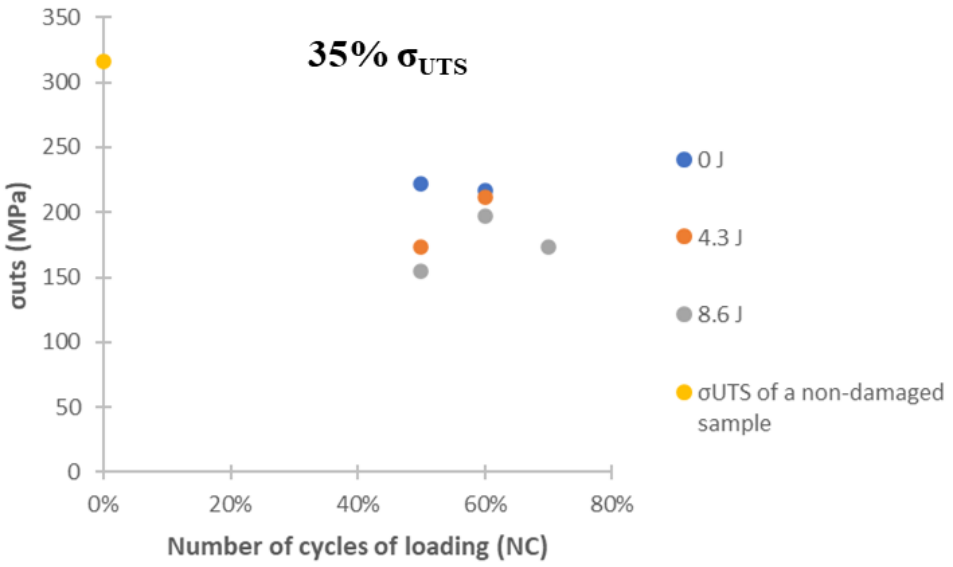

Figure 123: The ultimate tensile strength of a non-damaged sample (yellow) and those of: samples subjected to fatigue loading (maximum stress level of 35% σ_{UTS}) (blue), samples subjected to impact post-fatigue (maximum stress level of 35% σ_{UTS}) impacted at energy level of 4.3 J (orange) and samples subjected to impact post-fatigue impacted at energy level of 8.6 J (grey).

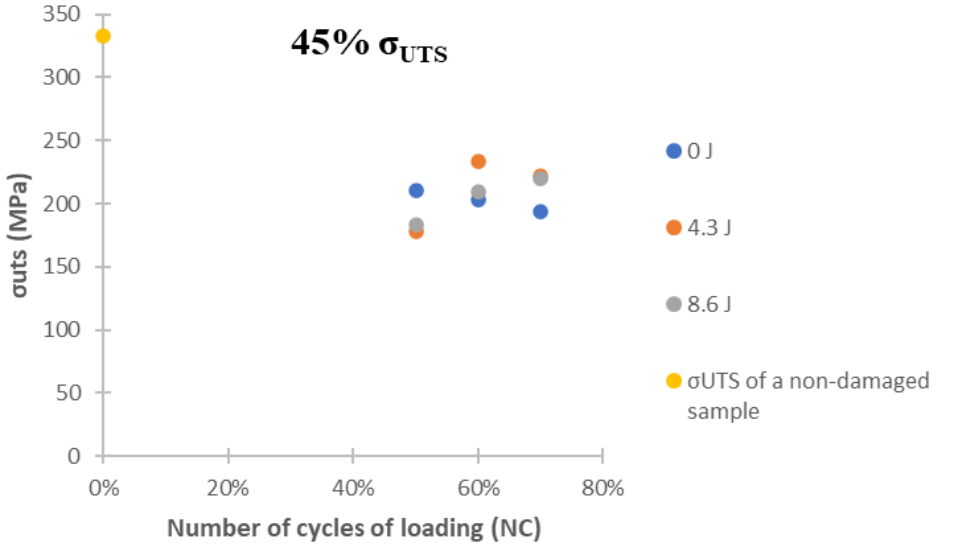

Figure 124: The ultimate tensile strength of a non-damaged sample (yellow) and those of: samples subjected to fatigue loading (maximum stress level of 45% σ_{UTS}) (blue), samples subjected to impact post-fatigue (maximum stress level of 45% σ_{UTS}) impacted at energy level of 4.3 J (orange) and samples subjected to impact post-fatigue impacted at energy level of 8.6 J (grey).

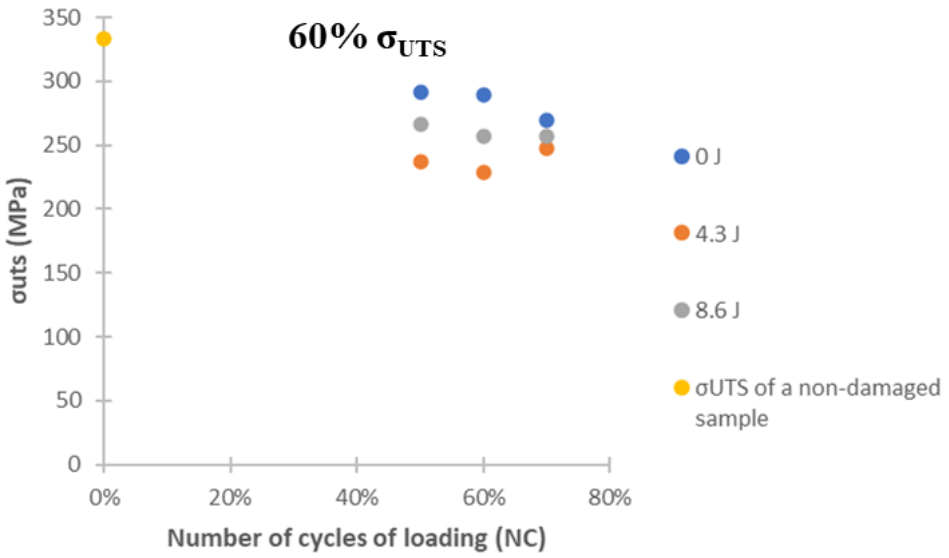

Figure 125: The ultimate tensile strength of a non-damaged sample (yellow) and those of: samples subjected to fatigue loading (maximum stress level of 60% σ_{UTS}) (blue), samples subjected to impact post-fatigue (maximum stress level of 60% σ_{UTS}) impacted at energy level of 4.3 J (orange) and samples subjected to impact post-fatigue impacted at energy level of 8.6 J (grey).

V. Conclusion

The evaluation and the assessment of the influence of damage resulting from low-velocity impact events, tension-tension fatigue loadings and impact post-fatigue combination on the residual properties, has been discussed in this chapter. Quasi-static tensile tests have been achieved on samples subjected to impact at different levels of energies, fatigue tests at different combination of parameters reflecting the condition that the composite material need to withstand, and a combination of impact and fatigue loading, respectively. The impact energies along with the fatigue parameters are chosen to reproduce similar testing conditions and to enable to compare the different results. One should remind that the aim of this research work is not to characterize the behavior of the polyamide-based material, but to provide a qualitative assessment of the effect of the different loading modes on the residual properties of the composite material. IR monitoring and post-mortem investigation took place during and after the mechanical tests to identify the area most likely to contain the final rupture initiation and to analyze the cracks propagation pattern. These observations have shown that, in all samples, damaged and non-damaged, the final rupture is initiated from the edges of the samples. Indeed, it was found that:

(i) on the samples subjected to low-velocity impact events, the cracks start at the edges and propagate to join the post-impact damage localized in the center, before causing the final failure. The post-mortem observations of the samples have shown that on the impacted surface, the sample rupture follows a straight line, while deviations in the cracks' propagation pattern occur to join the pre-induced impact damage, are noticed on the non-impacted surface.

(ii) on the samples subjected to fatigue loadings, the final rupture follows a clean straight line, regardless of the loading conditions.

(iii) on the samples subjected to impact post-fatigue loadings, the rupture patterns depend on the impact energy and the extent of damage resulting from the cyclic loading. Indeed, the final rupture does not necessarily go through the central impact damage. One can assume that this is due to localized and deteriorated zones resulting from fatigue loading.

The mechanical response of the different samples under quasi-static tensile loading have been assessed. It was found that:

(i) the samples subjected to a low-velocity impact event exhibit two stages of damage growth as the impact energy increases. It was shown that the magnitude of the residual strength reduction depends on the impact energy. The first stage, corresponding to impact energies ranging from 7 J to 12.6 J, points-out the initiation and propagation phase from the first to the second layer of the laminate, as seen through X-ray tomography analysis. This stage is characterized by matrix cracking and fibers breakage. A minor but quantifiable decrease of less than 5% of the residual strength of the composite is noticed. The second stage, with energies varying from 12.6 J to 24 J, indicates the range of energies where the damage propagates in the second layer and through-thickness to the third layer of the woven composite. This stage is associated with the propagation and coupling of matrix micro-cracks, delamination and fibers breaking. The σ_{UTS} reduces about 13% to 30% in this stage, indicating that the composite is extremely damaged.

(ii) A difference in the values of σ_{UTS} of samples subjected to fatigue loadings and that of a non-loaded sample is noticed. Three levels of maximum stress loads are considered, and the fatigue tests are conducted at different stage of the number of cycles to failure (composite's fatigue life). It was shown that the samples loaded at the highest maximum stress level (60%) exhibit lower loss of the residual strength

as the number of cycles varies. The experimental findings point-out to the fact that the final rupture, when the composite has undergone cyclic loadings at high maximum stress levels, occur suddenly after 70% NC since the loss in the residual strength between 50% and 70% NC is less than 20%. In addition, the residual resistance values relative to the two sets of samples loaded at 35% and 45% σ_{UTS}, respectively, are in the same range of magnitude.

(iii) A clear gap between the values of the residual strength of the non-loaded sample, the samples subjected to low-velocity impact events and fatigue tests, respectively, and these of the samples undergoing impact post-fatigue loading was found. However, a quantitative assessment of the experimental findings has not been the purpose of this research project. A vast number of samples undergone the necessary mechanical experiences was not available and therefore, only qualitative conclusions have been drawn on this particular research aspect, based on limited number of samples. Moreover, interesting observations have been made that could be further investigated in the future. Indeed, the objective of the post-fatigue impact testing campaign is to preliminary observe the decrease of the residual properties when coupling two modes of loading, namely fatigue and low-velocity impact.

Consequently, the present work consists of the proposition of an experimental methodology to assess the residual properties after an event (impact, fatigue loading and impact post-fatigue). The achieved preliminary study should be completed by a thorough experimental campaign allowing a quantitative assessment of the damage induced by the impact post-fatigue. It is important to consider enough samples to quantify the loss in the residual properties due to fatigue loading and low-velocity impact events.

VI. References

Agarwal, B., & Broutman, LJ Chandrashekhara, K. (2006). Analysis and performance of fiber composites. In *Materials Science and Engineering: A* (3rd editio, Vol. 151, Issue 1). John Wiley & Sons. https://doi.org/10.1016/0921-5093(92)90189-8

Curtis, P. (2000). Mechanical Testing of Advanced Fibre Composites. In J. Hodgkinson (Ed.), *Mechanical Testing of Advanced Fibre Composites*. Woodhead publishing limited. https://doi.org/10.1201/9781439822791

Dhakal, H. ., Zhang, Z. Y., Bennett, N., & Reis, P. N. B. (2012). Low-velocity impact response of non-woven hemp fibre reinforced unsaturated polyester composites: Influence of impactor geometry and impact velocity. *Composite Structures*, *94*(9), 2756–2763.

Reifsnider, K., Schulte, K., & Duke, J. (1983). *Long-Term Fatigue Behavior of Composite Materials*.

Shahzad, A. (2018). Investigation into fatigue strength of natural/synthetic fiber-based composite materials. In *Mechanical and Physical Testing of Biocomposites, Fibre-Reinforced Composites and Hybrid Composites*. Elsevier Ltd. https://doi.org/10.1016/B978-0-08-102292-4.00012-6

General conclusions and further works

The present work aimed at the investigation of damage in a polyamide-based composite intended for structural automobile applications. The objective was to propose experimental methodologies founded on Non-Destructive Evaluation (NDE) methods enabling to evaluate the damage state of the PA66/6 reinforced composite subjected to mechanical loading. The NDE experimental approach focused on two main axes: (i) the study of the mechanical response of the composite material undergoing three types of applied load, namely low-velocity impacts, fatigue loadings and impact post-fatigue loading, and (ii) the assessment and the characterization of the induced damage, in the microscopic and the mesoscopic scale, using suitable NDE methods.

For the low-velocity impact loading, a total of twenty-one samples, pre-conditioned at 50% RH, were impacted at energies ranging between 6.7 J and 24 J. The results of seven samples, representing different levels and ranges of the barely visible impact damage (BVID), were discussed. The mechanical data relative to the drop weight impact tests were analyzed and processed, and the different parameters were extracted. It was found that the maximum force, the maximum deflection, as well as the absorbed energy increased with the increase of the impact energy.

A thorough experimental procedure consisting of a meticulous characterization of external (surface) and through-thickness damage was followed. Visual inspection pointed out to the fact that the damage was more diffused on the non-impacted surfaces as the impact energy raised. Indeed, the cracks network propagate along the fibers' axes and their size grew as the impact energy increased. An ultrasound-based method consisting of bulk waves propagation was performed to measure and estimate the permanent indentation (PI), i.e., the print left the impactor on the sample after an impact event. The efficiency of the C-scan based-method was verified using optical profilometry. The two methods exhibited an excellent correlation. The experimental findings showed that the depth of the PI raised as the impact energy grew.

Through-thickness X-ray micro-computed tomography (mCT) was carried out to identify the different damage stages namely, the initiation, the accumulation and the propagation. The investigation of the 3D reconstruction of damaged volumes indicated that the detected damage mechanisms were similar to those observed post-monotonic tension loading (Pomarède et al.,

2018). Furthermore, matrix cracking was the first damage mechanism to appear on the non-impacted surface of the thin laminate starting from an impact energy of 10.54 J. As the latter kept rising, the micro-cracks grew on surface and diffused into and between the yarns resulting in fibers' rupture and the deterioration of the fiber/matrix interface. Delamination occurred as the cracks propagated from layer to layer leading to the degradation of the multilayer composite integrity.

Quantitative assessment of the impact damage was then achieved using ultrasound-based methods. First, a stiffness reduction estimation method was employed. It was founded on the determination of the velocity of propagation of bulk waves in different planes of the investigated structure. This method pointed-out to the fact that C_{11} and C_{33} were the most impacted components. All the experimental findings were cross-linked and led to an important conclusion: by estimating the PI, one could predict the damage state and through-thickness propagation and capture the evolution of the relative stiffness reduction. Afterwards, a Lamb waves-based method consisting of the assessment of the wave's velocity of propagation as a function of the angle of emission/reception of the ultrasonic signal, simultaneously, was proposed. This method enabled the establishment and the assessment of velocity profiles for all the investigated samples, representative of the stiffness evolution. To quantify the influence of induced damage of the propagation velocity, a damage indicator consisting of the estimation of the area under the curves was proposed. A good correlation between PI measurement and the suggested Lamb waves-based damage indicator revealed that both indicators were very efficient and reliable when dealing with low-velocity impact damage. Consequently, the proposed method could be used individually to reflect the damage state resulting from LVI (Low-Velocity Impact) events.

Tension-tension fatigue tests were carried out on sample with a special geometry developed in this work. Knowing that the objective was not to mechanically characterize the behavior of the composite under cyclic loading, the geometry of the samples was chosen to contain damage in the gauge area of the sample, and more specifically in the central area. The geometry was verified by performing quasi-static tensile tests and tension-tension fatigue tests. Fatigue tests at a frequency of 3 Hz were performed, first until failure to reconstruct the Wohler curve. Interrupted fatigue tests were achieved afterwards to initiate progressive damage in the samples. The assessment of the mechanical measurements revealed scattered experimental findings suggesting a difference in the response of the samples due to the microstructure variability and the nature of the cyclic loading. In addition, the fatigue damage resulting from cyclic loading

was categorized as diffused damage in the entire section, unlike impact damage that is more localized in the impacted area. The developed Lamb waves-based method was tested on the pos-fatigue sample. The main objective was to confirm the detectability of a diffused damage using the suggested Lamb waves-based technique. The discrepancy of the results, as already seen during mechanical data analysis, was noticed. To establish if the discrepancy was related to the mechanical test (behavior of the samples under fatigue loadings), the Lamb waves investigation results were compared to the voids content measurement performed using mCT. The comparison demonstrated the effectiveness of the method in the detection of different stages of damage. Consequently, the proposed Lamb waves propagation technique proved its reliability and performance in the detection and quantification of different types of surfaces and through-thickness damage. Ultrasonic stiffness reduction method was also conducted on the samples subjected to cyclic loading. However, scans at different angle and planes, enabling the estimation of the velocities of the longitudinal mode, were not possible to achieve due to the geometrical limitations of the experimental set-up. Moreover, the method enabled to obtain complete velocity profiles in one of the scanned planes that showed changes the velocity of the longitudinal mode as the applied loading conditions varied. These results indicated that the latter could be employed as a qualitative damage indicator for the studied composite.

As a final step of the present research work, the influence of damage, resulting from LVI events, tension-tension fatigue loading and impact post-fatigue, on the residual strength and stiffness, respectively of the multilayered woven composite was assessed. Monotonic tensile tests until failure were performed on samples, conditioned at 50% RH, subjected to drop-weight impact tests at various levels of energies, cyclic loading at different combinations of stress levels and numbers of cycles' to failure, and impact post-fatigue loading, respectively. For comparison reasons, the testing parameters and geometries were equivalent and comparable between all three configurations of loading. The scope of this experimental campaign was to qualitatively evaluate the influence of the pre-loading on the residual properties of the laminate composite. It was found that regardless of the loading conditions, the final rupture was always initiated from the edges of the samples. Moreover, on the samples that underwent LVI events, cracks networks started at the edge and diffused through the composite's section until joining the impact damage localized in the center. In terms of residual properties, no quantifiable variation was noticed in the values of the Young's modulus between damaged and non-damaged samples. However, when measuring the residual ultimate tensile strength, a gradual decrease of the values was observed as the impact energy increased. Consequently, one could

link the drop in the residual strength to the damage through-thickness propagation and permanent indentation.

The samples subjected to tension-tension fatigue tests all exhibited a final rupture following a clean straight line. Indeed, whatever the loading conditions, the maximum stress and the number of cycles of loading, the composite adopted the same rupture patterns as in the case of a non-loaded sample. Nevertheless, differences in terms of residual strength were noticed between non-loaded and loaded samples function of the loading conditions. It was found that the samples loaded at a maximum stress level of 60% σ_{UTS} demonstrated a loss of the residual strength ranging from 12% to 19%, depending on the number of cycles of the loading, which was lower than the samples loaded at 35% σ_{UTS} and 45% σ_{UTS} as maximum stress levels. Furthermore, as the maximum stress level decreased, the number of cycles of the loadings was considerably higher. Consequently, more important strength reduction was observed.

The combination of impact and fatigue loading was a very complex phenomenon. The prediction of the final rupture patterns and the residual strength depended on the understanding of the complex aspect of this type of combined load. Generally, the cracks were initiated on the edges and propagated until they join the localized impact damage, as noticed on the samples submitted to LVI tests only. However, some disturbances were also observed. As expected, the fatigue loading followed by LVI tests had a significant effect on the rupture patterns. Indeed, the final rupture did not always go through the impact damage. Nevertheless, fatigue loading was found to generate micro-damage in different areas of the samples leading hence to the deterioration of localized zones, making the final rupture more susceptible to occur in these areas. A clear difference between the residual strength of loaded and non-loaded samples was noticed. Due to the fact that a quantitative assessment was not the purpose of impact post-fatigue testing campaign, a vast number of samples were not available, therefore only qualitative conclusions were drawn on this particular research aspect. Thus, interesting observations in terms of rupture patterns were noticed discussed.

As further works, numerical simulation of the low-velocity impact tests, fatigue tests and impact-post fatigue tests can be achieved to compare and understand the kinetics of damage initiation and accumulation. The proposed Lamb waves-based method can then be performed to properly understand the wave propagation patterns when encountering any type of damage. This numerical simulation will help upgrade the method in such a way that one could understand how the ultrasonic waves propagate in the multilayered material and could identify

the part of the signals that are affected by the damage. Furthermore, the complex aspect of the studied composite makes the waves propagation patterns difficult to foresee.

Moreover, the concept of digital twins is more and more widespread in the industrial field. All the experimental the numerical results will help implement a data base that will be used to develop and validate the constitutive laws describing the behavior of the employed material at the microscale. The digital twins of the structures or the automotive parts are then subjected to different types of loading. The retrieved data are compared to those experimentally obtained on operational structures using the proposed Lamb waves method. The behavioral laws and the digital twins are consequently updated.

The proposed experimental Lamb waves propagation method can be automatized. Indeed, the previously assessed method in terms of effectiveness and performance can be tested and adjusted to be adapted to other types of materials. As a preliminary development process, this method was developed using research laboratory equipments. One can employ the same principle to develop a portable investigation device enabling the sensors (transducer) to rotate in order to perform the inspection operations without having to move or disassemble/ take apart the structure. This device can be used as a decision support tool with the help of the developed digital twin to determine the criticality of the damage. Indeed, the numerical simulations of a certain load or combination of loads can be representative of the damage state of the real structures and automotive parts. When comparing the signals recorded using this investigation device with those obtained using the numerical simulations, one can decide whether the structural part needs to be changed.

Résumé étendu

I. Introduction générale

La hausse des prix du pétrole et du carburant ainsi que les exigences européennes strictes en matière d'émissions de CO2 poussent l'industrie automobile à créer une nouvelle génération de voitures (EU Climate Action, 2019; US department of energy, 2011). L'aspect clé de cette approche est la fabrication de véhicules légers en remplaçant les éléments métalliques structurels par des matériaux légers à faible densité et propriétés mécaniques élevées (Böhm et al., 2020; Sarfraz et al., 2021). Pour atteindre cet objectif, l'intérêt pour l'utilisation de composites à base de polymères s'est accru au cours des dernières décennies(Ishikawa et al., 2018; Li et al., 2018; Lukaszewicz, 2013). Cet intérêt résulte de l'amélioration de certaines propriétés mécaniques, telles que le rapport résistance/poids, la résistance à la corrosion, etc. Les matériaux composites offrent une opportunité de concevoir des matériaux avec une large gamme de propriétés que l'on ne trouve pas dans les matériaux minéraux existants (Lopes & Ribeiro, 2012). De plus, en termes de production de masse, la flexibilité ainsi que la possibilité de faire du sur-mesure ont encouragé l'utilisation de matériaux composites dans l'industrie automobile (Cramer & Taggart, 2002; Lopes & Ribeiro, 2012).

Les éléments composites utilisés dans l'industrie automobile sont généralement divisés en deux catégories : (i) les composites qui résistent aux températures élevées et à l'humidité, et (ii) les composites destinés à améliorer les performances structurelles du véhicule (Lopes & Ribeiro, 2012). Ces derniers sont fortement sollicités, sont opérationnels près de leur limite de résistance mécanique et doivent respecter les exigences de sécurité et de sûreté opérationnelle. Par conséquent, l'identification des chargements potentielles que la structure composite peut subir en service et l'étude de son comportement sous ces chargements restent essentielles.

Malgré leur excellent rapport résistance/poids, les composites sont plus sensibles aux endommagements internes (Agrawal et al., 2013), notamment au délaminage qui peut se produire à différentes étapes de la vie de la structure (fabrication, opération de maintenance ou en service). De plus, les composites présentent des mécanismes d'endommagement qui sont différents de ceux qui se créent dans les matériaux métalliques en termes d'initiation et

d'accumulation. En effet, à l'échelle microscopique, les mécanismes d'endommagement vont se développer progressivement au cours du service et s'accumuler dans tout le volume du matériau. La combinaison des mécanismes concomitants entraîne la détérioration des propriétés locales conduisant à la rupture finale mésoscopique.

Les matériaux composites à base de thermoplastiques sont connus pour être très sensibles aux impacts à faible vitesse (LVI) (Sierakowski & Newaz, 1995) et aux chargements répétitives, telles que la fatigue. Ces deux types d'événements sont considérés comme des menaces pour l'intégrité des structures. Après un événement d'impact, de l'endommagement microscopique diffus est créé à travers l'épaisseur alors que seules de petites traces d'indentation, restent sur la surface impactée. Ce type d'endommagement, invisible, entraîne une réduction significative des propriétés mécaniques et influence donc considérablement les performances des structures composites. En effet, des études ont montré que l'endommagement interne lié aux événements d'impact réduisent les propriétés mécaniques de la structure de plus de 50% (Richardson & Wisheart, 1996; Shah et al., 2019). De plus, dans des conditions de chargement cyclique, la propagation et l'accumulation de l'endommagement se produisent dans la structure et peuvent entraîner une rupture en service catastrophiques.

Par conséquent, pour des raisons de sécurité, des plis supplémentaires sont ajoutés pour rendre les structures composites plus résistantes (Shah et al., 2019). Cependant, l'ajout des plis entraîne l'augmentation du poids des structures composites, réduisant ainsi leur compétitivité par rapport aux métaux. Ainsi, l'amélioration de la tolérance à endommagement des composites est d'une grande importance dans l'industrie du transport, notamment pour les applications automobiles. La prise de conscience de l'importance de la sécurité et de la fiabilité dans la conception et la résistance des pièces structurelles, ainsi qu'une identification et une évaluation correctes des endommagements survenant au cours de la vie en service sont essentielles pour respecter les normes de tolérance à l'endommagement. En effet, le risque de perte de vies humaines résultant d'une défaillance structurelle inattendue a motivé la communauté scientifique vers des projets innovants dans les différentes branches de l'ingénierie, dont la détection et l'évaluation de l'endommagement dans les composants automobiles.

Un grand intérêt est porté au Contrôle Non- Destructif (CND) comme moyen de détection précoce de l'endommagement. L'identification de l'endommagement à son début vise à prévenir les défaillances structurelles et à planifier la réparation ou le remplacement des composants endommagés. Par conséquent, des contrôles périodiques méticuleux de l'intégrité

des composants sont nécessaires. Les techniques prédominantes de CND visant à l'identification des dommages dans les structures composites comprennent la thermographie infrarouge, l'émission acoustique, la propagation des ondes ultrasonores, etc. Néanmoins, ces techniques ont été progressivement testées quant à leur capacité à rassembler à la fois la détectabilité et la faisabilité.

De nombreuses recherches portant sur la propagation des ondes ultrasonores ont été menées pour démontrer leur capacité exceptionnelle à inspecter de grandes structures, et leur grande sensibilité à détecter l'endommagement interne, tels que le délaminage. Il s'avère que l'investigation par ultrasons fournit des informations primordiales pour une évaluation de haute qualité de l'endommagement (Aymerich & Meili, 2000; Castaings et al., 2012). Dans le cas de structures en forme de plaques, les ondes ultrasonores élastiques guidées, connues également sous le nom d'ondes de Lamb, ont prouvé leur efficacité et leur fiabilité en matière de détection de l'endommagement. En outre, la capacité de sélectionner les modes et les fréquences rend la détection et la localisation de l'endommagement en surface, comme les microfissures et la corrosion, et les dommages interlaminaires précises (Su & Ye, 2008). Leur utilisation polyvalente a encouragé la réalisation de recherches approfondies pour développer des outils de détection de l'endommagement qui soient faciles à utiliser, efficaces et peu coûteux.

Le présent projet de recherche est réalisé dans le cadre de l'OpenLab "Materials and processess" créé et financé par Stellantis. La démarche ' Open innovation' adoptée par l'ancien Groupe PSA réunit plusieurs partenaires scientifiques : Arts et Métiers Sciences et Technologies, GeorgiaTech Lorraine (Georgia Tech-CNRS IRL 2958). L'objectif des OpenLabs est d'associer des entreprises scientifiques aux partenaires académiques les plus avancés dans leur domaine afin de bénéficier de leur expertise, d'avoir accès aux meilleures connaissances scientifiques et technologiques possibles et d'explorer de nouveaux champs de recherche. Cette recherche consiste en un partenariat entre Stellantis, le laboratoire de mécanique, microstructures et matériaux (LEM3-UMR CNRS 7239) et le laboratoire d'ultrasons et de contrôle non destructif (GeorgiaTech-Lorraine).

Ce travail de recherche porte sur l'étude et l'évaluation non destructive de l'endommagement induits dans un composite à base de polyamide renforcé par un tissu de fibre de verre destiné à une application structurelle dans l'industrie automobile. L'objectif principal est de développer une approche expérimentale qui permet de détecter et de quantifier l'état d'endommagement des structures composites soumises à deux types de chargement qu'une structure composite typique

peut subir en service, à savoir un impact à faible vitesse et un chargement en fatigue ainsi que la combinaison des deux chargements. Le composite à base de thermoplastique étudié, appelé ci-après VizilonTM SB63G1-T1.5-S3, est fabriqué par Dupont De Nemours et est constitué de trois couches de fibres de verre tissées imprégnées dans une matrice polyamide 66/6. Des recherches antérieures réalisées en 2013 sur le même matériau ont indiqué qu'il était possible de détecter des endommagements critiques dans ce matériau. Pomarède (Pomarède, 2018) a étudié le comportement du composite Vizilon employé par Stellantis (Groupe PSA) soumis à des chargements de type quasi-statique. Plusieurs techniques de CND ont été développées et employées pour évaluer l'endommagement résultant des chargements mécaniques. Deux nouveaux indicateurs d'endommagement qui reposent sur la propagation des ondes ultrasonores ont été proposés et ont montré leur efficacité pour estimer et quantifier le niveau d'endommagement de la structure composite causé par des chargements de traction quasi-statiques. L'objectif principal de ce travail est de proposer un outil CND pratique, facile à utiliser et efficace qui détecte et estime l'état d'endommagement de la structure composite quel que soit le type d'endommagement induit.

Pour ce faire, ce manuscrit est structuré comme suit :

- Une présentation du matériau de l'étude, sa sensibilité à la température et à l'humidité relative ainsi que ses propriétés mécaniques.

- Une étude expérimentale approfondie de l'endommagement résultant des événements d'impact à faible vitesse. Une procédure expérimentale détaillée permettant d'étudier et de quantifier l'endommagement est proposée.

- Une étude expérimentale de l'endommagement résultant de chargements en fatigue (traction-traction) ainsi que sa détection grâce aux méthodes déjà présentées.

- Une estimation des propriétés résiduelles post-chargements (impact, fatigue et impact post-fatigue).

II. Matériau de l'étude

Le matériau de l'étude est un composite tissé sergé 2.2 appelé VizilonTM SB63G1-T1.5-S3, fabriqué par DuPont de Nemours par thermocompression. Il s'agit d'un co-polyamide 6.6 / 6 (matrice polymère thermoplastique semi-cristalline) renforcé par une superposition de trois couches de fibres de verre en tissu équilibré orientées à 0°/90° (correspondant respectivement aux sens de la trame et de la chaîne). Les plaques composites ont une épaisseur de 1,53 mm, avec un rapport de poids de fibres de 63% correspondant à une fraction volumique de fibres de 43%.

Le **Tableau 1,** fourni par DuPont de Nemours, présente la densité, le module d'Young (E) et la résistance ultime (σ_{UTS}) et la déformation (ε_{UTS}) du matériau composite étudié. La microstructure et l'architecture du renforcement du matériau sont présentées sur la **Figure 126.**

Pomarède (Pomarède 2018) a étudié la réponse en traction du composite renforcé PA6.6/6 sous deux configurations, 0° et 45°. En termes de constantes élastiques, les composantes de la matrice de rigidité sont déterminées expérimentalement (Pomarède, 2018) et sont comparées à celles obtenues numériquement par homogénéisation périodique (Praud, 2018) comme représenté sur la **Figure 126.**

Pour la réponse globale du matériau, il est montré que le comportement mécanique est fortement influencé par l'orientation des fibres. En effet, sous chargement en traction, le matériau en configuration 0° (ainsi que 90°) présente une réponse linéaire et fragile alors qu'en configuration 45°, le matériau présente une réponse ductile non linéaire due à la rhéologie de la matrice. Des courbes typiques de contrainte-déformation montrant la réponse du PA6.6/6 renforcé de verre tissé à 0° (ou 90°) et celle à 45° sont données dans la **Figure 127.**

Dans le présent travail, des essais d'impact sont effectués sur des échantillons découpés par jet d'eau. Les plaques ont une forme rectangulaire de 100 par 150 mm et une épaisseur de 1,53 mm, en accord avec les normes ASTM D7136/D7136M. L'état initial non endommagé est examiné et vérifié pour tous les échantillons par C-scan. Les échantillons sont ensuite conditionnés à 50% d'humidité relative.

Tableau 1 : Caractéristiques mécaniques du composite PA6/66 renforcé de fibres de verre tissées.

Composantes de la matrice de rigidité (GPa)	**C_{11}**	**C_{12}**	**C_{13}**	**C_{22}**	**C_{23}**	**C_{33}**	**C_{44}**	**C_{55}**	**C_{66}**
Homogénéisation périodique	**20**	**2.1**	**1.5**	**20**	**1.5**	**4.5**	**2.3**	**1.3**	**1.3**
Expérimentalement	**22.21 (0.2)**	**2.57 (0.15)**	**1.41 (0.76)**	**21.81 (0.08)**	**--**	**4.1 (0.07)**	**2.33 (0.09)**	**1.58 (0.21)**	**--**

Caractéristiques mécaniques	Densité	E_0°(GPa) direction chaîne	E_90° (GPa) direction trame	σ_{UTS} (MPa) direction chaîne	ε_{UTS} (%) direction chaîne
	1.78	17.7	18.1	303	1.9

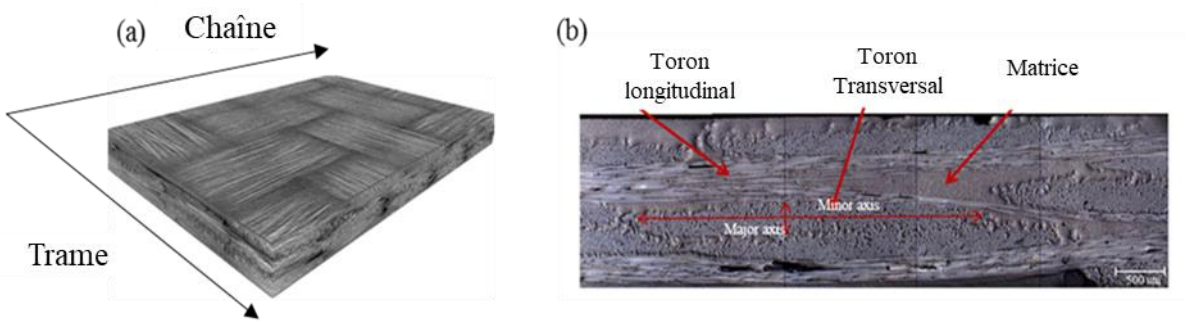

Figure 126 : Observation microscopique de la mésostructure (a) et de la microstructure (b) du composite tissu de verre-PA66-6 montrant l'orientation de la chaîne et de la trame (Pomarède, 2018).

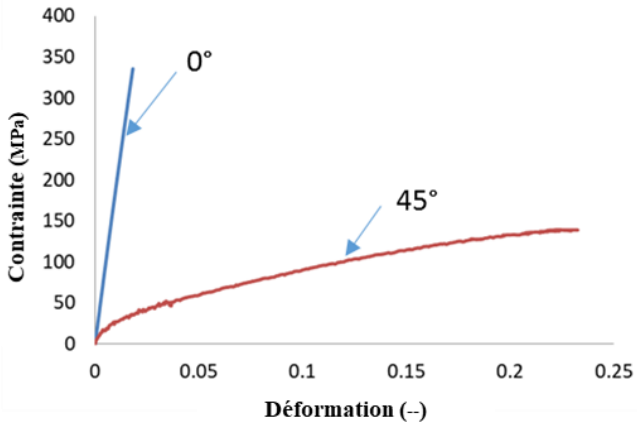

Figure 127 : Contrainte-déformation du composite PA66-6 renforcé de fibres de verre tissées sous chargement quasi-statique dans les directions 0° et 45° (Pomarède, 2018).

III. Impact à faible vitesse

1. Procédure expérimentale

La géométrie de l'échantillon est choisie en accord avec les normes ASTM D7136/D7136M. Les essais d'impact à basse vitesse sont effectués sur des plaques de forme rectangulaire de dimensions 100 par 150 mm et d'une épaisseur de 1,6 mm conditionnées à 50% d'humidité relative.

Les essais d'impact sont réalisés à l'aide d'un dispositif d'essai équipé d'un impacteur de 1,02 kg ayant une extrémité hémisphérique de 16 mm de diamètre. Il convient de mentionner qu'un assemblage d'une série de masses est utilisé pour atteindre la masse désirée. Le dispositif expérimental, est composé d'un capteur de charge piézoélectrique et de deux capteurs de déplacement laser, ainsi que d'un système d'acquisition de données. Les plaques composites sont serrées aux deux extrémités. Le déplacement de l'échantillon est ensuite mesuré sous la plaque impactée à l'aide d'un capteur de déplacement laser. L'acquisition du déplacement de l'impacteur, le déplacement du centre de la plaque et la force de contact sont mesurés pour l'analyse des données. En variant uniquement la hauteur de l'impact, différents niveaux d'énergie sont obtenus.

Vingt et un échantillons sont impactés à des hauteurs variant de 1 m à 3 m, trois échantillons par hauteur choisie. En effet, pour des raisons de répétabilité, et pour réduire les incertitudes expérimentales, chaque trois échantillons sont impactés de la même hauteur. En raison du grand nombre d'échantillons considérés, les résultats de seulement sept d'entre eux sont discutés.

Le post-traitement des données mécaniques permet de calculer la vitesse d'impact, l'énergie d'impact réelle et l'énergie absorbée. En effet, à partir de la courbe déplacement-temps de l'impacteur, la vitesse d'impact est estimée. Elle consiste en la pente de la première partie de la courbe (**Figure 128**). Ainsi l'énergie réelle d'impact est calculée. La deuxième partie de ce même graphique représente le déplacement de l'impacteur après l'évènement d'impact. En effet, elle consiste en le rebond de l'impacteur après avoir percuté l'échantillon. L'énergie absorbée est calculée à partir de la différence des carrés des deux vitesses. Un exemple illustrant les vitesses estimées à l'aide de la courbe déplacement-temps correspondant à l'essai d'impact de l'échantillon impacté à 12,6 J est présenté dans la **Figure 128**. Les paramètres calculés, à savoir la vitesse d'impact, l'énergie d'impact réelle et l'énergie absorbée pour les sept échantillons choisis, sont représentés dans le **Tableau 2.**

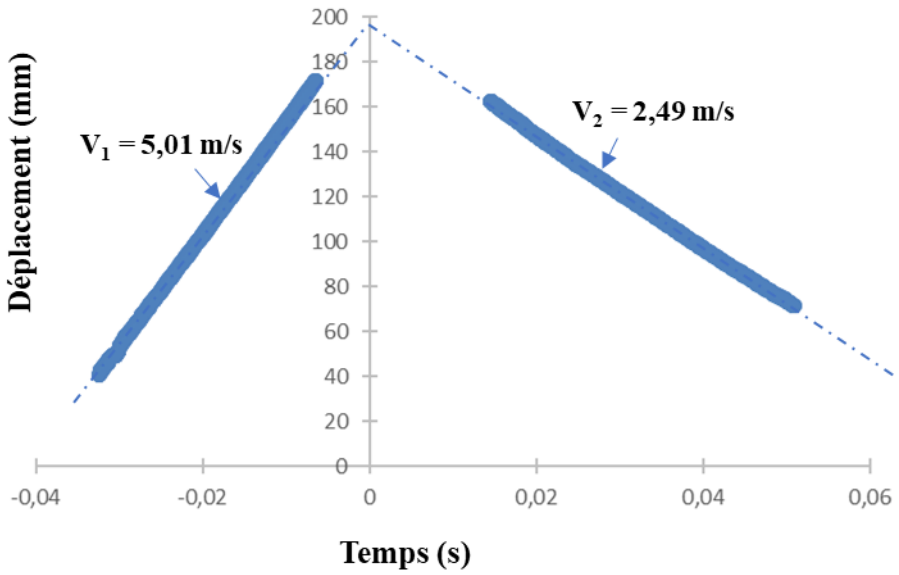

Figure 128 : Courbe déplacement-temps de l'impacteur pour l'échantillon chargé à 12.6 J détaillant la méthode suivie pour calculer l'énergie absorbée montrant la vitesse d'impact V1 et la vitesse de rebond V2.

Tableau 2 : Vitesse d'impact et énergie absorbée pour les sept échantillons considérés, impactés à 7,20 J, 10,54 J, 12,6 J, 14,58 J, 19 J, 21,15 J et 24 J respectivement.

Energie d'impact (J)	7,20	10,54	12,6	14,58	19	21,15	24
Vitesse d'impact (m/s)	3,778	4,633	5,010	5,383	6,170	6,504	6.928
Energie absorbée (J)	4,09	7,40	9,30	11,43	14,90	16,95	21.77

2. Mesure de l'indentation permanente

L'indentation permanente (IP) est connue pour être un paramètre très fiable pour une estimation de l'état d'endommagement dans le cas d'un endommagement par impact (Bouvet, 2011; Miqoi et al., 2021; Mustapha et al., 2016). Elle représente l'empreinte résiduelle post-évènement d'impact. Une estimation correcte de ce paramètre communique des informations sur les dommages causés par un événement d'impact. Ce paramètre clé est déterminé par une mesure ultrasonique utilisant d'abord l'imagerie C-scan pour localiser la zone d'impact et ensuite B-scan pour mesurer la profondeur de l'empreinte laissée sur la surface impactée. Les valeurs trouvées sont ensuite confirmées par une méthode plus résolue, en utilisant un profilomètre optique.

Une augmentation substantielle des dimensions, de la profondeur et des diamètres de l'IP est constatée lorsque l'énergie d'impact est élevée. Néanmoins, la mesure ultrasonique de l'IP s'accompagne d'une incertitude significative, comme le montre le **Tableau 3**.

Tableau 3 : Valeurs de la profondeur de l'indentation permanente obtenues par la méthode d'estimation par ultrasons pour les sept échantillons considérés impactés à 7,20 J, 10,54 J, 12,6 J, 14,58 J, 19 J, 21,15 J et 24 J respectivement.

Energie d'impact(J)	**7,20**	**10,54**	**12,6**	**14,58**	**19**	**21,15**	**24**
Profondeur (μm) ± 7 μm	-	59,5	44,36	62,84	122	177	199,3
Diametre (mm) ± 0,1 mm	-	6,3	3,9	5,1	3,6	7,2	5,7

Pour évaluer la pertinence de cette méthode, des mesures sont réalisées par le biais d'un profilomètre optique. Une comparaison entre les résultats fournis par les deux méthodes pour les sept échantillons considérés et également pour tous les échantillons étudiés, est établie et représentée respectivement dans la **Figure 129**. La même tendance est retrouvée dans les deux figures confirmant ainsi l'aspect représentatif des sept échantillons choisis. Les valeurs de la profondeur IP augmentent jusqu'à atteindre une énergie de 10,54 J, puis se stabilisent et recommencent à augmenter lorsque l'énergie dépasse 19 J. La comparaison montre une bonne corrélation entre les deux méthodes ainsi qu'une précision satisfaisante pour la méthode basée sur les ultrasons. Cependant, dans le cas de faibles indentations résultant de très faibles énergies d'impact, l'IP ne peut pas être mesuré en utilisant la méthode basée sur les ultrasons en raison de sa résolution relativement faible par rapport à la profilométrie optique. En effet, l'état d'endommagement à de faibles énergies d'impact rend la localisation de la zone endommagée très compliqué, et donc la mesure de la profondeur de la zone indentée est inaccessible.

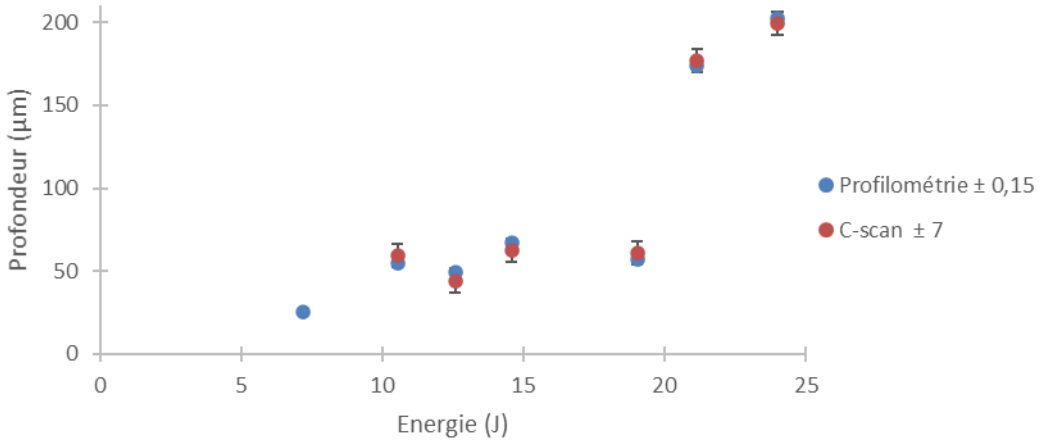

Figure 129 : Comparaison entre les valeurs de la profondeur de l'indentation permanente (IP) obtenues en utilisant à la fois la méthode basée sur les ultrasons et le profilomètre optique pour les sept échantillons considérés impactés à 7,20 J, 10,54 J, 12,6 J, 14,58 J, 19 J, 21,15 J et 24 J montrant une bonne corrélation entre les deux méthodes et validant ainsi la méthode basée sur les ultrasons comme une méthode efficace pour une estimation correcte de l'IP.

3. Mécanismes d'endommagement

Pour observer l'étendu de l'endommagement causé par l'impact, une investigation par tomographie à rayons est réalisée. Elle consiste en une reconstruction 3D du volume impactée permettant d'identifier les mécanismes d'endommagement résultant des évènements d'impact à différentes énergies. Ces derniers génèrent la création de vide qui est représenté en noir lors de la traversée du faisceau de rayons X. Il est à noter que pour l'échantillon impacté à une énergie de 7.20 J, les résultats de la tomographie n'indiquent aucun dommage dans la zone impactée confirmant ainsi que ce niveau d'énergie n'est pas suffisant pour créer un endommagement interne permanent dans le matériau étudié. L'initiation, l'accumulation ainsi que la propagation des mécanismes d'endommagement sont données dans la **Figure 130**.

Les mécanismes d'endommagement développés dans le composite tissé renforcé de verre étudié, soumis à un chargement d'impact à faible vitesse, sont similaires à ceux observés sous chargement monotone (Pomarède et al., 2018). Les cinétiques d'endommagement pour l'initiation, l'accumulation et la propagation sont les suivantes : le premier mécanisme d'endommagement distingué est la fissuration de la matrice. Cette dernière est introduite dans la surface non impactée attribuable à la nature du matériau (matériau mince) et se propage en surface, dans les deux directions longitudinale et transversale, en raison de l'effet de flexion lié aux conditions aux limites. Lorsque l'énergie d'impact augmente, ces fissures commencent à se propager dans les torons, provoquant la détérioration de l'interface fibre/matrice. Les fissures

se diffusent ensuite entre les torons dans les zones riches en polymère, entrainant la rupture des renforts.

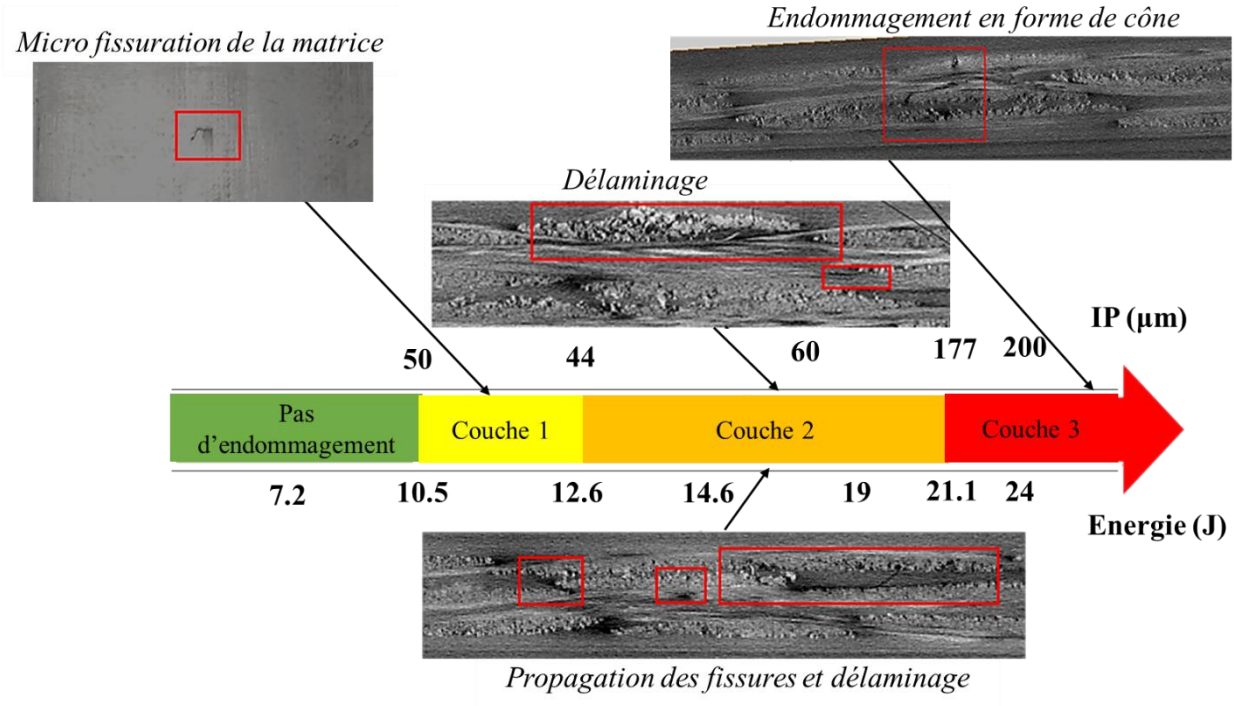

Figure 130 : Evolution des mécanismes d'endommagement en fonction de l'énergie d'impact.

4. Evaluation non-destructive de l'endommagement

4.1. Evaluation de la rigidité

Cette méthode consiste en la détermination du tenseur de rigidité du matériau de l'étude à partir de la mesure de la vitesse de propagation des ondes de volumes émises dans différents plans du composite. En effet, l'équation de Christoffel lie la rigidité à la vitesse de propagation des modes longitudinal et transversal. Pour des raisons de géométrie (faible épaisseur), des acquisitions dans les deux plans 1-3 et 2-3 (**Figure 131**) sont réalisées pour les sept échantillons considérés. Par conséquent, sept/ neuf composantes de la matrice de rigidité sont obtenues.

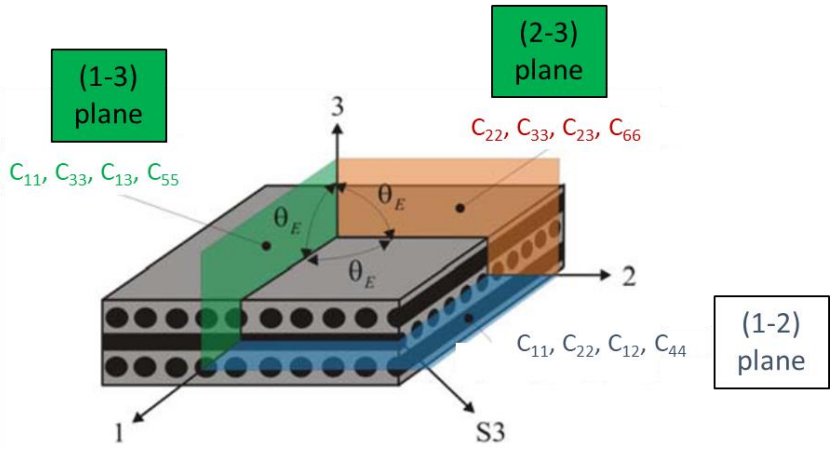

Figure 131 : Illustration des trois plans principaux de propagation des ondes ultrasonores considérés dans le cas d'un matériau orthotrope (Huffenbach, 2006).

Une diminution progressive est remarquée pour les valeurs des composantes C_{11} de 7.20 J à 14.58 J **(Figure 132(a)).** Les valeurs se stabilisent ensuite. Pour la composante C_{22} (**Figure 132(a)**), une diminution est remarquée aux énergies les plus élevées, plus précisément à 19 J. Les valeurs de cette composante ne semblent pas avoir de variation importante avant la dernière énergie. Une chute importante des valeurs de la composante C_{33} **(Figure 132(b))** est visible à partir de 12.6 J. Une chute moins marquée est observée pour le reste des composantes C_{66}, C_{55}, C_{13} et C_{23} **(Figure 132(d)** et **Figure 132(c)** respectivement). Cela dit, C_{23} varie comme suit : les valeurs diminuent à partir de 10,54 J jusqu'à atteindre un seuil où elles sont maintenues même à des énergies plus élevées (**Figure 132(c)**). Comme pour C_{13}, les valeurs diminuent progressivement avec l'augmentation l'énergie d'impact (**Figure 132(c)**). Cependant, les valeurs de C_{66} et C_{55} ne semblent pas changer (**Figure 132(d)**). Enfin, la valeur du composant C_{44} diminue à partir de 7,20 J jusqu'à 14,58 J, puis les valeurs se stabilisent lorsque l'énergie d'impact augmente.

On peut conclure que plusieurs composantes diminuent avec l'augmentation de l'énergie d'impact. La variation de certaines composantes plutôt que d'autres dépend principalement du type de chargement. Cependant, certaines valeurs estimées présentent une incertitude relativement élevée.

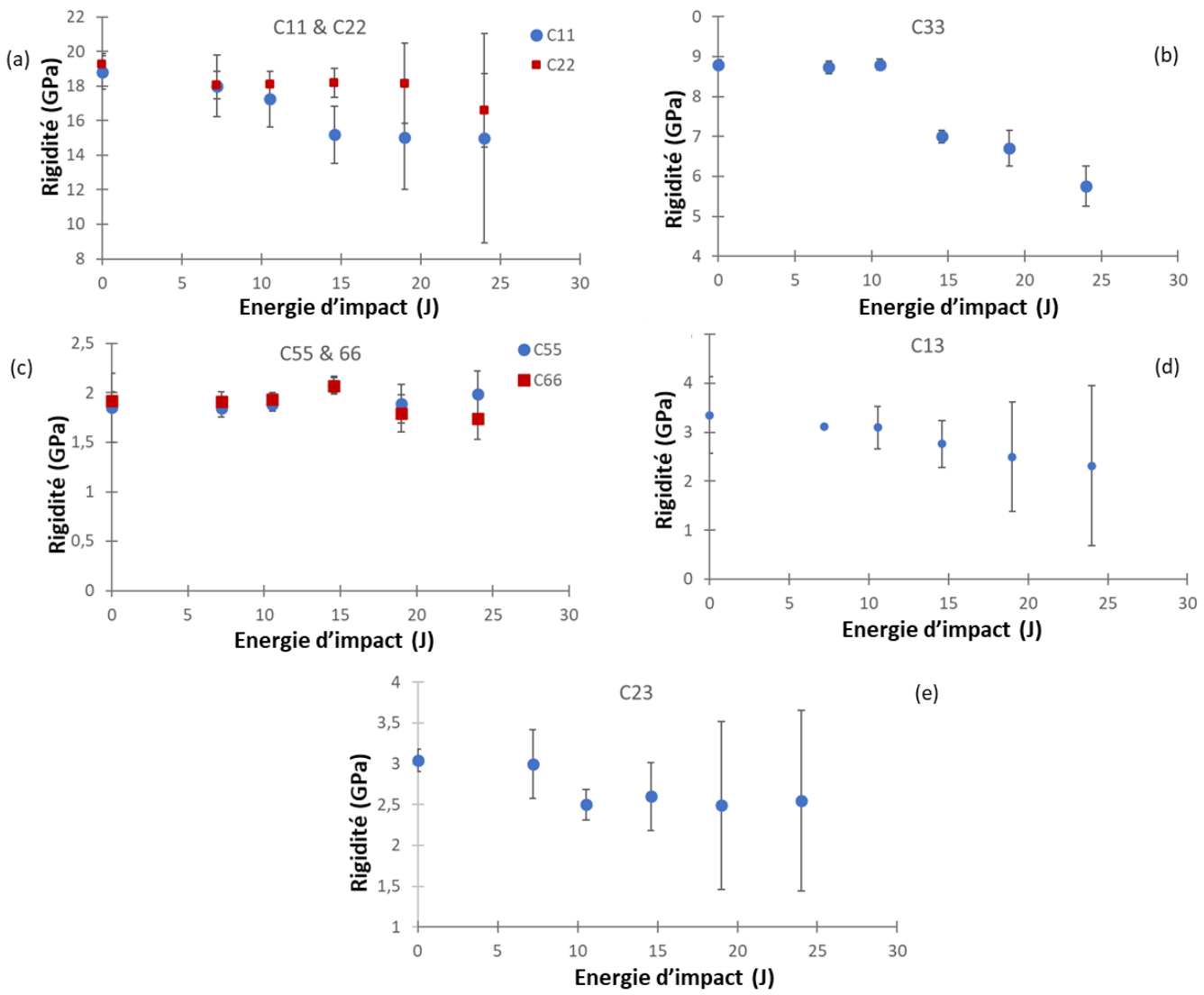

Figure 132 : Evolution des sept composantes de rigidité en fonction de l'énergie d'impact, à savoir : (a) C11 et C22, (b) C33, (c) C55 et C66 et (d) C23.

4.2. Investigation par ondes de Lamb

Les ondes guidées sont utilisées pour déterminer les endommagements dans le matériau composite de l'étude. En effet, les ondes de Lamb se révèlent très efficaces pour l'évaluation et l'étude de l'état d'endommagement d'une structure complexe. Elles permettent d'évaluer l'état d'endommagement d'une large structure en une mesure. L'idée principale est de varier la direction de propagation de l'onde guidée dans l'échantillon, et de calculer la vitesse de propagation pour chaque direction. La vitesse de propagation étant directement liée à la rigidité du milieu ainsi qu'à la variation des angles d'émission/réception (direction de propagation),

permet de récupérer des informations concernant l'anisotropie résultant de l'initiation de l'endommagement.

Les résultats seront présentés sous forme de profils de vitesse en fonction de la position angulaire décrivant l'interaction entre l'onde et le milieu de propagation.

Différentes étapes sont suivies pour développer un dispositif expérimental opérationnel. Les tests préliminaires mettent en évidence différents paramètres qui doivent être pris en compte. Ces paramètres sont divisés en deux catégories : les paramètres ultrasoniques et les paramètres géométriques. Le paramètre ultrasonore le plus important est la fréquence. En effet, le choix de la bonne fréquence du signal est crucial pour une bonne évaluation des signaux. Comme paramètres géométriques, on peut citer la distance entre les transducteurs, la position de ces derniers sur l'axe Z, et le positionnement de l'échantillon. Des travaux préliminaires sont considérés pour répondre à chacun des aspects mentionnés. En effet, une procédure est suivie pour la détermination de la fréquence d'émission. Des solutions sont proposées pour minimiser l'erreur due aux variations géométriques principalement de la position des transducteurs et de la position de l'échantillon.

4.3. Dispositif expérimental

Un signal composé d'un cycle sinusoïdal est généré à une fréquence de 150 KHz avec une amplitude de 10 V en utilisant un générateur Hewlett Packard 33120 A. Ce dernier est connecté à l'un des transducteurs (l'émetteur). Le signal se propage dans l'échantillon et est ensuite capté par le récepteur. Les transducteurs utilisés dans ce dispositif expérimental sont des transducteurs de 1 MHz de la marque Olympus. Connaissant l'effet d'atténuation que le composite a sur le signal, un amplificateur Krohen-Hite modèle 7500 est utilisé. La sortie de l'amplificateur est reliée à un oscilloscope Lecroy waverunner 64Xi qui permet la visualisation et l'enregistrement des signaux. Il est à noter que toutes les acquisitions sont réalisées au Laboratoire LUNE situé à GeorgiaTech Lorraine (**Figure 133**).

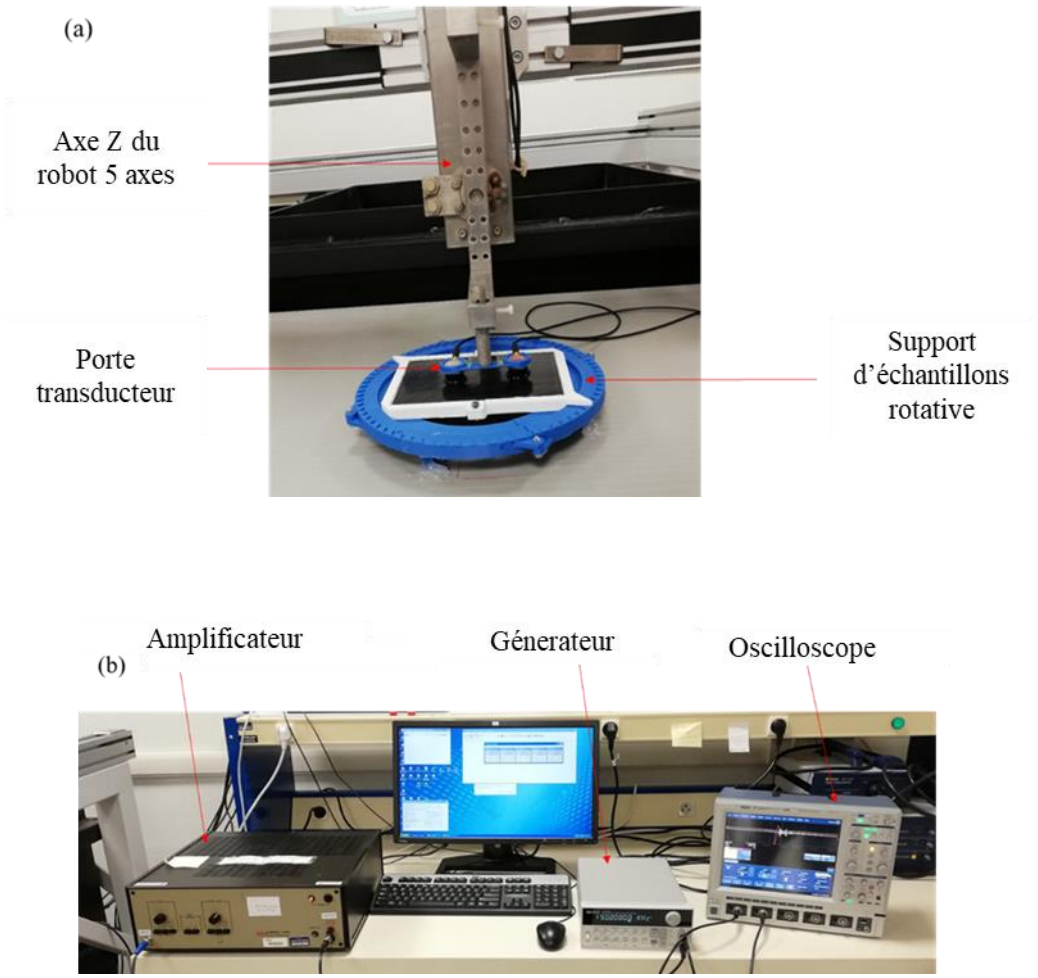

Figure 133 : Le dispositif expérimental utilisé montrant : (a) les transducteurs maintenus par le support imprimé en 3D fixé sur le robot à cinq axes permettant la translation sur l'axe Z ainsi que le dispositif imprimé en 3D conçu sur mesure permettant la rotation de l'échantillon avec un pas prédéfini de 5°, et (b) le dispositif utilisé pour générer et enregistrer le signal révélant le générateur, l'amplificateur et l'oscilloscope.

4.4. Post-traitement et résultats

Après avoir enregistré les 13 signaux à chaque angle pour tous les échantillons considérés (échantillons de référence et sept échantillons impactés), l'étape suivante consiste à identifier le temps d'arrivée du premier mode de propagation. Pour ce faire, une convolution entre un signal de référence et les signaux enregistrés pour chaque échantillon à chaque position définie est effectuée. Le signal de référence correspond au premier paquet d'ondes (du deuxième au sixième pic) du signal enregistré sur l'échantillon de référence à l'angle 0. Chaque signal est comparé et corrélé au premier paquet d'ondes du signal se propageant à 0° dans l'échantillon non impacté. Cette méthode permet de déterminer la position exacte où il existe une corrélation entre le signal de référence et le reste des signaux. Cette position correspond au temps d'arrivée du premier pic, c'est-à-dire le mode S_0, qui conduira par conséquent au calcul de la vitesse.

Connaissant la distance entre l'émetteur et le récepteur, la vitesse de propagation pour tout échantillon à chaque position est calculée.

La **Figure 134** montre qu'il existe une différence entre les profils de vitesse correspondant à l'échantillon de référence et ceux relatifs aux échantillons impactés. En effet, tous les profils de vitesse sont inférieurs au profil de vitesse de l'échantillon de référence. Cet écart s'explique par la réduction de la rigidité aux premiers stades de la création de l'endommagement et son développement au fur et à mesure que l'énergie d'impact augmente. Pour quantifier clairement l'effet des dommages sur la diminution de la vitesse de propagation, le calcul de l'aire sous la courbe est proposé. Par conséquent, un indicateur de dommage est suggéré.

$$D = 1 - \frac{A_{damaged}}{A_{ref}}$$

Avec $A_{damaged}$ la surface sous le profil de vitesse d'un échantillon endommagé et A_{ref} la surface sous le profil de vitesse de l'échantillon de référence.

Après le calcul des valeurs de l'indicateur d'endommagement (D) pour chaque échantillon, les résultats peuvent être illustrés comme le montre la **Figure 135** . On peut clairement voir l'augmentation du D avec l'augmentation de l'énergie d'impact.

Comparé aux résultats obtenus précédemment lors de la mesure de l'indicateur d'endommagement basé sur la mesure de l'indentation permanente (**Figure 135**), le présent indicateur d'endommagement a prouvé son efficacité à décrire l'évolution de la fonction d'endommagement de l'impact.

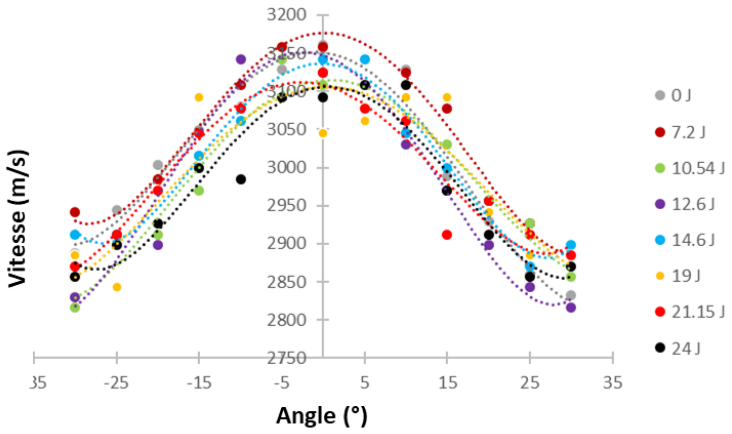

Figure 134 : Les profils de vitesse de chacun des échantillons considérés, à savoir l'échantillon de référence et les sept échantillons impactés chargés à : 7,2 J, 10,54 J, 12,6 J, 14,58 J, 19 J, 21,15 J et 24 J avec une approximation polynomiale du quatrième degré.

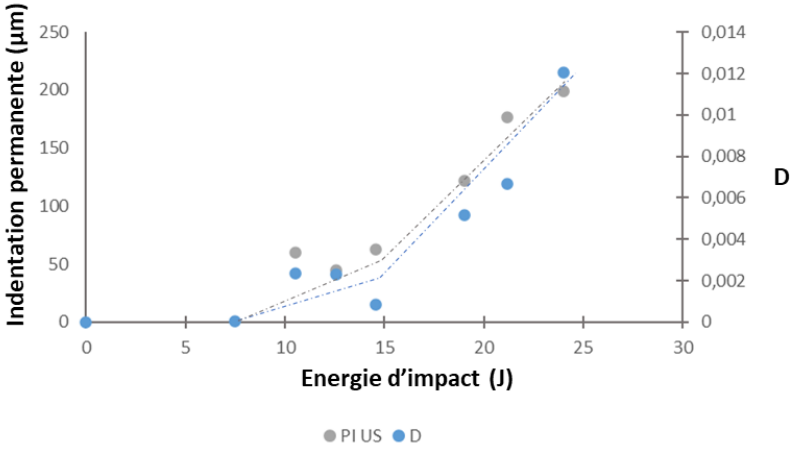

Figure 135 : Comparaison entre l'évolution de l'indentation permanente mesurée par la méthode ultrasonore et l'évolution de l'indicateur d'endommagement proposé pour les sept échantillons impactés respectivement à des énergies de : 7,20 J, 10,54 J, 12,6 J, 14,58 J, 19 J, 21,15 J et 24 J.

IV. Fatigue en traction-traction

L'endommagement des polyamides renforcés se produit en raison des chargements opérationnelles, de la température, et est affecté par les conditions d'humidité relative comme le rapportent (Arif et al., 2014; Giurgiutiu, 2015; Pomarède et al., 2018; Robert & Benaarbia, 2015). Contrairement à l'endommagement par impact, qui est considéré comme le résultat d'événements accidentels provoquant une diminution soudaine des propriétés mécaniques du composite, l'endommagement dû au chargement opérationnel induit une dégradation progressive de ce dernier.

1. Essais mécaniques

Des essais de fatigue interrompus sont réalisés pour initier et propager un type d'endommagement étendu et diffus dans le composite étudié. Sachant que l'endommagement généré par le chargement cyclique reste complexe en termes d'accumulation, son évaluation à l'aide d'une technique de détection résolue est d'une grande importance. En effet, il présente une distribution diffuse dans toute la section de l'échantillon. L'objectif est de valider la méthode des ondes de Lamb qui a prouvé son efficacité dans la détection des endommagements localisés dus aux événements d'impact à faible vitesse. Les échantillons composites testés sont chargés à trois niveaux différents de leur durée de vie, et à trois niveaux (proportion) de la contrainte à rupture, respectivement. Ainsi, neuf combinaisons de paramètres de chargement sont considérées et sont résumées dans le **Tableau 4**. Au total, vingt-sept échantillons sont testés, soit trois spécimens par combinaison de paramètres de chargement.

Tableau 4 : Neuf combinaisons de paramètres utilisées pour les essais de fatigue interrompue sur des échantillons préconditionnés à 50% d'humidité relative.

Niveau de chargement	**35% σ_{UTS}**			**45% σ_{UTS}**			**60% σ_{UTS}**		
Nombre de cycles (%)	50%	60%	70%	50%	60%	70%	50%	60%	70%
Nombre de cycles	222061	266473	310885	33015	39618	46221	1851	2222	2592

Le module de Young relatif aux premiers (E_0) et aux derniers cycles (E) des chargements sont mesurés. Pour quantifier l'endommagement résultant des essais de fatigue, les résultats sont représentés comme le rapport (D) de E sur E_0, fonction du nombre de cycles. La **Figure 136** représente l'évolution de l'endommagement en fonction du nombre de cycles de chargement pour le lot d'échantillons chargé à σ_{max} = 60% σ_{UTS}.

Les résultats expérimentaux ne présentent pas de tendance claire. Par conséquent, la baisse de rigidité ne peut pas être considérée comme indicateur fiable de l'endommagement dans le cas d'un chargement en fatigue.

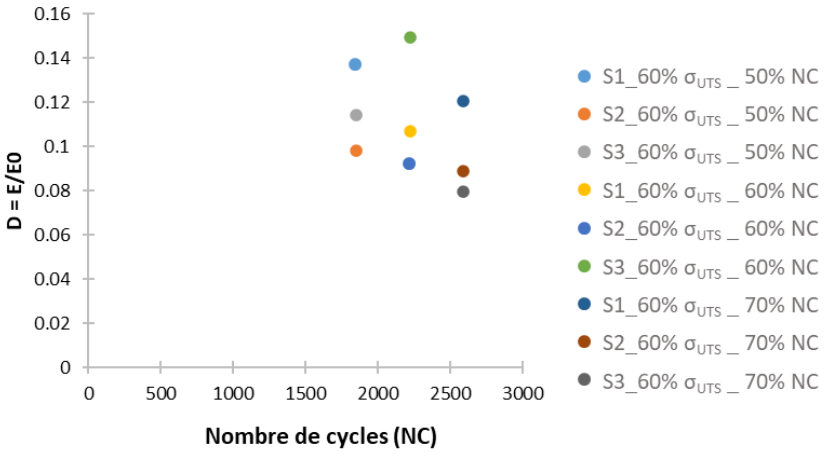

Figure 136 : Variation de l'endommagement (D) calculé à partir des données mécaniques en fonction des conditions de chargement : 60% σ_{UTS}. Une dispersion des résultats est observée. Elle peut être expliquée par la variabilité des essais de fatigue et la variabilité de la microstructure du matériau causée par le processus de thermo-compression.

2. Investigation par ondes de Lamb

Une étude des ondes de Lamb est menée pour évaluer l'état d'endommagement des échantillons post-fatigue. Le protocole expérimental de détection est celui utilisé précédemment sur les échantillons impactés. La seule différence réside dans la gamme d'angles étudiés. En effet, la section étant plus petite que celle des échantillons d'impact, la surface évaluée est comparativement plus réduite, et par conséquent, le nombre de points de mesure est réduit. Néanmoins, une gamme d'angles variant entre ± 15° est considérée avec un incrément de 5°. En conséquence, sept angles ont été exploités pour construire le profil de vitesse des échantillons de fatigue, qui sont divisés en trois ensembles en fonction du niveau de chargement. Un échantillon non endommagé avec la même géométrie est considéré comme un échantillon de référence. Chaque ensemble d'échantillons est testé individuellement avec l'échantillon de référence. Ainsi, chaque ensemble d'échantillons a ses propres données de référence enregistrées dans les mêmes conditions d'essai. Le fait d'avoir les mêmes conditions de test (la pression appliquée par les transducteurs sur la surface du matériau et le positionnement de l'échantillon) entre les échantillons endommagés et l'échantillon de référence réduit l'apparition d'erreurs expérimentales.

Un exemple des profils de vitesse obtenus correspondant au lot d'échantillons chargé à 60% σ_{UTS} est présenté dans la **Figure 137**. Une différence entre le profil vitesse de l'échantillon de référence et le reste des échantillons est remarquée.

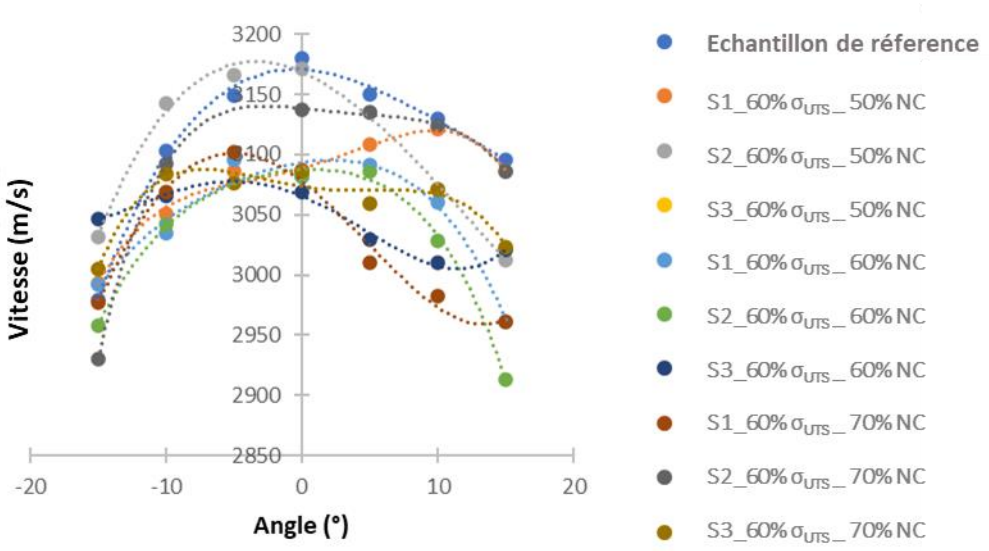

Figure 137 : Profils de vitesse obtenus par la méthode proposée de propagation des ondes de Lamb sur des échantillons soumis à une charge de fatigue à 60% σ_{UTS} et 50%, 60%, et 70% du nombre de cycles à rupture (se référer au tableau 4 pour les nombres réels de cycles).

Les surfaces sous les profils de vitesse sont calculées et l'endommagement résultant est quantifié par le biais de l'indicateur d'endommagement présenté dans la section précédente. Un exemple des résultats obtenues pour le lot d'échantillons chargé à 60% σ_{UTS} est présentée dans la **Figure 138**.

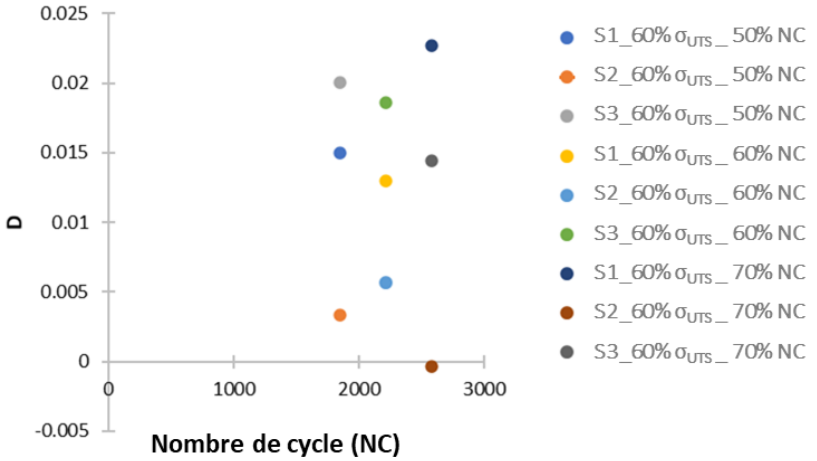

Figure 138 : Valeurs de l'indicateur d'endommagement proposé calculé à partir de la surface sous les profils de vitesse pour le lot d'échantillon chargé à 60% σ_{UTS} et 50%, 60%, et 70% du nombre de cycles jusqu'à la rupture.

Une différence claire entre les échantillons endommagés et l'échantillon de référence est remarquée, confirmant ainsi l'efficacité de l'indicateur de dommages basé sur l'investigation des ondes de Lamb pour distinguer entre les échantillons endommagés et non endommagés. En

effet, la première étape dans le développement d'une technique CND est la capacité de différencier les échantillons endommagés des échantillons non endommagés.

Cependant, on peut facilement voir que les résultats ne présentent pas une tendance claire. Une augmentation graduelle de la valeur de l'indicateur d'endommagement est attendue avec l'augmentation du nombre de cycles de chargement. Cependant, une dispersion des valeurs de l'indicateur d'endommagement est observée. Des valeurs différentes sont obtenues pour les échantillons chargés dans les mêmes conditions. Plusieurs paramètres peuvent être à l'origine de cette dispersion des résultats expérimentaux obtenus. En effet, outre la dispersion communément admise, induite par le chargement en fatigue, notamment pour les matériaux composites, il convient de mentionner que les éprouvettes n'ont pas été découpées dans la même zone des plaques composites. En effet, le processus de thermo-compression peut induire certaines variabilités en termes de microstructure. Même si le nombre de VER considéré est le même à chaque fois, les éprouvettes ne sont pas totalement strictement identiques à l'échelle microscopique. La résistance d'une éprouvette avec un toron complet sur les bords de la plus petite section ne se comportera pas comme celle d'une éprouvette avec une zone inter-toron ou une partie du toron sur les bords. De plus, des défauts d'architecture sont observés sur certains échantillons lors de l'examen tomographique à rayons X. Certains de ces défauts peuvent être induits par des facteurs externes. Certains de ces défauts peuvent être induits pendant le processus de fabrication, et d'autres, comme le flambage des torons, peuvent être le résultat du chargement répétitif dans la direction des renforts. Ces défauts influencent la vitesse de propagation des ondes expliquant ainsi les résultats dispersifs. De plus, les endommagements induits par le chargement cyclique sont répartis de manière aléatoire dans toute la section, rendant la propagation de l'onde moins prévisible et son estimation moins précise.

Une investigation par tomographie à rayons X visant l'estimation du taux de vide est effectuée pour valider la pertinence de cette méthode. Une comparaison entre l'évolution du taux de vide et l'évolution de l'indicateur d'endommagement est réalisée.

Les résultats obtenus pour le lot d'échantillons chargés à 60% σ_{UTS} sont représentés sur la **Figure 139**. En comparant le positionnement de chaque échantillon considéré dans la mesure du taux de vide avec celui sur les résultats obtenus par la technique des ondes de Lamb, on constate que les points étudiés présentent la même tendance. Les résultats obtenus sont en totale corrélation avec ceux obtenus par la méthode basée sur la propagation des ondes de Lamb. Par conséquent, on peut conclure que la dispersion des résultats de fatigue est principalement due au

comportement des échantillons et à la variabilité de la microstructure en plus du type de chargement appliquée. En effet, étant donné l'hétérogénéité de la microstructure du composite et le fait que les échantillons sont découpés dans plusieurs zones des plaques, chaque échantillon peut se comporter différemment sous les mêmes conditions de chargement. Cependant, l'efficacité de la méthode proposée pour détecter l'état d'endommagement de chaque échantillon est prouvée.

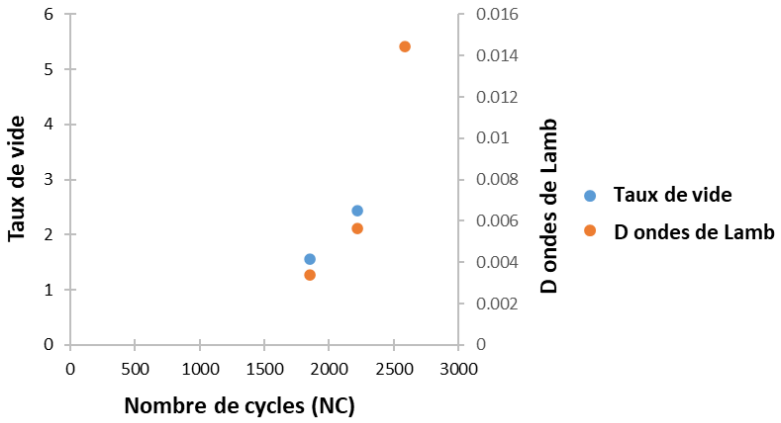

Figure 139 : Comparaison entre le taux de vide et la valeur de l'indicateur d'endommagement (ondes de Lamb) pour les échantillons chargés à 60% σ_{UTS}.

V. Les propriétés résiduelles

Les structures composites peuvent subir plusieurs types de chargements transitoires, telles que l'impact à faible vitesse et les chargements en fatigue, qui provoquent souvent la dégradation progressive de l'intégrité des structures. Cette détérioration se manifeste par la diminution des propriétés résiduelles du composite. Par conséquent, l'estimation de la réduction de la résistance à la traction des composites après chargements est obligatoire pour garantir la tolérance aux endommagement et les marges de sécurité dans la conception des composants composites (Shahzad, 2018).

Une méthodologie expérimentale permettant d'évaluer et d'analyser l'effet de la nature de chargement sur la réponse quasi-statique des propriétés résiduelles du matériau composite après un événement (impact, chargement en fatigue et impact post-fatigue). A cet effet, des essais de traction quasi-statiques sont réalisés sur des échantillons soumis respectivement à des

événements d'impact à faible vitesse et à des chargements de fatigue. Une comparaison entre la réponse des éprouvettes vierges et celle des échantillons endommagés est réalisée. Des essais d'impact post-fatigue sont réalisés dans des conditions équivalentes à celles des essais d'impact à faible vitesse et des chargements de fatigue, respectivement. L'analyse de (i) l'effet de l'endommagement, résultant de l'impact à faible vitesse, sur la résistance à la traction résiduelle des échantillons pré-fatigués, et (ii) l'effet de la précharge de fatigue sur la réponse à l'impact des échantillons composites, est établie.

1. Propriétés résiduelles post-impact

La **Figure 140** représente la réponse en traction des huit échantillons considérés, notamment l'échantillon non-endommagé et les sept échantillons impactés. Les courbes de contrainte-déformation montrent un comportement quasi-fragile du matériau composite étudié. Une comparaison entre la réponse en traction de l'échantillon non impacté et celle des échantillons impactés est réalisée (**Figure 140**). A première vue, le module de Young ne semble pas être affecté par le chargement. En effet, aucune diminution importante du module, avec l'augmentation de l'énergie d'impact, n'est remarquée. Les résultats expérimentaux indiquent que la variation du module d'Young n'est pas l'indicateur représentatif le plus approprié de la détérioration des échantillons composites à base de polyamide.

La **Figure 141** représente l'évolution de σ_{UTS} en fonction de l'énergie d'impact. En observant attentivement la fonction σ_{UTS} de la courbe d'énergie d'impact, on peut voir que la réponse du matériau présente deux phases de développement de l'endommagement lorsque l'énergie d'impact augmente. La première phase, correspondant à des énergies d'impact allant de 7 J à 12,6 J, indiquant la plage d'initiation et de propagation de l'endommagement du premier au deuxième pli du stratifié. Elle est caractérisée par la fissuration de la matrice et la rupture des fibres. Un effet léger mais quantifiable sur la contrainte à rupture du composite est remarqué à ce stade. Les mécanismes d'endommagement entraînent une diminution de la σ_{UTS} résiduelle de moins de 5%.

La deuxième partie de la courbe d'évolution, de 12,6 J à 24 J, indique la gamme d'énergies où les fissures se propagent dans la deuxième couche et à travers l'épaisseur jusqu'à la troisième couche du composite tissé. Cette étape est associée à la croissance et à l'accumulation des fissures de la matrice conduisant au délaminage et à la rupture des fibres comme étape finale de la rupture macroscopique. La contrainte à rupture diminue d'environ 13% à 30%, indiquant ainsi que le composite à base de polyamide est remarquablement endommagé.

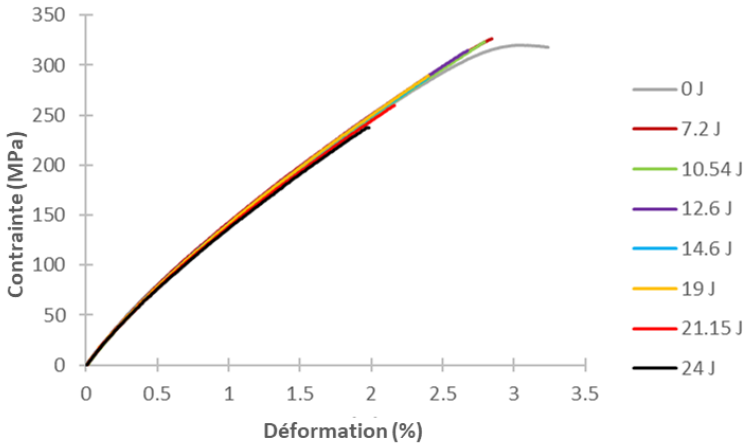

Figure 140 : Courbes de contrainte de traction-déformation d'un échantillon non endommagé ainsi que des sept échantillons impactés à 7,2 J, 10,54 J, 12,6 J, 14,6 J, 19 J, 21,15 J et 24 J respectivement.

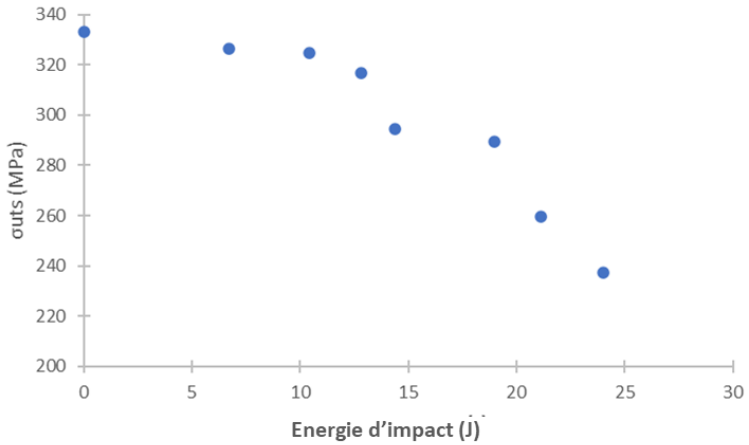

Figure 141 : L'évolution de la résistance à la traction ultime (σ_{UTS}) de l'échantillon de référence et des sept échantillons soumis à un impact à faible vitesse à des niveaux d'énergie de 7,2 J, 10,54 J, 12,6 J, 14,6 J, 19 J, 21,15 J et 24 J, respectivement.

2. Propriétés résiduelles post-fatigue

Une comparaison est établie entre la réponse en traction d'un échantillon vierge et celle présentée par les échantillons chargés aux neuf combinaisons de paramètres précédemment détaillés dans le **Tableau 4.**

En analysant la réponse mécanique, on peut observer que la contrainte maximale diminue en raison du chargement cyclique. Cependant, la réduction de cette valeur observée visuellement suggère que l'effet du chargement à de faibles niveaux de contrainte et à un nombre élevé de

cycles est plus significatif pour la résistance résiduelle du matériau composite. Pour quantifier la perte des propriétés résiduelles post-fatigue des échantillons étudiés, la valeur de contrainte maximale de chacune des courbes de contrainte-déformation est extraite et comparée à celle d'un échantillon non chargé.

La **Figure 142** représente l'évolution de la résistance à la traction ultime (σ_{UTS}) des échantillons soumis à des chargements en fatigue interrompues à trois niveaux de contrainte, à savoir 35%, 45% et 60% σ_{UTS}. A première vue, on peut constater que les valeurs de résistance à la rupture résiduelle sont plus faibles pour les ensembles d'échantillons, chargés à une contrainte maximale correspondant à 35% et 45% σ_{UTS}. En effet, on constate que, pour l'ensemble des échantillons chargés à un niveau de contrainte maximale de 35% σ_{UTS}, l'échantillon chargé à 50% NC (nombre de cycles jusqu'à la rupture) présente une perte de résistance résiduelle d'environ 33%. La réduction de la valeur de la contrainte à rupture se poursuit lorsque le nombre de cycles augmente jusqu'à 35% pour l'échantillon chargé à 60% NC, et jusqu'à environ 43% pour l'échantillon chargé à 70% NC. Les échantillons chargés à un niveau de contrainte maximale de 45% σ_{UTS} montrent également une diminution de la résistance résiduelle causée par le chargement répétitif en traction-traction. La baisse de la contrainte à rupture est comprise entre 37% et 42% lorsque le nombre de cycles augmente. Le troisième ensemble d'échantillons chargés à un niveau de contrainte maximale de 60% σ_{UTS} montre une perte de la résistance résiduelle plus faible lorsque le nombre de cycles varie. En effet, elle est d'environ 12% à 13% pour l'échantillon chargé à 50% et 60% NC, respectivement, et de 19% pour l'échantillon chargé à 70% NC. Ces résultats expérimentaux mettent en évidence le fait que la rupture finale des échantillons soumis à un chargement en fatigue à des niveaux de contrainte maximale élevés se produit soudainement après 70% NC, puisque la perte de la résistance résiduelle entre 50% et 70% NC est inférieure à 20%. De plus, les performances résiduelles des deux ensembles d'échantillons chargés à 35% et 45% σ_{UTS}, respectivement, sont proches et comparables. Il est important de mentionner qu'aucune équivalence entre les différentes combinaisons de paramètres n'est établie. Cette dernière nécessite une campagne d'essais méticuleuse considérant un grand nombre d'échantillons. L'objectif est d'observer l'influence du chargement de fatigue sur les propriétés mécaniques dans le cadre d’une approche qualitative.

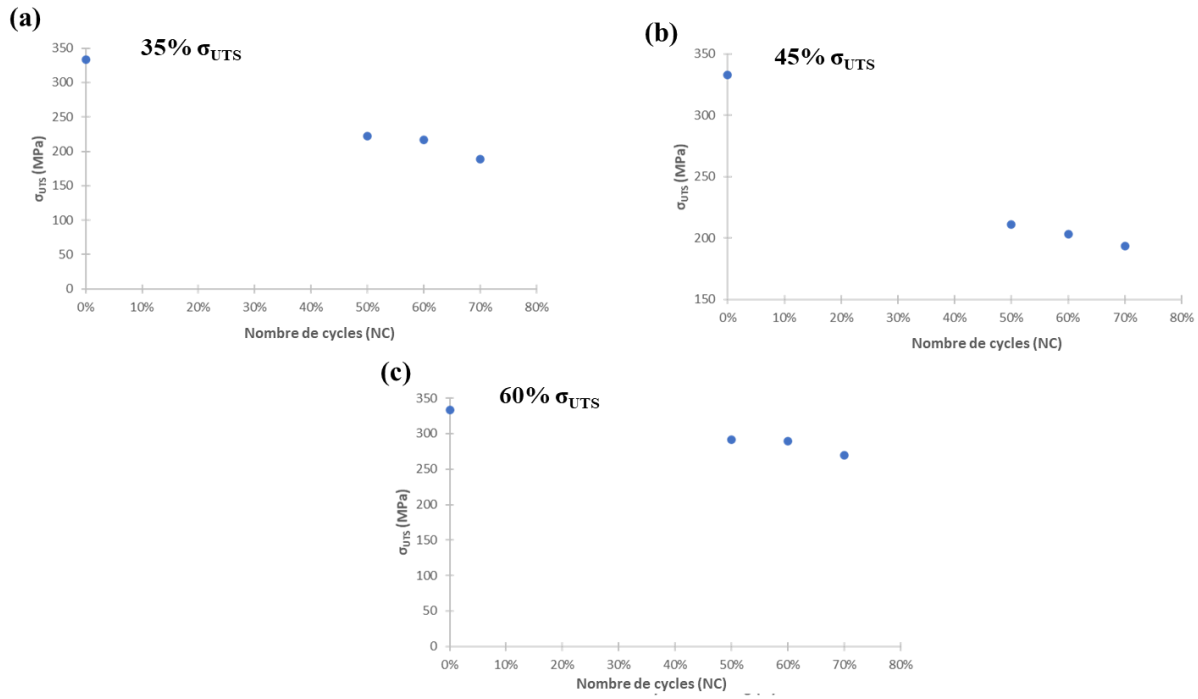

Figure 142 : L'évolution de la contrainte à rupture (σ_{UTS}) de l'échantillon de référence et des trois échantillons soumis à une charge de fatigue à un niveau de contrainte maximale de : (a) 35%, (b) 45% et (c) 60% σ_{UTS} pour 50%, 60% et 70% du nombre de cycles jusqu'à la rupture, respectivement.

3. Impact post-fatigue

Les essais d'impact post-fatigue font l'objet de cette section. Ces essais sont réalisés afin d'inspecter l'influence du couplage des chargements en fatigue et de l'impact à faible vitesse sur les propriétés résiduelles du matériau composite. Dans la littérature, l'impact post-fatigue reste un sujet relativement peu étudié dans le domaine des matériaux composites. Le manque de références et de travaux de recherche approfondis rend l'interprétation des résultats obtenus très difficile en raison de la complexité des modes de chargement. Dans cette étude, une procédure expérimentale pour réaliser le couplage de l'impact à faible vitesse et du chargement de fatigue est proposée. La réponse macroscopique du composite en termes de résistance résiduelle sera le point central. Une évaluation qualitative des résultats expérimentaux est réalisée. Le but principal est d'observer qualitativement l'effet du (i) chargement en fatigue sur la résistance résiduelle et la rigidité des échantillons impactés, et (ii) des essais d'impact à faible vitesse sur les propriétés résiduelles des échantillons soumis à des chargements cycliques répétitives. Deux ensembles d'échantillons préalablement chargés en fatigue suivant les neuf combinaisons de paramètres sont détaillés dans le **Tableau 5**. Des essais d'impact à basse vitesse sont effectués sur les mêmes échantillons à deux niveaux différents d'énergie d'impact.

Tableau 5 : Paramètres des essais de post-fatigue par impact pour les dix-huit échantillons considérés, impactés respectivement de 0,5 m et 1 m, indiquant le niveau de contrainte maximum, le nombre de cycles de chargement, l'énergie d'impact et l'énergie absorbée.

Niveau de chargement	35% σ_{UTS}			45% σ_{UTS}			60% σ_{UTS}		
Nombre de cycles (%)	50%	60%	70%	50%	60%	70%	50%	60%	70%
Nombre de cycles	222061	266473	310885	33015	39618	46221	1851	2222	2592
Energie d'impact (J) (hauteur d'impact 0.5 m)	4.34	4.09	-	4.25	4.32	4.38	4.26	4.44	4.34
Energie absorbée (J) (hauteur d'impact 1 m)	3.93	3.50	-	3.77	3.52	3.60	3.73	3.78	3.75
Energie d'impact (J) (hauteur d'impact 1 m)	9.1	8.61	8.79	8.9	7.52	9.2	8.63	8.26	8.35
Energie absorbée (J) (hauteur d'impact 1 m)	8.37	8.1	8.45	8.1	7	8.7	8	7.65	7.69

L'analyse des données mécaniques montre qu'il y a une différence entre les échantillons endommagés et non endommagés. Néanmoins, les résultats expérimentaux ne présentent pas une tendance claire en termes d'évolution (**Figure 143**). Une diminution progressive de la valeur de la résistance résiduelle était attendue avec l'augmentation du nombre de cycles de chargement et de l'énergie d'impact à faible vitesse.

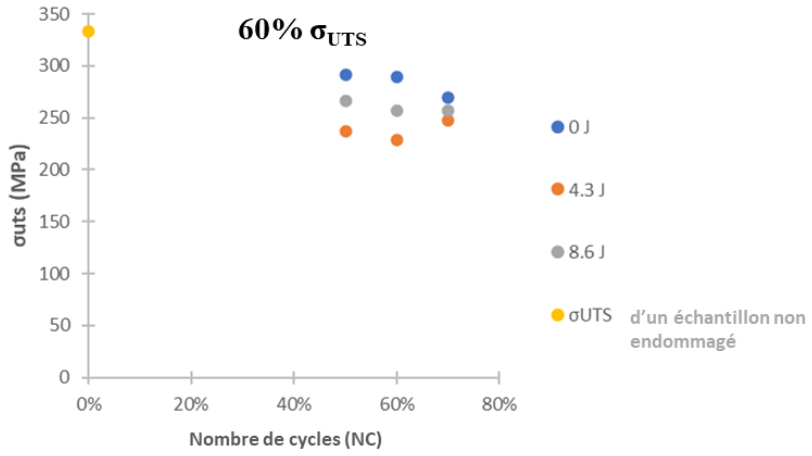

Figure 143 : La contrainte à rupture ultime d'un échantillon non endommagé (jaune) et celle d'échantillons soumis à des chargements en fatigue (niveau de contrainte maximal de 60% σ_{UTS}) (bleu), d'échantillons soumis à un impact post-fatigue (niveau de contrainte maximal de 60% σ_{UTS}) impactés à un niveau d'énergie de 4,3 J (orange) et d'échantillons soumis à un impact post-fatigue impactés à un niveau d'énergie de 8,6 J (gris).

De telles dispersions sont attendues lors de l'évaluation de l’endommagement par fatigue dans les matériaux composites. Ces résultats expérimentaux peuvent être expliqués par de multiples paramètres tels que :

(i) le fait que les échantillons ne sont pas complètement identiques, puisque le processus de thermo-compression peut induire une certaine variabilité dans la microstructure et que la découpe des échantillons a été effectuée dans différentes zones des plaques composites.

(ii) la géométrie de l'échantillon : la résistance d'un échantillon avec un toron entier sur les bords de la plus petite section ne se comportera pas comme celle d'un échantillon avec une zone inter-toron ou une partie du toron sur les bords.

(iii) la variabilité et la nature dissipative de l'endommagement par fatigue

(iv) les micro-endommagements présents dans le composite avant les différents chargements causés par le processus de découpe et/ou le processus de fabrication.

Par conséquent, cette section est considérée comme une phase d'essai préliminaire permettant de fournir des résultats préliminaires et de saisir les différentes tendances. Le présent travail doit être complété par une campagne expérimentale approfondie permettant de fournir une évaluation quantitative des dommages induits par l'impact post-fatigue. De plus, il est important d'avoir suffisamment d'échantillons pour quantifier l'influence de la combinaison de la fatigue et des événements d'impact à faible vitesse sur la durée de vie du matériau composite à matrice polyamide.

VI. Conclusions et perspectives

Le présent travail visait à étudier l'endommagement d'un composite à matrice polyamide destiné à des applications structurelles automobiles. L'objectif était de proposer des méthodologies expérimentales fondées sur des méthodes d'évaluation non destructive (END) permettant d'évaluer l'état d'endommagement du composite renforcé PA66/6 soumis à un chargement mécanique. L'approche expérimentale NDE s'est concentrée sur deux axes principaux : (i) l'étude de la réponse mécanique du matériau composite soumis à trois types de chargements appliqués, à savoir des impacts à faible vitesse, des chargements de fatigue et des chargements post-fatigue, et (ii) l'évaluation et la caractérisation des endommagements induits, à l'échelle microscopique et mésoscopique, en utilisant des méthodes END appropriées.

Un total de vingt et un échantillons, préconditionnés à 50% d'humidité relative, ont été impactés à des énergies allant de 6,7 J à 24 J. Les résultats de sept échantillons, représentant différents niveaux et gammes d'endommagement d'impact à peine visibles, ont été discutés. Les données mécaniques relatives aux essais d'impact par poids tombant ont été analysées et traitées, et les différents paramètres ont été extraits. Il a été constaté que la force maximale, la déflexion maximale, ainsi que l'énergie absorbée augmentaient avec l'énergie d'impact.

Une procédure expérimentale complète consistant en une caractérisation méticuleuse des endommagements externes (surface) et à travers l'épaisseur a été suivie. L'inspection visuelle a mis en évidence le fait que les endommagements étaient plus diffus sur les surfaces non impactées lorsque l'énergie d'impact augmentait. En effet, le réseau de fissures se propageait le long des axes des fibres et leur taille augmentait avec l'énergie d'impact. Une méthode basée sur les ultrasons consistant en la propagation d'ondes de masse a été appliquée pour mesurer et estimer l'indentation permanente (IP), c'est-à-dire l'empreinte laissée par l'impacteur sur l'échantillon après un événement d'impact. L'efficacité de la méthode basée sur le C-scan a été vérifiée en utilisant le profilomètre optique. Les deux méthodes ont montré une excellente corrélation. Les résultats expérimentaux ont montré que la profondeur de l'IP augmentait avec l'énergie de l'impact.

La tomographie à rayons X (mCT) à travers l'épaisseur a été réalisée pour identifier les différentes phases d'endommagement à savoir, l'initiation, l'accumulation et la propagation. L'étude de la reconstruction 3D des volumes endommagés a indiqué que les mécanismes d'endommagements détectés étaient similaires à ceux observés après un chargement de traction

monotone (Pomarède, 2018). En outre, la fissuration de la matrice a été le premier mécanisme d'endommagement à apparaître sur la surface non impactée du stratifié mince à partir d'une énergie d'impact de 10,54 J. Au fur et à mesure que cette dernière augmentait, les microfissures se sont développées en surface et se sont diffusées dans et entre les torons, entraînant la rupture des fibres et la détérioration de l'interface fibre/matrice. Le délaminage s'est produite lorsque les fissures se sont propagées de couche en couche, entraînant la dégradation de l'intégrité du composite multicouche.

L'évaluation quantitative des endommagements causés par l'impact a ensuite été réalisée à l'aide de méthodes basées sur les ultrasons. Tout d'abord, une méthode d'estimation de la réduction de la rigidité a été employée. Elle était fondée sur la détermination de la vitesse de propagation des ondes de volume dans différents plans de la structure étudiée. Cette méthode a mis en évidence le fait que les composants C_{11} et C_{33} étaient les plus touchés. Tous les résultats expérimentaux ont conduit à une conclusion importante : en estimant l'IP, on peut prédire l'état d'endommagement et la propagation à travers l'épaisseur et saisir l'évolution de la réduction de la rigidité. Ensuite, une méthode basée sur la propagation des ondes de Lamb consistant à évaluer la vitesse de propagation de l'onde en fonction de l'angle d'émission/réception du signal ultrasonore, simultanément, a été proposée. Cette méthode a permis d'établir et d'évaluer des profils de vitesse pour tous les échantillons étudiés, représentatifs de l'évolution de la rigidité. Pour quantifier l'influence de l'endommagement induit sur la vitesse de propagation, un indicateur d'endommagement consistant en l'estimation de l'aire sous les courbes a été proposé. Une bonne corrélation entre la mesure de l'IP et l'indicateur d'endommagement suggéré a révélé que les deux indicateurs étaient très efficaces et fiables lorsqu'il s'agit de la quantification de l'endommagement causé par un évènement d'impact à faible vitesse. Par conséquent, la méthode proposée pourrait être utilisée individuellement pour refléter l'état d'endommagement résultant de l'impact à faible vitesse.

Des essais de fatigue en traction-traction ont été réalisés sur des échantillons ayant une géométrie spéciale développée dans ce travail. Sachant que l'objectif n'était pas de caractériser mécaniquement le comportement du composite sous chargement cyclique, la géométrie des échantillons a été choisie pour que l'endommagement soit contenu dans la zone de jauge de l'échantillon, et plus particulièrement dans la zone centrale. La géométrie a été vérifiée en réalisant des essais de traction quasi-statique et des essais de fatigue en traction-traction. Des essais de fatigue à une fréquence de 3 Hz ont été réalisés, d'abord jusqu'à rupture pour reconstruire la courbe de Wöhler. Des essais de fatigue interrompus ont ensuite été réalisés pour

initier un endommagement progressif des échantillons. L'évaluation des mesures mécaniques a révélé des résultats expérimentaux dispersés suggérant une différence dans la réponse des échantillons due à la variabilité de la microstructure et à la nature du chargement cyclique. En outre, les endommagements résultant du chargement cyclique ont été classés comme des endommagements diffus dans la section entière, contrairement aux endommagements résultant de l'impact qui sont plus localisés dans la zone impactée. La méthode développée, basée sur la propagation des ondes de Lamb, a été testée sur l'échantillon post-fatigue. L'objectif principal était de confirmer la détectabilité des endommagements de type diffus en utilisant la technique suggérée. La dispersion des résultats, déjà constatée lors de l'analyse des données mécaniques, a été remarquée. Afin d'établir si la dispersion était liée à l'essai mécanique (comportement des échantillons sous des chargement en fatigue), les résultats de l'investigation par ondes de Lamb ont été comparés à la mesure du taux de vide effectuée à l'aide du mCT. La comparaison a démontré l'efficacité de la méthode dans la détection de différents stades de dommages. Par conséquent, la technique de propagation des ondes de Lamb proposée a prouvé sa fiabilité et ses performances quant à la détection et la quantification de différents types d'endommagements à travers l'épaisseur. La méthode de réduction de la rigidité par ultrasons a également été appliquée aux échantillons soumis à une charge cyclique. Cependant, les acquisitions à différents angles et plans, permettant l'estimation des vitesses du mode longitudinal, n'ont pas pu être réalisés en raison des limitations géométriques du dispositif expérimental. De plus, la méthode a permis d'obtenir des profils de vitesse complets dans l'un des plans considérés qui ont montré des changements de la vitesse du mode longitudinal lorsque les conditions de chargement appliquées varient. Ces résultats indiquent que cette dernière pourrait être employée comme un indicateur qualitatif d'endommagement pour le composite étudié.

L'étape finale de ce travail de recherche a consisté en l'évaluation de l'influence des endommagements résultant des événements d'impact à faible vitesse, des chargements en fatigue en traction-traction et de l'impact post-fatigue, sur la résistance résiduelle et la rigidité, respectivement, du composite tissé multicouche. Des essais de traction monotones jusqu'à la rupture ont été effectués sur des échantillons, conditionnés à 50 % d'humidité relative, soumis à des essais d'impact par poids tombant à différents niveaux d'énergie, à des chargements cycliques à différentes combinaisons de niveaux de contrainte et de nombres de cycles jusqu'à rupture, et à des chargements d'impact post-fatigue, respectivement. Pour des raisons de comparaison, les paramètres et les géométries d'essai étaient équivalents et comparables entre

les trois configurations de chargement. Le but de cette campagne expérimentale était d'évaluer qualitativement l'influence du pré chargement sur les propriétés résiduelles du composite stratifié. Il a été constaté que, quelles que soient les conditions de chargement, la rupture finale était toujours initiée à partir des bords des échantillons. De plus, sur les échantillons qui ont subi des événements d'impact à faible vitesse, les réseaux de fissures sont initiés au niveau des bords et se sont diffusés à travers la section du composite jusqu'à rejoindre l'endommagement de l'impact localisés au centre. En termes de propriétés résiduelles, aucune variation quantifiable n'a été observée dans les valeurs du module d'Young entre les échantillons endommagés et non endommagés. Cependant, lors de la mesure de la contrainte résiduelle, une diminution progressive des valeurs a été observée avec l'augmentation de l'énergie d'impact. Par conséquent, on pourrait lier la baisse de la résistance résiduelle à la propagation des endommagements à travers l'épaisseur et à l'indentation permanente.

Les échantillons soumis à des essais de fatigue par traction-traction ont tous présenté une rupture finale suivant une ligne droite nette. En effet, quelles que soient les conditions de chargement, la contrainte maximale et le nombre de cycles de chargement, le composite a adopté les mêmes schémas de rupture que dans le cas d'un échantillon non endommagé. Néanmoins, des différences en termes de contrainte résiduelle ont été constatées entre les échantillons non chargés et chargés en fonction des conditions de chargement. Il a été constaté que les échantillons chargés à un niveau de contrainte maximale de 60% σ_{UTS} ont démontré une perte de la résistance résiduelle allant de 12% à 19%, en fonction du nombre de cycles de chargement, ce qui était inférieur aux échantillons chargés à 35% σ_{UTS} et 45% σ_{UTS} comme niveaux de contrainte maximale. De plus, à mesure que le niveau de contrainte maximale diminuait, le nombre de cycles de chargement était considérablement plus élevé. Par conséquent, une réduction plus importante de la résistance a été observée.

La combinaison des chargements en impact et en fatigue était un phénomène très complexe à étudier. La prédiction des modèles de rupture finale et de la résistance résiduelle dépendait de la compréhension de l'aspect complexe de ce type de chargement combiné. En général, les fissures ont été initiées sur les bords et se sont propagées jusqu'à ce qu'elles rejoignent les endommagements localisés résultant de l'impact, comme cela a été remarqué sur les échantillons soumis à des évènements d'impact à faible vitesse uniquement. Cependant, certaines perturbations ont également été observées. Comme prévu, la charge de fatigue suivie des essais d'impact à faible vitesse a eu un effet significatif sur la zone de rupture finale. En effet, la rupture finale ne passait pas toujours par la zone impact. Néanmoins, on a constaté que

le chargement en fatigue générait des micro-endommagements dans différentes zones des échantillons, entraînant ainsi la détérioration de zones localisées, rendant la rupture finale plus susceptible de se produire dans ces zones. Une nette différence entre la résistance résiduelle des échantillons endommagés et non endommagés a été constatée. Étant donné qu'une évaluation quantitative n'était pas le but de la campagne d'essais d'impact post-fatigue, un grand nombre d'échantillons n'était pas disponible, donc seules des conclusions qualitatives ont été tirées sur cet aspect particulier. Ainsi, des observations intéressantes en termes de mode de rupture ont été discutées.

Dans le cadre de travaux ultérieurs, la simulation numérique des essais d'impact à faible vitesse, des essais de fatigue et des essais d'impact post-fatigue peut être réalisée pour comparer et comprendre l'initiation et de l'accumulation des endommagements. La méthode proposée, basée sur les ondes de Lamb, peut alors être appliquée pour comprendre correctement les trajectoires de propagation des ondes en présence de tout type d'endommagement. Cette simulation numérique permettra de comprendre comment les ondes ultrasonores se propagent dans le matériau multicouche et d'identifier la partie des signaux qui est affectée par l'endommagement.

Par ailleurs, le concept de jumeaux numériques est de plus en plus répandu dans le domaine industriel. L'ensemble des résultats expérimentaux et numériques permettra de constituer une base de données qui sera utilisée pour développer et valider les lois constitutives décrivant le comportement du matériau employé à l'échelle microscopique. Les jumeaux numériques des structures ou des pièces automobiles sont ensuite soumis à différents types de chargement. Les données obtenues sont comparées à celles obtenues expérimentalement sur des structures opérationnelles en utilisant la méthode des ondes de Lamb proposée. Les lois de comportement et les jumeaux numériques sont ainsi mis à jour.

La méthode expérimentale de propagation des ondes de Lamb proposée peut être automatisée. En effet, la méthode précédemment évaluée en termes d'efficacité et de performance peut être testée et ajustée pour être adaptée à d'autres types de matériaux. Dans un premier temps, cette méthode a été développée en utilisant des équipements de laboratoire de recherche. Il est possible d'utiliser le même principe pour développer un dispositif d'investigation portable permettant la rotation des capteurs (transducteurs) afin d'effectuer les opérations d'inspection sans avoir à déplacer ou démonter la structure. Ce dispositif peut être utilisé comme un outil d'aide à la décision pour déterminer la criticité des endommagements. En effet, les simulations

numériques d'une certaine charge ou combinaison de charges peuvent être représentatives de l'état d'endommagement des structures réelles et des pièces automobiles.

VII. Références

Agrawal, S., Kalyan Kumar, S., & Sarkar, P. (2013). Impact damage on fibre-reinforced polymer matrix composite – A review. Journal of Composite Materials, 48(3). https://doi.org/https://doi.org/10.1177/0021998312472217

Arif, M. F., Meraghni, F., Chemisky, Y., Despringre, N., & Robert, G. (2014). In situ damage mechanisms investigation of PA66 / GF30 composite : Effect of relative humidity. COMPOSITES PART B, 58, 487–495. https://doi.org/10.1016/j.compositesb.2013.11.001

Aymerich, F., & Meili, S. (2000). Ultrasonic evaluation of matrix damage in impacted composite laminates. Composite Part B, 31, 1–6.

Böhm, R., Hornig, A., Weber, T., Grüber, B., & Gude, M. (2020). Experimental and Numerical Impact Analysis of Automotive Bumper Brackets Made of 2D Triaxially Braided CFRP Composites. Materials, 13(3554). https://doi.org/10.3390/ma13163554

Bouvet, C. (2011). Dommages d'impact sur stratifié composite Dommages d'impact sur stratifié composite Impact damages on composite laminate. https://hal.archives-ouvertes.fr/hal-00597428

Castaings, M., Singh, D., & Viot, P. (2012). Sizing of impact damages in composite materials using ultrasonic guided waves. NDT and E International, 46, 22–31. https://doi.org/10.1016/j.ndteint.2011.10.002

Cramer, D. R., & Taggart, D. F. (2002). Design and Manufacture of an Affordable Advanced-Composite Automotive Body Structure. The 19th International Battery, Hybrid and Fuel Cell Electric Vehicle Symposium & Exhibition, 1–12.

EU Climate Action. (2019). Research and Development in Carbon Fibres & AdvancedHigh-Performance Composites Supply Chain in Europe: A roadmap for Challenges and the Industrial Uptake. https://ec.europa.eu/clima/citizens/eu_en

Giurgiutiu, V. (2015). Structural health monitoring of aerospace composites. In Elsevier (Ed.), Structural Health Monitoring of Biocomposites, Fibre-Reinforced Composites and Hybrid Composites. https://doi.org/10.1016/B978-0-08-102291-7.00003-4

Ishikawa, T., Amaoka, K., Masubuchi, Y., & Yamamoto, T. (2018). Overview of automotive

structural composites technology developments in Japan. Composites Science and Technology, 155, 221–246. https://doi.org/10.1016/j.compscitech.2017.09.015

Li, S., Sun, T., Liu, C., Yang, W., & Tang, Q. (2018). A study of laser surface treatment in bonded repair of composite aircraft structures. Royal Society Open Science. https://doi.org/10.1098/rsos.171272

Lopes, H., & Ribeiro, J. (2012). Structural health monitoring in composite automotive elements. In J. Carmo & J. Ribeiro (Eds.), New Advances in Vehicular Technology and Automotive Engineering (pp. 286–302). InTech Edition.

Lukaszewicz, D. (2013). Automotive composite structures for crashworthines. In A. Elmarakbi (Ed.), In Advanced Composite Materials for Automotive Applications: Structural Integrity and Crashworthiness.

Miqoi, N., Pomarede, P., Meraghni, F., Declercq, N. F., Guillaumat, L., Le Coz, G., & Delalande, S. (2021). Detection and evaluation of barely visible impact damage in woven glass fabric reinforced polyamide 6.6/6 composite using ultrasonic imaging, X-ray tomography and optical profilometry. International Journal of Damage Mechanics, 30(3), 323–348. https://doi.org/10.1177/1056789520957703

Mustapha, S., Ye, L., Dong, X., & Makki, M. (2016). Evaluation of barely visible indentation damage (BVID) in CF / EP sandwich composites using guided wave signals. Mechanical Systems and Signal Processing, 76–77, 497–517. https://doi.org/10.1016/j.ymssp.2016.01.023

Pomarède, P. (2018). Détection de l'endommagement dans un composite tissé PA66,6/6 Fibres de verre à l'aide de techniques ultrasonores en vue d'une prédiction de la durabilité de pièces automobiles. ENSAM ParisTech.

Pomarède, P., Meraghni, F., Peltier, L., Delalande, S., & Declercq, N. F. (2018). Damage Evaluation in Woven Glass Reinforced Polyamide 6 . 6 / 6 Composites Using Ultrasound Phase-Shift Analysis and X-ray Tomography. Journal of Nondestructive Evaluation, 123. https://doi.org/10.1007/s10921-018-0467-3

Praud, F. (2018). Multi-scale modelling of thermoplastic-based woven composites, cyclic and time-dependent behaviour. Ecole Nationale Supérieure d'Arts et Métiers.

Richardson, M., & Wisheart, M. (1996). Review of low-velocity impact properties of composite

materials. Composite Part A: Applied Science and Manufacturing, 1123–1131.

Robert, G., & Benaarbia, A. (2015). In fl uence of relative humidity and loading frequency on the PA6 . 6 thermomechanical cyclic behavior : Part II . Energy aspects. Polymer Testing, 41, 92–98. https://doi.org/10.1016/j.polymertesting.2014.10.012

Sarfraz, M. S., Hong, H., & Kim, S. S. (2021). Recent developments in the manufacturing technologies of composite components and their cost-effectiveness in the automotive industry: A review study. Composite Structures, 266(February), 113864. https://doi.org/10.1016/j.compstruct.2021.113864

Shah, S. Z. H., Karuppanan, S., Megat-Yusoff, P. S. M., & Sajid, Z. (2019). Impact resistance and damage tolerance of fiber reinforced composites: A review. Composite Structures, 217(February), 100–121. https://doi.org/10.1016/j.compstruct.2019.03.021

Shahzad, A. (2018). Investigation into fatigue strength of natural/synthetic fiber-based composite materials. In Mechanical and Physical Testing of Biocomposites, Fibre-Reinforced Composites and Hybrid Composites. Elsevier Ltd. https://doi.org/10.1016/B978-0-08-102292-4.00012-6

Sierakowski, R. L., & Newaz, G. M. (1995). Damage tolerance in advanced composites (T. P. Company (ed.); First edit).

Su, Z., & Ye, L. (2008). Lamb wave-based quantitative identification of delamination in composite laminates. In Delamination Behaviour of Composites: A volume in Woodhead Publishing Series in Composites Science and Engineering (pp. 169–216). Elsevier Ltd. https://doi.org/10.1533/9781845694821.2.169

US department of energy. (2011). Report on the first quadrennial technology review.

Nada MIQOI

Detection and quantification of damage in a polyamide-based composite submitted to the fatigue-pre and/or post-impact by advanced

Résumé

La détection et la caractérisation des endommagements dans des composantes automobiles fabriquées en matériaux composites restent un souci majeur que les constructeurs automobiles cherchent à confronter. Le projet de thèse a comme but l'analyse qualitative et quantitative des endommagements induits par différentes sollicitations dans un composite à matrice polyamide 66/6. Une méthodologie expérimentale qui repose sur l'utilisation des méthodes de contrôle non-destructif est établit et a pour but l'évaluation de l'endommagement induit par différents chargements. En effet, les mécanismes d'endommagement liés aux multiples sollicitations sont observés et leurs degrés de propagation en fonction du type et du niveau de chargement sont examinés. En outre, une investigation basée sur la propagation des ondes de Lamb est menée. A l'issu de cette étude, des indicateurs d'endommagement, permettant de quantifier l'état d'endommagement induit dans chaque échantillon inspecté, sont proposés. Finalement, des essais de traction quasi-statique sont réalisés pour la prédiction des propriétés résiduelles post-chargement.

Mots clés : Composite, Impact, Fatigue, Endommagement, Ultrasons, Ondes de Lamb.

Résumé en anglais

The detection and characterization of damage in automotive components made of composite materials remains a major concern that automotive manufacturers are seeking to address. The aim of this thesis project is to qualitatively and quantitatively analyze the damage induced by different solicitations in a polyamide 66/6 based composite intended for automotive applications. An experimental methodology relying on the use of non-destructive testing methods (NDT) is established and aims at the assessment of the damage induced by different types of loads. The damage mechanisms associated with the multiple loadings are observed and their degrees of propagation as a function of the type and level of loading are examined. Furthermore, a Lamb waves-based investigation is conducted. As a result of this study, several damage indicators are proposed to quantify the damage state induced in each inspected specimen. A good correlation between all experimental results is found indicating the efficiency of the developed Lamb waves-based method. Finally, quasi-static tensile tests are carried out to estimate the post-loading residual properties.

Keywords: Composites, Impact, Fatigue, dammage, ultrasound, Lamb waves.